Computational Modeling of Gas Adsorption, Separation, and Reactivity within Coordinatively Unsaturated Metal–Organic Framework Materials

A DISSERTATION
SUBMITTED TO THE FACULTY OF THE GRADUATE SCHOOL
OF THE UNIVERSITY OF MINNESOTA
BY

Allison Lee Dzubak

IN PARTIAL FULFILLMENT OF THE REQUIREMENTS
FOR THE DEGREE OF
Doctor of Philosophy

Professor Laura Gagliardi

March, 2015

Acknowledgements

I would like to thank my adviser, Professor Laura Gagliardi, for first encouraging me to enter graduate school and for providing me with the most incredible research opportunities. I would also like to thank Professor Christopher J. Cramer for kind and considerate ears, and Professor J. Ilja Siepmann for helpful suggestions. I would also like to thank Professor Berend Smit for his patience and practical perspective.

Of course I must thank my cohorts in the Gagliardi and Cramer groups. We have shared so much over the years, including (but not limited to): lunches, rehearsal presentations, happy hours, preliminary exam stresses and celebrations, CramLiardi bowling cups, conference road trips, birthday parties, occasionally regretful karaoke nights, and general shenanigans. Thanks to Bess Vlaisavljevich, Nora Planas Roure, David Semrouni, William Isley, Pere Miró, Dongxia Ma, Giovanni Li Manni, Ivan Infante, César Beuchat, Abdul Rehaman Moughai Shahi, Riccardo Spezia, Antonio Sanchez Diaz, Zahid Ertem, Stuart Winikoff, Joshua Borycz, Rebecca Carlson, Chad Hoyer, Huiliang Shi, Yiyi (Sarah) Yao, Aaron League, and Alison McManus. I would specifically like to thank: Bess for being an enduring and admirable role model, Nora for being an amazing intermediary/interpreter and a terrible 'bad cop', David for helping me maintain some sanity amongst the chaos, Will for all the support and restorative walks around Smith, Pere for technical troubleshooting and for being the token hipster barista, and Dongxia for always explaining things logically. Additionally, thanks to collaborators Li-Chiang Lin, Joseph Swisher, Roberta Poloni, and Sergey Maximoff for making trips to Berkeley so enjoyable and rewarding.

Thanks to my family, friends, and loved ones for all of the support. Specific thanks to Mom, Dad, Patrick Thomas, and the late Phyllis Clark. Your generosity made this possible.

Dedication

For my parents, Mary and Alan

For my brother, John

& For Matt

Abstract

In this work, computational methodologies are used to investigate the behavior of Metal-Organic Frameworks (MOFs) that are of potential utility in gas separation applications. MOFs are three-dimensional porous materials that are desirable due to their high porosity and internal surface area. Given the myriad of possible framework topologies, computational tools are necessary in order to aid and complement experimental efforts. The focus of this dissertation is specifically coordinatively unsaturated MOFs, a subclass of MOFs for which there are additional computational challenges in treating the exposed metal site. The collection of studies presented here are grouped into four categories: force field parameterization, gas reactivity within MOFs, nature of adsorbate–MOF bonding, and multireference treatment of metal–metal bonds. *Ab initio* force fields are parameterized for various MOF–gas interactions, where the the NonEmpirical Modeling (NEMO) philosophy is adopted. Wave-Function Theory (WFT) is used for the calculation of the reference energies of the intermolecular terms. Møller-Plesset Perturbation Theory to 2^{nd} order (MP2) and Complete-Active Space Perturbation Theory to 2^{nd} order (CASPT2) are applied for closed-shell and open-shell cases, respectively. These derived force fields are utilized in Grand Canonical Monte Carlo (GCMC) simulations for the MOF + adsorbate systems. Results from GCMC simulations include adsorption isotherms, Henry coefficients, and isosteric heats of adsorption that are compared with the available experimental data, demonstrating the predictive capabilities of this computational procedure. A reaction mechanism between CO_2 and amines grafted within the pores of a MOF is proposed based on DFT results, and both DFT and CASPT2 results are utilized to elucidate the nature of a reactive Fe-Oxo intermediate at the exposed Fe site in the MOF. Coupled Cluster (CC), MP2, CASPT2, and DFT are all used to rationalize adsorbate–MOF bonding trends, and the Extended-Transition State Natural Orbitals for Chemical Valence (ETS-NOCV) is used as a comparative tool. Complete-Active Space Self-Consistent Field (CASSCF) and CASPT2 are used for the studies of metal–metal multiple bonded species, and compared with results from DFT.

Contents

List of Tables

List of Figures

List of Acronyms

Acronym	Meaning
ADF	Amsterdam Density Functional
ANO-RCC	Atomic Natural Orbital Relativistic Correlation Consistent
AO	Atomic Orbital
B2PLYP	functional based on Becke and Lee-Yang-Parr
B3LYP	Becke 3-parameter Lee-Yang-Parr funciontal
bdc	benzenedicarboxylate
BET	Brunauer-Emmett-Teller
BHM	Born-Huggins-Mayer
BO	Bond Order
BP86	Becke Perdew86 functional
BSSE	Basis Set Superposition Error
CAS	Complete-Active Space
CASPT2	Complete-Active Space Perturbation Theory to 2^{nd} order
CASSCF	Complete-Active Space Self-Consistent Field
CASSI	Complete-Active Space State Interaction
CBS	Complete Basis Set
CCS	Carbon Capture and Sequestration
CCSD	Coupled Cluster Singles and Doubles
CD	Cholesky Decomposition
CM5	Charge Model 5
CN	Coordination Number

Continued on next page

Continued from previous page

Acronym	Meaning
COSMO	Conductor-like Screening Model
CP	CounterPoise
CPO-27	Coordination Polymer of Oslo *(also see MOF-74)*
CPU	Central Processing Unit
def	default Karlsruhe basis sets
def2	2^{nd} generation default Karlsruhe basis sets
DFT	Density Functional Theory
DKH	Douglas-Kroll-Hess
DLPOLY	software package developed at Daresbury Laboratory
dobdc	2,5-dioxido-1,4-benzenedicarboxylate
dobpdc	4,4'-dioxido-3,3'-biphenyldicarboxylate
DZP	Double Zeta (ζ) plus Polarization
DZVP	Double Zeta (ζ) Valence plus Polarization
EBO	Effective Bond Order
ECP	Effective Core Potential
EFP	Effective Fragment Potential
ETS	Extended Transition State
EXAFS	Extended X-ray Absorption Fine Structure
FF	Force Field
FNO	Frozen Natural Orbital
FSR	Formal Shortness Ratio
GCMC	Grand Canonical Monte Carlo
HF	Hartree-Fock
HOMO	Highest Occupied Molecular Orbital
IAST	Ideal Adsorbed Solution Theory
IRMOF	IsoReticular Metal-Organic Framework
IRMOF-1	$Zn_4O(bdc)_3$ *(also see MOF-5)*
KS	Kohn-Sham
LMCT	Ligand-to-Metal Charge Transfer

Continued on next page

Continued from previous page

Acronym	Meaning
LoProp	Localization of Properties
LPNO	Local-Pair Natural-Orbital
LUMO	Lowest Unoccupied Molecular Orbital
M06	Minnesota 06 functional
M11	Minnesota 11 functional
MB	Minimal Basis
MBO	Mayer Bond Order
MC	Monte Carlo
MD	Molecular Dynamics
MEA	Monoethanolamine
MLCT	Metal-to-Ligand Charge Transfer
mmen	N,N'-dimethylethylenediamine
MO	Molecular Orbital
MOF	Metal-Organic Framework
MOF-5	$Zn_4O(bdc)_3$ *(also see IRMOF-1)*
MOF-74	M_2(dobdc) where M=Metal *(also see CPO-27)*
MOLCAS	software package developed at Lund University
MP2	Møller-Plesset perturbation theory to 2^{nd} order
NBO	Natural Bond Order
NEMO	NonEmpirical Modeling
NOCV	Natural Orbitals for Chemical Valence
ORCA	software package written by F. Neese
PAW	Projector-Augmented Wave
PBE	Perdew-Burke-Ernzerhof functional
PBE0	Perdew-Burke-Ernzerhof hybrid functional
PEC	Potential Energy Curve
PES	Potential Energy Surface
PT2	Perturbation Theory to 2^{nd} order
QZVP	Quadruple Zeta (ζ) Valence plus Polarization

Continued on next page

Continued from previous page

Acronym	Meaning
RDF	Radial Distribution Function
RI	Resolution of the Identity
ROHF	Restricted Open-shell Hartree-Fock
ROMP2	Restricted Open-shell Møller-Plesset perturbation theory to 2^{nd} order
SAPT	Symmetry Adapted Perturbation Theory
SCF	Self-Consistent Field
SDD	pseudopotentials using Dunning and Stuttgart/Dresden ECPs
SDF	Spatial Distribution Function
SI	Supporting Information
SIBFA	Sum of Interactions Between Fragments Ab initio computed
SIESTA	Spanish Initiative for Electronic Simulations with Thousands of Atoms
SO	Spin-Orbit
SV(P)	Split-Valence partially Polarized
SVP	Split-Valence Polarized
TD-DFT	Time-Dependent Density Functional Theory
TE	Thermal Energy
TIP3P	3 site water model
TPSSh	Tao, Perdew, Staroverov, and Scuseria hybrid functional
TraPPE	Transferable Potentials for Phase Equilibria
TURBOMOLE	software package developed at the University of Karlsruhe
TZ2P	Core Double Zeta (ζ) Valence Triple Zeta (ζ) Doubly Polarized
TZVP	Triple Zeta (ζ) Valence plus Polarization
$+U$	Hubbard U Correction
UFF	Universal Force Field
VACF	Velocity AutoCorrelation Function
VASP	Vienna Ab initio Simulation Package
vdW	van der Waals

Continued on next page

Continued from previous page

Acronym	Meaning
vdW-DF	van der Waals Density Functional
vdW-DF2	van der Waals Density Functional 2nd version
VDZP	Valence Double Zeta (ζ) plus Polarization
VTZP	Valence Triple Zeta (ζ) plus Polarization
WFT	Wave-Function Theory
xc	exchange-correlation
ZORA	Zero-Order Regular Approximation
ZPE	Zero-Point Energy

Preface

This dissertation contains copyrighted material that has been reproduced and adapted with permission. The citations and links are presented below.

Chapter 2: Force Field Parameterization

***Ab Initio* Carbon Capture in Open-Site Metal-Organic Frameworks**
A. L. Dzubak, L. -C. Lin, J. Kim, J. A. Swisher, R. Poloni, S. N. Maximoff, B. Smit, and L. Gagliardi. *Nature Chem.* **2012**, *4*, 810. Copyright 2012, Nature Publishing Group. `http://www.nature.com/nchem/journal/v4/n10/abs/nchem.1432.html`

CO_2 Adsorption in Fe_2(dobdc): A Classical Force Field Parameterized from Quantum Mechanical Calculations
J. Borycz, L.-C. Lin, E. D. Bloch, J. Kim, A. L. Dzubak, R. Maurice, D. Semrouni, K. Lee, B. Smit, L. Gagliardi. *J. Phys. Chem. C* **2014**, *118*, 12230. Copyright 2014, American Chemical Society. `http://pubs.acs.org/doi/abs/10.1021/jp500313j`

Uranyl–Peroxide Nanocapsules in Aqueous Solution: Force Field Development and First Applications
P. Miró, B. Vlaisavljevich, A. L. Dzubak, S. Hu, P. C. Burns, C. J. Cramer, R. Spezia, L. Gagliardi. *J. Phys. Chem. C* **2014**, *118*, 24730. Copyright 2014, American Chemical Society. `http://pubs.acs.org/doi/abs/10.1021/jp504147s`

Chapter 3: Gas Reactivity within MOFs

The Mechanism of Carbon Dioxide Adsorption in an Alkylamine-Functionalized Metal-Organic Framework

N. Planas, A. L. Dzubak, R. Poloni, L. -C. Lin, A. McManus, T. M. McDonald, J. B. Neaton, J. R. Long, B. Smit, L. Gagliardi. *J. Am. Chem. Soc.* **2013**, *135*, 7402. Copyright 2013, American Chemical Society. `http://pubs.acs.org/doi/abs/10.1021/ja4004766`

Oxidation of Ethane to Ethanol by N_2O in a Metal-Organic Framework with Coordinatively Unsaturated Iron(II) Sites

D. J. Xiao, E. D. Bloch, J. A. Mason, W. L. Queen, M. R. Hudson, N. Planas, J. Borycz, A. L. Dzubak, P. Verma, K. Lee, F. Bonino, V. Crocella, J. Yano, S. Bordiga, D. G. Truhlar, L. Gagliardi, C. M. Brown, J. R. Long. *Nature Chem.* **2014**, *6*, 590. Copyright 2014, Nature Publishing Group. `http://www.nature.com/nchem/journal/v6/n7/abs/nchem.1956.html`

Chapter 4: Nature of Adsorbate–MOF Bonding

Design of a Metal-Organic Framework with Enhanced Back Bonding for Separation of N_2 and CH_4

K. Lee, W. C. Isley III, A. L. Dzubak, P. Verma, S. J. Stoneburner, L. -C. Lin, J. D. Howe, E. D. Bloch, D. A. Reed, M. R. Hudson, C. M. Brown, J. R. Long, J. B. Neaton, B. Smit, C. J. Cramer, D. G. Truhlar, L. Gagliardi. *J. Am. Chem. Soc.* **2014**, *136*, 698. Copyright 2014, American Chemical Society. `http://pubs.acs.org/doi/abs/10.1021/ja4102979`

Reversible CO Binding Enables Tunable CO/H_2 and CO/N_2 Separations in Metal-Organic Frameworks with Exposed Divalent Metal Cations

E. D. Bloch, M. R. Hudson, J. A. Mason, S. Chavan, V. Crocellà, J. D. Howe, K. Lee, A. L. Dzubak, W. L. Queen, J. M. Zadrozny, S. J. Geier, L. -C. Lin, L. Gagliardi, B.

Smit, J. B. Neaton, S. Bordiga, C. M. Brown, J. R. Long. *J. Am. Chem. Soc.* **2014**, *136*, 10752. Copyright 2014, American Chemical Society. http://pubs.acs.org/doi/abs/10.1021/ja505318p

Chapter 5: Multireference Treatment of Metal–Metal Bonds

A Combined Spectroscopic and Computational Study of a High-Spin S = 7/2 Diiron Complex with a Short Iron–Iron Bond

C. M. Zall, D. Zherebetskyy, A. L. Dzubak, E. Bill, L. Gagliardi, C. C. Lu. *Inorg. Chem.* **2012**, *51*, 728. Copyright 2012, American Chemical Society. http://pubs.acs.org/doi/abs/10.1021/ic202384b

Assessing Metal–Metal Multiple Bonds in Cr–Cr, Mo–Mo, and W–W Compounds and a Hypothetical U–U Compound: A Quantum Chemical Study Comparing DFT and Multireference Methods

G. Li Manni, A. L. Dzubak, A. Mulla, D. W. Brogden, J. F. Berry, L. Gagliardi. *Chem. Eur. J.* **2012**, *18*, 1737. Copyright 2012, John Wiley and Sons. http://onlinelibrary.wiley.com/doi/10.1002/chem.201103096/abstract

Chapter 1

Introduction

1.1 Background Information

Currently there are formidable global energy challenges such as climate change, natural gas utilization, and nuclear energy concerns. The work contained herein involves the investigation of selected Metal–Organic Framework (MOF) materials that may be useful in addressing such challenges.

Anthropogenic CO_2 emissions must be scaled down in order to mitigate climate change issues, and one proposed solution is Carbon Capture and Sequestration (CCS). At stationary sites such as coal-fired power plants, post-combustion capture would involve an 'end-of-pipe' apparatus to selectively separate CO_2 from the flue gas, while ideally not imposing a high energy penalty for solvent (or material) regeneration. The typical flue gas composition by weight is approximately 70-75% N_2, 10-15% CO_2, 5-7% H_2O, 3-4% O_2, and trace amounts of CO, SO_x and NO_x.[1]

$$2RNH_2 + CO_2 \underset{H_2O}{\overset{\Delta}{\rightleftharpoons}} [RNHCOO]^- + [RNH_3]^+$$

Figure 1.1: General Amine–CO_2 reaction typical for industrial CO_2 capture applications.

The current industrial CO_2 capture technology involves the reaction of CO_2 with an aqueous solution of amines, which is shown in Figure 1.1. In this scheme, the CO_2 reacts

selectively with an amine (typically monoethanolamine, MEA), yielding an ammonium carbamate and a protonated amine in solution. While this process is very selective for CO_2 over the other flue gases, it imposes a harsh energy penalty on the power plant in order to reverse the reaction with heat for solvent regeneration.

Some selected MOFs (illustrated in Figures 1.2 and 1.3) are examined for post-combustion CO_2 capture applications in Sections 2.1 and 3.1. An advantage of these materials over typical amine solutions is that they could curtail the energy cost, since a large volume of water would not have to be heated for solvent regeneration. Given the % composition of flue gas, selective CO_2 separation from N_2 is important for post-combustion capture, and is considered in Section 2.1. Although CO_2 is selectively adsorbed over N_2 in those MOFs, the materials would not be selective to CO_2 over H_2O. For that reason, the utilization of amines is revisited in Section 3.1, where diamine functionalizities are grafted within a MOF in an attempt to achieve high selectivity for CO_2 even in the presence of water, while still avoiding the use of aqueous solvents. Given the trace amounts of CO present, the separation of CO from N_2 is also considered in Section 4.2.

For the utilization of natural gas, N_2 is a contaminant that must be removed. This separation of N_2 from methane poses difficulties, in that both gases lack a permanent dipole and have similar polarizabilities, boiling points, and kinetic diameters. Although cryogenic distillation is currently utilized for separation of these gases, the cost- and capital-intensive nature of this separation has led to development of a number of competing processes, such as membrane- or kinetics-based separations, which generally suffer from low selectivities.[2] This particular separation using MOFs is explored in Section 4.1. Additionally, the conversion of ethane to ethanol is investigated in Section 3.2.

The mobility of actinides in environmental conditions is of great interest, specifically in water. The solution chemistry of the uranyl ion, $[U^{VI}O_2]^{2+}$, the most common form of uranium in aqueous solution, is central to the development of an advanced nuclear energy cycle and in developing remediation strategies for contaminated sites.[3] It is still difficult to predict the behavior of actinides, and much more difficult to gain nanoscale control over actinide materials. The properties and behavior of the uranyl ion and its function as a building block for actinide nanocapsules is explored in section 2.3.

Metal–Organic Frameworks (MOFs) are three-dimensional materials, composed of

organic linkers connected through metal vertices, that are ubiquitous for their high internal surface area and porosity. Two examples studied herein are illustrated in Figure 1.2, where $Zn_4O(bdc)_3$ (bdc = benzenedicarboxylate) is commonly referred to as MOF-5 (left) and $M_2(dobdc)$ (M = Metal, dobdc = 2,5-dioxido-1,4-benzenedicarboxylate) is commonly referred to as MOF-74 or CPO-27 (right). Their respective metal vertices are shown in the center to emphasize the difference between coordinatively saturated metal sites (top, MOF-5) and coordinatively unsaturated metal sites (bottom, MOF-74).

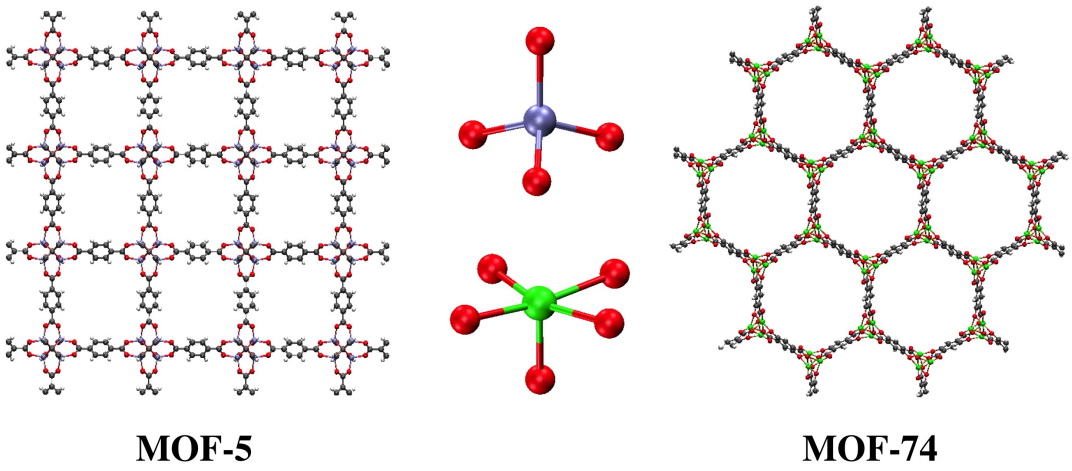

Figure 1.2: Two dimensional truncated representation of the periodic MOF-5 (left) and MOF-74 (right) framework topologies, with their respective metal vertices (center). The tetrahedral coordinatively saturated metal site, as in MOF-5 (top) is compared to the coordinatively unsaturated metal site, as in MOF-74 (bottom).

The MOF-5 metal node is a saturated tetrahedral geometry, while the MOF-74 metal node is an unsaturated octahedral geometry where the 6^{th} site is 'open' as it was previously occupied by a solvent molecule that has been evacuated from the framework post-synthetically. The importance of these unsaturated metal sites is that they provide an opportunity for the metal site to interact with gas mixtures for potentially unique separations and reactivity that would otherwise not be possible in solution or with molecular species. MOF-74 has been synthesized with different metal analogues, some of which are investigated here. Other analogues not yet experimentally synthesized (specifically V-MOF-74 in Section 4.1) have been studied here theoretically.

As previously mentioned, there is interest in grafting diamine functionalities within the MOF for carbon capture applications. In order to accomplish this, and extended version of MOF-74 was synthesized, which has pores large enough to accommodate the amine functionalities. This is illustrated in Figure 1.3, where the conventional MOF-74 with its dobdc linker (left) is compared to the extended analogue (right) with a dobpdc (4,4-dioxido-3,3-biphenyldicarboxylate) linker. The amine functionalities grafted within the extended MOF are shown in greater detail, along with their reactivity with CO_2, in Section 3.1.

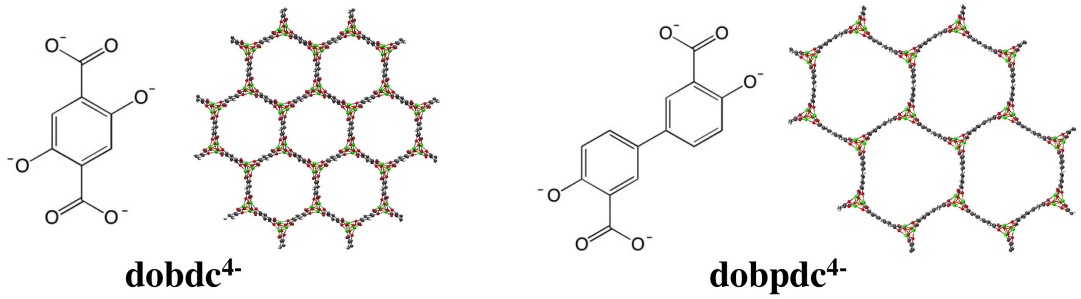

Figure 1.3: Comparison between (left) Mg_2(dobdc) (i.e. Mg-MOF-74) and its extended-linker analogue (right) Mg_2(dobpdc) in which the pores are large enough to graft diamine functionalities may be at the open-metal sites.

In order to predict the performance of a given MOF for a specific separation application (e.g. CO_2/N_2 for post-combustion carbon capture), reliable adsorption properties of the gases within the MOF must be computed. One could use quantum chemical levels of theory such as wave-function theory (WFT) or density functional theory (DFT) to obtain relative binding energies or enthalpies of different gases at various adsorption sites on the MOF, such as what was done for CH_4 versus N_2 binding described in Section 4.1. From quantum chemically calculated electronic binding energies, a number of corrections could be applied in order to get adsorption at different temperatures. Another approach might be taken, in which Langmuir adsorption behavior is assumed and isotherms are fitted from DFT binding energy data.[4]

A more common approach is to use classical molecular simulations with a monte carlo (MC) algorithm in order to obtain the relative adsorption properties of interest.

This involves the evaluation of an energy expression at millions of points, which becomes computationally impractical at the quantum level of theory. It is for this reason that force fields are commonly utilized in these types of simulations, which makes it possible to perform the millions of computations required. Force fields are composed of energy expressions that approximate the functional behavior of the system with some associated parameters that are typically pre-determined for atom-types or atom-pairs. The types of functions and parameters may be divided into two general classes, bonded terms and non-bonded terms. The bonded terms contain expressions for bond stretching, angle bending, and torsional motion (among others), while the non-bonded terms contain expressions for the intermolecular interactions.

There are notable cases of framework flexibility, where the framework pore can expand or contract upon in response to some external stimuli (e.g. pore filling or evacuation).[5] The MOFs studied in this work have not exhibited such behavior, for this reason we commonly approximated the framework model as rigid. For such cases, the bonded terms of the MOF are not needed, so the work here focuses on the non-bonded (MOF–gas) interactions. From this point onward, the parameters discussed should be thought of as the non-bonded intermolecular terms unless otherwise noted.

There are two broad approaches to force field parameterization: empirical versus *ab initio*. In the former approach, the energy expressions and parameters are fitted against an existing set of experimental data, with the goal being to minimize the error of the evaluated energy for the entire set. This results in a set of effective parameters that, in principle, should be used for systems and properties similar to those against which the parameters were fitted. This poses a problem for systems that may be radically different from those used in the fitting or training sets. This is specifically an issue with MOFs, since not only is there a huge variety in the choice of metal and linker, but specifically metals that are coordinatively unsaturated will have much different interactions with gases than the same metal would have in a fully coordinated environment. For these reasons, we have chosen to adopt the *ab initio* approach, where quantum chemical energies are used as the reference data, opposed to the empirical approach where the existence of reliable experimental data is a requirement for the fitting. However, then the size of the system and quantum level of theories are both limited based on the computational resources available.

Most *ab initio* approaches to force field parameterization involve some type of energy partitioning, such that the functional forms of the energy terms are physically represented and each term can be systematically improved. For example, the total intermolecular interaction energy is commonly partitioned into contributions that are either electrostatic or van der Waals. The electrostatic contribution can be classically understood, while the van der Waals contribution results purely from the quantum chemical behavior of the interacting systems.

The electrostatic energy contribution could be thought of as a sum of point-charge interactions between molecules in space. This so-called point charge approximation involves the assignment of a charge value to a site such as an atomic center. Once assigned, the evaluation of the charge-charge contribution to the electrostatic interaction is a straightforward pairwise-additive sum as a function of the atomic site separations, r_{ij}. The primary difficulty here is that there is no single procedure to divide and distribute the total molecular electronic density onto the atomic sites. For this reason, many such localization procedures and charge models exist, each with their advantages and disadvantages. While the electrostatic contribution can be systematically improved with the addition of higher-order terms e.g. charge-dipole, dipole-dipole, etc. interactions, many force fields truncate the expansion at the charge-charge term. With this in mind, many point charge models may have values either higher or lower than conventionally expected, since they are effectively attempting to include the higher-order terms.

Intermolecular polarization is an electrostatic contribution to the total energy, which is the change in the molecular electrostatic field due to the presence of an interacting molecule, which results in a change of the electrostatic field in the first molecule, etc. This effect may be calculated iteratively until convergence, but is rarely included in the classical molecular simulations due to the additional time the iterations would require at each monte carlo step.

The van der Waals contribution to the total interaction energy, for historical reasons, is conventionally represented by a Lennard-Jones potential:

$$V_{\mathrm{LJ}} = 4\epsilon_{ij}\left[\left(\frac{\sigma_{ij}}{r_{ij}}\right)^{12} - \left(\frac{\sigma_{ij}}{r_{ij}}\right)^{6}\right] \tag{1.1}$$

where σ_{ij} and ϵ_{ij} are the pre-determined parameters, and r_{ij} is the interatomic separation. The r^{12} term approximates the exchange-repulsion energy, and the r^6 term approximates the dispersion energy. While there are roots for the r^6 term from perturbation theory, the r^{12} term was adopted for computational convenience. Just as the electrostatic energy is improved by additional terms in the multipolar expansion, the dispersion energy is also improved through the use of additional terms. In order to reproduce the quantum chemical behavior of the exchange repulsion, we represent it by an exponential term throughout this work.

There are many examples of molecular simulations of gas adsorption in MOFs utilizing existing force fields, which perform well for cases in which the interactions are dominantly of the van der Waals type i.e. when no strong metal–gas interactions are present. However, with the emergence of these coordinatively unsaturated MOFs, it becomes clear that the existing force fields no longer adequately describe the MOF–gas interactions, specifically at low pressures when the metal–gas interactions are dominant. This inadequacy is demonstrated by the left hand side of Figure 1.4, where Grand Canonical Monte Carlo (GCMC) simulations were used to predict CO_2 adsorption in Mg-MOF-74. These simulations utilized the Universal Force Field (UFF) with Mulliken atomic point charges, the same procedure which functioned well for other gas–MOF simulations. As shown by the right hand side of Figure 1.4, the primary adsorption site for CO_2 is located at the exposed Mg metal node. These exposed Mg sites become saturated before the rest of the pore fills with weaker adsorption sites, which can be seen in the experimental isotherm with the sharp adsorption increase at low loading (Mg–Oxygen of CO_2), followed by saturation and pore filling. It was this discrepancy between experimental and simulation predictions that motivated the work performed in Section 2.1.

In Section 2.1, we applied an *ab initio* interaction energy partitioning technique to MOF–gas interactions for the first time in the reported literature (to our knowledge). This was done in order to parameterize intermolecular force fields from quantum chemical reference data that can accurately describe the MOF–gas interactions when these exposed metal sites are present. The already existing partitioning technique that we used (NEMO) had already been applied successfully to other systems, but had never been applied to study a periodic system such as a MOF. Details of the methodological

choices and results results are presented in Section 2.1 and the associated supplementary information.

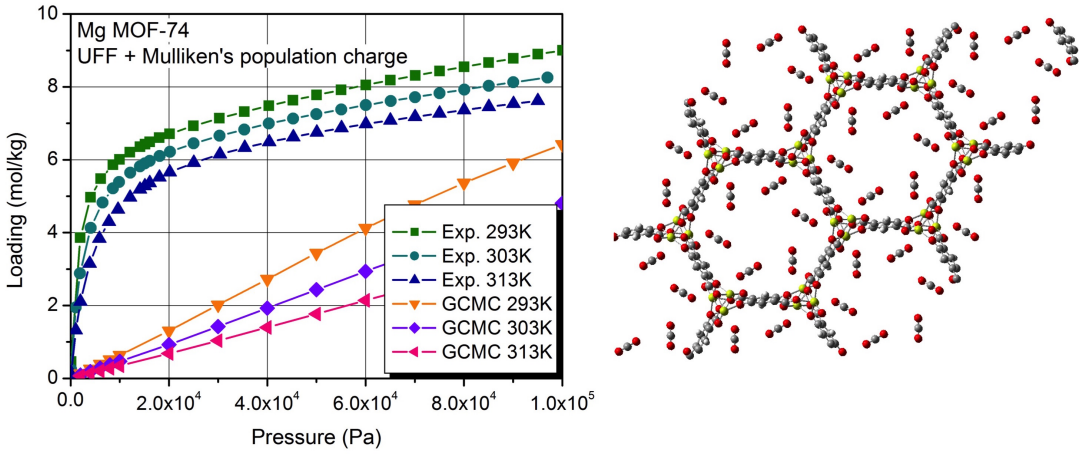

Figure 1.4: Adsorption isotherms of CO_2 in Mg-MOF-74 comparing experimental data with simulation predictions using UFF (left) and a two dimensional visual truncated representation of the MOF–CO_2 system at a loading of 1 CO_2 per 1 Mg center (right).

As shown in Section 2.1 Results, one of the notable findings was that although the low pressure regime was well-described, the simulated isotherm overestimated the gas adsorption at higher pressures compared with the experimental data. Agreement between simulation and experiment could only be achieved after scaling the experimental data, which would most likely be attributed to computational errors or models that are too approximate. However, as shown by Figure 2.3, this can be explained by structural defects in the experimental structures. This has resulted in studies examining how to incorporate experimental defects e.g. pore blockages in the theoretical models. Another consideration that results from this finding is that the gas–gas cooperative effects, in some cases such as this, may enhance adsorption so that it exceeds what might be expected from a Langmuir fitting.

Although the same *ab initio* approach was applied to the Zn-MOF-74 analogue, the quantum chemical method used to obtain the reference data was a closed-shell single-reference implementation. This was unfortunately limiting, since many other M-MOF-74 (M=Metal) analogues have been experimentally synthesized, and should be

investigated in the future regardless of the nature of the metal. An extension to the Fe-MOF-74 analogue was performed, and is described in Section 2.2. In this case, the Fe center in Fe-MOF-74 has a quintet d^6 single-reference electronic configuration, but addressing its open-shell nature had not been done previously. This was done within a multi-reference software implementation, extending the possibility for multi-reference MOF–adsorbate force field parameterization in the future.

This approach is shown to be transferable to the more conventional coordinatively saturated MOFs; however it must be noted that the parameter *values* are not transferable between different MOF systems, but that the same procedure is transferable to obtain parameters for the other MOFs. This can lead to a very arduous and time-consuming parameterization procedure, which would be impossible to apply to databases of thousands of structures (which would be ideal for MOF application screening). A simplified parameterization procedure was applied in Section 2.2 to minimize the number of quantum chemical calculations required to develop the force field. The parameterization scheme was simplified by computing new parameters only for the interaction between the open metal site and the oxygen of CO_2.

This parameterization scheme has only been applied for cases in which the MOF systems may be assumed rigid (stimuli unresponsive). In Section 2.3, the same energy partitioning scheme is used to develop a force field to study uranyl-peroxide nanocapsules. In addition to the non-bonded terms, a 'building block' approach was taken in order to scale the MP2 results to larger systems, and the bonded terms are also parameterized.

While molecular simulations are effective for the purposes of non-reactive separation applications, these are strictly non-reactive force fields. In the force field applications previously mentioned, there is no bond making or bond breaking in the simulations. Briefly mentioned earlier, one of the advantages of having these exposed metal sites within the MOF is that species can be grafted there to perform unprecedented chemistry that would otherwise not occur in other media e.g. aqueous solution. In Mg_2(dobpdc), the 'extended-linker' version of Mg-MOF-74 shown on the right hand side of Figure 1.3, the pores were large enough to introduce diamines where one end of the amine bonded to the unsaturated metal site, and the other end of the amine is left dangling in the pore to react with the gases upon entrance into the pore. A cartoon of the

amine grafted MOF is shown within the plot of Figure 1.5, where the grafted diamine is N,N'-dimethylethylenediamine, which we hereafter refer to as mmen.

The simplified overall reaction scheme for industrial CO_2 capture using aqueous solutions of amines is shown in Figure 1.1. Since the reaction occurs in aqueous solution, the products are charged species which are stabilized by the polar media. It is important to note that the reaction stoichiometry is 2:1 (amine:CO_2). This is a relevant mechanistic detail of the reaction, since after the N–C bond starts to form, the second amine comes in and functions as the proton acceptor to yield the products shown in Figure 1.1.

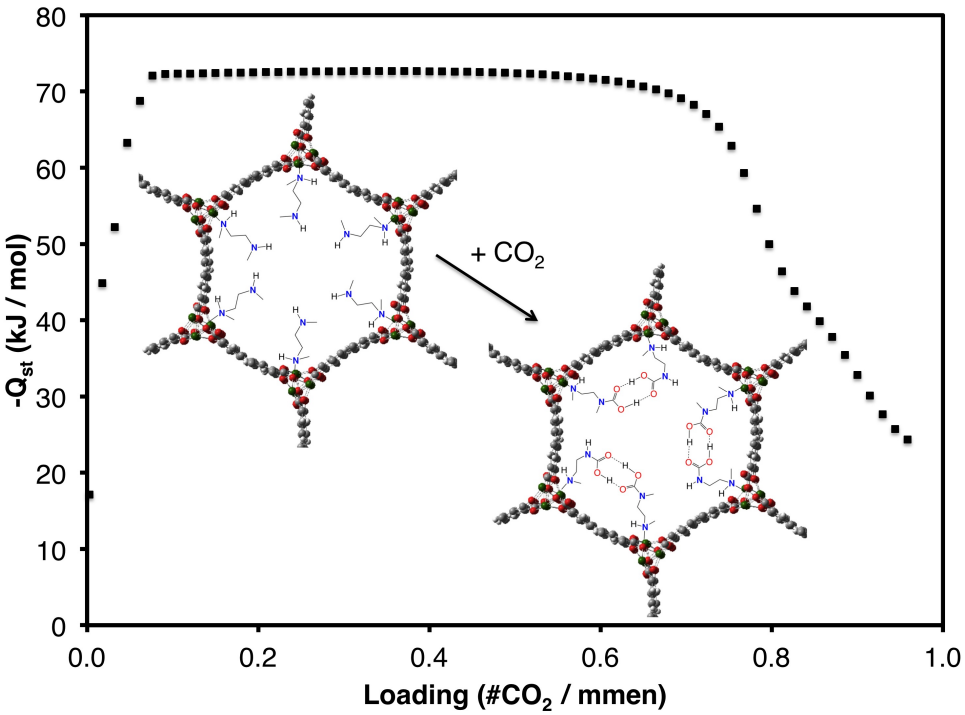

Figure 1.5: Isosteric heat of CO_2 adsorption in the mmen-grafted Mg_2(dobpdc) as a function of (CO_2 / mmen) loading. Inset: cartoon of (left) mmen-grafted Mg_2(dobpdc) and (right) DFT proposed final product.

Once the mmen were grafted within the MOF and CO_2 was introduced into the pores, the isosteric heat of adsorption plot shown in Figure 1.5 raised three important

questions that could not be explained by the simple reaction scheme in Figure 1.1. The first was that the reaction stoichiometry had to be greater than 2:1 (amine:CO_2), since the primary adsorption site (dangling end of the amine) becomes saturated after the ratio 0.5 CO_2 / mmen. The second was that the value of the heat of adsorption was approximately -71 kJ/mol, which is smaller in magnitude than what would be expected for the conventional reaction in aqueous solution. The final was that there was some kind of critical pressure of CO_2 that was required in order for the primary adsorption site to become available. This work was motivated by these experimental observations that could not be explained by the available commonly accepted reaction mechanism. In Section 3.1, we attempt to explain these experimental observations with a proposed mechanism at the DFT level of theory.

Although more details are presented in Section 3.1 and the associated supplementary information, a summary of the previously proposed amine–CO_2 reaction mechanisms are summarized in Figure 1.6. The zwitterion mechanism (Scheme 1-3) is extensively used to describe chemical kinetics observed for the CO_2 capture process in aqueous solutions of primary and secondary alkanolamines,[6,7,8] This two-step mechanism suggests that the reaction between CO_2 and an amine (denoted here as AmH) proceeds through the formation of a zwitterion as an intermediate which is consecutively deprotonated by a base (B) present in the reaction media. More recently, the so-called termolecular mechanism has been proposed as an alternative mechanism that can also explain the kinetics observed for such systems (Scheme 4).[9,10,11] In this mechanism the amine bonding to CO_2 and proton transfer to the base (B) take place simultaneously, and the carbamate formation occurs in a single-step reaction. Several researchers claim that the latter mechanism was best-suited to describe the nature of reactions occurring in these aqueous systems.[9,10,12,13,14] Nevertheless in both mechanisms, when the role of a base is played by a second amine the overall reaction, which accounts for carbamate/protonated-amine formation in solution, corresponds to an overall 1:2 (CO_2:amine) reaction stoichiometry (Scheme 5). Some recent studies have shown that the main product for the reaction of CO_2 with amines in aprotic polar solvents is free carbamic acid (Scheme 6), whereas in aprotic apolar solvents the same reactants yield the precipitation of the corresponding [carbamate][ammonium] salt (Scheme 7).[15,16]

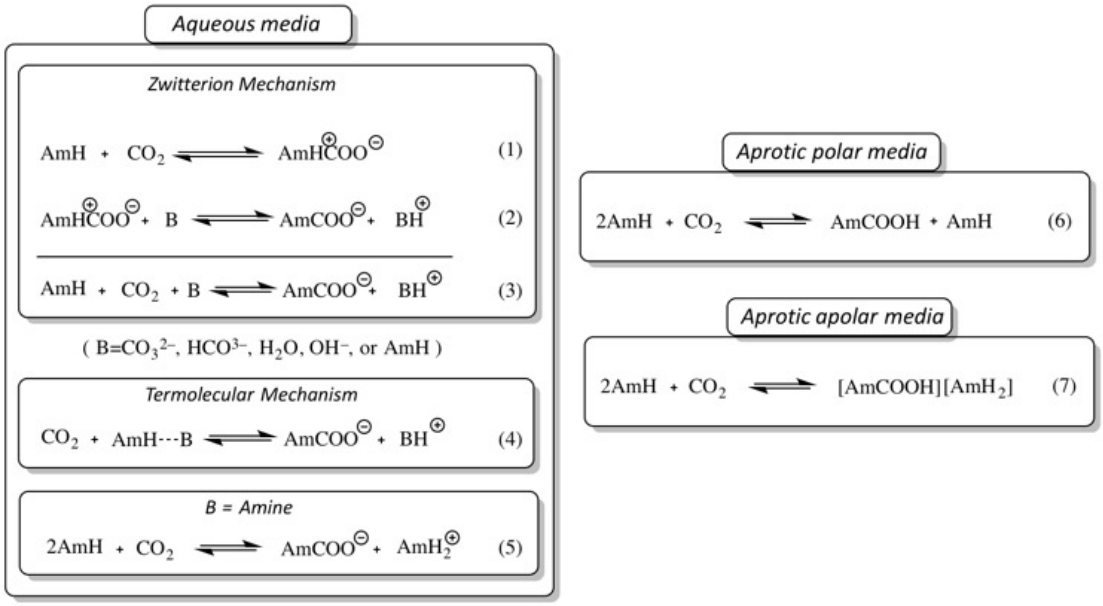

Figure 1.6: Different reactivity currently proposed for amine–CO_2 reactions in solution. In the zwitterion mechanism, the Am-C bond formation occurs followed by deprotonation by a base, while in the termolecular mechanism, the base abstracts the proton during formation of the Am-C bond. Both aqueous media proposed mechanisms result in the carbamate + protonated base products. In aprotic polar media, the products are predicted to be neutral acid + amine species, while in aprotic apolar media, the product is predicted as a [carbamate][ammonium] salt.

The reaction mechanism proposed in Section 3.1 rationalized the previously unexplained experimental observations. The study also provided hypotheses which could validate or refute the proposed mechanism. Based on the proposed mechanism, changing the linker or length of the amine would result in drastic changes to the heat of adsorption, however changing the metal would not. This prompted additional experiments, which are ongoing.

In Section 3.2, the oxidation of ethane to ethanol occurs in Fe-MOF-74, which raises the question with respect to what the active oxidant is within the MOF. In cases such as these, where the mechanistic details aren't available experimentally, theoretical calculations play an important role.

Although molecular simulations with FFs yield information about the relevant separations, and DFT/WFT calculations can provide mechanistic pathways, it is also important for predictive design to be able to rationalize why one system would perform a given separation better than another. In two studies presented in Chapter 4, we used both DFT and WFT to rationalize why some metals in the MOF-74 series would be ideal candidates to separate N_2 from CH_4 (Section 4.1) and how to rationalize observed spectroscopic trends for the metal series for CO binding (Section 4.2). There are some cases, for example for metal–metal multiply bonded species, where single reference WFT treatment is insufficient. Chapter 5 investigates those cases, comparing results from WFT and DFT. The hope being that these types of systems could be incorporated within MOFs in the future to provide unique reactivity.

1.2 Organization of Dissertation

In **Chapter 2**, force fields are parameterized for MOF–gas interactions (Sections 2.1 and 2.2) and for Uranyl–peroxide nanocapsules (Section 2.3). Section 2.1 focuses on CO_2 adsorption and CO_2/N_2 separation in Mg-MOF-74, with an extension to Zn-MOF-74, the extended linker analogue of Mg-MOF-74 Mg_2(dobpdc), and MOF-5, and Section 2.2 focuses on CO_2 adsorption in Fe-MOF-74. Section 2.3 uses the same parameterization procedure to study uranyl-peroxide nanocapsule formation, with an extension to parameterization of intramolecular terms.

Chapter 3 shows the utility of both wave function theory and density functional theory to provide mechanistic insights for reactions occurring within the pores of MOFs. Section 3.1 proposes a mechanism for the mmen amine–CO_2 reaction occurring within the pores of Mg_2(dobpdc). Section 3.2 uses DFT and WFT to elucidate the nature of a reactive Fe-Oxo intermediate at the exposed metal site of Fe-MOF-74.

In **Chapter 4**, both wave function theory and density functional theory are used to rationalize metal–gas bonding trends that occur at the exposed metal sites in a series of MOF-74 metals. Section 4.1 compares the adsorption of CH_4 and N_2 at the metal site in Fe-MOF-74, and the yet unsynthesized V-MOF-74. In Section 4.2, CO bonding is compared for along the M-MOF-74 series where M = Mg, Mn, Fe, Co, Ni, and Zn for utilization in CO/H_2 or CO/N_2 separations.

With the hope that unique catalytic species possessing metal–metal bonds could be incorporated within a MOF, **Chapter 5** compares multireference treatment with density functional theory for the nature of bonding of metal–metal multiply bonded species.

Chapter 2

Force Field Parameterization

2.1 *Ab Initio* Carbon Capture in Open-Site Metal-Organic Frameworks

During the formation of metal-organic frameworks (MOFs), metal centres can coordinate with the intended organic linkers, but also with solvent molecules. In this case, subsequent activation by removal of the solvent molecules creates unsaturated open metal sites known to have a strong affinity for CO_2 molecules, but their interactions are still poorly understood. Common force fields typically underestimate by as much as two orders of magnitude the adsorption of CO_2 in open-site Mg-MOF-74, which has emerged as a promising MOF for CO_2 capture. Here we present a systematic procedure to generate force fields using high-level quantum chemical calculations. Monte Carlo simulations based on an *ab initio* force field generated for CO_2 in Mg-MOF-74 shed some light on the interpretation of thermodynamic data from flue gas in this material. The force field describes accurately the chemistry of the open metal sites, and is transferable to other structures. This approach may serve in molecular simulations in general and in the study of fluid-solid interactions.

Adapted with permission from A. L. Dzubak, L.-C. Lin, J. Kim, J. A. Swisher, R. Poloni, S. N. Maximoff, B. Smit, L. Gagliardi. *Nature Chem.* 2012, *4*, 810.[17] Copyright 2012, Nature Publishing Group. A.L.D. and L.-C.L. contributed equally to this work. Author contributions and additional information may be found in section 3.2.5.

2.1.1 Introduction

Most energy scenarios project a significant increase in the role of renewable energy sources.[18] These scenarios also predict an even higher increase in our energy needs. As a consequence, although the relative consumption of fossil fuels will be decreasing, in absolute terms we will continue to burn more coal. In such a scenario, carbon capture and sequestration will be one of the only viable technologies to mitigate CO_2 emissions.[18,19] At present the cost associated with the capture of CO_2 from flue gas is one of the bottlenecks in the large-scale deployment of this technology. Of particular concern is that the efficiency of a coal-fired power plant decreases by as much as 30-40%[20] because of the energy required to separate and compress CO_2. The aim of decreasing this parasitic load has motivated the search for novel materials.[21,22]

A promising class of materials is metal-organic frameworks (MOFs).[21,23] MOFs are crystalline materials that consist of metal centres connected by organic linkers. These materials have an extremely large internal surface area and, compared to other common adsorbents, promise very specific customization of their chemistry. By changing the metal and the linker, one can in principle generate many millions of possible materials. In practice, however, we can synthesize only a very small fraction of these materials, and it is important to develop a theoretical method that supports the experimental efforts to identify an ideal MOF for carbon capture. A key aspect is the ability to predict the properties of a MOF before the material is synthesized. At present it is possible to carry out accurate quantum chemical calculations on these types of systems.[24] State-of-the-art density functional theory (DFT) calculations provide important insights into the energetics and siting of CO_2 at zero Kelvin.[24] The separation of flue gas, however, requires thermodynamic information (for example, adsorption isotherms) at flue-gas conditions (40 °C and 1 atm). This type of information can be obtained from molecular simulations using classical force fields.

For some classes of MOFs these predictions still pose significant difficulties, namely for MOFs with unsaturated metal sites.[25,26,27,28,29,30,31,32] These materials crystallize in such a way that both linkers and solvent molecules coordinate to the metal centres. The stability of the materials allows the removal of the solvent, which creates an open metal site. This site has a very high affinity for CO_2, which makes the material very promising for carbon capture. Often, reasonable predictions on the ability of a material

to adsorb CO_2 can be made using existing generic force fields.[33,34,35] However, for these materials Krishna and van Baten observed that, exactly at the conditions that are important for flue-gas capture, the universal force field (UFF)[36] fails to describe correctly the adsorption of CO_2.[35] The reason is that an open metal site imposes a chemical environment very different from those considered in the development of these force fields.[29]

Ideally, we would use state-of-the-art quantum chemical calculations to evaluate the energy for each state point of a grand canonical Monte Carlo (GCMC) simulation to compute the adsorption isotherm. However, such calculations would require millions of years of central processing unit time. In this work, we developed a methodology to obtain accurate force fields (parameters that describe the potential energy of a system) from quantum calculations to predict correctly the adsorption isotherms of CO_2 and N_2 on MOFs with open metal sites. Our approach is based on the non-empirical model potential (NEMO) methodology,[37,38] which decomposes the total electronic interaction energy obtained from quantum chemical calculations into the various contributions (electrostatic, repulsive, dispersion and so on). The force-field expression closely matches the functional form of the NEMO decomposition, which allows us to fit accurately the parameters of the force field to reproduce the quantum calculations. We developed a strategy to obtain the interaction for each atom type of the MOF with CO_2 (or N_2).

The UFF[36] or Dreiding[39] force field are used frequently to describe the interaction of gas molecules with the atoms of the MOF.[33,34,40] In these force fields, the energy of non-covalently bonded atoms is described by a Lennard-Jones potential plus Coulomb interactions. As these force fields are employed for many different systems, the parameters should give a reasonable description of the interaction of CO_2 with Mg in many different chemical environments. Our quantum calculations, however, show that owing to the open metal site of Mg-MOF-74, CO_2 (and N_2) can get closer to the magnesium centre than is predicted by the UFF. The aim of this work is to develop a systematic methodology to obtain force fields from quantum chemical calculations that describe correctly the interaction of the guest gas with the open metal site. To our knowledge, no existing force field is able to describe this interaction correctly.

Our aim is to determine a complete isotherm at flue-gas conditions, which requires taking into account ensemble averages that involve billions of different configurations.

Therefore, in the development of a force field we have to ensure that a large number of different configurations for the system are described in a reasonable way, and not just the minimum energy configuration, which is usually the focus of a quantum chemical calculation.

2.1.2 Results and Discussion

We employed quantum chemical calculations based on a NEMO decomposition of the total energy of the MOF-CO_2 and MOF-N_2 systems. Energies obtained with Møller-Plesset second-order perturbation theory (MP2) are decomposed into the corresponding electrostatic, repulsive and attractive contributions, which include dispersion, exchange interactions and polarization (see Supplementary Information, part 1, for details). The importance of this decomposition is that we can fit the corresponding terms in our force field separately.

Force Field Parameter Determination

In our force field, the electrostatic interactions are described by charges estimated using the LoProp scheme.[41] With this approach it is possible to partition molecular properties, such as multipole moments and polarizabilities, into atomic and interatomic contributions. The method requires a subdivision of the atomic basis set into occupied and virtual basis functions for each atom in the molecular system. Initial tests showed that the repulsive interactions could not be described accurately with a Lennard-Jones potential. (The Lennard-Jones potential is a mathematically simple model that approximates the interaction between a pair of neutral atoms or molecules with $1/r^6$ and $1/r^{12}$ terms, where r is the distance between the two atoms or molecules). A modified Buckingham potential was used in addition to the Coulomb interaction:

$$u^{\mathrm{rep}}(r) = \begin{cases} \infty & r < r_{\mathrm{min}} \\ A\exp(-Br) & r > r_{\mathrm{min}} \end{cases} \tag{2.1}$$

which can be fitted very accurately. For the attractive part, we used, in addition to the conventional r^6 term, an r^5 term to obtain a better representation of the decomposed energies:

$$u^{\mathrm{att}}(r) = \frac{C}{r^5} + \frac{D}{r^6} \tag{2.2}$$

To determine the parameters of this force field, we used the following procedure. First, we generated sets of configurations organized into paths, with one path for each type of atom in the framework, that is, Mg, O_a, O_b, O_c, C_a, C_b, C_c and C_d in Mg-MOF-74 (Supplementary Fig. S1). Along each path, CO_2 (or N_2) approaches a specific atom type in such a way that for each configuration on this path the MP2 energy mainly represents the interaction of CO_2 (or N_2) with this particular atom type. These energies should thus contribute the most to the fitting of the parameters of the force field for this particular atom type. As it is infeasible to carry out MP2 calculations for the full periodic MOF, we defined for each atom type (and corresponding path) a finite cluster of atoms within the MOF that should represent the electronic environment of this atom type in the MOF. The size of the cluster was set such that the interaction of CO_2 (or N_2) with this atom type mimics the interaction in the full MOF.

The decomposition in electrostatic, repulsive and attractive interactions for each path allowed us to fit this relatively large number of force-field parameters efficiently and accurately. This procedure was used to determine the interactions of the end atom of the guest molecules (O of CO_2) with the atoms of the MOF. We then performed Monte Carlo simulations, which showed that the oxygen atoms dominate the interactions with the framework. The interactions with the interior atom of the guest molecules (that is, C of CO_2) were too weak to be included in this process.

For each of these paths, we selected a portion of the Mg-MOF-74 framework that was sufficiently large to represent accurately the chemical environment of the targeted atom. The size of the cluster was chosen in a compromise between accuracy and computational cost, with the size of the basis set as a constraint. The clusters corresponding to the eight paths and the details of the MP2 calculations are described in the Supplementary Information, parts 1, 10.

Figure 2.1(a,b) shows a typical outcome of the NEMO decomposition of the total MP2 energies into repulsive (Fig. 2.1a) and attractive (Fig. 2.1b) contributions for the Mg atom–CO_2 interaction, along with the fitted force fields. The electrostatic (charge-charge) contribution is identical to the leading term of the grouped-term NEMO decomposition, so no fitting is required. This figure illustrates that, indeed, the interaction of CO_2 with Mg dominates the total energy along this path. The repulsive interactions on this path are described accurately with our force field. As the attractive interaction

contains many different contributions and the functional form of the attractive interaction in our model only approximates the corresponding MP2 interactions, the fit of the attractive part is less accurate than that of the repulsive part. Similar results were obtained for the other paths. Figure 2.1(c,d) shows that our force field can reproduce the total MP2 energies for all paths to within 1-2 kJ mol^{-1}.

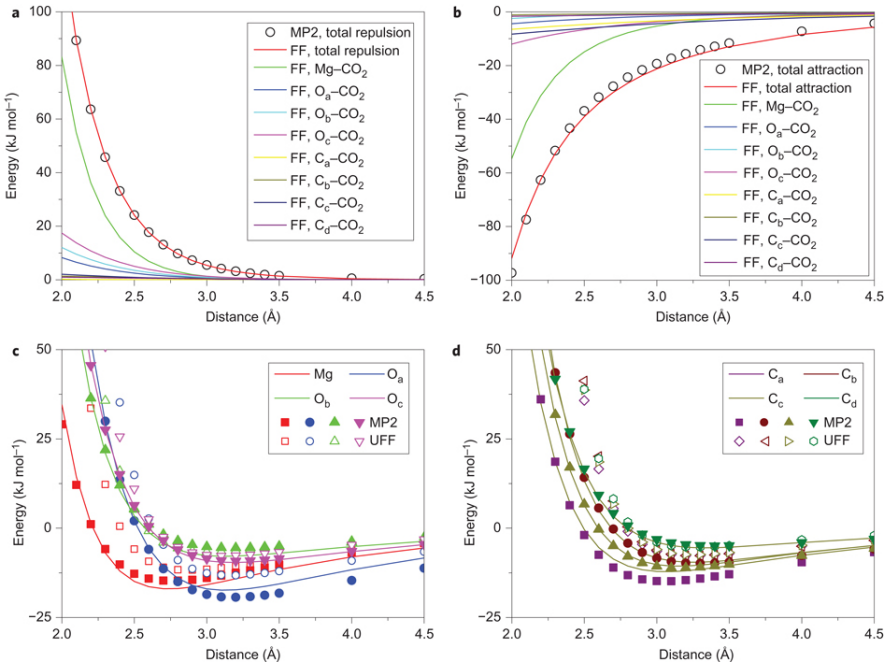

Figure 2.1: Interaction energy comparison of force fields with decomposed MP2 and UFF. (a,b) NEMO decomposition of the MP2 energies on the Mg path into repulsive (a) and attractive (b) interactions. The black circles are the MP2 results and the solid lines are the fitted force fields for the various atoms. The red line gives the contribution of Mg. (c,d) Comparison of the MP2 repulsive and attractive energies (filled symbols) for the eight different paths with the force-field results (lines). Mg and O paths (c) and C paths (d) are compared with the predictions from UFF (open symbols).

To further validate our procedure, we compared the energies obtained from our force field with those obtained from DFT calculations on the fully periodic framework for two different paths. These DFT calculations include dispersive interactions as implemented in van der Waals density functional (vdW-DF), and the computed CO_2–MOF binding

energies and geometries are similar to those reported by Valenzano *et al.*[24] (see Supplementary Information, part 2). Figure 2.2 shows that our results are in good agreement with the DFT results. It is important that the path shown in Fig. 2.2a includes the minimum energy configurations, a feature that is reproduced well by our force field. The detailed force fields for the interactions of CO_2 and N_2 with Mg-MOF-74 are reported in Supplementary Tables S4-S13.

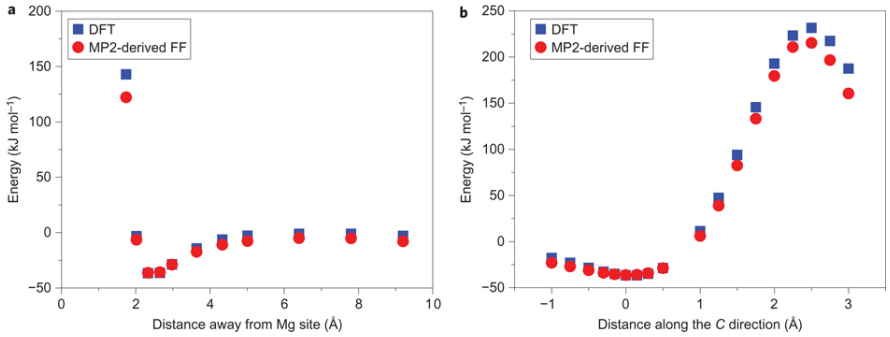

Figure 2.2: Interaction energy comparison of force field with periodic DFT. (a,b) The MOF–CO_2 interaction energy is plotted along two different paths that cross the minimum energy configuration of CO_2 in Mg-MOF-74: CO_2 approaching the open metal site from the centre of the pore (a) and CO_2 approaching the open metal site in the C-direction (b). Blue curves are DFT calculations that include van der Waals interactions and red curves are obtained from our force field. Both paths are computed in the periodic system.

It is instructive to compare our force field with that obtained by UFF. In Fig. 2.1(c,d) we compare the UFF predictions of the total energies on the eight different paths. For the Mg path, we observe that the UFF does not allow the CO_2 molecule to approach the Mg atom as close as the MP2 calculations predict. As a consequence, the electrostatic and dispersive interactions are underestimated significantly. That we can incorporate these chemical differences in our force field is essential for a correct description of these systems; otherwise, it would not possible to reproduce the results of the quantum calculations.

Predictions from Simulations that Utilize the New Force Field

As a first test of our force field we computed the heat of adsorption and compared it with the experimental values obtained by Simmons *et al.*,[42] Dietzel *et al.*[27] and Mason *et al.*[28] (Fig. 2.3). Our simulations reproduced quantitatively the observed dependence of the heat of adsorption as a function of loading. We predicted an inflection at exactly one CO_2 molecule per Mg, but the experiments show this inflection at slightly lower loadings ($\sim$0.8 CO_2 molecule per Mg). In our simulation we assumed a perfect crystalline material in which every Mg atom was activated–as all Mg atoms are equivalent, one would expect this inflection to occur at exactly one CO_2 molecule per Mg. These observations support the conclusion of Dietzel *et al.*,[27] according to which, not all Mg sites are accessible in the real system. Our simulations, in agreement with the experimental data of both Dietzel *et al.*[27] and Simmons *et al.*,[42] showed an increase in the heat of adsorption as a function of the loading. Mason *et al.*,[28] however, did not report such an increase. They obtained the heat of adsorption from a fitting procedure to a dual-site Langmuir isotherm. This procedure imposes a monotonic decrease of the heat of adsorption as a function of loading. In this study we computed the experimental heat of adsorption directly from our simulations,[43] and hence our results are independent of the interpretation of the isotherms.

In Fig. 2.4 we compare the predicted adsorption isotherms with the experimental isotherms for CO_2 and N_2 in Mg-MOF-74.[27,28,42,44,45,46,47,48] We obtained excellent agreement with experimental data, and the agreement is best when we take into account that not all the Mg sites are accessible in the experiments. Comparison with the simulation using the UFF illustrates the significant improvement in predictions made by our force field. In the Henry regime, the conventional force field underestimates the adsorption by as much as two orders of magnitude. An interesting observation is that we were not able to describe the simulated (and experimental) adsorption isotherms for CO_2 with a dual-site Langmuir isotherm (see Fig. 2.5). Langmuir isotherms assume that each adsorption site is independent. The heat of adsorption data already show that CO_2–CO_2 interactions cannot be ignored for the CO_2 binding to the Mg sites and, because of these interactions, it becomes easier to add another CO_2 molecule in the MOF. If we have a loading of approximately one CO_2 per six Mg, we observe a significant collective effect that makes it easier to add an additional CO_2 molecule adjacent

to those already adsorbed. Figure 2.5 shows that these relatively small energies (1.6 kJ mol^{-1}), provided by the CO_2–CO_2 interactions, essentially enhance the uptake of CO_2 by up to 15% at the condition of carbon capture. This suggests that in the design of a carbon-capture material one would also want to optimize these collective effects inside the material. In addition, therefore, we performed simulations to predict the adsorption isotherms for a CO_2–N_2 mixture (see Supplementary Information, part 8). To the best of our knowledge, mixture adsorption isotherms have not been measured for this system, yet they are essential to determine the performance of a material for carbon capture.

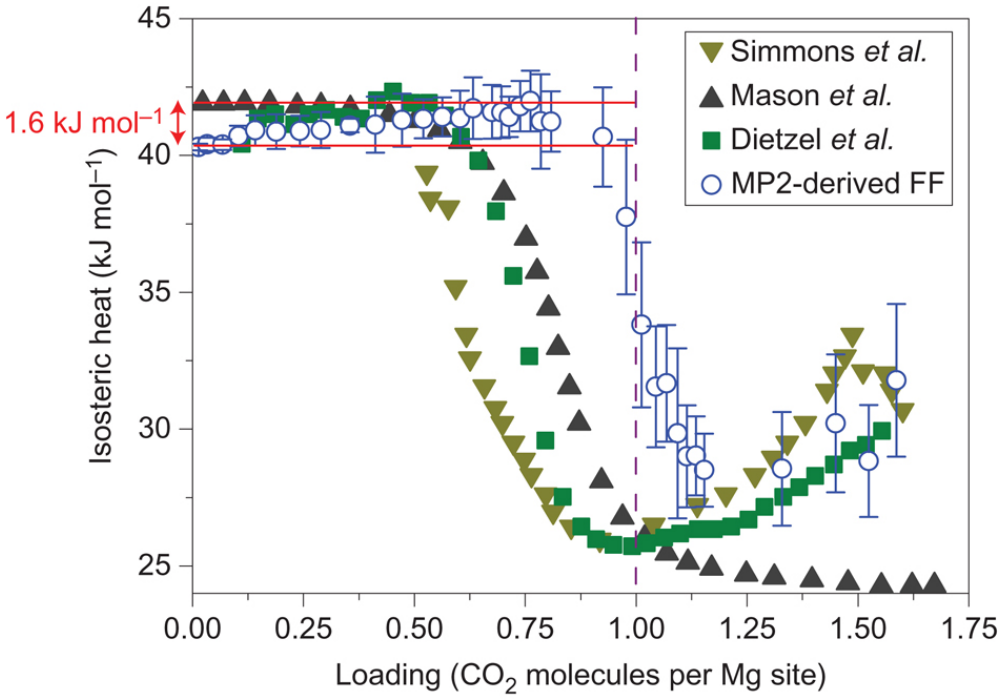

Figure 2.3: Comparison of the experimental and simulated isosteric heats of adsorptions as a function of loading. The loading is plotted as the number of CO_2 molecules per open metal site. For an ideal material, for which all metal sites are active, the molecular simulations (blue symbols) predict that one CO_2 binds to one open metal site. The black, green and olive symbols give the reported experimental data of Mason *et al.*,[28] Dietzel *et al.*[27] and Simmons *et al.*,[42] respectively. Red lines indicate the enhancement of the CO_2 heat of adsorption caused by cooperative effects and was predicted from the molecular simulations.

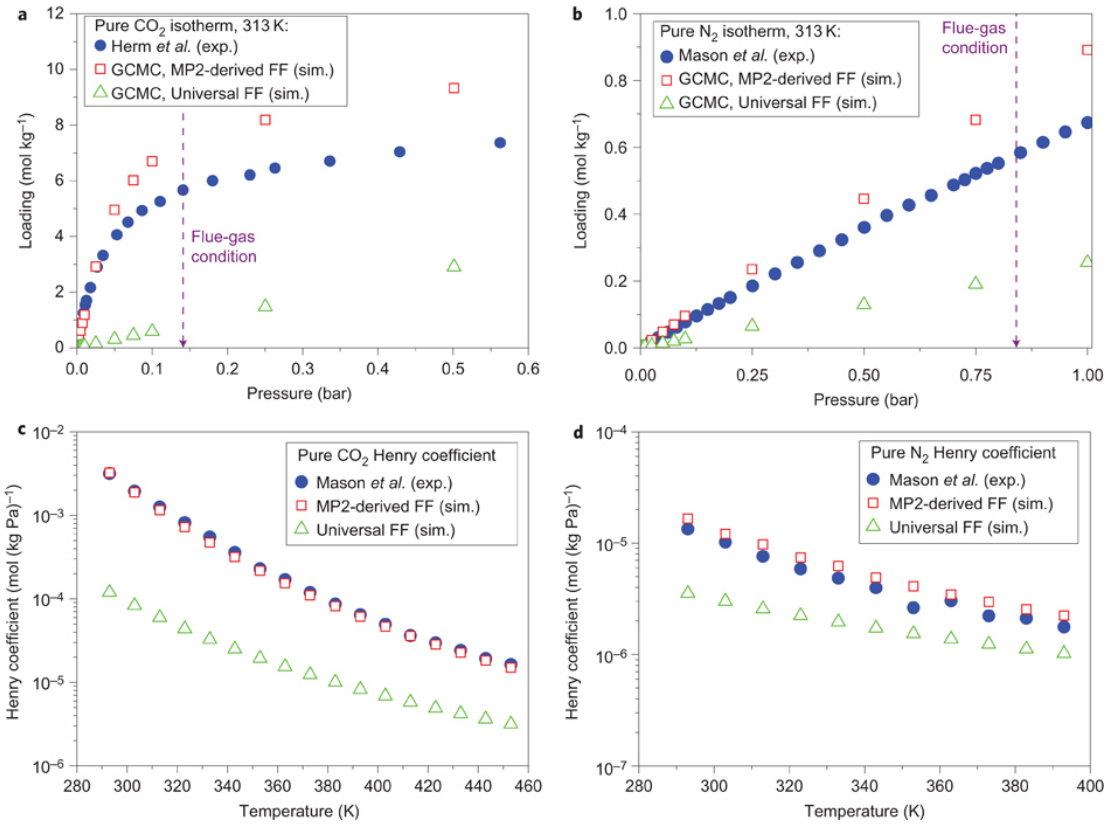

Figure 2.4: Comparison of simulated and experimental adsorption isotherms and Henry coefficients. (a,b) Experimental (exp.) and predicted (sim.) adsorption isotherms are shown for CO_2 (a) and N_2 (b) in Mg-MOF-74. The experimental data of Herm *et al.*[47] or Mason *et al.*[28] are shown by the filled blue circles. The open symbols are the simulation results: the green symbols are the results of using the UFF and the red symbols are from the present force field. At low pressure the adsorption is linear in pressure (the proportionality coefficient is defined as the Henry coefficient). (c,d) The Henry coefficients are shown as a function of the temperature for CO_2 (c) and N_2 (d).

At this point it is instructive to compare our approach with the multi-Langmuir approach that Sauer *et al.*[49] developed. In the multi-Langmuir method, the MP2 energies at the binding sites are used directly to estimate the corresponding adsorption coefficient (or Henry coefficient) of the different adsorption sites and hence the use of force fields is avoided. The multi-Langmuir approach relies on the assumption that the

isotherms can be described with a Langmuir equation and so a few well-defined binding sites dominate adsorption. As for the adsorption of CO_2 in Mg-MOF-74, the use of a force field is essential to capture the enhancement at low loading and to describe correctly the adsorption at high loading.

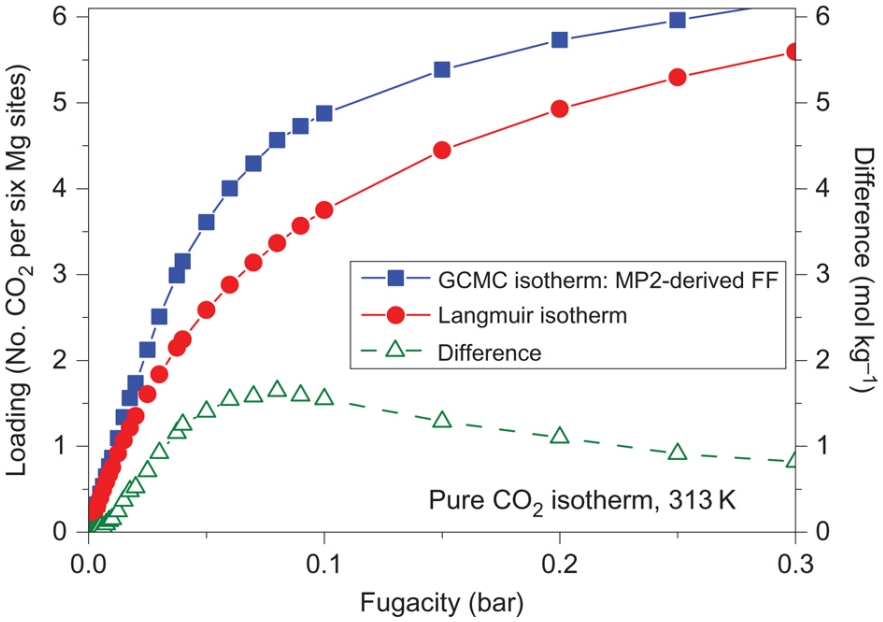

Figure 2.5: Enhancement of the adsorption of CO_2 as a function of loading. In this figure we compare a Langmuir isotherm (red) with the results from GCMC simulations (blue). The parameters of the Langmuir isotherm are obtained from the Henry coefficient from the GCMC simulations and the maximum loading, which is set to one CO_2 per Mg site. The difference between these curves (green) indicates the enhancement induced by the presence of other CO_2 molecules.

2.1.3 Transferability

We now discuss the transferability of our approach. Recently, McDonald *et al.*[32] synthesized Mg_2(dobpdc) (in which dobpdc is 4,4'-dioxido-3,3'-biphenyldicarboxylate), a material similar to MOF-74, but with an extended linker. As this linker contains atom types similar to those in MOF-74, we can compute the isotherms for Mg_2(dobpdc) using the force field derived for Mg-MOF-74. Figure 2.6a shows that the predicted isotherm is

in good agreement with the experimental data that McDonald *et al.*[32] reported. We also investigated the effect of changing the metal in MOF-74. In Supplementary Information, part 6, we show that the Zn-MOF-74 isotherm can be computed by recalculating the force field for the CO_2 metal interactions, but keeping all other interactions the same as those in Mg-MOF-74. This result is further confirmation that our approach is transferable. In Fig. 2.6b we compare the predicted isotherms for Zn-MOF-74 with the corresponding isotherm for Mg-MOF-74. Unfortunately, Zn-MOF-74 is much more difficult to activate and hence there are no definitive experimental results to compare our predictions against. Finally, we employed our approach to study CO_2 in MOF-5, which does not have open metal sites. Figure 2.6c shows that the CO_2 simulated isotherm is in excellent agreement with the experimental one that Walton *et al.*[50] reported. This set of results confirms that our methodology is applicable to different types of structures.

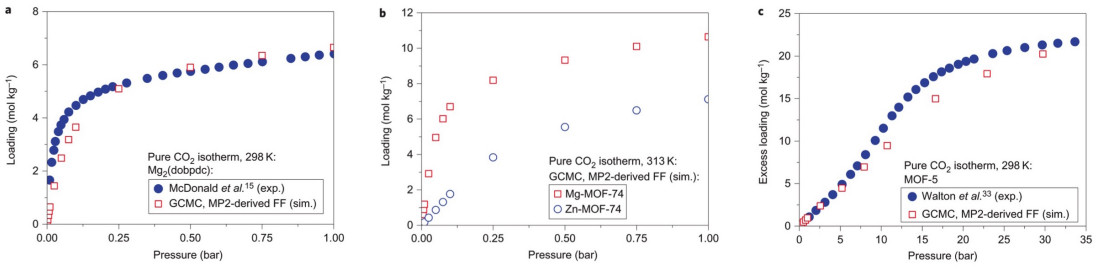

Figure 2.6: Adsorption isotherms of CO_2 in additional frameworks. (a-c) Transferability of the methodology was studied in three additional frameworks: Mg_2(dobpdc), which is a material with an extended linker using the same atom types as in the Mg-MOF-74 material (a); Mg-MOF-74 and Zn-MOF-74, in which we tested the transferability of our force field for the metal sites by replacing the Mg by the Zn force field, but keeping the force field for the atoms in the linker identical (b); MOF-5, a material that does not have open metal sites (c). Closed and open symbols represent the experimental and simulation adsorption isotherms, respectively.

2.1.4 Conclusions

In summary, a novel methodology that yields accurate force fields for CO_2 and N_2 in an open-site MOF from high-level quantum chemical calculations was developed. These force fields take into account the subtle changes in the chemical environment induced by the presence of open metal sites in MOFs. Our method allows us to reproduce the

experimental adsorption isotherms for both CO_2 and N_2 in Mg-MOF-74 and to predict the mixture isotherms at flue-gas conditions. We also showed that our methodology is transferable to systems that contain different metals, linkers and topologies. The same approach will be used to predict properties of open-site MOFs that have not yet been synthesized.

2.1.5 Methods

MP2 Calculations

In this work, we used MP2 to describe interactions of CO_2 and N_2 with MOF sites. MP2 is adequate for the treatment of electron correlation in cases where strong correlations are not present. In the Mg-MOF-74, we defined eight representative clusters of the MOF to compute interactions with the guest, each cluster chosen to best represent the atom type to be parameterized (excluding H atom types). Within each cluster, the basis functions were chosen such that a larger contraction was used for the guest atoms, the atom type being approached in the MOF, and its nearest neighbours. A smaller contraction was used for all atoms farther away. The choice of clusters, basis function contractions and discussion of convergence are given in the Supplementary Information, parts 1, 10. The interaction energies were determined by the supermolecular approach, counterpoise corrected for the basis-set superposition error.[51] All calculations were performed using the MOLCAS software version 7.6.[52] Resolution of the identity and Cholesky decomposition techniques was employed to treat the two electron integrals.[53,54,55] The Douglas-Kroll-Hess Hamiltonian[56] was used in conjunction with basis functions of the atomic natural orbital relativistic correlation consistent (ANO-RCC)[57,58] type.

DFT Calculations

The optimized crystal structure was obtained from DFT as implemented in the Vienna *Ab Initio* simulation package (VASP),[59,60] employing the Perdew-Burke-Ernzerhof gradient-corrected exchange-correlation functional. Interaction energies were computed using the vdW-DF[61,62] as implemented in SIESTA.[63,64] Basis-set superposition errors were counterpoise corrected. More details about our DFT calculations are given in the Supplementary Information.

SIESTA calculations used variationally optimized double-Z polarized basis sets that imply the presence of *d*-orbitals for C, N and O. Non-local, norm-conserving fully separable Trouiller-Martins pseudopotentials were used. C (*2s2p*), O (*2s2p*) and Mg (*2s2p3s*) electrons were included explicitly in the valence. Real-space integrals were performed on a mesh with a 300 Ry cutoff. VASP calculations use projector-augmented wave potentials to describe the interaction between core and valence electrons. C (*2s2p*), O (*2s2p*), Mg (*3s3p*) and Zn (*4p3d*) valence electrons were included explicitly in the valence. A plane-waves kinetic energy cutoff of 500 eV was used and the integration over the irreducible Brillouin zone was carried out over a 2 × 2 × 8 Monkhorst-Pack grid. Atomic positions were relaxed until the forces were lower than 0.02 eV $Å^{-1}$.

NEMO Decomposition and Force-Field Parameterization

Using the MP2 interaction energies as a reference, the NEMO decomposition[38] was used to partition the energy into repulsion, polarization, dispersion and electrostatic components (functional form given in the Supplementary Information, part 1.5) for all clusters and paths. The electrostatic moments to second order and dipole–dipole polarizabilities were obtained using the LoProp method[41] based on the MP2 densities.[65] The terms were then grouped into repulsive, attractive and electrostatic terms, in which the charge-charge interactions and repulsions remained constant, and the polarization, dispersion and effects of dipoles and quadrupoles were grouped into attraction terms (see equations (2.1) and (2.2)), for which the parameters were then fitted by atom pairs. For this mapping procedure, in which the decomposed energies were parameterized separately, only the parameters for the interaction between the target-atom type and the guest molecule were adjusted to reproduce the NEMO-decomposed energy. This mapping was carried out in two phases. We first took all atoms of a particular element and minimized the error over all paths for that element simultaneously. This adjustment was done moving outwards from the metal, and started over again interactively until convergence. For the second phase, we optimized the force-field parameters for each atom type individually with an ordering based on its relative contribution to the total energy. The ratio of the energy between the target-atom type and the guest molecule to the total energy was computed, and the paths were taken in sequence from the highest to the lowest ratio. This procedure was repeated until all the parameters were converged

(Supplementary Information, part 3).

GCMC Simulations

Adsorption (pure and mixture) isotherms for CO_2 and N_2 in Mg-MOF-74 were predicted using the GCMC technique, in which a constant chemical potential (fugacity), volume and temperature were imposed.[66] The heat of adsorption was calculated directly using the procedure developed by Vuong and Monson.[43] The energies of guest–framework interactions were computed using the potential model described above and guest–guest interactions were described using the transferable potentials for phase equilibria force fields.[67] Electrostatic energy was computed using the Ewald summation technique. Short-range interactions were cut off and shifted to zero at a distance of 12.8 Å, and the simulation box was extended by at least twice this distance in all orthogonal directions. No tail correction was used. To accelerate the calculation of molecule–framework interaction energies, the short-range part of the interaction was stored in a precomputed grid with a spacing of 0.10 Å and linearly interpolated between grid points. Trajectories were equilibrated for at least 20 million configurations before averages were taken over a further four million configurations.

2.1.6 Additional Information

Supplementary information is available in the online version of the paper. Reprints and permission information is available online at `http://www.nature.com/reprints`. Correspondence and requests for materials should be addressed to B. S. and L. G. The authors declare no competing financial interests.

Acknowledgements

The research was supported by the US Department of Energy under contracts DE-SC0001015, DE-FG02-11ER16283 (A.L.D and L.G.), DE-AC02-05CH11231, Advanced Research Projects Agency – Energy, and the Deutsche Forschungsgemeinschaft (DFG, Priority Program SPP 1570). A detailed description is given in the Supplementary Information. We thank G. Karlström, Lund University, and Roland Lindh, Uppsala University, for useful discussion.

Author Contributions

A.L.D. performed the cluster calculations at the MP2 level and the NEMO decomposition of the interaction energies, R.P. performed the periodic DFT calculations, L-C. L., J.A.S. and J.K. performed the molecular simulations, S.N.M. provided some of the optimized MOF structures, A.L.D. and L-C.L. optimized the force field and B.S. and L.G. conceived the research. A.L.D., L-C.L., B.S. and L.G. co-wrote the manuscript and all the authors discussed the results and commented on the manuscript.

2.2 CO_2 Adsorption in Fe_2(dobdc): A Classical Force Field Parameterized from Quantum Mechanical Calculations

Carbon dioxide adsorption isotherms have been computed for the metal-organic framework (MOF) Fe_2(dobdc), where dobdc^{4-} is 2,5-dioxido-1,4-benzenedicarboxylate. A force field derived from quantum mechanical calculations has been used to model adsorption isotherms within a MOF. Restricted open-shell Møller-Plesset second-order perturbation theory (ROMP2) calculations have been performed to obtain interaction energy curves between a CO_2 molecule and a cluster model of Fe_2(dobdc). The force field parameters have been optimized to best reproduce these curves and used in Monte Carlo simulations to obtain CO_2 adsorption isotherms. The experimental loading of CO_2 adsorbed within Fe_2(dobdc) was reproduced quite accurately. This parametrization scheme could easily be utilized to predict isotherms of various guests inside this and other similar MOFs not yet synthesized.

2.2.1 Introduction

Metal-organic frameworks (MOFs) are nanoporous materials that consist of metal nodes connected by organic linkers, and can be synthesized with a wide range of topologies, surface areas, and other structural characteristics. These materials can be used to

Adapted with permission from J. Borycz, L.-C. Lin, E. D. Bloch, J. Kim, A. L. Dzubak, R. Maurice, D. Semrouni, K. Lee, B. Smit, L. Gagliardi. *J. Phys. Chem. C* 2014, *118*, 12230.[68] **J.B. and L.-C.L. contributed equally to this work. Additional information may be found in section 3.1.4.**

store gases with different physical and chemical characteristics.[69,70,71] Experimental characterization of MOFs is necessary for gaining insight into their adsorption ability,[72,73,74,75,76] but experiment alone is not sufficient for the rapid characterization of MOFs due to many possible combinations of metals, linkers, and topologies that could be tested for various applications. Accordingly, one of the reasons that computational approaches play an important role in the screening process is that they can help experimentalists to efficiently screen MOFs that are worth considering for use in gas separations. Molecular simulations have been widely used to compute macroscopic properties such as adsorption isotherms. These classical simulations require the use of force fields for describing intermolecular interactions. The Grand-Canonical Monte Carlo (GCMC) approach with force fields such as Dreiding[77] and the Universal Force Field (UFF)[78] has been used with some success to study simple molecule adsorption within MOFs.[79,80,81] However, adsorption within MOFs that strongly bind guests, such as those with open-metal sites, cannot be described accurately with these force fields.[82,83] Although it is not possible to accurately compute adsorption isotherms for guests within open-metal site MOFs with general force fields, it is possible to parametrize force fields from quantum mechanical calculations that could be used to simulate these isotherms more accurately.

In previous work, intermolecular potentials were parametrized for the interaction of CO_2 and N_2 with Mg_2(dobdc), Zn_2(dobdc), and MOF-5 (also called IRMOF-1), which is $Zn_4O(bdc)_3$ (bdc^{2-} is 1,4-benzenedicarboxylate).[83] MOF fragments were used to design clusters to model these extended systems and were used to compute interaction energy curves with CO_2 and N_2. This approach yielded parameters that accurately predicted CO_2 and N_2 adsorption in closed-shell MOFs. Møller-Plesset second-order perturbation theory (MP2)[84] was used to compute interaction energies for Mg_2(dobdc) and Zn_2(dobdc) respectively cluster models with CO_2. Cluster models were designed to describe CO_2 interactions with every atom type present in these MOFs. These resulted in accurate force fields, but it was rather expensive. In this study, we simplified this parametrization scheme by computing new parameters only for the interaction between the open-metal site M and the oxygen of CO_2.

It should be noted that there are multiple ways to compute macroscopic characteristics of MOFs. The energy decomposition proposed in this article is useful both to derive

the force field, and also to understand the physics beyond the various terms contributing to the interaction energy, for example, electrostatics, induction, dispersion, and repulsion. This means that the derived force field will be accurate due to a correct description of the physics of the various terms rather than simply error cancellation. These decomposed terms can then either be used within a polarizable force field or be further simplified to effectively include polarization effects in a nonpolarizable force field, making calculations with large number of atoms possible. Examples of some of these energy partitioning schemes are the Sum of Interactions Between Fragments Ab Initio computed (SIBFA)[85] method, Symmetry Adapted Perturbation Theory (SAPT),[86] which is fully quantum mechanical and has been used on Fe_2(dobdc) before,[87] and the Effective Fragment Potential (EFP) method. The EFP method describes inert interactions with effective potentials, while describing an active region with quantum mechanics. EFPs have been used to compute energies for many types of interactions,[88,89,90] but to our knowledge this method has not been employed to study gas adsorption in MOFs.

In this work, we focus on another member of the M_2(dobdc) family, commonly referred to as the M-MOF-74 series, Fe-MOF-74 (see Figure 2.7), and its ability to bind CO_2. Species containing Fe(II) ions are known to be challenging to describe computationally. In some coordination environments, the low-spin and high-spin states of Fe(II) are so close in energy that it is difficult to predict which is the ground state,[91] and within spin states multiconfigurational character has been observed when binding guests to heme.[92,93] Furthermore, complex redox reactions occurring with guests have been observed in Fe-MOF-74 previously.[75] The coordination environment within Fe-MOF-74 favors the high-spin state for Fe(II) when bare[94] and when binding hydrocarbons.[87] The primary goal of this work was to compute isotherms for CO_2 adsorption within Fe-MOF-74 by extracting force field parameters from an interaction energy curve calculated with Restricted Open-shell Møller-Plesset second-order perturbation theory (ROMP2), while using UFF parameters to describe all nonmetal interactions instead of computing new parameters for each of these pairwise interactions.

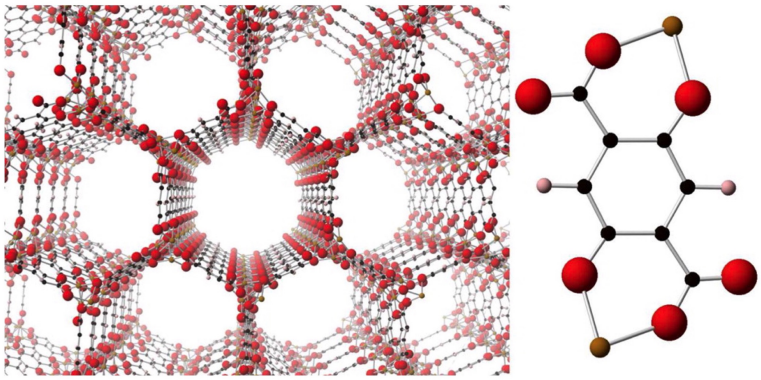

Figure 2.7: Structure of Fe-MOF-74 optimized using periodic density functional theory (DFT) with its stoichiometric unit pictured on the right. The brown atoms are iron, red are oxygen, black are carbon, and pink are hydrogen.

The isotherms simulated in this work are compared to new experimental Fe-MOF-74/CO_2 adsorption data. The surface area of Fe-MOF-74 was determined at low pressure and temperature by using pure N_2. CO_2 adsorption isotherms were measured at three temperatures by cycling pure CO_2 through an activated sample of Fe-MOF-74 at a constant rate. From these isotherms, we can obtain information on the surface area and binding characteristics of MOFs.[74,75,95]

This Article is organized as follows: In section 2.2.2, the experimental details, the clusters, and the interaction energy calculation method will be described, along with the parametrization method for obtaining the new force field parameters describing the adsorption of CO_2 within Fe-MOF-74. The specific details regarding the classical simulations will be reported in section 2.2.2. In section 2.2.3, the simulated CO_2 adsorption isotherms for Fe-MOF-74 and Mg-MOF-74 will be provided and compared to experimental data and previous simulation data. Finally, in sections 2.2.4 and 2.2.5, there will be a discussion and conclusions.

2.2.2 Methods

Gas Adsorption Measurements

Fe-MOF-74 was prepared and activated as reported in Bloch *et al.*[75] For the surface area determination and low-pressure CO_2 adsorption experiments, 85 mg of Fe-MOF-74 was transferred to a preweighed glass sample tube under an atmosphere of nitrogen and capped with a Transeal. The sample was then transferred to a Micromeritics ASAP 2020 gas adsorption analyzer and heated at a rate of 1 °C/min from room temperature to 160 °C. The sample was considered activated when the outgas rate at 160 °C was less than 2 μbar/min. The evacuated tube containing the activated sample was then weighed and transferred to the analysis port of the instrument where the outgas rate was again determined to be less than 2 μbar/min at 160 °C. High-purity N_2 (99.998%) and CO_2 (99.995%) were used for the adsorption experiments. Nitrogen adsorption at 77 K indicated a surface area of 1345 m^2/g (BET). Prior to CO_2 adsorption experiments, the sample was reactivated at 160 °C. The measurements at 25, 35, and 45 °C were performed using a recirculating dewar connected to an isothermal bath. The measured experimental data in terms of excess loadings were fit to a dual-site Langmuir–Freundlich model:

$$n = \frac{q_{\mathrm{sat},1}\, b_1\, P^{\nu_1}}{1 + b_1\, P^{\nu_1}} + \frac{q_{\mathrm{sat},2}\, b_2\, P^{\nu_2}}{1 + b_2\, P^{\nu_2}} \tag{2.3}$$

where n is the excess CO_2 adsorbed in mmol/g, P is the pressure in bar, q_{sat}, is the saturation capacity in mmol/g, b_i is the Langmuir parameter in bar^{-1}, and ν_i is the Freundlich parameter for the two sites indicated by the subscript i. The isotherms measured at 25, 35, and 45 °C were used to compute the isosteric heat of adsorption (Q_{st}) with the Clausius-Clapeyron equation:

$$(\ln P)_n = -\frac{Q_{\mathrm{st}}}{R}\left(\frac{1}{T}\right) + C \tag{2.4}$$

where P is pressure, n is the amount of CO_2 adsorbed, T is temperature, R is the universal gas constant, and C is a constant. The isosteric heat of adsorption at a given adsorbed amount of CO_2 was obtained from the slope of the plots of $(\ln\ P)_n$ as a function of $1/T$.

Quantum Mechanical Calculations

Model Structures

A neutron powder diffraction structure obtained at 4 K[75] was used as an initial structure for the geometry optimization of Fe-MOF-74 under periodic boundary conditions with the Vienna Ab Initio Simulation Package (VASP).[96,97,98,99] Projector-augmented wave[100] potentials that describe the interaction between electrons in the core and valence shells[101] were used in these calculations. The Perdew-Burke-Ernzerhof (PBE) gradient-corrected, exchange-correlation functional[102] was used with a rotationally invariant, effective Hubbard U correction[103] of 5 eV on the d levels of the Fe(II) centers. This U value was chosen to reproduce the Fe(II)–Fe(II) distances and lattice parameters of the experimental structure. The PBE+U approach was previously shown to give reasonable unit cell volumes, lattice parameters, and metal–metal distances within MOFs.[104,105] The periodic DFT optimization was done using a 54 atom primitive cell of Fe-MOF-74. A gamma point optimization of the unit cell volume, lattice parameters, and atom positions was performed with an energy cutoff of 1000 eV. The energy and force convergence criteria were set to 1×10^{-6} eV and 0.05 eV/Å, respectively.

A metal centered cluster similar to that from Dzubak *et al.*[83] was used to calculate an interaction energy curve of CO_2 with Fe-MOF-74. This reference curve was used to optimize the Fe(II)–O(CO_2) parameters in this force field. The role of the noncentral metal atoms was probed by comparing interaction energy curves upon replacement of Fe(II) by Mg(II) and Zn(II). These tests were performed to reveal whether or not the Fe(II)–O(CO_2) interaction within Fe-MOF-74 is sensitive to magnetic couplings between the metal atoms, and to see if calculations could be simplified by replacing some of the open-shell Fe(II) ions with diamagnetic ions of the same charge.

Seven other clusters were designed to model the immediate environments of the other atom types (i.e. O_a, O_b, O_c, C_a, C_b, C_c, and C_d) present in Fe-MOF-74 (see Supporting Information Figure S1). These clusters were adopted to compute the charges for these atom types, which were then used in the GCMC simulations. The positions at which the clusters were cut from the periodic DFT structure were capped with hydrogens, and the hydrogen positions were optimized using the PBE[102] functional and def2 basis sets[106,107,108] (def2-TZVP on Fe and O; def2-SV(P) on C and H) with Turbomole 6.4.[109]

MOF–CO_2 Interaction Energy Curves

In this work, one of our main goals was to provide a physical description of the Fe(II) interaction with CO_2 in Fe-MOF-74. To accomplish this, we decided to probe a configuration space that contains strong Fe(II)–O(CO_2) interactions. The configuration space used to calculate the potential energy curve (PEC) was determined by minimizing the UFF repulsion energy of CO_2 with all atoms present in the cluster except the Fe(II) ions. This was done to ensure that the interaction energies between the CO_2 and the Fe(II) ion of interest were the greatest contributor to the PEC.

The PEC was calculated with the Complete-Active Space second-order Perturbation Theory (CASPT2) formalism[110,111] using MOLCAS 7.8.[112] A quintet spin multiplicity on Fe(II) was specified on the basis of previous experimental and theoretical work.[73,75,87,94] The four singly occupied Fe(II) orbitals for each Fe(II) ion were included in the active space of the Complete-Active Space Self-Consistent Field (CASSCF) calculations. A high-spin (16,16) CASSCF wave function is monoconfigurational and is thus isomorphic to a Restricted Open-shell Hartree-Fock calculation (ROHF). To justify the accuracy of this active space, a (24,20) CASSCF calculation containing the five d^6 orbitals of each Fe(II) ion was performed. With this active space, the high-spin ground state had a maximal configuration weight of 0.997 (1 would correspond to a perfect monoconfigurational state). Thus, assuming that the lowest energy d orbital of each of the four Fe(II) ions is strictly doubly occupied was valid. The high-spin ($S = 8$) ground state of the 60-atom cluster is in agreement with previous studies indicating ferromagnetic nearest neighbor[73,75,94,113] and ferromagnetic next-nearest neighbor[94,113] interactions within Fe-MOF-74. The second-order Perturbation Theory (PT2) correction was used to capture more dynamic correlation, and an imaginary shift of 0.2 hartree was applied to prevent the occurrence of intruder states.[114] The Resolution of the Identitity (RI) and Cholesky Decomposition (CD) were used to decrease the computational cost associated with the two-electron integrals.[115,116,117] The Douglas-Kroll-Hess Hamiltonian[118,119] was used in conjunction with Atomic Natural Orbital Relativistic Core Correlated (ANO-RCC) basis sets[120,121] for the ROHF and ROMP2 calculations. The ANO-RCC Valence Double Zeta plus Polarization (ANO-RCC-VDZP) basis set was used for the central atom of each cluster, its nearest neighbor oxygen atoms, and the CO_2 atoms. The ANO-RCC Minimal Basis set (ANO-RCC-MB) was used for all of the remaining atoms. We applied a minimal basis set to the atoms not immediately

bound to the central atom to reduce the computational cost, assuming that it does not significantly affect the computed interaction energies.

Basis set superposition error (BSSE) was addressed with the counterpoise correction.[122] A simplified form of the equation used to compute the interaction energies is provided as eq 2.5. The explicit form of the counterpoise corrected interaction energy formula is provided in the Supporting Information. In this work, the Fe(II) cluster pictured in Figure 2.8 was the only one for which the CO_2 interaction energy curve was calculated because in this case the interaction between CO_2 and the open-metal site provides the most important contribution to the adsorption energy.[83] The interaction energy is given by the relation:

$$E_{\text{int}} = E_{\text{MOF–CO}_2} - E_{\text{MOF}} - E_{\text{CO}_2} \tag{2.5}$$

where E_{int} is the interaction energy between the MOF and CO_2, $E_{\text{MOF–CO}_2}$ is the energy of the interacting system, and E_{MOF} and E_{CO_2} are the energies of the MOF and CO_2, respectively. All energies were computed in the basis of the interacting system (see the Supporting Information).

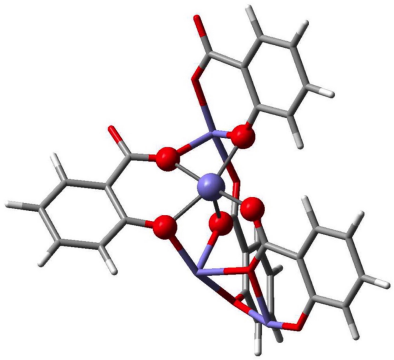

Figure 2.8: Sixty-atom cluster used to model the Fe(II) ion and its ligand environment within Fe-MOF-74. Blue atoms represent iron, red are oxygen, gray are carbon, and white are hydrogen.

Partitioning Molecular Properties

The point charge approximation is often used in force fields employed to compute adsorption isotherms of guests interacting with MOFs, because it is computationally convenient and reasonably accurate.[123] The Localization of Properties (LoProp)[124]

approach was chosen to compute the point charges. The LoProp approach was also used to extract dipoles, quadrupoles, and polarizabilities. The effects from these were included implicitly in the force field by optimizing parameters against reference data that include these contributions. The LoProp charges were computed by using the seven clusters analogous to those in Dzubak *et al.*[83] (see Supporting Information Figures S2-S8). The charge of the hydrogen atoms was chosen to neutralize the charge of the unit cell by distributing the nonzero charge between the hydrogen atoms equally.

It is often useful to partition interaction energies into multiple terms to try to understand which interactions are predominant and effectively account for more complex electron–electron interactions.[125] The Non-Empirical MOdeling (NEMO) approach[126] was used to decompose the interaction energy of the Fe(II) cluster with CO_2 into electrostatic, induction, dispersion, and repulsion terms, as provided in eq 2.6. The interaction energy was calculated using the procedure described in the MOF–CO_2 Interaction Energy Curves presented in the previous section. The NEMO intermolecular interaction energy is decomposed as follows:

$$E_{\text{int}} = E_{\text{elect}} + E_{\text{ind}} + \epsilon E_{\text{disp}} + E_{\text{rep}} \tag{2.6}$$

The electrostatic E_{elect}, induction E_{ind}, and dispersion E_{disp} terms were obtained from quantum mechanical reference calculations, and the repulsion energy E_{rep} was chosen to reproduce the reference intermolecular interaction energy, as shown in eq 2.7. It is important to note that a scaling parameter ϵ was applied to force the repulsion energy to be positive throughout the configuration space. The scaling parameter on the dispersion term can to some extent be justified by considering the fact that a small basis set, like the one used in this work, does not capture the long-range nature of the dispersion interaction.[127] The equations that were used to compute the explicit NEMO terms were taken from Stone,[128] and are reported in the Supporting Information as eqs S2-S5. The NEMO terms from eq 2.6 can be reorganized to calculate the repulsion energy as follows:

$$E_{\text{rep}} = E_{\text{int}} - (E_{\text{elect}} + E_{\text{ind}} + \epsilon E_{\text{disp}}) \tag{2.7}$$

The partial atomic charges of the CO_2 molecules during the NEMO energy decomposition were set to those used in the Transferable Potentials for Phase Equilibria

(TraPPE)[129] force field, because the parameters from this force field are generally considered reliable for the bulk phase of CO_2. The higher-order electrostatic, induction, and dispersion terms in eqs 2.6 and 2.7 were combined into a single attraction energy curve. The attraction and repulsion energy curves were used to optimize the force field parameters for the Fe(II)–O(CO_2) interaction. During the fitting of the attraction and repulsion parameters described in section 2.2.2, the scaling factor was further considered as a tunable constant to provide better fitting agreement.

ForceFields

The effective force field to be used for molecular simulations considers a rigid MOF and rigid CO_2 molecules. We included only pairwise intermolecular interaction terms. These approximations have been used to optimize force field parameters for MOF–guest interactions previously.[125,130] The form of the force field used in this work is

$$
\begin{aligned}
E_{\text{int}} &= \sum_{i}^{N_{\text{A}}} \sum_{j}^{N_{\text{B}}} \frac{1}{4\pi\epsilon_0} \frac{q_i q_j}{r_{ij}} + E_{\text{attr}}(i,j) + E_{\text{rep}}(i,j) \\
E_{\text{attr}}(i,j) &= -\frac{A_{ij}}{r_{ij}^6} \\
E_{\text{rep}}(i,j) &= \begin{cases} \infty & r_{ij} < r_{\text{min}} \\ B_{ij} \exp(-C_{ij} r_{ij}) & r_{ij} > r_{\text{min}} \end{cases}
\end{aligned}
\tag{2.8}
$$

where $E_{\text{attr}}(i, j)$ and $E_{\text{rep}}(i, j)$ are the attraction and repulsion energies. The q_i and q_j terms are the charges of atoms i and j. The r_{ij} term represents the distance between atoms i and j within molecules A and B, which contain N_{A} and N_{B} atoms, respectively. The vacuum permittivity is provided as ϵ_0, while A_{ij}, B_{ij}, and C_{ij} are parameters to be fitted from the NEMO decomposed, quantum mechanical reference data. The E_{attr} term contains contributions from the dipole, quadrupole, induction, and dispersion interactions. The E_{rep} term was computed by fitting an exponential function to the curve resulting from eq 2.7. The r_{min} value present in this term was chosen to prevent the Buckingham potential from going to negative infinity as r_{ij} approaches zero.

Note that during the parametrization procedure all of the pairwise interactions besides Fe(II)–O(CO_2) between the cluster atoms and the CO_2 atoms were calculated using a point charge interaction term and a conventional Lennard-Jones potential with

standard UFF parameters. To determine the Fe(II)–O(CO_2) parameters in eq 2.8, a simple grid searching method was implemented. A one-dimensional array was used to minimize the deviation with respect to the reference attraction energy curve. A two-dimensional array containing different ranges for the B_{ij} and C_{ij} parameters was constructed, and the pair of parameters that minimized the deviation with respect to the reference repulsion energy curve was chosen. The attractive parameters (A_{ij}) and repulsive parameters (B_{ij},C_{ij}) derived from the PEC were fitted separately.

In summary, three force fields were combined to give the overall force field used in this work. The first and most important van der Waals (vdW) parameters define the vdW interaction between Fe(II) and the oxygen of CO_2. These were the parameters optimized in this work. The second set regards all other pairwise interactions between the MOF and CO_2. These parameters were taken directly from UFF because it often describes organic molecules[131] and nonbonding interactions within closed shell, closed site MOFs quite well.[132] The third set of vdW parameters was used to describe the vdW CO_2–CO_2 interactions. These were taken from the Transferable Potential for Phase Equilibria (TraPPE) force field,[129] which is a reliable and transferable force field for intermolecular interactions of CO_2 molecules. The Lorentz-Berthelot mixing rules were used for the vdW interactions.[133,134] Note that in all cases the MOF atomic point charges were computed with LoProp, and the CO_2 atomic point charges were obtained from the TraPPE force field.[129]

GCMC Simulations

Adsorption isotherms of CO_2 were simulated using the GCMC technique. In the grand-canonical ensemble, the chemical potential, the volume, and the temperature are held constant. In these simulations, both the framework and the guest molecules were regarded as rigid. A $1 \times 1 \times 4$ supercell (see Supporting Information Figure S10 and Table S2) was chosen to ensure that all of the potentially relevant vdW interactions are consistently accounted for. The vdW interactions were truncated and shifted to zero at the cutoff radius of 12.8 Å. No tail correction was used. The electrostatic energy was computed using the Ewald summation technique. Several million configurations were sampled in each simulation. These configurations were generated by random CO_2 translation, rotation, insertion, and deletion to obtain a satisfactory statistical average.

Detailed descriptions of the parameters for the vdW interactions and the atomic charges of the framework atoms can be found in sections 2.2.2 and 2.2.3.

2.2.3 Results

Gas Adsorption Measurements

The optimized parameters for the dual-site Langmuir–Freundlich model (eq 2.3) are reported at three different temperatures in Table 2.1. Excess CO_2 adsorption isotherms in terms of CO_2 per Fe(II) cation are reported in Figure 2.9. The CO_2 loading per Fe(II) site increases with decreasing temperature. This is because the average kinetic energy of the CO_2 molecules allows a larger proportion of them to escape the binding wells that result from the open sites of the MOF. At a pressure of 1 bar, the number of CO_2 molecules per Fe(II) site is approximately 0.80 at 45 °C, 0.95 at 35 °C, and 1.10 at 25 °C. No saturation was observed under the chosen experimental conditions. The adsorption and desorption measurements both fit closely with the dual-site Langmuir–Freundlich plot at each temperature.

Table 2.1: Parameters for the Dual-Site Langmuir–Freundlich Fit of the Experimental Isotherm Data

temp (°C)	$q_{sat,1}$ (mmol/g)	b_1 (bar^{-1})	ν_1	$q_{sat,2}$ (mmol/g)	b_2 (bar^{-1})	ν_2
25	8.20	4.29	1.07	0.83	0.77	4.26
35	8.20	2.72	1.07	0.83	0.30	4.26
45	8.20	1.77	1.07	0.83	0.21	4.26

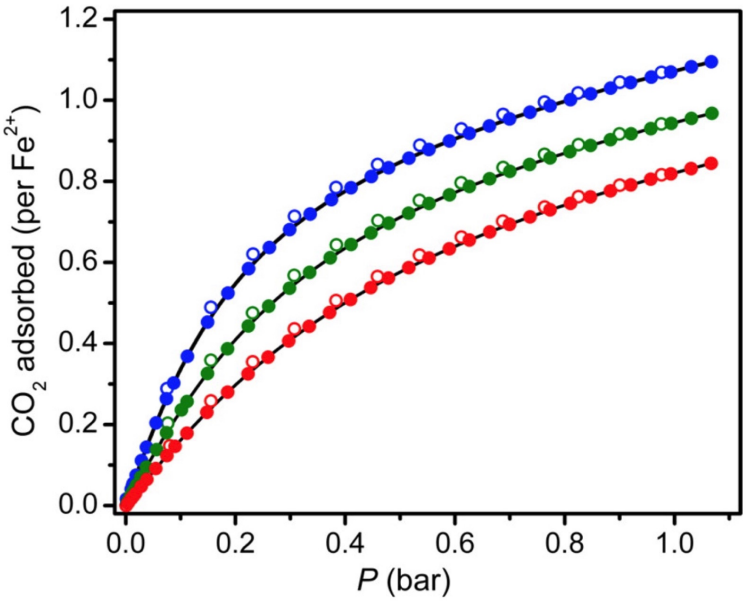

Figure 2.9: CO_2 adsorption isotherms in Fe-MOF-74 at 25 (blue), 35 (green), and 45 (red) °C; closed and open symbols represent adsorption and desorption, respectively. The continuous solid lines are the dual-site Langmuir–Freundlich fits using the parameters specified in Table 2.1.

Structural Analysis

The first coordination sphere of Fe-MOF-74 is pictured in Figure 2.10, and the bond distances computed with periodic DFT and the PBE and PBE+U functionals along with the Mg-MOF-74 bond distances optimized with PBE[83] are reported in Table 2.2. Table 2.2 indicates that PBE is not capable of reproducing experimentally determined metal–metal distances for Fe-MOF-74 with the present computational setup. When a Hubbard U correction of 5 eV was used on the 3d levels of Fe(II), the metal–metal distances within Fe-MOF-74 were closer to those determined by experiment.

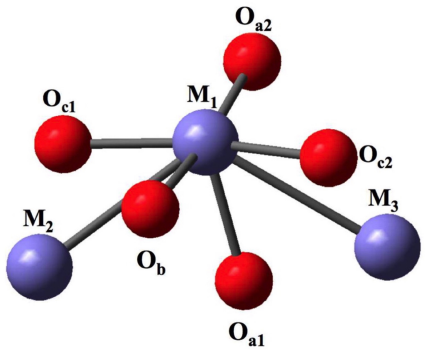

Figure 2.10: A single Fe(II) ion and its nearest neighbors within Fe-MOF-74. The O_a, O_b, and O_c labels correspond to atom types described in Supporting Information S1. M_1, M_2, and M_3 are Fe(II) ions.

Table 2.2: Bond Distances for the Nearest Neighbors of a Metal Ion in Fe-MOF-74 and Mg-MOF-74 Computed Using Periodic DFT

	length (Å)				
bond	Fe(PBE+U)	Fe(PBE)	Fe(exp)[a]	Mg(PBE)[b]	Mg(exp)[b]
M_1–M_2	3.00	2.80	3.00	2.94	2.94
M_1–M_3	3.00	2.79	3.00	2.94	2.94
M_1–O_{a1}	2.13	2.03	2.13	2.03	2.14
M_1–O_{a2}	2.07	2.06	2.17	2.04	2.01
M_1–O_b	2.11	2.03	2.11	2.08	2.18
M_1–O_{c1}	2.08	2.11	2.07	2.03	1.92
M_1–O_{c2}	2.07	2.04	1.99	2.03	1.86

[a] From Bloch *et al.*[75]
[b] From Dzubak *et al.*[83]

Interaction Energy Curves

Interaction energies for three versions of the 60-atom cluster, differing by the atoms that were used to represent the peripheral Fe(II) centers, are provided in Figure 2.11.

These interaction energy curves are within 1 kJ/mol of each other in the considered configuration space. Because this deviation is within the numerical uncertainty of the method, these curves are considered to be in good agreement. We can thus state that the *1Fe3Mg* and *1Fe3Zn* models are good approximations of the *4Fe* cluster when it comes to interaction with CO_2 in the chosen configuration space. The components of the NEMO force field from Figure 2.12 indicate that, with the model and level of theory used, the dispersion contribution to the binding of CO_2 with the Fe(II) ion of interest is quite small when compared to the electrostatic and induction quantities (see Figure 2.12). This finding may be ascribed to the small basis set used for the PEC calculations, which was chosen for computational efficiency. Because only the CO_2, the central Fe(II) ion, and the five oxygens coordinated to the Fe(II) had VDZP basis sets, much of the electron correlation energy is missed.

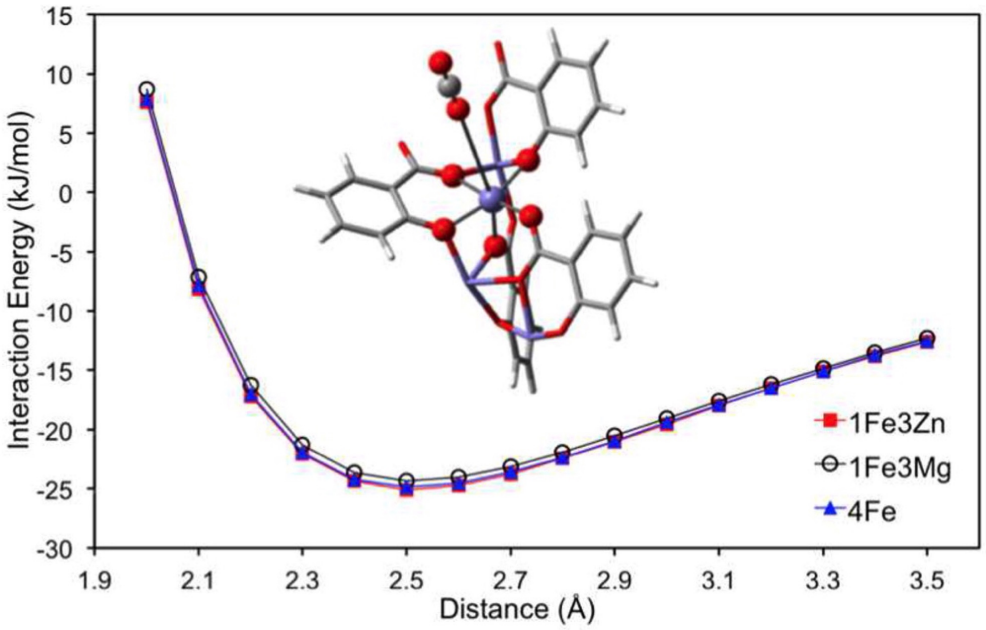

Figure 2.11: ROMP2 interaction energies computed for clusters in which the three noncentral metal atoms were modeled by Mg(II) ions (black curve), Zn(II) ions (red curve), and Fe(II) ions (blue curve). A view of the CO_2 path as it approaches the MOF fragment is also provided.

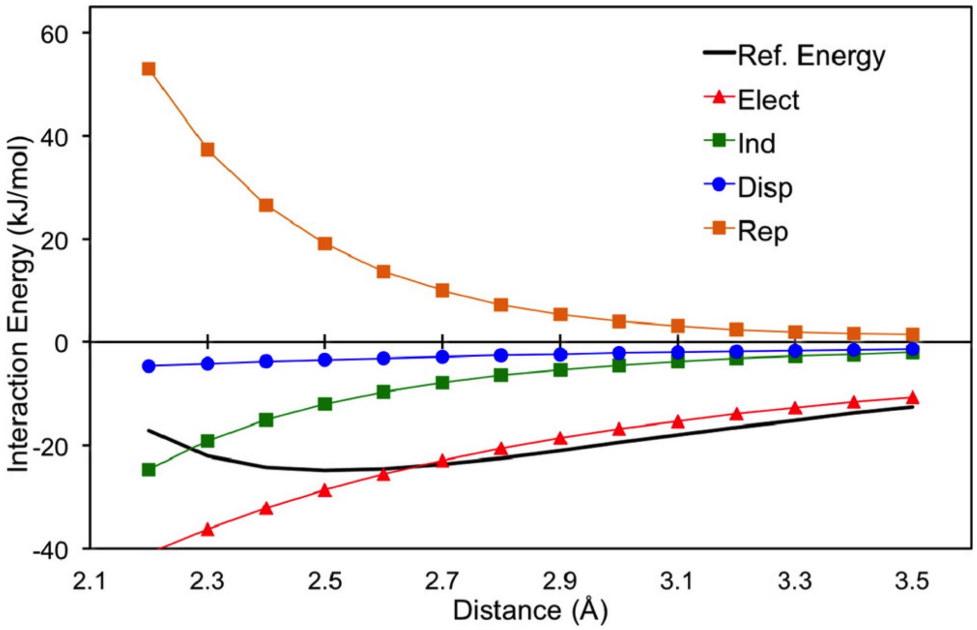

Figure 2.12: NEMO decomposition of the ROMP2 reference curve, including atomic dipole and quadrupole contributions, of the interaction of the 60-atom Fe-MOF-74 cluster with CO_2.

Force Fields

The LoProp charges used in the final force field and those previously used in the Mg-MOF-74 case[83] are reported in Table 2.3, with more significant numbers in Supporting Information Table S1. These charges were used in the Coulombic term reported in eq 2.8. The charges obtained for Fe-MOF-74 in Table 2.3 are quite similar to those previously obtained for Mg-MOF-74.[83] The ligand charges are all more positive in the Fe-MOF-74 case in part because of the more negative Fe(II) ions present in the model clusters. The large difference between the hydrogen charges is due to the fact that these charges were set to neutralize the charge of the unit cell.

The result of the final fitting of the attraction and repulsion curves for the Fe-MOF-74 case is plotted in Figure 2.13. These curves indicate that the Fe(II) ion contributes more to the attraction and repulsion energy than the other atom types within this configuration space. Also, the Fe(II) ion accounts for approximately one-half of the total attraction energy and a higher proportion of the repulsion energy. The dispersion

and repulsion curves that resulted from using other scaling factors on the dispersion energy term are provided in Supporting Information Figure S12.

Table 2.3: LoProp Charges for Fe-MOF-74 and Mg-MOF-74 Computed with ROMP2 Using the Clusters Provided in Supporting Information Figures S2-S8

	charge	
atom	Fe-MOF-74	Mg-MOF-74[a]
metal	1.51	1.56
O_a	−0.75	−0.77
O_b	−0.70	−0.71
O_c	−0.80	−0.83
C_a	0.61	0.48
C_b	−0.14	−0.14
C_c	0.23	0.19
C_d	−0.16	−0.18
H	0.21	0.39

[a]From Dzubak *et al.*[83]

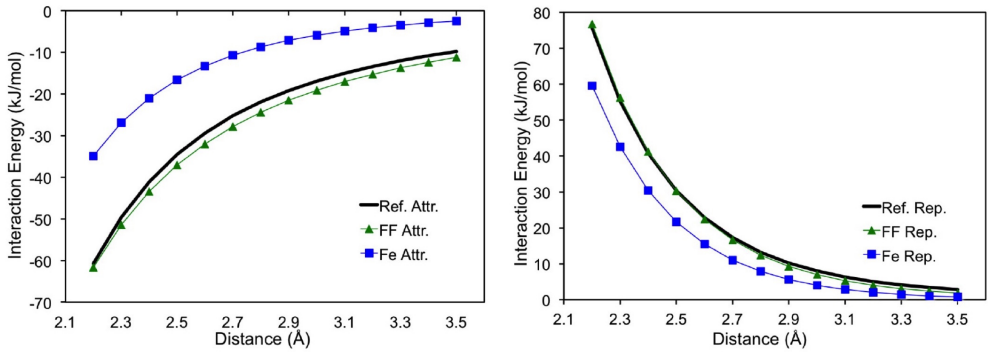

Figure 2.13: Force field fitting results for the ROMP2 interaction energies of CO_2 with the Fe-MOF-74 60-atom cluster. The attraction (Attr.) energy reference (Ref.) curve, force field fitting result (FF), and Fe(II) contribution are reported on the left; the same curves are reported on the right for the repulsion (Rep.) energy.

To validate further this parametrization method, we applied the same methodology proposed in this work to the Mg-MOF-74 case. The Mg-MOF-74 fitting results from this work match closely previous results from Dzubak *et al.*[83] The force field parameters for the Fe(II)–O(CO_2) interaction within Fe-MOF-74 are reported in Table 2.4 along with the parameters used for the Mg(II)–O(CO_2) interaction. Note that these new parameters reproduced satisfactorily the reference attraction and repulsion energy curves for both the Fe-MOF-74 and the Mg-MOF-74 cases (see Figures 2.13 and 2.14).

Table 2.4: Force Field Parameters for the Fe(II)–O(CO_2) and Mg(II)–O(CO_2) from This Work in the Form of Equation 2.8

	Fe(II)		Mg(II)	
	$\epsilon = 2.9$	$\epsilon = 3.7$	$\epsilon = 4.5$	$\epsilon = 2.0$
A (kJ/mol·Å^6)	2083	2932	3777	3616
B (kJ/mol)	317300	164000	99500	191400
C (Å^{-1})	4.040	3.664	3.373	3.815

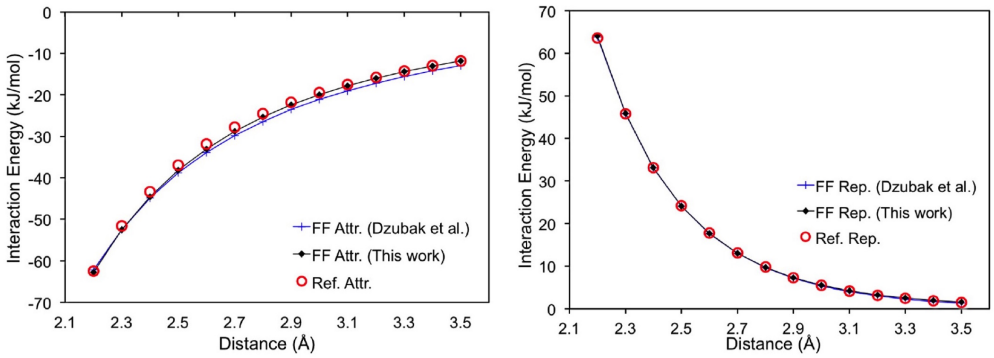

Figure 2.14: Force field fitting results for the MP2 interaction energies of CO_2 with the Mg-MOF-74 60-atom cluster. The result from fitting to the attraction energy is pictured on the left. The Ref. Attr. and Ref. Rep. lines represent the MP2 interaction energies separated into attractive and repulsive portions by NEMO. The repulsion fitting result from this work is provided on the right as FF Rep. along with the repulsion fitting result from Dzubak *et al.*[83] This fitting procedure was performed with a scaling factor of 2.0 on the dispersion term.

The vdW interaction energy curves resulting from this work are compared to the UFF curves in Figure 2.15. The vdW contribution to the interaction energy curve of the Fe-MOF-74 cluster and CO_2 obtained with UFF is similar to that predicted by our new force field. The minimum energy values are less than 1 kJ/mol apart, and the CO_2 equilibrium positions are different by approximately 0.1 Å. For Mg-MOF-74, on the other hand, UFF cannot properly capture the strong binding of CO_2 with the Mg(II) open-metal site and thus predicts much weaker binding than the force field fitted by Dzubak *et al.*[83] Dreiding predicts weaker CO_2 vdW minimum energies and longer minimum energy distances than both UFF and the fitted force field from this work.

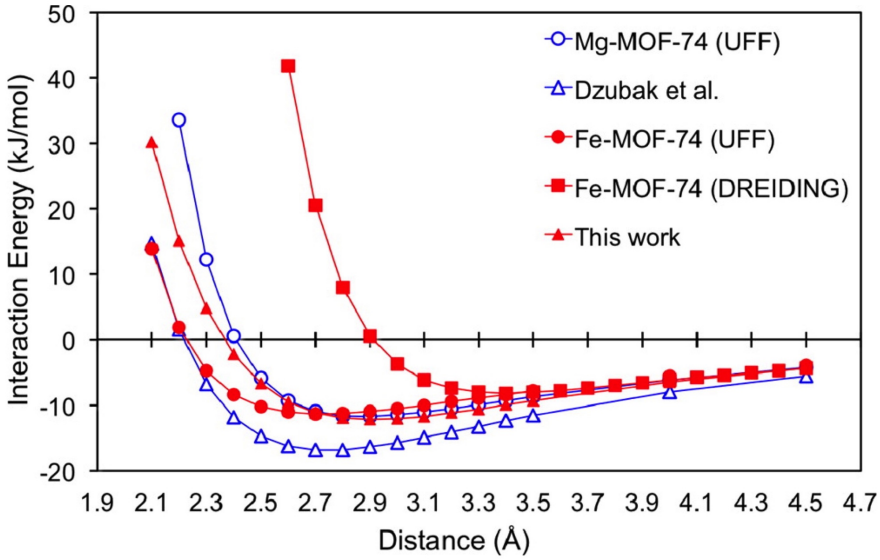

Figure 2.15: The vdW contributions to the interaction energy curves of the Mg-MOF-74 and Fe-MOF-74 cluster models with CO_2. The Dzubak *et al.* curve comes from reference Dzubak *et al.*[83]

Simulation of Isotherms

The experimental and theoretical Fe-MOF-74/CO_2 isotherms generated from this work are reported in Figure 2.16, and the isosteric heat of adsorption is provided in Figure 2.17. Isotherms simulated with UFF and Dreiding are shown for comparison. The force field from this work results in isotherms that are in good agreement with the

experimental isotherms of Fe-MOF-74 at multiple temperatures. Also, the interaction energy curves between the cluster model and CO_2 (see Figure 2.15) agree with findings of the classical simulations. The inflection points in the isosteric heat of adsorption curves predict the point at which open-metal binding sites are saturated with CO_2. This indicates that nearly all of the open-metal sites within Fe-MOF-74 were open for CO_2 binding. There is fairly good agreement between experiment and our force field considering that it is very difficult to exactly predict the Q_{st} inflection point when there is such a small difference in binding energy between the primary and secondary binding sites within Fe-MOF-74. An extended Q_{st} plot can be seen in Supporting Information Figure S13. To test the validity of this parametrization method, isotherms for the adsorption of CO_2 in Mg-MOF-74 were computed using the same approach. The attraction and repulsion fitting curves are reported in Figure 2.14, and are compared to the fittings from Dzubak *et al.*[83] The reference interaction energy curve was computed with MP2, which is numerically equivalent to the CASPT2 method with no active space. The same ANO-RCC basis sets used for the calculation of the reference PEC of CO_2 with Fe-MOF-74 were used for the Mg-MOF-74 case. The force field parameters for the Fe(II)–O(CO_2) and Mg(II)–O(CO_2) interactions are provided in Table 2.4.

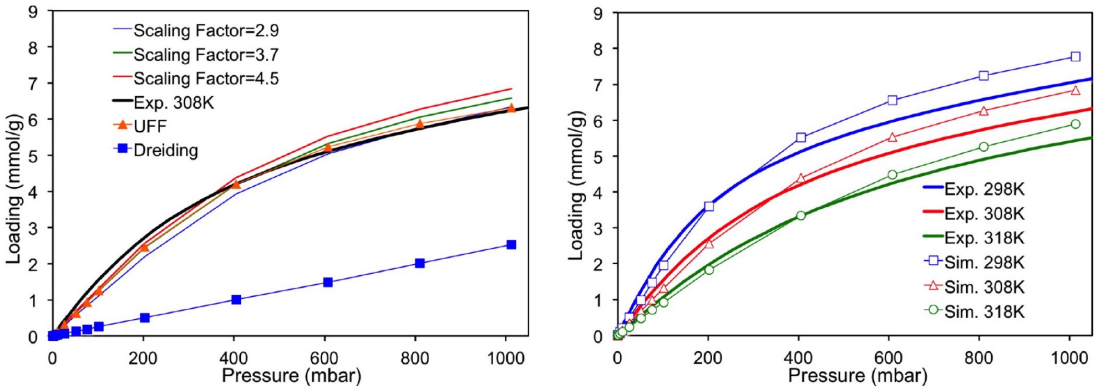

Figure 2.16: Experimental isotherm at 308 K is compared to the isotherm from the newly defined force field and the UFF and Dreiding force fields on the left. The picture on the left includes isotherms computed with different scaling factors on the dispersion term. The isotherms using the force field from this work are compared to experiment for multiple temperatures on the right.

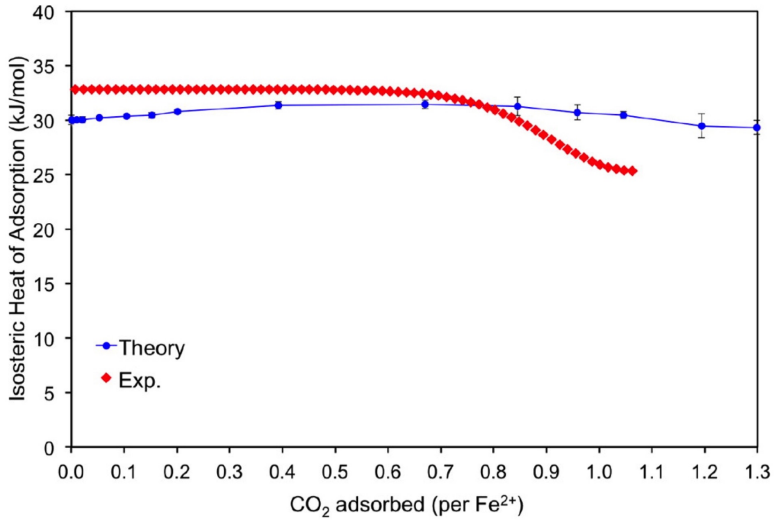

Figure 2.17: Experimental and theoretical Fe-MOF-74/CO_2 isosteric heat of adsorption curves derived in this work

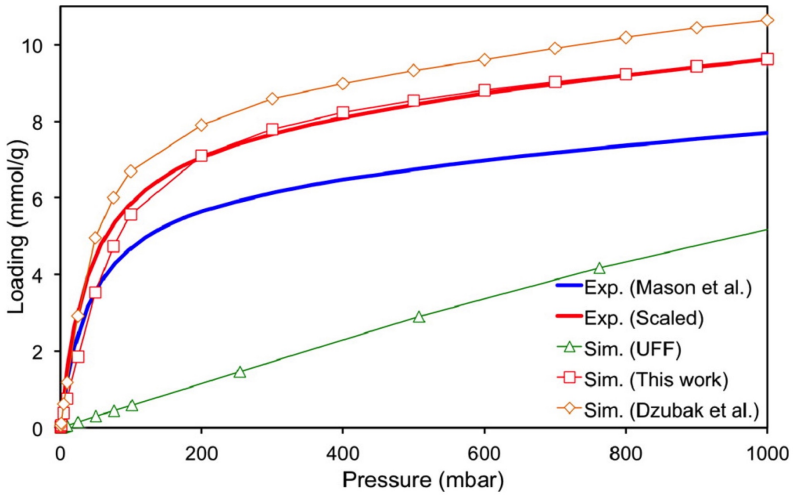

Figure 2.18: Isotherms of CO_2 adsorption in Mg-MOF-74. The experimental data were taken from Mason *et al.*[74] and were scaled assuming that 80% of the sites within Mg-MOF-74 were available for adsorption of CO_2 as demonstrated by Dzubak *et al.*[83] The experiment was performed at 313 K, which was the temperature considered in each simulation.

The fitted force field result from Dzubak *et al.*[83] is similar to the result obtained in this work. Our force field estimates that the attraction energy between CO_2 and the Mg(II) centered cluster is slightly weaker than the force field of Dzubak *et al.*[83] Simulations that used these two force fields are compared to experiment in Figure 2.18. Both force fields result in isotherms that are reasonably close to experiment, while UFF significantly underestimates the loading of CO_2.

2.2.4 Discussion

Figure 2.11 demonstrates that the interaction energy is not significantly affected by the way that the peripheral Fe(II) ions are modeled, provided that the effective charge of these ions is respected. This indicates that if the noncentral metals play a role in the adsorption, it is essentially electrostatic. This conclusion is in agreement with recent works that reported that the isotropic couplings between the Fe(II)–Fe(II) centers within this MOF are quite small.[73,94,104,113]

With the PBE functional, the obtained Fe(II)–Fe(II) distances in Fe-MOF-74 were found to be significantly smaller than experiment, while in the Mg-MOF-74 case, satisfactory results were obtained. Because the M(II)–M(II) distances are considered reliable experimental quantities (the positions of heavy atoms being obtained quite accurately), this shows a problem in the description of the Fe-MOF-74 electronic structure with the PBE exchange-correlation functional. The introduction of a U correction of 5 eV led to the best reproduction of the Fe(II)–Fe(II) distances in Fe-MOF-74. Note that a Hubbard U correction typically leads to the localization of the spin density on the paramagnetic centers, and corrects the unphysical, metallic behavior often obtained with the PBE exchange-correlation functional for open-shell systems, and is thus commonly applied to these systems.[104]

The current force field reproduces experimental findings quite well. The overestimation of CO_2 loading at higher pressures is probably due to imperfections in the experimental sample that are not present in our GCMC simulation. This was the reason cited for the scaling of the experimental isotherm discussed in Dzubak *et al.*[83] The scaling of the experimental isotherm was not replicated for Fe-MOF-74 because the inflection point from the experimental data occurred at between 0.90 and 0.95 (see Figure 2.17), indicating that nearly all of the metal sites within Fe-MOF-74 were open for CO_2

binding. Furthermore, the simulated Q_{st} curve did not have an obvious inflection point. However, imperfections in the experimental sample must be present even in this case, and thus such a good agreement between the two curves was not expected.

In Figure 2.16 and Supporting Information Figure S11, the effect of the dispersion scaling factor ϵ from eqs 2.6 and 2.7 is reported. These plots demonstrate that our force field is not heavily sensitive to changes in the ϵ parameter, once it is large enough to make the repulsion energy positive within the configuration space ($\epsilon = 2.9$). Additionally, Figure 2.15 shows that UFF provides reasonable results for Fe-MOF-74 but not for Mg-MOF-74. The UFF and fitted curves are similar for Fe-MOF-74 but are quite different in the Mg-MOF-74 case. UFF clearly overestimates the repulsion energy contribution for the Mg-MOF-74 cluster/CO_2 interaction. Also of note is the large underestimation in Fe-MOF-74 cluster/CO_2 binding predicted by Dreiding. Both Dreiding and UFF use a charge equilibration model. However, the Dreiding vdW parametrization was designed to describe primarily biological molecules, while UFF was meant to be more general. UFF and Dreiding parameters were each optimized with training sets that did not include metal sites similar to those in the MOF-74 series. As such, it was somewhat expected that these force fields would perform inconsistently for these systems, because they are outside of their respective training sets. These findings indicate that commonly used force fields do not yield consistent results for the MOF-74 series. In contrast, the force fields developed with the parametrization scheme proposed in this work do provide reasonable estimates for adsorption of CO_2 within Mg-MOF-74 and Fe-MOF-74.

The isotherm resulting from this work estimates less CO_2 adsorption than does the isotherm computed by Dzubak *et al.*[83] (see Figure 2.18). The main differences between these two force field parametrizations are that an r^{-5} attraction term was used in the force field of Dzubak *et al.*[83] to improve the fitting quality, and all eight clusters pictured in Supporting Information Figures S2-S8 were used to compute interaction energy curves with CO_2. NEMO energy decompositions were then performed on each of the resulting PECs, and pairwise parameters were optimized for the interaction of each atom type with O(CO_2). In this work, only the metal–O(CO_2) interaction parameters were computed, and the other parameters were taken from UFF. The remaining clusters were used only to compute LoProp charges. A comparison of the resulting force field fittings is plotted in Figure 2.14. When the vdW parameters optimized with the Mg-MOF-74

oxygen and carbon atom-type clusters were used, the resulting force field did not yield an accurate prediction of CO_2 adsorption within Fe-MOF-74, and it is difficult to rationalize because so many variables are present in this force field parametrization. Because UFF has demonstrated some success in cases where there is not a strong interaction between the guest and an open-metal site, we decided to use these parameters to describe the nonmetal, vdW interactions between the MOF and CO_2. In this way, the laborious determination of pairwise parameters from a large number of calculations was avoided. Note that the force fields proposed in this work and those computed by Dzubak *et al.*[83] are both fairly system specific because the open-metal site within the MOF-74 series is unique and the structural changes that result from switching metals have non-negligible effects on CO_2 binding. These force fields, on the other hand, are less dependent on minor changes to the topology of the MOFs. The important improvement made in this work with respect to the work of Dzubak *et al.*[83] is the reduction in the number of quantum calculations necessary to simulate new isotherms, and the extension of the method to open-shell MOFs. The energies computed by our new force field and the one proposed by Dzubak *et al.*[83] are comparable along the metal–CO_2 path. The Mg-MOF-74 study in this work demonstrates that the metal–CO_2 interaction is key to improving the prediction of adsorptive properties within open-metal site MOFs. Furthermore, this result provides validation for the approach proposed in this work for CO_2 adsorption within Fe-MOF-74. By only optimizing the parameters for the interaction of the CO_2 oxygen atoms with an open-metal site, it is possible to provide reasonable descriptions of adsorptive properties.

2.2.5 Conclusions

High-purity CO_2 was flowed through activated Fe-MOF-74, and isotherms were measured at 25, 35, and 45 °C. The dual-site Langmuir–Freundlich model provided a fairly precise fit to the experimentally determined adsorption and desorption measurements at three different temperatures. The CO_2 loading increases with decreasing temperature, and no saturation was observed under the chosen experimental conditions.

The simulated isotherms of the adsorption of CO_2 within Fe-MOF-74 using the UFF and Dreiding force fields were not consistently accurate as compared to experiment. Additionally, the CO_2 adsorption within Mg-MOF-74 predicted by UFF differed from

experiment by approximately 1 order of magnitude at low pressure. Thus, force field parameters were optimized to better describe the strong open-metal site interaction with CO_2. A CASSCF calculation was used to confirm that the Fe(II) ions within Fe-MOF-74 are in a monoconfigurational quintet state. ROMP2 was then used to compute a reference PEC, and the NEMO approach was used to partition this interaction curve into attractive and repulsive terms. The Fe(II)–O(CO_2) Buckingham interaction parameters were fit against these terms. The CO_2–CO_2 interactions were modeled using the TraPPE force field. The remaining vdW parameters were all taken from UFF. This was done based on the success of UFF with MOFs that do not have open-metal sites,[79,80,81] and to simplify the parametrization scheme. With this scheme, a force field was derived that can accurately predict CO_2 adsorption for a MOF containing high-spin Fe(II) ions by using LoProp charges and optimizing three vdW parameters describing the Fe(II)–O(CO_2) interaction.

To further validate the parametrization scheme proposed in this work, the isotherm of CO_2 within Mg-MOF-74 was computed in a way that was similar to the Fe-MOF-74 case, and compared to experiment and the results of Dzubak *et al.*[83] The isotherm of CO_2 within Mg-MOF-74 computed in this work is in good agreement with the previously reported experimental and computational results, suggesting that parametrizing the metal–O(CO_2) interactions for these two MOFs was sufficient for the simulation of accurate CO_2 adsorption isotherms. This indicates that force fields for MOFs with dominant metal–guest interactions could be parametrized quickly with this scheme. Furthermore, this method makes the computation of adsorption isotherms involving multiconfigurational states feasible.

2.2.6 Additional Information

Supplementary information is available in the online version of the paper. The Supporting Information includes: Clusters and unit cells, equations used to perform the NEMO decomposition, a plot showing the effect of the scaling factor on the dispersion term, and an isosteric heat of adsorption plot of CO_2 in Fe_2(dobdc). This material is available free of charge at `http://pubs.acs.org`. Correspondence and requests for materials should be addressed to B. S. and L. G. The authors declare no competing financial interests.

Acknowledgements

We thank Sijie Luo for assisting with periodic DFT calculations, and William C. Isley III, Stuart G. Kohl, and Prof. Christopher J. Cramer for their help and support. This research was supported by the U.S. Department of Energy, Office of Basic Energy Sciences, Division of Chemical Sciences, Geosciences and Biosciences under Award DE-FG02-12ER16362. A.L.D. was supported by the US Department of Energy under contract DE-SC0001015.

2.3 Uranyl–Peroxide Nanocapsules in Aqueous Solution: Force Field Development and First Applications

The self-assembly of uranyl-peroxide nanocapsules in aqueous solution is unique in uranium chemistry and has potential applications in the fabrication and reprocessing of actinide-based materials. We present the first study of these species in aqueous solution by means of classical molecular dynamics simulations. To this end, we parametrized a uranyl-peroxide force field from interaction energies computed with second order Møller-Plesset perturbation theory and fit to a Born-Huggins-Mayer potential. Bonded parameters were fit from density functional theory calculations. The solvent and counterion structures surrounding four different systems ($[U^{VI}O_2]^{2+}$, $[(U^{VI}O_2)_2(\mu^2\text{-}O_2)]^{2+}$, $[(U^{VI}O_2)_5(\mu^2\text{-}O_2)_5]$, and $[(U^{VI}O_{20}(\mu^2\text{-}O_2)_{30}]^{20-}$) were studied in aqueous solution. The largest studied system is predicted to encapsulate an ice-like water cluster.

2.3.1 Introduction

Understanding and controlling the solution chemistry of the uranyl ion, $[U^{VI}O_2]^{2+}$, the most common form of uranium in aqueous solution, is central to the development of an advanced nuclear energy cycle and in developing remediation strategies for contaminated sites.[136] Gaining nanoscale control over actinide materials may result in a more

Adapted with permission from P. Miró, B. Vlaisavljevich, A. L. Dzubak, S. Hu, P. C. Burns, C. J. Cramer, R. Spezia, L. Gagliardi. *J. Phys. Chem. C* 2014, *24730*.[135] Copyright 2014, American Chemical Society. Author contributions and additional information may be found in section ??.

effective method for processing nuclear materials with applications not only in materials fabrication but also in fuel reprocessing.[137] Nanoscale clusters and nanocapsules of actinides may also form in the environment, and the impact of such materials on the mobility of actinides under environmental conditions is of great interest.

Recent experimental work has led to the characterization of a family of polyoxometalate nanocapsules containing uranyl polyhedra bridged through peroxide and hydroxyl groups.[138,139,140,141,142,143,144] More recently, larger linking groups like oxalate or pyrophosphate have also been employed in the formation of uranyl-based cage clusters.[142,144,145,146] The self-assembly of these species occurs in aqueous solution over a broad range of pH conditions at room temperature and is unique in actinide chemistry.[147] In most cases, the uranyl polyhedron is a hexagonal bipyramid, the apexes of which correspond to the oxygen atoms of the uranyl cation. The bipyramids then bind to each other by sharing equatorial edges with adjacent polyhedra. At least some of these shared edges correspond to peroxide groups. Clusters containing up to 124 uranyl polyhedra have been characterized. They exhibit a wide range of high symmetry topologies including (but not limited to) the well-known fullerene topologies.[148]

The presence of peroxide groups that bridge uranyl ions is thought to play a fundamental role in capsule formation. The inherently bent U–O_2–U dihedral angle fosters curvature and formation of nonplanar species that ultimately close into a capsule.[149,150] Additionally, the alkali countercations that are present during synthesis may influence the nanocapsules topology, since the curvature of the walls of the resulting capsule is controlled, to some extent, by cation coordination.[151,152] Experiments and first-principles studies have provided some information on the position of the encapsulated counterions, but typically not of the counterions outside the capsule as a consequence of structural disorder. Furthermore, the solvent structure and counterion positions inside the larger capsules remain largely unknown, although X-ray diffraction studies of crystals built from clusters have provided locations of some counterions.[139,141] Analogous with classical transition metal polyoxometalates, the polyanionic nature of these capsules encourages interaction with the countercations present in solution.[153] Understanding the solvent and counterion dynamics surrounding uranyl-peroxide nanocapsules is fundamental toward their use in applications (e.g. uranium reprocessing through ultrafiltration of uranyl-peroxide nanocapsules).[154]

We have developed a uranyl-peroxide force field starting from the simplest fundamental building blocks of the nanocapsules (e.g. the uranyl ion and a uranyl-peroxide-uranyl dimer) in order to study these capsules in solution by means of classical molecular dynamics simulations. This study focuses on four systems: $[U^{VI}O_2]^{2+}$ (**U$_1$**), $[(U^{VI}O_2)_2(\mu^2\text{-}O_2)]^{2+}$ (**U$_2$**), $[(U^{VI}O_2)_5(\mu^2\text{-}O_2)_5]$ (**U$_5$**), and $[(U^{VI}O_{20}(\mu^2\text{-}O_2)_{30}]^{20-}$ (**U$_{20}$**) (Figure 2.19). All of these uranyl-peroxide species have been previously synthesized.[139] **U$_2$**, the smallest known uranyl-peroxide species, has been proposed as the first step toward the formation of **U$_5$**, **U$_{20}$**, and the remaining larger nanocapsules.[149] Likewise, **U$_5$** has been proposed as a building block of the **U$_{20}$** nanocapsule that is composed of 12 pentagonal units.[139] Furthermore, since little is known about the solvent structure surrounding these species, an objective of this work is to shed some light onto the hydration properties of uranyl-peroxide species and the differences (if any) among the studied species, as well as to identify the solvent structure inside the cavity of **U$_{20}$** in aqueous solution.

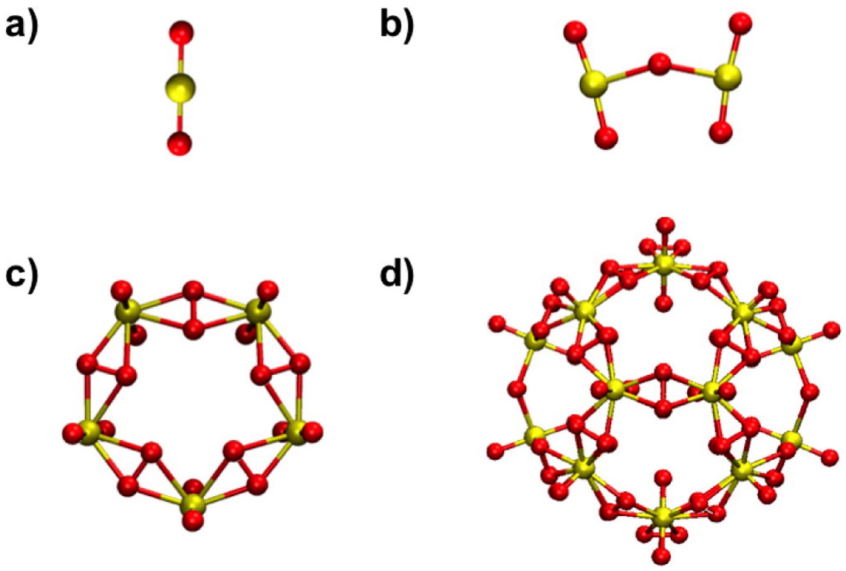

Figure 2.19: Uranyl and uranyl-peroxide systems studied in this work: $[U^{VI}O_2]^{2+}$ (a), $[(U^{VI}O_2)_2(\mu^2\text{-}O_2)]^{2+}$ (b), $[(U^{VI}O_2)_5(\mu^2\text{-}O_2)_5]$ (c), and $[(U^{VI}O_{20}(\mu^2\text{-}O_2)_{30}]^{20-}$ (d). Color code: Uranium and oxygen atoms are shown as yellow and red spheres, respectively.

2.3.2 Computational Details

All of the molecular dynamics simulations were performed using the DLPOLY classic package developed at Daresbury Laboratory.[155] The systems presented in Figure 2.19 were simulated using the force field parametrized in this work, while the solvent interactions (water–water) were described using the TIP3P water model.[156] The counterion interactions (water–sodium and sodium–sodium) were treated using the parameters proposed by Lee and Rasaiah.[157]

Electrostatic interactions were accounted for using the Ewald summation technique[158] with a convergence parameter of 0.210 $Å^{-1}$ and considering a maximum of six wave vectors in each direction. The Verlet leapfrog algorithm[159] was used to integrate the equations of motion with a time step of 1 fs and a cutoff of 10 Å. In order to optimize CPU usage, we have used a Verlet neighbor list[158] with a cutoff radius of 11 Å. Rigid body rotational motion is handled under the leapfrog scheme with Finchams implicit quaternion algorithm[160] with a tolerance of 10^{-5} Å.

The systems were solvated using a different number of water molecules depending on the system size (Table 2.5). The smaller species ($\mathbf{U_1}$ and $\mathbf{U_2}$) were simulated including 512 water molecules, whereas the larger species $\mathbf{U_5}$ and $\mathbf{U_{20}}$ used 1024 and 2048 water molecules, respectively. In the $\mathbf{U_{20}}$ simulations, 20 Na^+ ions were also included to neutralize the system. All of the systems were equilibrated for 100 ps in the canonical ensemble (NVT) followed by 500 ps in the isobaric-isothermal ensemble (NPT) ensemble. In the NVT simulations, the temperature was held fixed using the Nosé-Hoover thermostat with a relaxation time τ_T equal to 20 fs.[158,161,162] For NPT simulations, the pressure was kept fixed using the Nosé-Hoover barostat with a relaxation time equal to 40 fs.[158] Once equilibrated, we performed longer production simulations in different ensembles. Simulations at constant temperature were performed at room temperature (298 K), while those at constant pressure where performed at 1 atm. The details of the production runs for each system are given in the Supporting Information. In the production simulations, the positions and velocities of the system were stored every 10 time steps for analysis a posteriori. Furthermore, simulations were run for both flexible and rigid solutes.

Table 2.5: Details of the Systems Investigated

	$\mathbf{U_1}$	$\mathbf{U_2}$	$\mathbf{U_5}$	$\mathbf{U_{20}}$
box size (Å)[a,b]	25.1	24.9	31.3	39.3
no. of H_2O	512	512	1024	2048
no. of Na^+				20

[a]The simulated systems were fixed as cubic ($a = b = c$, $\alpha = \beta = \gamma = 90°$)

[b]Box size was obtained from NPT equilibration (isotropic barostat) for the flexible simulations

The procedure employed in developing this force field is presented in detail in the following section, and the quantum chemical calculations that were used as reference values for the force-field parametrization were performed as follows. Interaction energies were computed using second-order Møller-Plesset perturbation theory (MP2) for $\mathbf{U_1}$ and $\mathbf{U_2}$ with water as implemented in the MOLCAS 7.6 package.[163] While previous work by our group used the complete active space self-consistent field approach with corrections from second order perturbation theory (CASPT2) to fit uranyl–water interactions, our tests revealed that MP2 total energies were quantitatively similar to CASPT2 for $\mathbf{U_1}$. For this reason, MP2 was used since CASPT2 would be significantly more computationally demanding for $\mathbf{U_2}$ without yielding commensurately more accurate total energies. Counterpoise correction was used to account for basis set superposition error and relativistic effects were included using the scalar Douglas-Kroll-Hess Hamiltonian.[164,165] An ANO-RCC-VDZP basis set was used for all atoms.[166,167,168,169,170] Additionally, the Cholesky decomposition technique was combined with Local Exchange screening to significantly reduce the computational cost involved in generating the two-electron integrals.[171,172,173,174,175]

Geometry optimizations were performed for $\mathbf{U_2}$, $\mathbf{U_5}$ and $\mathbf{U_{20}}$ using density functional theory (DFT) as implemented in the Amsterdam Density Functional (ADF2010) program.[176,177,178] This level of theory was chosen since it has been used successfully to study the $\mathbf{U_{20}}$ and $\mathbf{U_{28}}$ clusters.[151,152] We chose to use geometries and frequencies to fit the intramolecular potential using a level of theory that could be used to treat the

full nanocapsules. The Perdew-Burke-Ernzerhof exchange-correlation functional (PBE) was employed together with a triple-ζ plus two polarization function basis set (TZ2P) on all atoms.[179] For non-hydrogen atoms, a small relativistic frozen-core potential was used. Relativistic corrections were introduced by the scalar-relativistic zero-order regular approximation (ZORA).[180,181,182,183,184] Bulk aqueous solvent effects were introduced using the COSMO continuum solvent model.[185,186,187,188] Geometries were fully optimized taking advantage of symmetry when present and their harmonic vibrational frequencies were computed.

2.3.3 Uranyl–Peroxide Force Field

While a handful of force fields for uranyl in water have been presented in the literature,[189,190,191] parameters are not available for uranyl peroxides (in particular, parameters for the peroxide oxygen atoms). Given our interest in a wide range of cluster topologies, we here develop a uranyl-peroxide force field from first-principles calculations based on the fundamental nanocapsule building blocks $[U^{VI}O_2]^{2+}$ $\mathbf{U_1}$ and $[(U^{VI}O_2)_2(\mu^2\text{-}O_2)]^{2+}$ $\mathbf{U_2}$. The nonbonded interactions were parametrized from second-order Møller-Plesset perturbation theory (MP2) calculations,[192] while the bonded interactions were parametrized from density functional theory (DFT) calculations.[193] Since all of the uranyl-peroxide species contain only UVI centers, the ground state is a closed shell singlet as expected.

In a previous study,[189] uranyl–water curves where computed using the complete active space SCF (CASSCF) method with corrections to the energy from second order perturbation theory (CASPT2). This approach has been used successfully to study actinide-containing systems, in particular to study the nature of covalent bonding in small molecules.[194,195,196,197] However, the relevant active spaces under consideration here contain only orbitals with contributions from the uranyl ion itself. Given that CASPT2 would be computationally intensive for $\mathbf{U_2}$, we also computed MP2 interaction energy curves between fragments. MP2 and CASPT2 yield quantitatively similar results for $\mathbf{U_1}$; therefore, only MP2 energies are reported in this work. This result should not be surprising given that MP2 can properly describe the ground state of the uranyl dication.

We computed several $\mathbf{U_1}$–H_2O and $\mathbf{U_2}$–H_2O interaction energy curves with different water orientations in order to sample the most relevant interactions between the

uranyl and peroxide fragments with the solvent (Figure 2.20). The uranyl-oxygen bond ($U–O_{uranyl}$) in $\mathbf{U_1}$ was fixed at 1.705 Åand a rigid TIP3P water model was used. The nonbonded interaction is composed of two terms: an electrostatic term and a nonelectrostatic term, V_{ij}^{NB}.

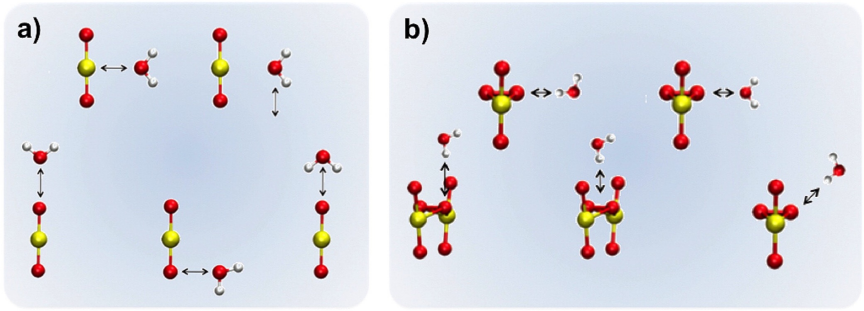

Figure 2.20: Pathways along which interaction energy curves were derived for the $\mathbf{U_1}$–H_2O (a) and $\mathbf{U_2}$–H_2O (b) interactions. Legend: Uranium, oxygen, and hydrogen atoms are shown as yellow, red, and white spheres, respectively.

In the electrostatic term, atomic partial charges derived from DFT calculations were used. In particular, the scheme developed by Swart *et al.* was used to obtain partial atomic charges for $\mathbf{U_1}$, $\mathbf{U_2}$, and $\mathbf{U_5}$ (see Table 2.6.[198] While running a DFT calculation on a building block to obtain charges is trivial, the final form of the force field should not require DFT calculations for novel clusters to obtain starting charges. Moreover, since the nanocapules have a large negative charge (even for the relatively small $\mathbf{U_{20}}$ nanocapsule), their DFT charges deviate significantly from those used in the fitting of the nonbonded parameters. Consequently, we set the charges for the oxygen atoms in the capsule equal to those in the $\mathbf{U_2}$ building block for both the uranyl and peroxide oxygen atoms. Then, the uranium charge was scaled in order to maintain the overall charge of the species.

Table 2.6: Atomic Partial Charges Used for Electrostatic Terms in the Molecular Dynamics Simulations

species	U	O_{uranyl}	$O_{peroxide}$
$\left[\left(U^{VI}O_2\right)\right]^{2+}$	2.54000	-0.27000	
$\left[\left(U^{VI}O_2\right)_2\left(\mu^2\text{-}O_2\right)\right]^{2+}$	2.45990	-0.46710	-0.52570
$\left[\left(U^{VI}O_2\right)_5\left(\mu^2\text{-}O_2\right)_5\right]$	2.52699	-0.59136	-0.67213
$\left[\left(U^{VI}O_2\right)_{20}\left(\mu^2\text{-}O_2\right)_{30}\right]^{20-}$	1.51130	-0.46710	-0.525700

The electrostatic term was subtracted from the quantum mechanically calculated reference total interaction energy curves prior to fitting the nonelectrostatic term to the Born-Huggins-Mayer (BHM) potential[199,200,201]

$$V_{ij}^{NB} = \sum_{i,j}\left(A_{ij}\exp\left(-B_{ij}r_{ij}\right) - \frac{C_{ij}}{r_{ij}^6} - \frac{D_{ij}}{r_{ij}^8}\right) \tag{2.9}$$

where A_{ij}, B_{ij}, C_{ij}, and D_{ij} are the parameters defined for each atom pair and r_{ij} is the interatomic distance. Long range parameters C_{ij} and D_{ij} were fitted without any sign constraints. The parameters for the O–O_{water}, U–O_{water}, and $O_{peroxide}$–O_{water} atom pairs are reported in Table 2.7. The nonelectrostatic parameters for the oxygen centers in the studied species and the sodium counterions were considered to be equivalent to water–sodium interactions, since the nonbonded term in the uranium–sodium interactions is considered to be negligible as the interaction is so dominated by the electrostatic term.

The U–O_{uranyl} and $O_{peroxide}$–$O_{peroxide}$ bond stretching parameters were fit to a harmonic potential from the vibrational frequencies obtained from DFT calculations. Single point energy calculations were performed at the same level of theory along the uranyl angle (O_{uranyl}–U–O_{uranyl}) and uranyl-peroxide angle (O_{uranyl}–U–$O_{peroxide}$) reaction coordinates in $\mathbf{U_1}$ and $\mathbf{U_2}$, respectively. The potential energy curves were then fit to a harmonic potential. The pliability of the U–$(O_{peroxide})_2$–U dihedral has been demonstrated experimentally and computationally.[149,150] Our force field does not define any dihedral explicitly since they are already indirectly included by the defined O_{uranyl}–U–$O_{peroxide}$ angle bending modes. All bonded parameters are given in Table 2.7.

Table 2.7: Intermolecular Parameters for the Nonbonded Term Using the Born–Huggins–Mayer[a] Potential Presented in eq 2.9 and Bond Stretching[b] and Angle Bending[c] Modes Using Harmonic Potentials $V_{ij} = 0.5K_{ij}\left(r_{ij} - r_{ij}^0\right)^2$ and $V_{ij} = 0.5K_{ijk}\left(\phi_{ijk} - \phi_{ijk}^0\right)^2$, Respectively

atom			parameters			
Nonbonded (Born–Huggins–Mayer)[a]						
i	j	k	A	B	C	D
U	O_{water}		360.92331	0.68480	58103.45591	−283958.20450
O_{uranyl}	O_{water}		−3898.95694	1.30286	−59841.66996	138921.01370
$O_{peroxide}$	O_{water}		−29.49020	0.21039	−8536.38565	0.00000
Bonded (Harmonic)[b,c]						
i	j	k	K_{ij}	K_{ijk}	r_{ij}^0	ϕ_{ijk}^0
U	O_{uranyl}		8537.71935		1.769	
$O_{peroxide}$	$O_{peroxide}$		4848.29742		1.446	
U	$O_{peroxide}$		1876.71236		2.338	
O_{uranyl}	U	O_{uranyl}		657.61177		180.0
O_{uranyl}	U	$O_{peroxide}$		590.80666		93.0

[a] A in kJ·mol^{-1}, B in Å^{-1}, C in kJ·Å^6·mol^{-1}, and D in kJ·Å^8·mol^{-1}
[b] K_{ij} in kJ·mol^{-1}·Å^{-2}, and r_{ij}^0 in Å
[c] K_{ijk} in kJ·mol^{-1}·deg^{-2}, and ϕ_{ijk}^0 in deg .

2.3.4 Results

Uranyl and Uranyl–Peroxide Dimer

As a first validation step, the fundamental building blocks used in the parametrization process (**U_1** and **U_2**) were studied. For **U_1**, our results are compared with previous experimental results[202,203] and simulations performed with classical molecular dynamics with nonpolarizable, polarizable, and DFT-based force fields (Table 2.8).[189,190,191,204,205,206,207] Unlike uranyl, there are no previous molecular dynamics studies of **U_2** in solution. For this reason, we will make comparisons with the complex $K_6[(U^{VI}O_2)_2(\mu^2\text{-}O_2)(C_2O_4)_4]$ synthesized by Sigmon *et al.* and characterized by single crystal X-ray diffraction.[139] Simulations were run treating the solutes as either rigid or flexible. Information regarding the structure of the various solvation shells was extracted from our simulations by plotting the radial distribution function, $g(r)$, of U–O_{water} as

reported in Figure 2.21 for the flexible simulations (and in Figure S1 of Supporting Information for the rigid ones). The first peak in the U–O_{water} $g(r)$ corresponds to the first solvation shell for both $\mathbf{U_1}$ and $\mathbf{U_2}$. Both the rigid and the flexible simulations of $\mathbf{U_1}$ predict a U–O_{water} distance in the uranyl polyhedron equal to 2.39 Åand a water coordination number (CN) of five, in good agreement with the previous simulations and experimental EXAFS and X-ray scattering studies (Table 2.8).[202,203]

The U–O_{water} distance in $\mathbf{U_2}$ is slightly longer when compared with $\mathbf{U_1}$ (Table 2.8). Our simulations confirm that one uranyl unit alone, $\mathbf{U_1}$, coordinates five water molecules in its equatorial plane (Figure 2.22 left). On the other hand, in $\mathbf{U_2}$ four waters coordinate to each uranium center. Each uranium also coordinates a μ^2-O_2 ligand making the total CN in $\mathbf{U_2}$ equal to six. In 2005, Burns reported a survey of the known uranyl minerals and inorganic compounds and found the average distances between uranium and equatorial oxygen atoms in pentagonal bipyrimids was 2.37 Å, while in hexagonal bipyrimids it was 2.45 Å.[208] Therefore, we attribute the elongation observed in the U–O_{water} distance with a change in total CN from five in $\mathbf{U_1}$ to six in $\mathbf{U_2}$ (in $\mathbf{U_2}$ four coordination sites are occupied by water molecules and two by the peroxide bridge). Moreover, a hexa-coordinate uranium center in uranyl-peroxide species has been observed in nearly all solid-state uranyl-peroxide species.[139,146,147]

Table 2.8: Structural Hydration Properties of $\mathbf{U_1}$, $\mathbf{U_2}$, and $\mathbf{U_5}$ Species[a]

	method	d(U-O_{uranyl})	d(U-O_{water})	α(O-U-O)	ϕ(U-(μ^2-O_p)-U)	CN
U_1						
this work	MD	1.705	2.39	180.0		5.0
this work	MD[b]	1.78[c]	2.39	175.7		5.0
Wipff *et al.*[190]	MD	1.80	2.45	nr[f]		5.0
Rai *et al.*[191]	MD, MC[d]	1.76	2.41	nr[f]		5.0
Hagberg *et al.*[189]	MD[e]	1.705	2.40	180.0[g]		5.0
Spezia *et al.*[204]	CPMD[b,e]	1.81[c]	2.41	nr[f]		5.0
Bühl *et al.*[205]	CPMD[b,e]	1.81[c]	2.48	nr[f]		5.0
Nichols *et al.*[206]	CPMD[b,e]	1.77[c]	2.44	174.1		5.0
Frick *et al.*[207]	QMCF[b,e]	1.66	2.49	nr[f]		5.0
experimental[202,203]		1.77	2.41–2.42			5.3
U_2						
this work	MD	1.80	2.42	180.0	151.5	3.8
this work	MD[b]	1.78	2.45	175.2	171.0	4.0
experimental[139,h]		1.79		178.0	153.0	4.0
U_5						
this work	MD	1.705	2.42	180.0	145.7	2.0
this work	MD[b]	1.77	2.42	173.5	165.6	2.0
experimental[139,h]		1.80		179.0	144.0	2.0

[a] Uranium–H_2O distance (Å) is extracted from the first peak in the U–O_{water} g(r) and coordination number (CN) is the corresponding integral
[b] Flexible model
[c] Averaged
[d] Bond distances were fixed but angles were allowed to vary in some MC simulations
[e] Polarizable model
[f] Not reported value
[g] Fixed value
[h] X-ray diffraction results in which oxalate ligands fill the uranium coordination sphere

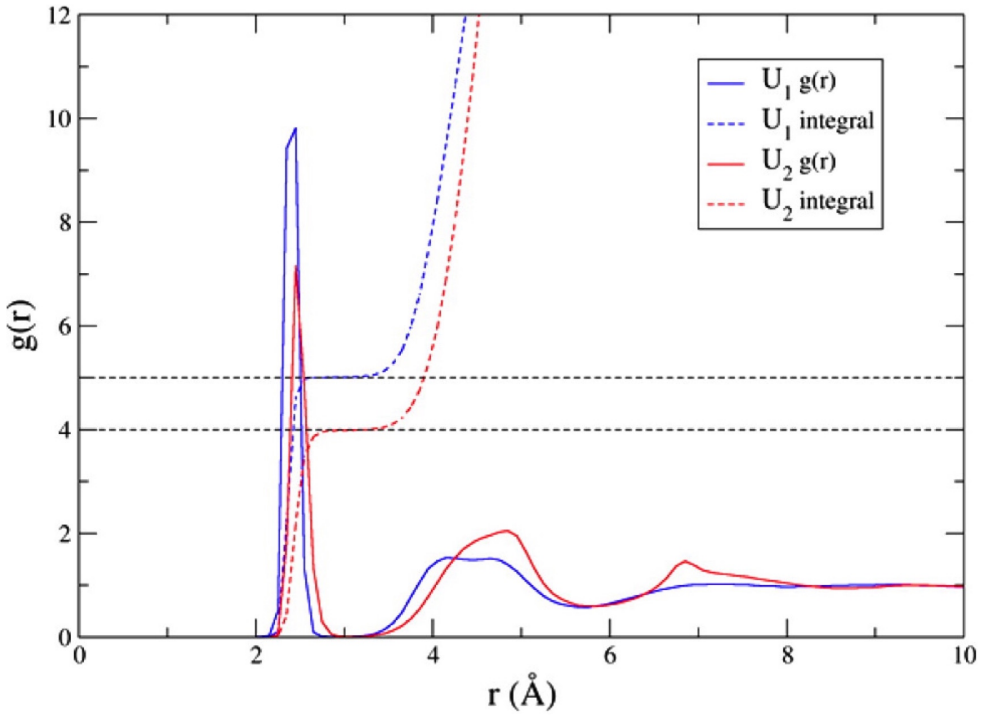

Figure 2.21: Radial distribution function, $g(r)$, between U–O_{water} of the flexible $\mathbf{U_1}$ (blue line) and $\mathbf{U_2}$ (red line) with the integration in dashed lines. Water coordination number (CN) of each uranium center (dashed black lines).

When comparing the rigid and flexible simulations, the CN for $\mathbf{U_1}$ remains unchanged; however, in $\mathbf{U_2}$ the water CN increases slightly from 3.8 to 4.0. The three-dimensional probability distribution of the solvent surrounding rigid $\mathbf{U_2}$ can be analyzed by means of a spatial distribution function (SDF) (Figure 2.22). The SDF of $\mathbf{U_2}$ consists of four probability basins of O_{water} density for each uranium center which is consistent with the RDF results presented in Figure 2.21. Furthermore, the combination of O_{water} and H_{water} density reveals the most probable water position during the $\mathbf{U_2}$ simulations.

For the simulations performed with the solute ($\mathbf{U_1}$ and $\mathbf{U_2}$) treated as flexible, the average values of the bond, angle, and dihedral oscillations in time are presented in Table 2.8. For both systems, the average U–O_{uranyl} bond and O_{uranyl}–U–O_{uranyl} angle are in good agreement with previous theoretical studies and experimentally determined

values.[139,202,204] Furthermore, the U–(μ^2–$O_{peroxide}$)$_2$–U dihedral angle fluctuates during the simulation ranging from approximately 160° to 180° in $\mathbf{U_2}$ with an average value of 172.9°. Recall that the U–(μ^2–$O_{peroxide}$)$_2$–U dihedral angle is very pliable.[149] Not only has this been demonstrated by means of DFT, but combined experimental and theoretical work has shown that crystal packing effects can influence the observed dihedral angle in the solid state.

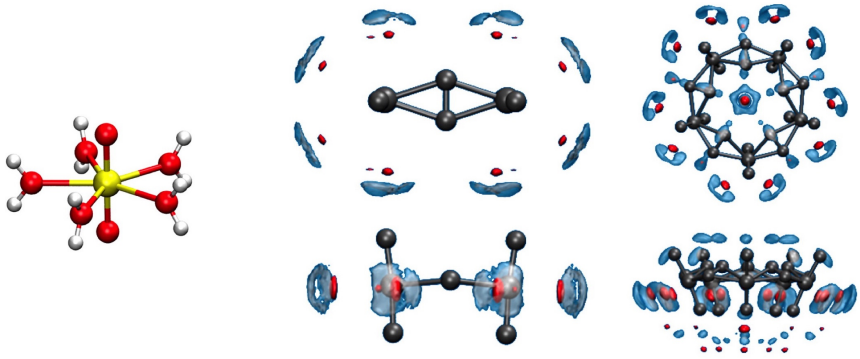

Figure 2.22: Ball and stick representation of the rigid $\mathbf{U_1}$ (left) and equatorial water molecules. Top and side view of the spatial distribution function (SDF) of the rigid $\mathbf{U_2}$ (center) and $\mathbf{U_5}$ (right) at 0.4 and 0.1 isosurfaces, respectively. The water oxygen and hydrogen probabilities are shown red and semitransparent white. The uranyl and uranyl-peroxide structures are presented in gray. Movies showing $\mathbf{U_1}$, $\mathbf{U_2}$ and $\mathbf{U_5}$ dynamics are in the Supporting Information. The $\mathbf{U_1}$ SDF is not presented as rotations around the uranyl unit lead to smearing effects. See the Supporting Information for details.

Uranyl in water has been studied in detail both experimentally and theoretically. The current consensus is that water molecules do not strongly interact (hydrogen bond) with the uranyl oxygen atoms.[202,204] Within classical simulations, the description of this interaction is highly dependent on the force field and previously reported non-polarizable force fields overestimate this interaction.[190,191] Polarizable potentials and first-principles dynamics are in agreement with experimental results.[202,203] The O_{uranyl}–O_{water} and O_{uranyl}–H_{water} $g(r)$ indicate the absence of strong apical hydrogen bonds in our simulations (see Figures S2-S5 in the Supporting Information). The observed peak at approximately 3 Åin the O_{uranyl}–O_{water} $g(r)$ corresponds to the five water molecules

in the first coordination sphere. Likewise, the first two peaks in the O_{uranyl}–H_{water} plot are assigned to the H atoms of these same waters. Our results are consistent with those of Hagberg *et al.*[189] who reported that the equatorial waters were the nearest neighbors of the uranyl oxygen atoms. Additionally, the velocity autocorrelation function (VACF) was computed as a means to generate the power spectrum. The symmetric and asymmetric bending modes of the uranyl moiety in $\mathbf{U_1}$ and $\mathbf{U_2}$ were identified at approximately 1240 and 1320 cm^{-1}, respectively. Likewise, the stretching mode of the peroxide group in $\mathbf{U_2}$ is located at 800 cm^{-1}. Experimentally peroxide and uranyl stretch modes are approximately 500-600 and 850-950 cm^{-1}. The large discrepancies between the calculated and experimental modes can be corrected through a direct scaling factor applied to the power spectra (0.70) a posteriori or scaling both bond and angle force constants presented in Table 2.7 during the simulation (see Supporting Information for details).

Salvation of the Uranyl–Peroxide Pentamer

The $\mathbf{U_5}$ cluster (Figure **??**c) has been proposed as a building block of larger uranyl peroxide nanoclusters.[139,141,149,150,151] As in the larger clusters, little is known regarding its hydration at a molecular level; however, our simulations allow us to address this question. While direct comparisons with experiment cannot be made for $\mathbf{U_5}$ in solution, the complex $K_{10}[(U^{VI}O_2)(\mu^2\text{-}O_2)(C_2O_4)]_5(H_2O)_{13}$ has been characterized in the solid state.[139] This structure contains a $\mathbf{U_5}$ cluster where the nonperoxide and nonbridging coordination sites on each uranium center are occupied by an oxalate ligand. Although qualitative, a comparison of the relevant geometric parameters within the $\mathbf{U_5}$ group can be made (Table 2.8) for the solid state and the average values from our flexible simulation. First, the uranium CN in our simulation and for the compound in the solid state is the same. In the simulation, the average U–O_{uranyl} bond distance and O_{uranyl}–U–O_{uranyl} angle are in good agreement with solid state experiments, 1.77 Åand 173.5°, respectively.[139] Furthermore, the U–(μ^2–$O_{peroxide}$)$_2$–U dihedral angle fluctuates during the simulation, ranging from 128.9° to 200.5° (i.e. inverted through planarity) with an average value of 165.6°. Again, these values are in a reasonable range when compared with the solid state.

Moreover, our simulations suggest that water around the isolated pentagonal unit

is even more ordered than in the dimer, $\mathbf{U_2}$. Each of the uranium centers is hexa-coordinated (two sites by water molecules and four by the peroxide bridges) for both rigid and flexible simulations, which is in agreement with our conclusions from the $\mathbf{U_1}$ and $\mathbf{U_2}$ simulations. However, in $\mathbf{U_5}$ each uranium center is coordinated by two μ^2–O_2^{2-} ligands and has a water CN of 2.0 as shown in the U–O_{water} $g(r)$ (Figure 2.23 for flexible simulation. See Figure S6 in the Supporting Information for the rigid one). The first peak is centered at 2.42 Åfor the rigid and flexible simulations, similar to that obtained for $\mathbf{U_2}$. The remaining peaks at longer distances correspond to water ligands located on neighboring uranium centers. Additionally, the SDF was plotted to show water coordination in three-dimensions (Figure 2.22).

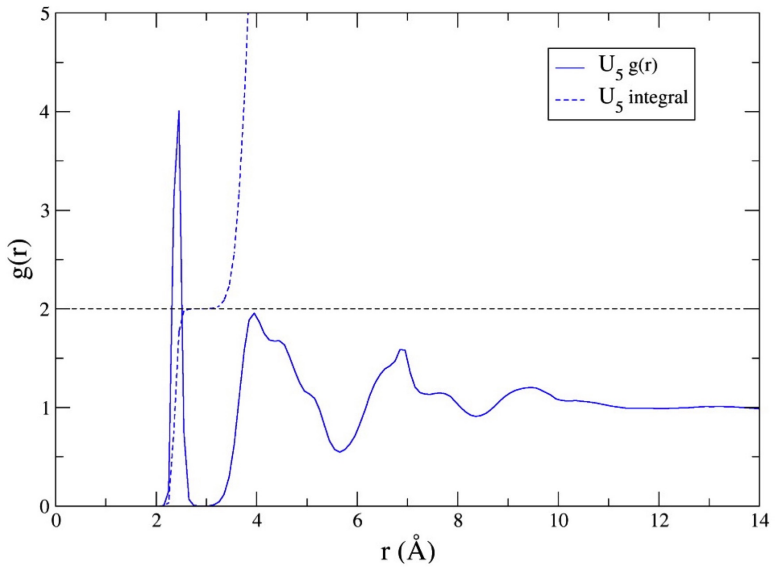

Figure 2.23: Radial distribution function, $g(r)$, between U–O_{water} of the flexible $\mathbf{U_5}$ (blue line) with the integration as a dashed line. Water coordination number (CN) of each uranium center (dashed black lines).

For $\mathbf{U_5}$, as for $\mathbf{U_2}$, the equatorial water molecules are represented by probability basins, two for each uranium center. The most interesting feature appears in the center of the pentagonal unit where a single water molecule is positioned underneath five uranyl oxygen atoms. Previous X-ray diffraction studies have consistently shown water or counterions occupying this position not only in the pentagonal unit but also in topologies

with square or hexagonal windows.[137,138,139,140,141,142,143,144,145]

Finally, the entire $\mathbf{U_5}$ unit is able to invert, from concave to convex, during the course of our simulations making use of our flexible potential (see the Supporting Information for details). Recently, inversion of uranyl peroxide squares has been shown by means of ^{31}P NMR in the $\mathbf{U_{24}}$–P cluster.[209] Although the $\mathbf{U_{24}}$–P capsule does not contain any pentagonal units, this experimental observation suggests that the inversion of $\mathbf{U_5}$ observed in our simulations is entirely plausible.

Salvation of a Uranyl–Peroxide Nanocapsule

Sigmon *et al.* synthesized the smallest known uranyl-peroxide nanocapsule containing only uranyl polyhedra, $[(U^{VI}O_{20}(\mu^2\text{-}O_2)_{30}]^{20-}$ ($\mathbf{U_{20}}$).[139] This nanocapsule consists of 12 $\mathbf{U_5}$ groups arranged in a fullerene topology, such that there are 12 pentagonal rings in the cluster. We have studied $\mathbf{U_{20}}$ to evaluate how our force field can be used to study the interactions of solvent and counterions with large uranyl-peroxide nanocapsules by means of molecular dynamics simulations. Since breathing in the $\mathbf{U_{20}}$ nanocapsule is fundamental to determination of the volume of the inner cavity and consequently the number of encapsulated solvent/ion molecules, we only performed simulations using the flexible force field.

The initial configuration of water molecules for species with solvent accessible cavities requires special attention since the number of waters inside the $\mathbf{U_{20}}$ cavity must be chosen carefully. We noted that in our $\mathbf{U_5}$ simulations a water molecule occupied the site centered under the pentagonal unit; therefore, we placed a water molecule in each of the 12 interior faces of $\mathbf{U_{20}}$ in the starting configuration. To determine an appropriate loading of water in the remaining space inside $\mathbf{U_{20}}$, we followed the example of the protein simulation community and chose an initial number of water molecules that gave the correct density of liquid water in the pore volume. We have taken the volume of the $\mathbf{U_{20}}$ cavity to be 200 Å^3 (a radius of 6 Å) and filled it with 13 water molecules in addition to the 12 under the pentagonal faces. Three different initial conditions were studied in the $\mathbf{U_{20}}$ simulations: (i) 12 encapsulated counterions and eight randomly distributed in the solvent (inspired by the experimentally determined counterion positions in the solid state), (ii) 25 water molecules placed in 3 concentric shells of 1, 12, and 12 water

molecules, respectively, with counterions randomly placed outside the capsule, and finally (iii) with a single counterion placed inside the internal cavity of the nanocapsule, replacing one water, and all other counterions external. The results of these simulations were the following:

(i) In the simulations starting with 12 counterions inside the capsule as in the experimental X-ray structure, the counterions exited the capsule rapidly, leaving just a few (less than three) ions in the cavity. Additionally, very few water molecules entered the capsule on the time scale of our simulations. As such behavior suggests that the other starting conditions may be more representative of equilibrium conditions, we will now consider results from the later set of simulations.

(ii) In the simulations with three concentric shells of 1, 12, and 12 water molecules in a $\mathbf{U_{20}}$ capsule with no sodium ions inside the nanocapsule, we studied the water distribution by defining a point X at the center of mass of the capsule and the RDF of water oxygen atoms from this point is given in Figure 2.24. From the X_{center}–O_{water} RDF alone, it is clear that the water inside the capsule forms a highly ordered, ice-like structure (Figure 2.24). The RDF displays two distinct peaks at 1.75 Åand 4.25-4.50 Åfrom the center of the nanocapsule that correspond to 6 and 12 water molecules, respectively. The first set forms a cluster with the same symmetry as the $\mathbf{U_{20}}$ cage, while the remaining 12 are directly underneath each pentagonal face. Additionally, a water molecule is present at the center of the capsule (at position X_{center} in the RDF). Therefore, in the absence of counterions inside the $\mathbf{U_{20}}$ cavity, we predict that a 6-water cluster may surround a single central water inside $\mathbf{U_{20}}$. This water cluster is templated by the symmetry of the capsule, the 12 waters in the pentagonal pores, and the available space in the cavity. Note that the generation of this structure requires 6 water molecules originally placed inside $\mathbf{U_{20}}$ to depart during the course of the simulation.

The innermost waters are localized in an octahedral shaped water cluster consisting of a four-member ring sandwiched by two water molecules above and below (Figure 2.25, left). The spatial distribution function of the encapsulated water molecules corroborates the formation of an octahedral innermost water cluster and confirms that the 12 water molecules under the pentagonal faces in U20 are analogous to those observed in $\mathbf{U_5}$.

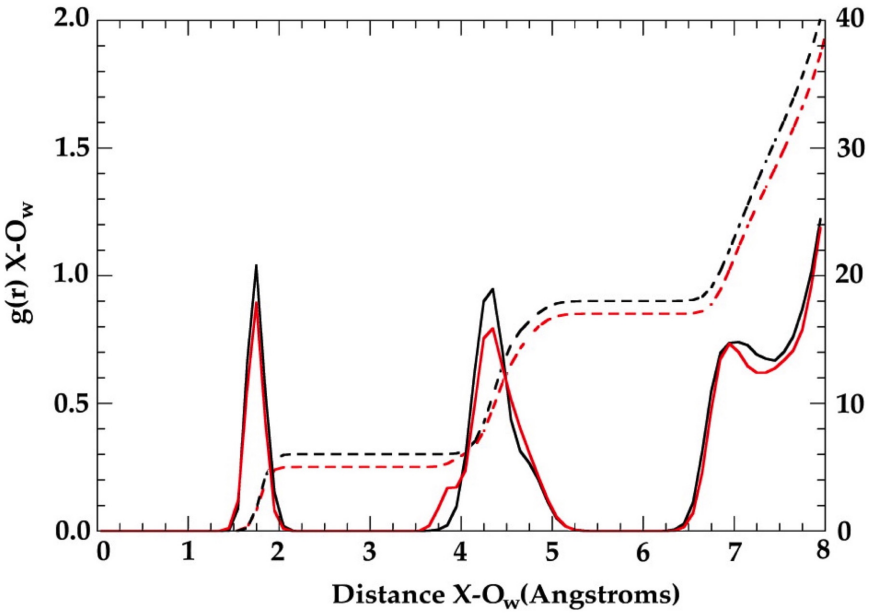

Figure 2.24: Radial distribution function, $g(r)$, between X–O_w of the flexible $\mathbf{U_{20}}$ with no cations (black line) and with one Na inside the capsule cavity (red line). Integration shown as a dashed line.

(iii) While the results for 19 interior waters are provocative, the interior water cluster could easily be disrupted if alkali counterions are at lower chemical potential inside the cavity (and can enter and exit freely). The disruption of an ice-like water structure by alkali ions has been observed in molybdenum-based polyoxometalates (e.g. Mo_{132}).[210,211] Furthermore, this is in agreement with reported ion exchanges between encapsulated and free counterions in other uranyl peroxide nanocapsules.[212] In our $\mathbf{U_{20}}$ simulations where counterions were randomly distributed and none or one was placed inside, we were able to identify three different binding sites for the counterions by visually inspecting snapshots from the simulations (Figure 2.26). Sodium ions were found located above the pentagonal face interacting with the water molecule in the face, below the pentagonal face interacting with a water molecule located just outside the face, or completely inside the capsule. In the simulations with one sodium counterion placed inside the nanocapsule, the orientation of the hydrogen of the water molecules is affected since the sodium cation occupies a water oxygen site in the encapsulated inner water cluster (Figure 2.26,

right); however, no major changes are observed in the water oxygen positions.

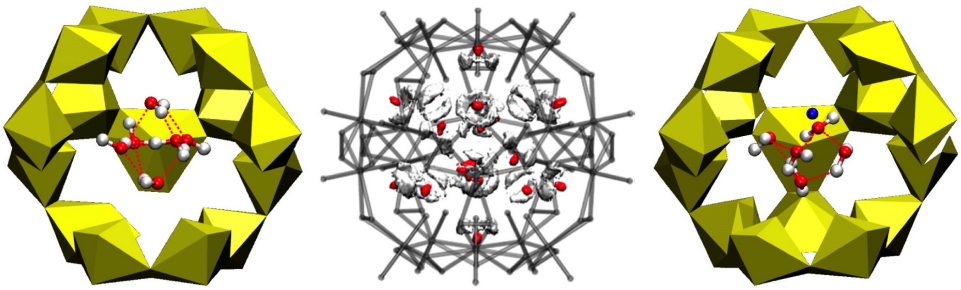

Figure 2.25: Left: Selected snapshot of the encapsulated $(H_2O)_6$ water cluster inside a $\mathbf{U_{20}}$ (polyhedral representation with some uranium polyhedra removed for clarity). Hydrogen bonds in dashed red lines. Center: The spatial distribution function (SDF) at a 0.05 isosurface. The water oxygen and hydrogen probabilities are shown red and white and the $\mathbf{U_{20}}$ nanocapsule in semitransparent gray. Right: Selected snapshot of the encapsulated $Na(H_2O)_5$ water cluster inside a $\mathbf{U_{20}}$ (polyhedral representation with a some uranium polyhedra removed for clarity). Hydrogen bonds in dashed red lines. Color code: Oxygen in red, hydrogen in white, and sodium in blue.

This result is shown quantitatively by comparing the RDFs for the simulations from scenarios (ii) and (iii) (Figure 2.24). A single sodium counterion is shown to disrupt the inner ice-like water structure only slightly. Furthermore, given that the capsule holds a large negative charge and is polyoxometalate-like in nature, we anticipate a variable distribution of counterions inside the nanocapsules surface, but the actual determination of an equilibrium distribution would require much longer trajectories than are currently practical. The presence of counterions in the $\mathbf{U_{20}}$ nanocapsule would introduce a large amount of crystallographic noise if it were to be isolated. Thus, it would be unlikely to observe ice-like water clusters in the presence of small counterions like alkali metals. It might be possible, however, to observe this ice-like water inside the cluster if large counterions, unable to enter the nanocapsule, are used instead. Such behavior would be similar to what has been observed in molybdenum polyoxometalate nanocapsules when guanidinium or NH_4^+ were introduced through the use of ion exchange membranes.[211] Furthermore, the importance of the polarization of solvent molecules is well-known when

treating confined cavities as in proteins so its importance in uranyl-peroxide nanocapsules and other polyoxometalate-based nanocapsules is of fundamental interest and will be pursued in future studies.[213]

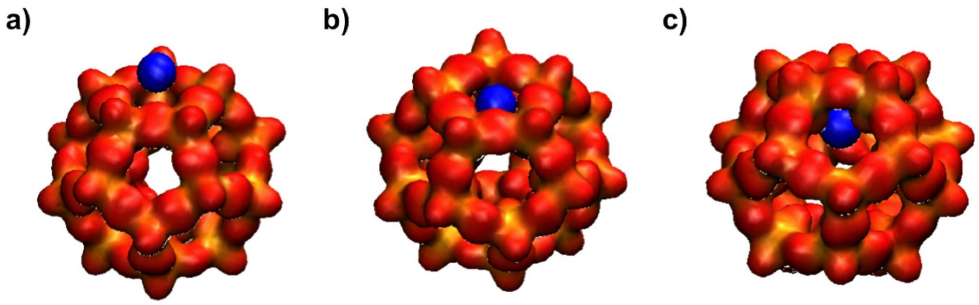

Figure 2.26: Selected snapshots from the flexible $\mathbf{U_{20}}$ simulation: Sodium counterion above the pentagonal face (Na^+–H_2O) (a), below the pentagonal face (H_2O–Na^+) (b), and inside of the $\mathbf{U_{20}}$ nanocapsule (c).

2.3.5 Conclusions

We have developed a force field from first-principles calculations on $\mathbf{U_1}$ and $\mathbf{U_2}$ that has been employed to study uranyl-peroxide nanocapsules in aqueous solution. Currently, our force field can be applied to all uranyl-peroxide nanocapsules fully bridged by peroxide units. We have made use of it to study solvent and ion-pairing for two highly relevant structures (the pentamer, $\mathbf{U_5}$, and the smallest nanocapsule formed by assembling 20 uranyl bipyramids, $\mathbf{U_{20}}$) in the presence of sodium ions in aqueous solution. Our force field retains the ability to correctly describe the behavior of uranyl, $\mathbf{U_1}$, in water while using an accurate but computationally inexpensive Born-Huggins-Mayer (BHM) two-body potential. Moreover, simulations of the small uranyl peroxide units $\mathbf{U_2}$ and $\mathbf{U_5}$ result in uranium–water distances consistent with a hexa-coordinate environment. Additionally, we show how the flexibility of the system affects the interaction with solvent molecules. Finally, we have studied the $\mathbf{U_{20}}$ nanocapsule with both rigid and flexible models. The force field has been designed using a building block approach. Additional bridging groups can be parametrized in an analogous manner without requiring reparameterization of the entire force field. Furthermore, other experimentally

relevant counterions can be used in our force field without requiring parametrization. Last but not least, the use of our force field does not require initial DFT calculations to be performed on the uranyl peroxide capsule in order to determine any capsule-specific parameters.

Our simulations of $\mathbf{U_{20}}$ in water suggest that, when interior water molecules are not perturbed by interior or immediately exterior monatomic counterions, they form an ice-like structure inside the capsule. Although this water structure has been observed in our simulations, it is expected that if sodium counterions enter the capsule, it will be disrupted. Indeed, on the time scale of our simulations we observed Na^+ ions displacing water molecules to interact with the capsule, although our trajectories would need to be extended far longer to demonstrate equilibrium. Three Na^+ interaction sites have been identified: above the pentagonal face, below the pentagonal face, or more toward the interior of the capsule.

Future work will focus on properly determining the number of encapsulated species at equilibrium. In classical molecular dynamics, events occurring relatively infrequently with respect to the total simulated time are poorly sampled. In the $\mathbf{U_{20}}$ simulations, water and counterion exchanges rarely occur. As a consequence, our group plans future studies using grand canonical Monte Carlo simulations to ascertain the number of water and counterions present inside of uranyl-peroxide nanocapsules at equilibrium as well as using umbrella sampling techniques to address transport across the pores.

This is of particular interest in the larger uranium peroxide capsules where encapsulated species cannot be resolved with X-ray diffraction. Moreover, the degree to which polyoxometalates are flexible is a topic of ongoing debate in the community. For uranyl peroxides in particular, little is known regarding how flexible these cages may be, and therefore additional research, both experimental and theoretical, is required in order to assess whether our flexible model offers clear advantages over the rigid model.

2.3.6 Additional Information

Supplementary information is available in the online version of the paper. The Supporting Information includes: $\mathbf{U}_1$, $\mathbf{U}_2$, $\mathbf{U}_5$, and $\mathbf{U}_{20}$ structures, force field parameterization data, additional radial and spatial distribution functions, selected MD snapshots, and

movies. This material is available free of charge at `http://pubs.acs.org`. Correspondence and requests for material should be addressed to R. S. and L. G. The authors declare no competing financial interests.

Acknowledgements

L.G., B.V., and P.C.B. were supported by the Materials Science of Actinides, an Energy Frontier Research Center funded by the U.S. Department of Energy, Office of Science, and Office of Basic Energy Sciences under Award Number DE-SC0001089. B.V. also thanks the University of Minnesota for a Doctoral Dissertation Fellowship. P.M. and C.J.C. were supported by the U.S. National Science Foundation (CHE-0952054). R.S. thanks ANR 2010 JCJC 080701 ACLASOLV (Actinoids and Lanthanoids Solvation) for support. A.L.D. was supported by the US Department of Energy under contract DE-SC0001015.

Author Contributions

The manuscript was written through contributions of all authors. All authors have given approval to the final version of the manuscript.

Chapter 3

Gas Reactivity within MOFs

3.1 The Mechanism of Carbon Dioxide Adsorption in an Alkylamine-Functionalized Metal-Organic Framework

The mechanism of CO_2 adsorption in the amine-functionalized metal-organic framework mmen-Mg_2(dobpdc) (dobpdc^{4-} = 4,4'-dioxidobiphenyl-3,3'-dicarboxylate; mmen = N,N'-dimethylethylenediamine) was characterized by quantum-chemical calculations. The material was calculated to demonstrate 2:2 amine:CO_2 stoichiometry with a higher capacity and weaker CO_2 binding energy than for the 2:1 stoichiometry observed in most amine-functionalized adsorbents. We explain this behavior in the form of a hydrogen-bonded complex involving two carbamic acid moieties resulting from the adsorption of CO_2 onto the secondary amines.

3.1.1 Introduction

The predicted growth of the global economy and world population in the near future will lead to an increased demand for energy,[215] resulting in even further increases in

Adapted with permission from N. Planas, A. L. Dzubak, R. Poloni, L. -C. Lin, A. McManus, T. M. McDonald, J. B. Neaton, J. R. Long, B. Smit, L. Gagliardi. *J. Am. Chem. Soc.* 2013, *135*, 7402.[214] **N.P. and A.L.D. contributed equally to this work. Additional information may be found in section ??.**

the concentration of CO_2 in the atmosphere. The development and worldwide utilization of efficient carbon capture and sequestration (CCS) technologies could reduce the CO_2 emissions associated with the use of fossil fuels.[216] Current carbon capture technologies generally use aqueous solutions of alkanolamines to scrub the flue gases.[217] Amines are known to be very selective toward CO_2 capture from flue gases because of the strong chemical bonds formed in the chemisorption process. To overcome the energy penalty associated with the process, an important new development based on solid materials functionalized with amines has been proposed.[218,219,220,221,222,223,224] These materials have much lower heat capacities than aqueous amine solutions.[225] Of particular interest are amines grafted onto the open metal sites of metal-organic frameworks (MOFs). Indeed, recent experiments have shown that in the case of one particular MOF, Mg_2(dobpdc) (dobpdc^{4-} = 4,4'-dioxidobiphenyl-3,3'-dicarboxylate), N,N'-dimethylethylenediamine (mmen) can be bound to almost every open metal site lining the one-dimensional channels of the structure (Figure 3.1.[218] The high adsorption enthalpy of mmen-Mg_2(dobpdc) for CO_2 endows the adsorbent with a significant capacity for CO_2 down to very low pressures.

The regeneration energy of the solid adsorbent is lower than that of aqueous amine solutions because of its large working capacity and low heat capacity. Understanding reactivity differences between solid and liquid adsorbents is essential for understanding the optimum reaction enthalpy for CO_2, thus informing the design of next-generation adsorbents with further reduced regeneration energies.

One would expect this material to capture CO_2 following conventional ammonium carbamate chemistry, in which the adsorption of each CO_2 requires two amines, one to participate in a nucleophilic attack on the carbon atom of CO_2 to form a C–N bond and the other to act as a base to abstract the proton. Interestingly, the isosteric heat of adsorption (Q_{st}) as a function of fractional coverage for mmen-Mg_2(dobpdc) shows that 0.8 mol of CO_2/mol of amine is strongly adsorbed [Figure S2 in the Supporting Information (SI) adapted from the experimental adsorption data of McDonald *et al.*[218]]. As it is unlikely that all of the amines are accessible to CO_2, these adsorption experiments suggest a 1:1 amine:CO_2 stoichiometry, indicating that only one amine is needed for every CO_2 molecule. This suggests that a different type of chemistry takes place in the material. Here we present the results of a quantum-chemical study that elucidates

the reaction mechanism and explains the experimentally observed 1:1 stoichiometry for the CO_2 adsorption by amine molecules inside mmen-Mg_2(dobpdc). Our mechanism predicts the formation of a bis(carbamic acid) complex.

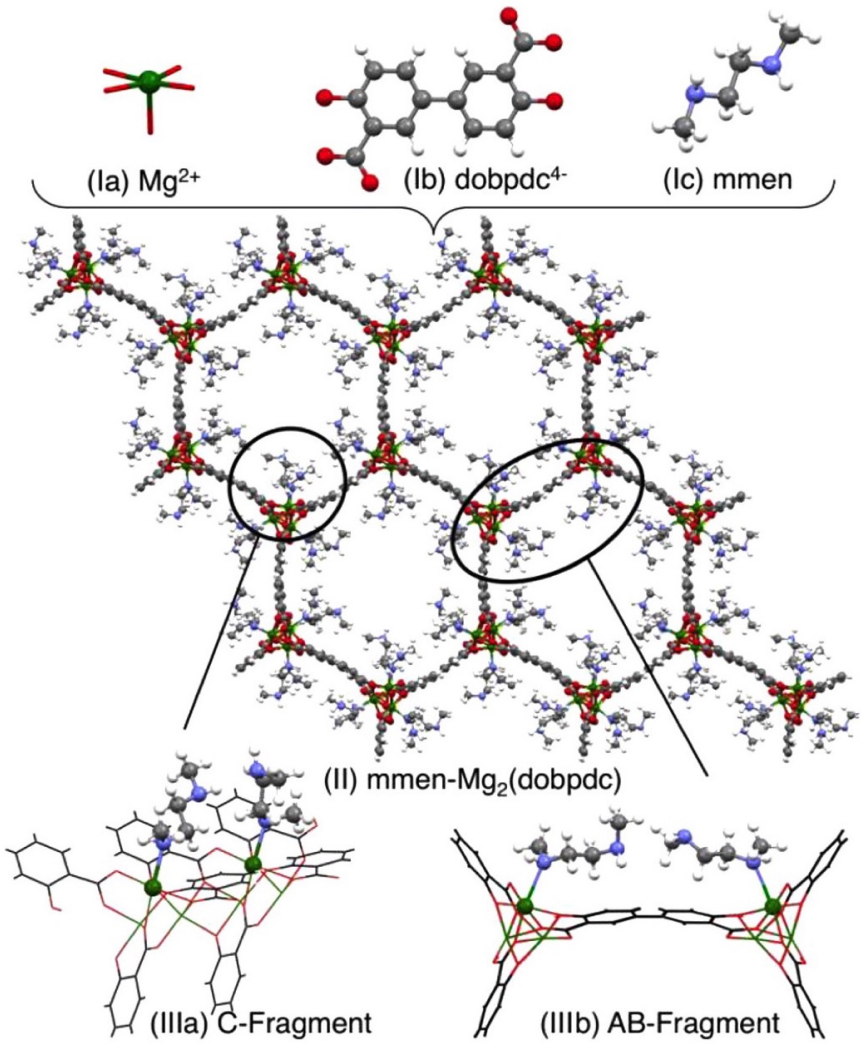

Figure 3.1: The mmen-Mg_2(dobpdc) structure used in this work. Color code: green, Mg; gray, C; blue, N; red, O; white, H. (Iac) Basic building blocks of mmen-Mg_2(dobpdc). (II) Minimum-energy configuration obtained from periodic density functional theory calculations, as shown from a view of the ab-plane cross section. (IIIa,b) The two fragments used as models in the calculations.

To date, aqueous alkanolamine solutions have been extensively studied and are still regarded as the state-of-the-art technology for CO_2 capture.[217] Different mechanisms have been proposed for the reaction between CO_2 and amines, depending on the nature of the amine and the reaction conditions.[226,227,228,229,230,231,232,233,234,235,236] These are summarized in section 3 in the SI. In this work, we investigated the CO_2–amine reaction mechanism in mmen-Mg_2(dobpdc), for which the reaction medium is quite different compared with an aqueous environment. First, the experiments were carried out with pure CO_2 gas in the absence of water or any polar solvent. Second, the amine groups are fixed by the position of the metal centers within the structure, which is in turn imposed by the coordination of the linker to the metal centers. Finally, as mentioned previously, the experimental adsorption data of McDonald *et al.*[218] indicate a 1:1 reaction stoichiometry instead of the conventional 2:1 stoichiometry (see section 2 of the SI for more detailed information).

3.1.2 Proposed Mechanism

To explore the reaction mechanisms, we identified two representative fragments to be used in this study. The C fragment allows for the consideration of interactions between nearest-neighbor amines along the crystallographic c axis (IIIa in Figure 3.1), and the AB fragment was considered in order to address the interactions between nearest neighbors across the organic linker (the ab plane) (IIIb in Figure 3.1). All of the computational details are reported in section 4 in the SI.

The starting point of our study is the minimum-energy configuration of the amines in the unreacted alkylamine-appended MOF mmen-Mg_2(dobpdc) (II in Figure 3.1). Our energy calculations show that the amines prefer to form hydrogen bonds along the c axis because the distance between the amines is sufficiently short (7.02 Å between the corresponding metal centers) for this interaction to be energetically favorable. Interestingly, the structure resulting from hydrogen bonding of two amines across the linker in the AB fragment–where there is a distance of 12.96 Å between the corresponding metal centers–is higher in energy than the structure corresponding to the noninteracting amines. This is due to the fact that the hydrogen bond between amine groups only forms at the expense of lengthening the Mg–N distance, which imposes an energetically unfavorable penalty. The Mg–amine binding energy was found to be -135.6 kJ/mol;

this is significantly greater than the Mg–CO_2 binding energy of -43.9 kJ/mol, which is consistent with the experimental heat of adsorption of CO_2 in Mg_2(dobpdc) in the absence of amines.[218] Thus, the possibility of amine substitution by CO_2 coordination to the metal center can be discarded. Importantly, the Mg–OH_2 binding energy was found to be -82.66 kJ/mol, which indicates that the water molecules bound to 20% of the metal sites will not be displaced by CO_2 either. Hence, we did not account for their presence in the mechanism reported herein.

We propose the mechanism shown in Figure 3.2. Inspired by the termolecular mechanism,[231] we propose a pathway in which all of the N–C bond formation steps are stabilized by the concerted breaking and forming of hydrogen-bonded adducts. These hydrogen bonds seem to play a critical role in avoiding the formation of formally charged reaction intermediates and products. As illustrated in Figure 3.2, the hydrogen-bonded lowest-energy diamine complex (A_I), which involves two nearest-neighbor amines along the c axis, initially forms a hydrogen bond between the noninteracting NH group (red H in A_I) and a CO_2 molecule, affording A_{II}. This interaction is required for the subsequent step, which yields a zwitterionic species stabilized by a hydrogen bond with a neighboring amine along the c axis (ZW_1). Subsequent proton exchange yields the carbamic acid represented in B_I. The B_I species, which is stabilized by two hydrogen bonds with the neighboring amine, then undergoes a reorganization that results in the more energetically favorable double hydrogen-bonding interaction shown in B_{II}.

Interestingly, in these systems we found that the conventional 2:1 chemistry does not lead to the most stable configuration. The addition of a second CO_2 molecule that forms a hydrogen bond with the carbamic acid–amine adduct (B_{II} to B_{III} in Figure 3.2) readily yields a second zwitterionic species, again stabilized by dual hydrogen bonds (ZW_2 in Figure 3.2). Subsequent proton exchange (to give C_I) followed by product reorganization yields a bis(carbamic acid) stabilized by double hydrogen bonding in a "head-to-tail" fashion in the final complex (C_{II}).

All of our attempts to compute the corresponding isolated (non-hydrogen-bonded) zwitterionic species or the more conventional ammonium carbamate complex converged to neutral products. Nonreacted amine and free CO_2 were obtained in the first case, and a carbamic acid hydrogen-bonded to the neighboring amine was computed in the second case.

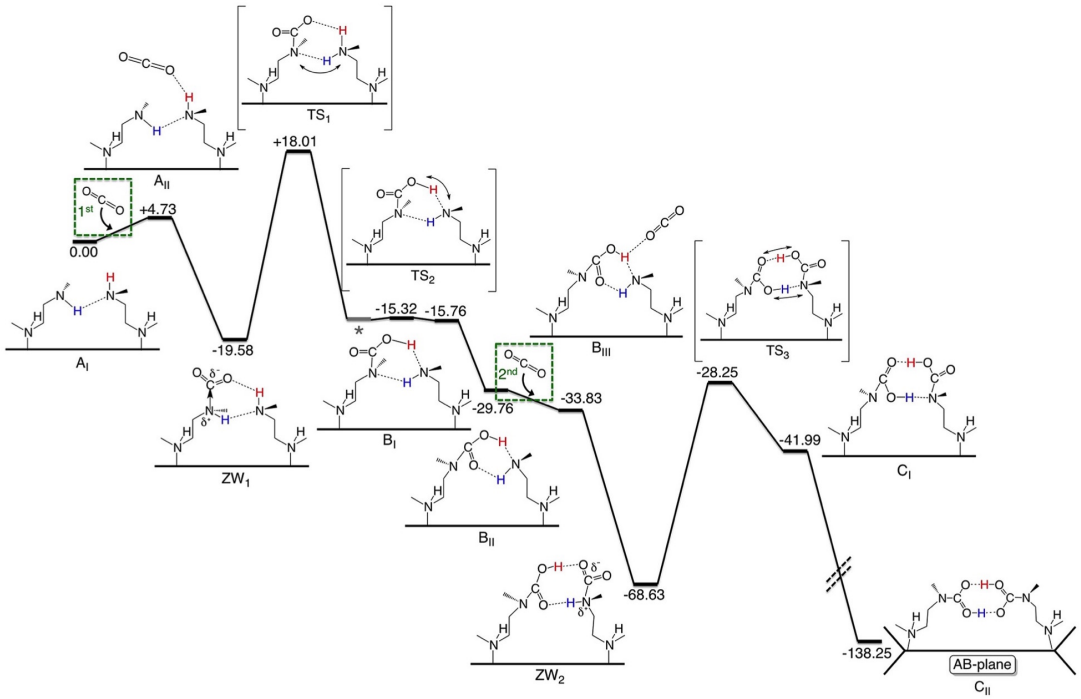

Figure 3.2: The proposed mechanism: (left) first CO_2 uptake (CO_2:amine = 1:2); (right) second CO_2 uptake (CO_2:amine = 2:2). The energy profile, ΔE, reported in kJ/(mol of model fragment), was calculated as $\Delta E = E_{\text{species}} - E_{\text{A}_\text{I}} - nE_{\text{CO}_2}$, where $n = 1$ (first uptake) or 2 (second uptake). The dashed diagonal lines indicate that the ΔE of species C_II is not drawn to scale. Coordinates and energies of all optimized species are given in sections 8-9 in the SI.

In addition, we explored the possible role of the MOF linker as a base. The three different types of O atoms of the dobpdc^{4-} linker (Ib in Figure 3.1) were considered. In all cases, the proton initially bound to the O atom of the framework went back to the amine N atom during the optimization process, again yielding final species with no formal charge. Attempts to obtain analogous species with the AB fragment cluster calculation failed. In this configuration, the distance between the amines in the ab direction imposed by the framework (12.96 Å across the ligand in the ab plane vs 7.02 Å along the c axis) is too long. This long distance frustrates the required hydrogen-bond formations for the different steps. However, the final bisacid head-to-tail conformation through the ab plane in C_II gives a more stable final product, since the CO_2 uptake

results in lengthening of the chain of the appended amine-derived species.

The two consecutive CO_2 uptake processes start with the formation of a hydrogen bond between the CO_2 an an amine (A_I) or an amine-derived species (B_{II}). In each case, the optimization of the newly formed species (A_{II} or B_{III}, respectively), in which the hydrogen-bonded CO_2 molecule has been rotated to obtain a spatial arrangement in which its carbon atom is facing toward the nitrogen atom of the neighboring amine, smoothly converges into the corresponding zwitterionic species (ZW_1 or ZW_2). Thus, the formation of the zwitterions is highly exothermic (releasing ca. 25 kJ/mol for ZW_1 and ca. 35 kJ/mol for ZW_2), and barrierless transformations occur. The primary difference between the two consecutive paths for CO_2 uptake lies in the transition states from the corresponding zwitterions to the carbamic acid species. In the first case, the formation of B_I requires two consecutive transitions, the first (TS_1) involving proton transfer from the zwitterion nitrogen (blue H in Figure 3.2) to the amine and the second (TS_2) involving proton exchange from the protonated amine (red H in Figure 3.2) to the newly formed carbamate. In the second case, the two protons are exchanged in a concerted transition (TS_3). This transition is enabled by the quasi-planar spatial disposition of the carboxylic moieties involved. The energy barriers for these two transformations are 40 kJ/mol, respectively. These barriers are of similar magnitude to those computed for alkanolamine reactions in solution as reported in the literature.[229] The origin of the mechanistic differences between the two transitions results from the structural differences between the corresponding zwitterionic species (see Figure S6A,B).

Amine–CO_2 reactions in aqueous solution, where zwitterionic and charged species are stabilized by the polar medium, usually occur with a CO_2:amine stoichiometry of 1:2. Our calculations have revealed that in the absence of solvent, reactions that result in the formation of charged species are no longer possible because neither the neighboring amines nor the framework act as proton acceptors. This new reactivity does not stop at the 1:2 CO_2:amine stoichiometry but instead recruits an additional CO_2 molecule, resulting in 2:2 stoichiometry. For the proposed mechanism, we calculated an adsorption energy of -138.25 kJ per 2 moles of CO_2, which corresponds to an average adsorption energy of -69.13 kJ/mol. Our predicted adsorption energy is in good agreement with the experimental Q_{st} value of -71 kJ/mol.[218]

3.1.3 Conclusions

The mechanism revealed in this work shows that there is a requirement for some amine ordering preceding the CO_2 adsorption, which is consistent with the delay to reach the primary adsorption site (corresponding to C_{II}) observed in the adsorption isotherms. Since the adsorption of the first CO_2 molecule is exothermic and the energy barriers for the two CO_2 uptake events are of similar magnitude, once the first CO_2 molecule is adsorbed, the second CO_2 molecule adsorbs immediately to form ZW_2, which evolves to C_{II}. Hydrogen bonds formed along the c axis are crucial for the adsorption mechanism to proceed. In the last step, however, the mmen ligands, which are elongated by the adsorption of CO_2, participate in more favorable hydrogen-bonding interactions across the linker. This reveals how crucial the length of the amine is for systems of this type, in which the structural constraints of the adsorbent govern the amine–amine interactions. The adsorption mechanism elucidated in this study is a clear example of the high potential of MOFs to exhibit new types of reactivity.

3.1.4 Additional Information

Supplementary information is available in the online version of the paper. The Supporting Information includes: Computational details, computed structures and energies, discussions of experimental data, and a summary of previously reported mechanisms. This material is available free of charge at `http://pubs.acs.org`. Correspondence and requests for materials should be addressed to B. S. and L. G. The authors declare no competing financial interests.

Acknowledgements

This research was supported by the U.S. Department of Energy under Contracts DE-FG02-11ER16283 (#SC0006860), DE-SC0001015, DE-AC02-05CH11231, and DE-FG02-12ER16362 (#SC0008688). (A detailed acknowledgement can be found in the SI.) A.L.D. is grateful for support through the Louise T. Dosdall Fellowship. We thank Jeffrey Reimer, Xueqian Kong, and Christopher J. Cramer for useful discussions.

3.2 Oxidation of Ethane to Ethanol by N_2O in a Metal-Organic Framework with Coordinatively Unsaturated Iron(II) Sites

Enzymatic haem and non-haem high-valent iron-oxo species are known to activate strong C-H bonds, yet duplicating this reactivity in a synthetic system remains a formidable challenge. Although instability of the terminal iron-oxo moiety is perhaps the foremost obstacle, steric and electronic factors also limit the activity of previously reported mononuclear iron(IV)-oxo compounds. In particular, although nature's non-haem iron(IV)-oxo compounds possess high-spin $S = 2$ ground states, this electronic configuration has proved difficult to achieve in a molecular species. These challenges may be mitigated within metal-organic frameworks that feature site-isolated iron centres in a constrained, weak-field ligand environment. Here, we show that the metal-organic framework Fe_2(dobdc) (dobdc^{4-} = 2,5-dioxido-1,4-benzenedicarboxylate) and its magnesium-diluted analogue, $Fe_{0.1}Mg_{1.9}$(dobdc), are able to activate the C-H bonds of ethane and convert it into ethanol and acetaldehyde using nitrous oxide as the terminal oxidant. Electronic structure calculations indicate that the active oxidant is likely to be a high-spin $S = 2$ iron(IV)-oxo species.

3.2.1 Introduction

The selective and efficient conversion of light alkanes into value-added chemicals remains an outstanding challenge with tremendous economic and environmental impacts,[238,239] especially given the recent worldwide increase in natural gas reserves.[240] In nature, C-H functionalization is carried out by copper and iron metalloenzymes, which activate dioxygen and facilitate two- or four-electron oxidations of organic substrates[241,242,243,244] through metal-oxo intermediates. Duplicating this impressive reactivity in synthetic systems has been the focus of intense research. In particular, iron(IV)-oxo complexes have

Adapted with permission from D. J. Xiao, E. D. Bloch, J. A. Mason, W. L. Queen, M. R. Hudson, N. Planas, J. Borycz, A. L. Dzubak, P. Verma, K. Lee, F. Bonino, V. Crocella, J. Yano, S. Bordiga, D. G. Truhlar, L. Gagliardi, C. M. Brown, J. R. Long. ***Nature Chem.*** **2014,** ***6*****, 590.[237] Copyright 2014, Nature Publishing Group. Author contributions and additional information may be found in section ??.**

now been characterized structurally in various geometries (octahedral, trigonal bipyramidal) and spin states ($S = 1$, $S = 2$), and have proved to be competent catalysts for a variety of oxygenation reactions.[245,246]

However, in the absence of a protective protein superstructure, terminal iron-oxo species are highly susceptible to a variety of decomposition pathways, which include dimerization to form oxo-bridged diiron complexes, intramolecular ligand oxidation and solvent oxidation.[247] Tethering a molecular iron species to a porous solid support, such as silica or polystyrene, could potentially prevent many of these side-reactions. In practice, however, complexes heterogenized in this manner are difficult to characterize using available techniques, and additional problems associated with steric crowding, site inaccessibility and metal leaching inevitably arise.[248,249] Iron cations can also be incorporated into zeolites, either as part of the framework or at extraframework sites, to produce reactive iron centres that have no direct molecular analogue. Fe-ZSM-5 (ZSM = Zeolite Socony Mobil), for example, has been shown to oxidize methane to methanol stoichiometrically when pretreated with nitrous oxide.[250] However, characterization of these materials is nontrivial because of the presence of multiple iron species, and the nature of the active sites in Fe-ZSM-5 remains largely a matter of speculation.[251]

The use of a metal-organic framework (MOF) to support isolated terminal iron-oxo moieties is a currently unexplored yet highly promising area of research. The high surface area, permanent porosity, chemical and thermal stability, and synthetic tunability displayed by many of these materials makes them appealing in this regard. Additionally, MOFs are typically highly crystalline with well-defined metal centres suited for characterization by single-crystal and/or powder-diffraction techniques. Furthermore, although molecular iron(IV)-oxo complexes generally utilize nitrogen-based chelating ligands, the metal cations in MOFs are often ligated by weaker-field ligands, such as carboxylates and aryl oxides, which are constrained in their coordination position by the extended framework structure. Thus, in addition to increased stability, terminal oxos in these materials might also have novel electronic properties and reactivity imparted by their unique coordination environment.

Herein we show that the high-spin iron(II) centres within Fe_2(dobdc) (dobdc^{4-} = 2,5-dioxido-1,4-benzenedicarboxylate) can activate N_2O, most likely forming a transient, high-spin iron(IV)-oxo intermediate, which rapidly reacts to afford $Fe_2(OH)_2$(dobdc).

Significantly, the magnesium-diluted analogue, $Fe_{0.1}Mg_{1.9}$(dobdc), is found to oxidize ethane into ethanol in the presence of N_2O under mild conditions.

3.2.2 Results and Discussion

Nitrous Oxide Coordination and Activation

Of the three-dimensional iron(II)-containing MOFs shown to be stable to desolvation,[252,253,254,255] few possess coordinatively unsaturated metal centres in a single, well-defined environment. The compound Fe_2(dobdc) (**1**), also known as Fe-MOF-74 or CPO-27-Fe, is rare in this regard, as the hexagonal channels of the framework are lined with a single type of square pyramidal iron(II) site (see Fig. 3.3a). The high density and redox-active nature of these open metal sites engender excellent O_2/N_2 and hydrocarbon separation properties.[255,256] However, with respect to the reactivity of the framework, only the hydroxylation of benzene into phenol and the oxidation of methanol into formaldehyde have been reported.[257,258] Thus, we embarked on a study of its reactivity towards nitrous oxide, a gaseous two-electron oxidant and O-atom transfer agent that is widely employed in industry, anticipating the generation of a highly reactive iron(IV)-oxo species capable of oxidizing strong C-H bonds.

We first investigated the binding of nitrous oxide to **1** under conditions in which the Fe–N_2O interaction is reversible. Experimental studies on the coordination chemistry of N_2O are scarce, as metal–N_2O adducts are challenging to synthesize because of the poor σ-donating and π-accepting properties of the molecule.[259] Indeed, of the several proposed binding modes, only one (end-on, η^1-N) has been structurally characterized in a molecular complex.[260] To establish the coordination mode of N_2O in **1**, powder neutron-diffraction data, which are very sensitive to the atomic assignment of O and N, were collected on a sample dosed with various loadings of N_2O. At low loadings, the best fit was an average of approximately 60% η^1-O and 40% η^1-N coordination, with Fe–N_2O distances of 2.42(3) and 2.39(3) Å, respectively. In both cases, a bent Fe–N_2O angle close to 120° was observed (see Fig. **??**b). Density functional theory (DFT) studies of N_2O-bound **1** using the M06 functional[261] show excellent agreement with experiment (see Supplementary Fig. 20). Furthermore, these calculations predict the η^1-O coordination mode to be favoured over the η^1-N mode by just 1.1 kJ mol^{-1} (see

Supplementary Tables 17 and 22). This is consistent with the nearly equal population split observed, although the magnitude of the difference in energy is smaller than the potential error associated with the calculations.

Although η^1-O coordination with a bent Fe–O–N angle has been proposed in a variety of systems ranging from isolated metal atoms to iron zeolites,[259,262,263] η^1-N coordination with a bent Fe–N–N angle is much more unusual. It suggests little π-back-bonding from the metal d orbitals into the π^* of N_2O. This is in contrast to previously reported vanadium- and ruthenium-N_2O adducts, which have linear metal–N–N–O geometries and for which π-interactions have been invoked as significant contributors to the stability of the complexes.[260,264,265,266] The bent geometry, long Fe–N_2O bond length and mixed N and O coordination indicate that N_2O is bound only weakly to the iron(II) centres in the framework, a hypothesis corroborated by in situ transmission-mode infrared spectroscopy. Spectra collected on a thin film of **1** dosed at room temperature with N_2O display a maximum at 2,226 cm^{-1}, which is very close to the fundamental ν(N–N) transition for unbound N_2O (2,224 cm^{-1}) and suggests a physically adsorbed phase with little to no perturbation of the N_2O molecule (see Supplementary Fig. 1). As expected, this interaction is fully reversible, and the band disappears completely under an applied vacuum. Consistent with these experimental results, DFT studies calculate binding energies of 45.6 and 44.5 kJ mol^{-1} for the η^1-O and η^1-N modes, respectively, with a natural bond order analysis[267] that shows weak back-bonding in both configurations (see Supplementary Table 23).

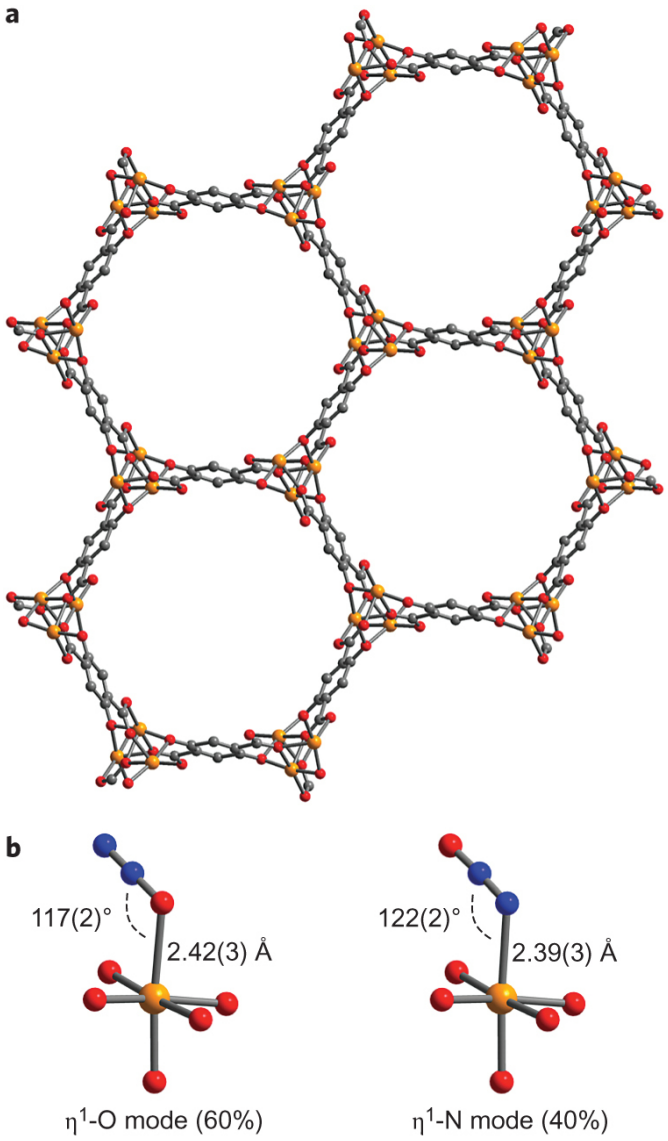

Figure 3.3: Structure of bare and N_2O-dosed Fe_2(dobdc) (**1**). (a) Structure of Fe_2(dobdc), showing hexagonal channels lined with five-coordinate iron(II) sites. The view is down the c axis, along the helical chains of iron(II) ions. (b) Experimental structures for N_2O binding in Fe_2(dobdc), solved from powder neutron diffraction data collected at 10 K. The molecule binds with a bent Fe–N_2O angle, with a mixture of 60% η^1-O coordination and 40% η^1-N coordination (for a comparison of calculated structures with experimental ones, see Supplementary Fig. 20). Orange, grey, dark blue and red spheres represent Fe, C, N and O, respectively; H atoms are omitted for clarity.

On heating the N_2O-dosed framework to 60 °C, the material undergoes a drastic colour change from bright green to dark red-brown, suggestive of oxidation. In addition, in situ infrared studies using CO as a probe molecule show that the open metal sites, which coordinate CO strongly, have been almost entirely consumed (see Supplementary Fig. 9). Characterization of the resulting product is consistent with the formulation $Fe_2(OH)_2$(dobdc) (**2**), in which each iron centre is in the +3 oxidation state and bound to a terminal hydroxide anion (see Fig. 3.4a). Compound **2** is likely to be formed via a fleeting iron-oxo intermediate, which rapidly undergoes hydrogen-atom abstraction, although the source of the hydrogen atom has not yet been determined. Mössbauer spectroscopy was used to probe the local environment of the iron centres in the oxidized material. The 57Fe Mössbauer spectrum of **2** consists of a doublet characterized by an isomer shift (δ) of 0.40(2) mm s^{-1} and a quadrupole splitting ($|\Delta E_Q|$) of 0.96(1) mm s^{-1} (see Fig. 3.4). The isomer shift for the iron centres in **2** is similar to the parameters obtained for the peroxide-coordinated iron(III) centres in $Fe_2(O_2)$(dobdc) from Bloch *et al.*,[255] and is consistent with other high-spin haem and non-haem iron(III) species.[268,269,270] In addition, the infrared spectrum of **2** shows the appearance of two new bands as compared to the unoxidized framework, which we assign as Fe–OH (667 cm^{-1}) and O–H (3,678 cm^{-1}) vibrations. These bands shift to 639 and 3,668 cm^{-1}, respectively, when $N_2^{18}O$ is employed for the oxidation; the observed differences of 28 and 10 cm^{-1} are very close to the theoretical isotopic shifts of 27 and 12 cm^{-1} predicted by a simple harmonic oscillator model (see Fig. 3.4b). Partial oxidation of the framework was achieved by heating at 35 °C for 12 hours, which led to the formation of $Fe_2(OH)_{0.6}$(dobdc) (**2'**), which has a similar infrared spectrum (although the bands associated with Fe–OH are less intense) and Mssbauer parameters (see Supplementary Table 9).

The framework maintains both crystallinity and porosity after oxidation, with a Brunauer-Emmett-Teller (BET) surface area of 1,013 m^2 g^{-1} and a Langmuir surface area of 1,171 m^2 g^{-1}. Rietveld analysis of powder X-ray diffraction data collected at 100 K on **2** firmly established the presence of a new Fe–O bond, but did not reveal whether a hydrogen atom was present. However, the Fe–OH bond distance of 1.92(1) Å is consistent with the bond lengths of previously reported octahedral iron(III)-hydroxide complexes (1.84-1.93 Å) (see Fig. 3.4d).[271] In addition, the trans Fe–O_{axial} bond is

slightly elongated (Fe–O_{axial} = 2.20(1) Å, average Fe–$O_{equatorial}$ = 2.04(1) Å), with the iron centre shifted slightly (by 0.23(1) Å) out of the plane of the four equatorial oxygen atoms. Extended X-ray absorption fine structure (EXAFS) analysis of the same sample, as well as periodic DFT calculations, provided bond lengths that are consistent with those obtained from the diffraction data (see Supplementary Table 8).

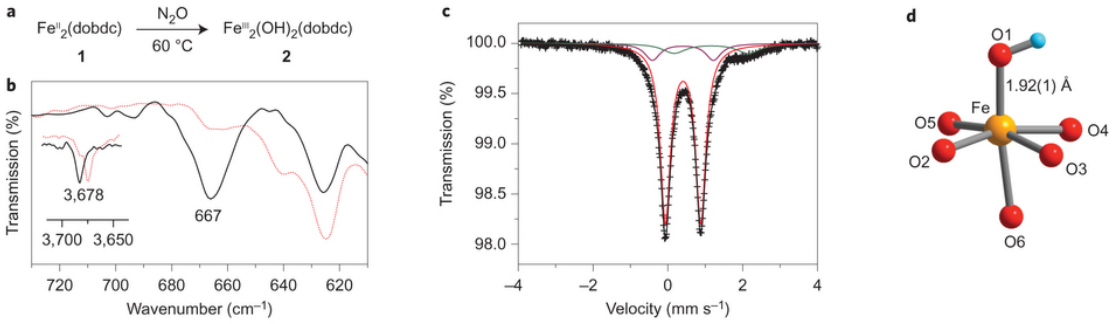

Figure 3.4: Preparation, spectroscopic characterization and structure of $Fe_2(OH)_2$(dobdc). (a) Reaction scheme for the preparation of $Fe_2(OH)_2$(dobdc) (**2**) from Fe_2(dobdc) (**1**). (b) Infrared spectrum of partially oxidized samples of $Fe_2(OH)_{0.6}$(dobdc) (**2'**) (black line) and Fe2(^{18}OH)$_{0.6}$(dobdc) (dotted red line). The peaks at 667 and 3,678 cm^{-1} shift to 639 and 3,668 cm^{-1}, respectively, when $N_2^{18}O$ is used, which confirms that these are, indeed, new bands derived from N_2O and not simply shifted framework bands. This also strongly supports the assignment of these peaks as Fe–OH and O–H vibrations. (c) Mössbauer spectrum of **2**, with the fit in black. The red component has parameters consistent with high-spin Fe(III) (δ = 0.40(2) mm s^{-1}, $|\Delta E_Q|$ = 0.96(1) mm s^{-1}, area = 80(2)%). A minor component (green) is assigned as unreacted Fe(II) sites, and another minor component (purple) is assigned as an amorphous Fe(III) decomposition product. (d) The structure of **2** obtained from powder X-ray diffraction data (100 K). The Fe–OH bond distance of 1.92(1) Å is consistent with that in previously reported Fe(III)–OH compounds. The hydrogen atom on the hydroxide is shown for clarity, but was not found from the diffraction data. Selected interatomic distances (Å) for **2**: Fe–O1 = 1.92(1), Fe–O2 = 2.01(1), Fe–O3 = 2.08(1), Fe–O4 = 2.04(1), Fe–O5 = 2.04(1), Fe–O6 = 2.20(1), Fe–Fe = 3.16(1). Orange, red and light blue spheres represent Fe, O and H, respectively.

Surprisingly, the iron(III)-hydroxide species is capable of activating weak C-H bonds. When the partially oxidized sample **2'** was exposed to 1,4-cyclohexadiene (C-H bond dissociation energy of 322 kJ mol^{-1})[272] at room temperature, benzene was produced as

the sole product in quantitative yield. In the process, the framework converted entirely back to iron(II), as determined by Mössbauer spectroscopy. Such reactivity is rare, but not unprecedented, for iron(III)-hydroxide compounds. For instance, lipoxygenase, an enzyme that converts 1,4-dienes into alkyl hydroperoxides, is believed to proceed through a non-haem ferric hydroxide intermediate5 and several molecular lipoxygenase mimics have also been reported to activate the C-H bond of 1,4-cyclohexadiene and other 1,4-dienes.[273,274] However, the oxidizing power of **2** and **2'** is limited, and no reaction was observed with less-activated C-H bonds.

Oxidation of Ethane to give Ethanol

As the isolation of an iron(III)-hydroxide product from a reaction that employs a two-electron oxidant strongly suggests the intermediacy of an iron(IV)-oxo species, we next carried out the oxidation in the presence of a hydrocarbon substrate that contained stronger C-H bonds, specifically ethane (C-H bond dissociation energy of 423 kJ mol^{-1}), hoping to intercept the oxo species before its decay. Indeed, flowing an N_2O:ethane:Ar mixture (10:25:65) over the framework at 75 °C led to the formation of various ethane-derived oxygenates, which included ethanol, acetaldehyde, diethyl ether and other ether oligomers, as determined by ^1H NMR spectroscopy of the extracted products (Supplementary Fig. 21). The formation of ether products is not unprecedented, as N_2O-treated Fe-ZSM-5 forms a small amount of dimethyl ether in addition to methanol when exposed to methane, via a mechanism proposed to involve methyl radicals as well as multiple iron sites.[275] We hypothesized that the complex mixture of products was related to the close proximity of reactive iron centres, which are 8.13(2) Å and 6.84(1) Å apart across and along a channel, respectively, in **1**. To avoid oligomerization and overoxidation, a mixed-metal MOF, $Fe_{0.1}Mg_{1.9}$(dobdc) (**3**), in which the iron(II) sites are diluted with redox-inactive magnesium(II) centres, was synthesized. The BET surface area of 1,670 m^2 g−1 for this material falls between the surface areas of the pure iron and pure magnesium frameworks (1,360 and 1,800 m^2 g−1, respectively). Although determining the exact distribution of metal centres in heterometallic MOFs is challenging, the unit-cell parameters of **3** are between those of Fe_2(dobdc) and Mg_2(dobdc) (see Supplementary Table 10), which suggests the formation of a solid solution rather than a mixture of two separate phases. Additionally, the Mössbauer spectrum of **3** shows sharp doublets with

a significantly different quadrupole splitting to that of the all-iron analogue (2.25(1) mm s^{-1} versus 2.02(1) mm s^{-1} in Fe_2(dobdc); see Supplementary Table 9), which indicates that the iron centres in the magnesium-diluted framework are in an altered, but uniform, environment. Thus, **3** is possibly best described as containing either isolated iron centres or short multiiron segments dispersed evenly throughout a magnesium-based framework.

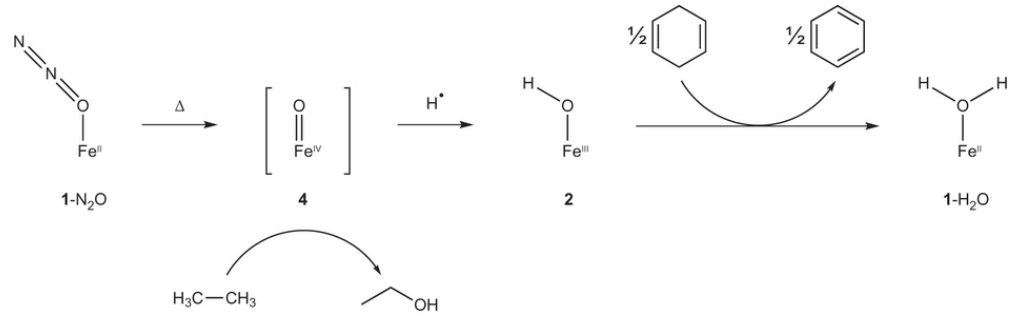

Figure 3.5: N_2O activation and reactivity of Fe_2(dobdc) in the oxidation of ethane and 1,4-cyclohexadiene. Heating of N_2O-bound Fe_2(dobdc) (**1**-N_2O) to 60 °C results in the formation of a transient high-spin Fe(IV)-oxo species (**4**), which can react with the strong C-H bonds of ethane. In the absence of a hydrocarbon substrate, the Fe(IV)-oxo quickly decays via hydrogen-atom abstraction into an Fe(III)-hydroxide (**2**), which is isolable and well characterized. This hydroxide species can react with weak C-H bonds, such as those in 1,4-cyclohexadiene, to form benzene and H2O-bound Fe_2(dobdc) (**1**-H_2O).

Exposure of **3** to N_2O and ethane under the same flow-through conditions yielded the exclusive formation of ethanol and acetaldehyde in a 10:1 ratio ratio (as shown in the ^{1}H NMR spectrum in Supplementary Fig. 22), albeit in low yield (60% with respect to iron). Gas chromatography analysis of the headspace revealed no ethanol, acetaldehyde or CO, which suggests the products remained bound to the framework (either at open iron or open magnesium sites), and may explain the high ethanol selectivity. Although the framework was still highly crystalline after N_2O/ethane treatment, Mössbauer spectroscopy revealed that roughly 90% of the iron centres decayed into a species with similar spectral parameters as those of **2** (see Supplementary Fig. 18 and Supplementary Table 9). We propose that the formation of iron(III)-hydroxide or -alkoxide decay products

prematurely halts the catalytic cycle, which leads to substoichiometric yields of hydroxylated product (see Fig. 3.5). As glass can be a source of H atoms, the reaction was subsequently repeated in a batch mode, rather than flow-through, in a Teflon-lined stainless-steel bomb. This produced both higher yields with respect to iron (turnover number = 1.6) and selectivities (25:1 ethanol:acetaldehyde). Though the yield based on ethane (roughly 1%) is still too low for practical purposes, this demonstrates that the system can, indeed, be modestly catalytic if competing substrates are excluded.

Electronic-Structure Calculations

As the high reactivity of the iron-oxo species precluded isolation in both Fe_2(dobdc) and its magnesium-diluted analogue, electronic structure calculations were performed on $Fe_2(O)_2$(dobdc) (**4**) to gain insight into the geometric and electronic structure of iron-oxo units supported within the framework. First, periodic PBE + U[276,277] geometry optimizations were performed on **4** for the singlet, triplet and quintet spin states. A quintet ground state was predicted, with a short Fe–O bond length of 1.64 Å, consistent with that of previously reported iron(IV)-oxo complexes (see Fig. 3.6 and Supplementary Table 11).[245] The periodic structure was then truncated to an 89-atom model cluster[278,279] that contained three metal centres, six organic linkers and an oxo moiety to facilitate calculations using more accurate methods. The cluster calculations were simplified by replacing the two peripheral iron(II) centres with closed-shell zinc(II) centres, which have the same charge and a similar ionic radius to iron(II) and magnesium(II) cations (see Supplementary Fig. 19). The geometry of this cluster was then optimized, with all atoms except for the central iron and its first coordination sphere frozen at the coordinates from the periodic PBE + U optimization. As shown in Table 3.1, the M06//M06-L[261] calculations also predict a quintet ground state. Further calculations were performed with several other exchange-correlation functionals, and in each case the ground state was found to be a quintet (see Supplementary Tables 11-16). Similar results were obtained when the Zn(II) centres in the 89-atom cluster were replaced with Mg(II) centres (see Supplementary Tables 20 and 21).

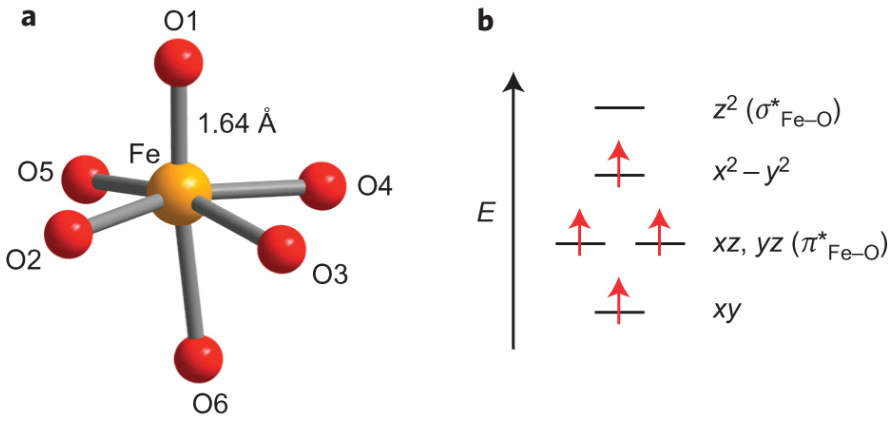

Figure 3.6: Structure and qualitative MO diagram of $Fe_2(O)_2$(dobdc) (**4**). (a) DFT and CASSCF/PT2 studies predict a short iron-oxo bond (1.64 Å) for $Fe_2(O)_2$(dobdc) (**4**). Selected interatomic distances (Å) for 4: Fe–O1 = 1.638; Fe–O2 = 2.004; Fe–O3 = 2.127; Fe–O4 = 2.019; Fe–O5 = 2.054; Fe–O6 = 2.140. Orange and red spheres represent Fe and O respectively. (b) DFT and CASSCF/PT2 studies all predict a high-spin $S = 2$ ground state for iron(IV)-oxo compounds installed in the Fe_2(dobdc) framework.

The electronic structure of the cluster model of **4** was examined further with single-point multiconfigurational complete active space (CASSCF) calculations followed by second-order perturbation theory (CASPT2).[280,281] Again, the ground state is predicted to be the quintet state (see Table 3.1 and Supplementary Table 18). Both M06//M06-L and CASPT2//PBE yield a spin density of 3.7 on iron, consistent with four unpaired spins localized mainly on the metal (see Supplementary Tables 13 and 19). Density functional and CASPT2 calculations were also performed on the cluster model of **2**; all calculations led to a high-spin sextet ground state for the iron(III) centre (see Supplementary Tables 1116 and Supplementary Table 18).

Table 3.1: Calculated Relative Energies ($kJ \cdot mol^{-1}$) of the Cluster Model of **4.** Density Functional and CASPT2 Calculations Were Performed on a Truncated Model of $Fe_2(O)_2$(dobdc) (**4**) that Contained a Central Iron Atom, Two Peripheral Zn(II) Atoms (to Replicate the Rigid Framework Structure) and Six Organic Linkers (See Supplementary Fig. 19). The Relative Energies of the Cluster Models in Different Spin States are Given Here. By Both Methods, the Quintet State (S=2) is the Calculated Ground State

S	M06//M06-L	CASPT2//PBE
0	210.6	249.4
1	136.4	127.6
2	0.0	0.0

Although spectroscopic and theoretical studies have long attributed the reactivity of non-haem enzymatic and synthetic iron(IV)-oxo complexes to a quintet spin state,[282] only a handful of mononuclear high-spin iron(IV)-oxo species have been characterized,[283,284,285,286] and all but one exhibit a trigonal bipyramidal coordination geometry.[287] In these systems, the oxo moiety is either extremely unstable ($[Fe(O)(H_2O)_5]^{2+}$, for example, has a half-life of roughly ten seconds) or inaccessible to substrates because of bulky ligand scaffolds, which lead to sluggish reactivity. However, the Fe_2(dobdc) framework features sterically accessible, site-isolated metal centres entrenched in a weak-field ligand environment. Utilizing these two properties, it is possible not only to generate such a species, albeit fleetingly, but also to direct it towards the facile activation of one of the strongest C-H bonds known.

3.2.3 Concluding Remarks

The foregoing results demonstrate, through reactivity studies, detailed characterizations of decay products and theoretical calculations, that the iron-based MOFs Fe_2(dobdc) and $Fe_{0.1}Mg_{1.9}$(dobdc) are very likely to be capable of supporting fleeting iron(IV)-oxo species that possess an unusual $S = 2$ spin state. With this, Fe_2(dobdc) has now been shown to stabilize iron-superoxo, -peroxo, -hydroxo and -oxo intermediates, which highlights the promise of MOFs both as catalysts and as scaffolds for interrogating reactive metal species. Future work will focus on (1) further exploring the reactivity

of Fe_2(dobdc) and its expanded analogues towards ethane and other hydrocarbon substrates, as well as continued efforts to isolate the iron-oxo species, (2) the use of dioxygen as the terminal oxidant in such systems and (3) the design, synthesis and reactivity of other MOFs with coordinatively unsaturated iron sites.

3.2.4 Methods

Synthesis of $Fe_2(OH)_{0.6}$(dobdc) (2') and $Fe_2(OH)_2$(dobdc) (2)

An evacuated Schlenk flask that contained fully desolvated Fe_2(dobdc) (100 mg, 0.33 mmol) was placed under an atmosphere of 30% N_2O and 70% N_2. The flask was immersed in an oil bath, and the temperature was increased by 10 °C every 12 hours, from 25 °C up to 60 °C, to obtain $Fe_2(OH)_2$(dobdc) as a dark red-brown solid. When the reaction was stopped after 12 hours at 35 °C, partially oxidized $Fe_2(OH)_{0.6}$(dobdc) (as determined by Mössbauer spectroscopy) was obtained. Analytical: $C_8H_4Fe_2O_8$ calculated, C, 28.28, H, 1.19; found, C, 29.18, H, 1.16. Infrared (solid attenuated total reflection (ATR)) spectroscopy: 3,679 (m), 1,532 (s), 1,450 (s), 1,411 (s), 1,361 (s), 1,261 (s), 1,154 (w), 1,129 (w), 1,077 (w), 909 (m), 889 (s), 818 (s), 807 (s), 667 (s), 630 (m), 594 (s), 507 (s).

Synthesis of $Fe_{0.1}Mg_{1.9}$(dobdc) (3)

In a 500-ml Schlenk flask, H_4(dobdc) (1.8 g, 8.8 mmol), $MgCl_2$ (1.5 g, 15 mmol) and $FeCl_2$ (0.84 g, 6.6 mmol) were dissolved in a mixture of 310 ml dimethylformamide (DMF) and 40 ml methanol. The reaction was stirred vigorously at 120 °C for 16 hours. The precipitate was filtered and stirred with 250 ml fresh DMF at 120 °C for three hours. Two more DMF washes at 120 °C were performed, after which the precipitate was filtered and soaked in methanol at 60 °C. The methanol exchanges were repeated until no DMF stretches were apparent in the infrared spectrum. The framework was desolvated fully under dynamic vacuum (¡15 μbar) at 210 °C for two days to afford $Fe_{0.1}Mg_{1.9}$(dobdc) as a bright yellow-green solid (2.0 g, 8.2 mmol, 93% yield). The iron-to-magnesium ratio was determined by inductively coupled plasma optical emission spectrometry. Analytical: $C_8H_2Fe_{0.1}Mg_{1.9}O_6$ calculated, C, 39.08, H, 0.82; found, C, 39.37, H, 0.43. Infrared (solid ATR) spectroscopy: 1,577 (s), 1,484 (m),

1,444 (s), 1,429 (s), 1,372 (s), 1,236 (s), 1,210 (s), 1,123 (m), 911 (m), 892 (s), 828 (s), 820 (s), 631 (s), 584 (s), 492 (s).

Reactivities of Fe_2(dobdc) (1) and $Fe_{0.1}Mg_{1.9}$(dobdc) (3) with N_2O and C_2H_6

In a typical flow-through experiment, a mixture of gases (2 ml min^{-1} N_2O, 10 ml min^{-1} C_2H_6 and 8 ml min^{-1} Ar for a total flow 20 ml min^{-1}) was flowed over a packed bed of MOF (50-100 mg) contained within a glass column. The column was heated to 75 °C for 24 hours, after which the products were extracted with CD_3CN (3 × 1 ml) and analysed by ^1H NMR spectroscopy using 1,4-dichlorobenzene as an internal standard. Although a cold bath maintained at -78 °C was installed downstream of the glass reactor to collect condensable organic products, at the temperatures tested all the products appeared to remain bound to the framework.

In a typical batch experiment, a Parr bomb was charged with N_2O (1.5 bar) and C_2H_6 (7.5 bar) and heated to 75 °C in a sand bath. After 24 hours, the bomb was cooled and the products extracted with CD_3CN.

Electronic Structure Calculations

The structures of **2** and **4** were optimized using periodic boundary conditions and the PBE + U exchange-correlation functional. From each of these structures, we carved out a model cluster that contained three iron centres along a single helical chain and six organic linkers. These clusters are analogous to the 88-atom cluster model of Fe_2(dobdc) employed previously.[278] The cluster models were simplified further by substituting the two peripheral iron(II) centres with zinc(II) centres, keeping only the central iron(II) in the cluster. Constrained geometry optimizations were performed in which only the central iron and the six oxygen atoms (plus the hydroxide hydrogen in compound 2) of its first coordination sphere were allowed to relax. Single-point multiconfigurational complete active space (CASSCF) calculations followed by second-order perturbation theory (CASPT2) were performed at PBE-optimized geometries of the cluster models of **2** and **4**, and M06 calculations were performed at M06-L geometries. Full computational details are in the Supplementary Information.

3.2.5 Additional Information

Supplementary information is available in the online version of the paper. Reprints and permission information is available online at `http://www.nature.com/reprints`. Correspondence and requests for materials should be addressed to J.R.L. The authors declare no competing financial interests.

Acknowledgements

Synthesis, basic characterization experiments and all of the theoretical work were supported by the US Department of Energy, Office of Basic Energy Sciences, Division of Chemical Sciences, Geosciences, and Biosciences under award DE-FG02-12ER16362. Reactivity studies were supported by the Laboratory Directed Research and Development Program of Lawrence Berkeley National Laboratory under US Department of Energy Contract No. DE-AC02-05CH11231. Work at the Molecular Foundry, and XAS experiments performed at the Advanced Light Source (BL 10.3.2), Berkeley, were supported by the Office of Science, Office of Basic Energy Sciences, of the US Department of Energy under Contract No. DE-AC02-05CH11231. X-ray diffraction experiments were performed at the Advanced Photon Source at Argonne National Laboratory (17-BM-B). Use of the Advanced Photon Source, an Office of Science User Facility operated for the US Department of Energy (DOE) Office of Science by Argonne National Laboratory, was supported by the US DOE under Contract No. DE-AC02-06CH11357. S.B., F.B. and V.C. acknowledge financial support from the Ateneo Project 2011 ORTO11RRT5. We also thank the National Science Foundation for providing graduate fellowship support (D.J.X. and J.A.M.). In addition, we are grateful for the support of E.D.B. through a Gerald K. Branch fellowship in chemistry, P.V. through a Phillips 66 Excellence Fellowship and M.R.H. through the National Institute of Standards and Technology/National Research Council Fellowship Program. We thank S. Chavan for help with the infrared spectroscopy experiments and fruitful discussion.

Author Contributions

D.J.X., E.D.B. and J.R.L. planned and executed the synthesis, characterization and reactivity studies. J.A.M., W.L.Q., M.R.H. and C.M.B. analysed the powder neutron and

X-ray diffraction data. N.P. and P.V. performed the cluster DFT calculations. J.B. and K.L. performed the periodic DFT calculations. A.L.D. performed the CASSCF/PT2 calculations. D.G.T. and L.G. conceived and managed the computational efforts. F.B., V.C. and S.B. carried out the in situ transmission Fourier transform infrared studies, and J.Y. supervised EXAFS analysis. All authors participated in the preparation of the manuscript.

Chapter 4

Nature of Adsorbate–MOF Bonding

4.1 Design of a Metal-Organic Framework with Enhanced Back Bonding for Separation of N_2 and CH_4

Gas separations with porous materials are economically important and provide a unique challenge to fundamental materials design, as adsorbent properties can be altered to achieve selective gas adsorption. Metal-organic frameworks represent a rapidly expanding new class of porous adsorbents with a large range of possibilities for designing materials with desired functionalities. Given the large number of possible framework structures, quantum mechanical computations can provide useful guidance in prioritizing the synthesis of the most useful materials for a given application. Here, we show that such calculations can predict a new metal-organic framework of potential utility for separation of dinitrogen from methane, a particularly challenging separation of critical value for utilizing natural gas. An open V(II) site incorporated into a metal-organic framework can provide a material with a considerably higher enthalpy of adsorption for

Adapted with permission from K. Lee, W. C. Isley III, A. L. Dzubak, P. Verma, S. J. Stoneburner, L. -C. Lin, J. D. Howe, E. D. Bloch, D. A. Reed, M. R. Hudson, C. M. Brown, J. R. Long, J. B. Neaton, B. Smit, C. J. Cramer, D. G. Truhlar, L. Gagliardi.*J. Am. Chem. Soc.* 2014, *136*, 698.[288] Copyright 2014, American Chemical Society. K.L., W.C.I., A.L.D., and P.V. contributed equally to this work. Additional information may be found in section 4.1.5.

dinitrogen than for methane, based on strong selective back bonding with the former but not the latter.

4.1.1 Introduction

Coordination of dinitrogen to transition-metal cations is important both fundamentally and industrially. Dinitrogen is highly inert and generally considered to be a poor ligand. In 1965, however, it was shown that a simple coordination complex, $[Ru(NH_3)_5]^{2+}$, could reversibly bind N_2.[289] In subsequent years, a number of dinitrogen-transition-metal complexes have been isolated for metals in varying oxidation states with various coordination numbers.[290,291] These complexes typically feature low-valent, relatively reducing metal cations coordinated to dinitrogen in an end-on binding mode. Activating dinitrogen at a metal center to promote its reduction by hydrogen to ammonia under moderate conditions remains a critical goal for homogeneous catalysis. Somewhat weaker metal-dinitrogen binding, however, may be useful for adsorptive separation of gas mixtures. An example is provided by the need to remove dinitrogen (an omnipresent but noncombustible contaminant) from natural gas or other methane-rich gases. This is an extraordinarily difficult separation based on physical properties alone, as both gases lack a permanent dipole and have similar polarizabilities, boiling points, and kinetic diameters. Although cryogenic distillation is currently utilized for separation of these gases, the cost- and capital-intensive nature of this separation has led to development of a number of competing processes, such as membrane- or kinetics-based separations, which generally suffer from low selectivities.[292]

Adsorptive separations utilizing porous solids containing transition-metal cations capable of reversibly binding dinitrogen may result in highly selective and efficient dinitrogen/methane separations. Metal-organic frameworks are particularly promising in this regard, as they offer a myriad of materials design opportunities and have already shown great potential for a number of gas separation applications.[293,294] These materials typically display high internal surface areas that can be decorated with both ligand- and metal-based functionalities.[295] In principle, this permits rational design of local environments tuned for selective binding of specific gases. The M-MOF-74 series of compounds having formula M_2(dobdc) (where dobdc^{4-} is 2,5-dioxido-1,4-benzenedicarboxylate) is an especially versatile and intensively studied structure type.[296,297,298,299,300,301] This

structure features 12 Å wide hexagonal channels, lined at the vertices with helical chains of five-coordinate divalent metal ions connected through dobdc^{4-} bridging ligands. Upon activation, these materials have an extremely high density of open metal coordination sites, leading to the possibility of a high working capacity for storage or separation applications.

M-MOF-74 structures containing Mg^{2+}, Mn^{2+}, Fe^{2+}, Co^{2+}, Ni^{2+}, Cu^{2+}, and Zn^{2+} have been synthesized. CH_4 and N_2 adsorption enthalpies reported for a number of these materials indicate they are likely not useful dinitrogen/methane separation materials. For example, Mg-MOF-74 has CH_4 and N_2 adsorption enthalpies of 4.4[302] and 5.0[303] kcal/mol, respectively. However, in principle, other dicationic metals could be incorporated into this structure type. As the synthesis of pure M-MOF-74 phases is often quite challenging, it would be advantageous to know a priori which variations are the best candidates for a given gas separation application. This is a predictive challenge appropriate for application of computational quantum chemistry, which can be used to pinpoint which cations might be anticipated to have interactions of significantly different strengths with competing guests. Interactions between M-MOF-74, corresponding to different M, and various adsorbates were investigated theoretically, which suggested that V-MOF-74 could be promising in N_2/CH_4 separation. We thus decided to study V-MOF-74 in detail. Here, we show, based on three models (Figure 4.1a-c) of the MOF, that selective back-bonding interactions[304,305] from the vanadium(II) cation centers in V-MOF-74 to the unoccupied π^* orbitals of N_2 can be used to separate N_2/CH_4 mixtures. We further use calculations by Kohn-Sham density functional theory[306] (DFT) and correlated wave function theory (WFT) to put this prediction on a quantitative basis and compare it with the experimentally characterized Fe-MOF-74.

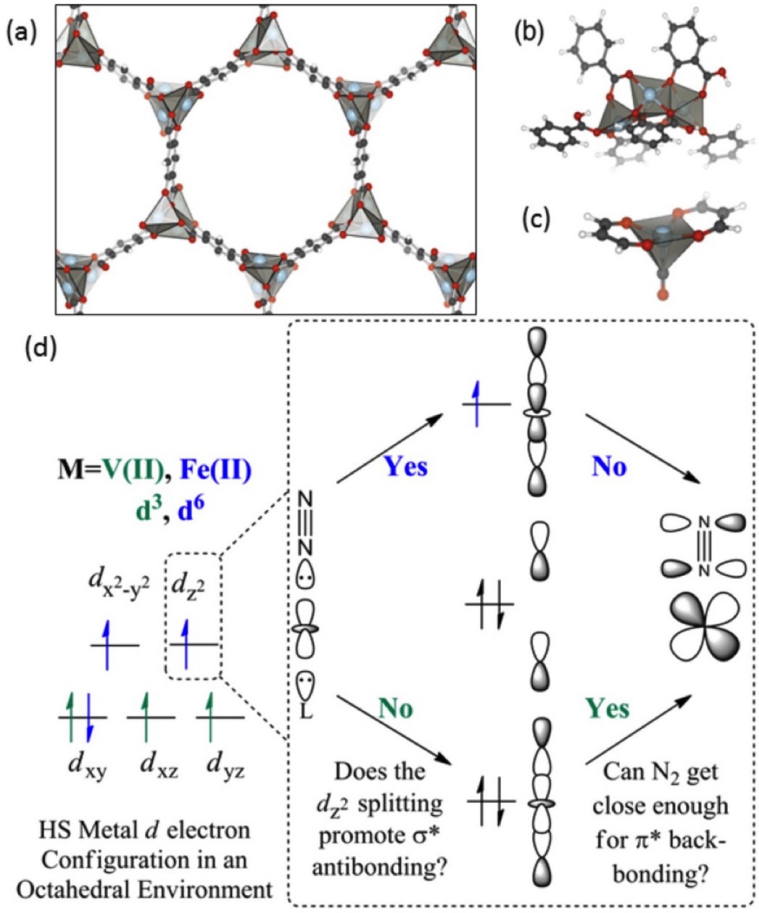

Figure 4.1: (a-c) Structural models used in this work. (a) Optimized periodic framework model, based on the symmetry of the experimental primitive cell. (b) Eighty-eight-atom cluster. (c) Small model. Light blue, red, dark gray, and white spheres represent vanadium, oxygen, carbon, and hydrogen atoms, respectively. (d) Three-center bonding diagram between framework O atoms, the metal, and a guest. On the left we show the d subshell occupancy of Fe(II) in both blue and green; V(II) would have only three electrons (green alone) in the d subshell, and the metal d_z^2 orbital would be empty. On the right, the middle section shows how the d_z^2 orbital splits upon interacting with the four lone pair electrons of two axial Lewis bases; occupancies shown are for Fe(II)–only four electrons would be present for V(II) because the d_z^2 orbital of V(II) is unoccupied. The right-most orbital diagram shows the nature of the interaction of the ligand-unoccupied π^* orbitals with the occupied d orbitals of the metal; when the antibonding orbital is occupied, the ligand cannot approach the metal as closely, and this interaction is substantially weaker.

4.1.2 Theoretical Methods

In order to treat the adsorption process reliably, we need to use electronic structure methods that include dynamical correlation, especially attractive medium-range noncovalent forces. Most exchange-correlation (xc) functionals currently used in DFT do not treat such medium-range correlation energy accurately; however, here we use two kinds of density functionals that overcome this limitation. (1) The Rutgers-Chalmers van der Waals density functionals[307] use a nonlocal formulation of the correlation part of the xc functional and can treat attractive van der Waals interactions at both medium range and long range. We use the vdW-DF2+U functional[308] of this type with Hubbard U corrections,[309] where U is a parameter for metal d electrons that is determined to reproduce oxidation energies. (2) The Minnesota functionals[310] include the local kinetic energy density in the xc functional and have been shown to yield accurate noncovalent attraction at van der Waals distances;[311] we will employ three such functionals, M06-L,[312] M06,[313] and M11-L,[314] because they are based on very different approaches: M06-L is a well-validated[310,311,313] local functional with global parameters, M11-L is a recent local functional employing different exchange and correlation parameters for short and long interelectronic distances, and M06 employs 27% Hartree-Fock exchange, as justified by adiabatic connection arguments[315] to reduce DFT self-interaction error.

We also employ two WFT methods, in particular, local-pair natural-orbital coupled cluster theory with single and double excitations[316] (LPNO-CCSD) and complete active space second-order perturbation theory with counterpoise corrections (CASPT2-CP).[317] The latter method has been shown to yield accurate energetics in systems containing transition-metal compounds.[318,319]

The DFT and WFT methods used here involve approximations that impose limits on their accuracy. Because they represent very different approaches to the electronic structure problem, confidence in the utility of their quantitative predictions is significantly increased when different models agree, even if the natures of the various approximations employed make it unclear which model is most accurate within the remaining variation.

Orbitals, Spin States, Cores, Relativistic Effects, and Metal Ions

In Kohn-Sham calculations and in the reference state for LPNO-CCSD, the V and Fe ions are in high-spin states (quartet and quintet, respectively) and all other orbitals are doubly occupied. For the CASPT2-CP calculation on the 88-atom cluster, we replace the two outer metal ions by closed-shell Zn(II) ions and treat the central metal in the active space. (None of the DFT calculations involve this Zn substitution.) Descriptions of the active spaces used for all species are given in the Supporting Information. The vdW-DF2 calculations with the Hubbard U correction employ the all-electron projector-augmented wave (PAW) method for scalar relativistic core electrons and ionic potentials; all other calculations treat all electrons explicitly. CASPT2-CP calculations use the Douglas-Kroll-Hess relativistic approximation, and the extended transition state (ETS) method for energy decomposition analysis combined with the natural orbitals for chemical valence (NOCV) theory calculations use the ZORA relativistic approximation. All other calculations are nonrelativistic.

Basis Sets

All vdW-DF2+U calculations employed a plane-wave basis with a 1000 eV kinetic energy cutoff. All other DFT calculations employed the def2-TZVP basis except the ETS-NOCV analysis, which used TZ2P. LPNO-CCSD calculations are extrapolated to a complete basis set from def2-TZVP and def2-QZVP. CASPT2-CP calculations for the small model employed the ANO-RCC-TZVP basis for all atoms, and for the 88-atom cluster they employed the ANO-RCC-DZVP basis for all atoms. References for basis sets are in Supporting Information.

Coordinates

We used a triclinic primitive unit cell containing 54 atoms including 6 metal centers and simultaneously optimized the lattice vectors and atomic positions in the unit cell with variable cell dynamics with PBE+U for bare MOFs and with vdW-DF2+U for adsorbates. The 88-atom clusters were taken out of these periodic structures. Optimization of binding geometry of adsorbates in the periodic MOFs and on the 88-atom cluster involved freezing the MOF and optimizing only the coordinates of the adsorbate;

this was carried out with all DFT calculations. The structure of the small model was fully optimized by M06-L, and these structures were used for the LPNO-CCSD and CASPT2-CP calculations. Full coordinates and absolute energies in hartrees of selected structures are in the Supporting Information.

Starting geometries for the periodic model were based on the experimental structures[296,297,298,300,320] of M-MOF-74 (Figure 4.1a) and further optimized by DFT; the primitive unit cell of experimental structure contains 54 atoms, including 6 metal centers. We defined two other models of M-MOF-74 to be studied at additional levels of theory. The cluster (Figure 4.1b) has 88 atoms, including three metal centers, and it was designed[301] to retain the local structure of MOF-74 about the central metal ion while remaining small enough for high-level electronic structure calculations. The small model (Figure 4.1c) has 19 atoms, including one metal center, and is small enough to conduct calculations by expensive wave function methods for comparison.

All iron and vanadium ions were modeled in their respective ground (high-spin) state. To maintain charge neutrality with all oxide ligands in the small model, we included a trans carbonyl ligand. Although carbonyl groups are usually considered to be strong-field ligands, the small model nevertheless maintains a high-spin ground state and an electronic structure consistent with the larger model. Indeed, the insensitivity of our conclusions to the nature of the trans ligand in the M-MOF-74 model provides particularly strong support for our analysis.

Charges

Partial atomic charges were calculated by charge model 5 (CM5).[321,322]

Software

Minnesota functionals, Gaussian 09;[323,324] vdW-DF2+U, VASP;[325] LPNO-CCSD, ORCA 2.9.1;[326]CASPT2-CP, MOLCAS 7.8;[327] ETS-NOCV, ADF.[328,329,330]

4.1.3 Results and Discussion

N_2 bonding motif to V-MOF-74 and Fe-MOF-74

A molecular orbital picture can be used to predict selective adsorption of N_2 over CH_4 with V-MOF-74. The model exploits the square-pyramidal coordination geometry of the metal in desolvated M-MOF-74 (Figure 4.1d). A key consideration is the d^3 electronic configuration of V(II). In the case of N_2 binding, our DFT calculations show that a three-center bond is formed between the framework oxo ligand trans to dinitrogen, the metal, and N_2 (Figure 4.1d). Given an end-on coordination geometry, a pair of nonbonding electrons on N_2 and its respective trans framework atom interact with the V(II) d_z^2 orbital, and the net result is a three-center bond with two electrons each in a bonding and nonbonding orbital. In addition to the resulting σ bond, the unoccupied π^* orbitals of N_2 can accept back-bonding electrons from the metal $d\pi$ orbitals. This back bonding is not present for methane, due to the lack of low-energy π^* orbitals on the hydrocarbon. Fe(II), in contrast, has a high-spin d^6 electronic configuration with a singly occupied d_z^2 orbital. In this case, the two doubly occupied lone pairs provide four electrons to the three-center bond and the occupation of the metal d_z^2 orbital provides one electron, for a total of five electrons in the three-center bond; so, one electron is in the antibonding orbital. As the N_2 approaches the metal site, it thus experiences unfavorable σ antibonding plus additional exchange repulsion from the occupied nonbonding orbital. Consequently, N_2 cannot approach the Fe(II) center closely enough to experience π^* back-bonding stabilization as favorable as is present in the V(II)-N_2 system.

In subsequent sections of this article, we confirm the differential stabilization effect with local and nonlocal DFT calculations, confirming our molecular orbital prediction that as-yet unsynthesized V-MOF-74 could be used to separate N_2 from CH_4. We also reinforce our DFT results with correlated wave function calculations to rule out the possibility of artificial back bonding[331] owing to the possible underestimation of the energy gap and the delocalization of d electrons in the DFT models. Finally, we analyze single-determinantal Kohn-Sham reference functions to confirm the above explanation of the effect.

N_2 and CH_4 Adsorption in V-MOF-74 and Fe-MOF-74

The key quantity we calculated is the differential adsorption energy defined by

$$\Delta E_{\text{ads}} = E_{\text{ads}}(N_2) - E_{\text{ads}}(CH_4) \tag{4.1}$$

where E_{ads} is the energy of adsorption (here defined as a positive number to denote that deadsorption is endoergic); thus, ΔE_{ads} is more positive when N_2 binds more strongly. The results are in Table 4.1. Across all levels of theory and all models, CH_4 binding is comparable between the two metals but N_2 is predicted to bind significantly more strongly than CH_4 to the coordinatively unsaturated metal site when the metal is V rather than Fe.

Table 4.1: N_2/CH_4 Adsorption Energy Differences, ΔE_{ads} (in kcal/mol)

	small model		large models[a]	
level of theory	V	Fe	V	Fe
DFT, vdW-DF2+U			6.0	0.4
DFT, vdW-DF2+U	4.9	0.4	5.8	0.3
DFT, M06-L	4.3	0.0	10.1	0.9
DFT, M06	4.5	0.1	6.9	0.4
DFT, M11-L	4.2	−0.8	5.9	−1.7
DFT, LPNO-CCSD/CBS	4.8	0.7	*b*	*b*
WFT, CASPT2 CP	3.8	0.3	2.1	0.3

[a]The first row is for the periodic model, and the other large-model calculations are for the 88-atom cluster

[b]Impractically computationally intensive

We noted above the consistent trend observed for calculated ΔE_{ads} values; the trends in calculated E_{ads} values are also consistent across the methods. Absolute adsorption energies for the 88-atom cluster and the periodic model are compared in Table 4.2. We see remarkable agreement between the adsorption energies calculated with the 88-atom cluster and the periodic model and further remarkable agreement between the absolute binding energies calculated by DFT with different functionals and by WFT; the good

agreement of results obtained with several methods that incorporate the physics in different ways adds confidence to the predictions. Inspection of Table 4.2 shows relatively large differences in the absolute binding energies between the large and small clusters. The enhanced attraction in the 88-atom cluster model can partially be attributed to greater medium-range correlation effects. One should also consider that the two models have different ligand coordination environments, and this too has an influence on the absolute binding energies.

Table 4.2: Absolute Binding Energies (kcal/mol)

	V–N_2	Fe–N_2	V–CH_4	Fe–CH_4
periodic model				
vdW-DF2+U	13.4	6.6	7.4	6.3
88-atom cluster				
vdW-DF2+U	12.0	4.5	6.2	4.2
M06-L	19.9	7.8	9.8	6.9
M06	17.5	8.1	10.6	7.7
M11-L	13.4	4.4	7.5	6.1
CASPT2 CP	7.4	3.3	5.3	3.0
small model				
vdW-DF2+U	8.5	3.2	3.6	2.9
M06-L	9.1	4.3	4.8	4.3
LPNO-CCSD/CBS	9.6	4.2	4.8	3.6
CASPT2 CP	6.5	3.3	2.7	3.0

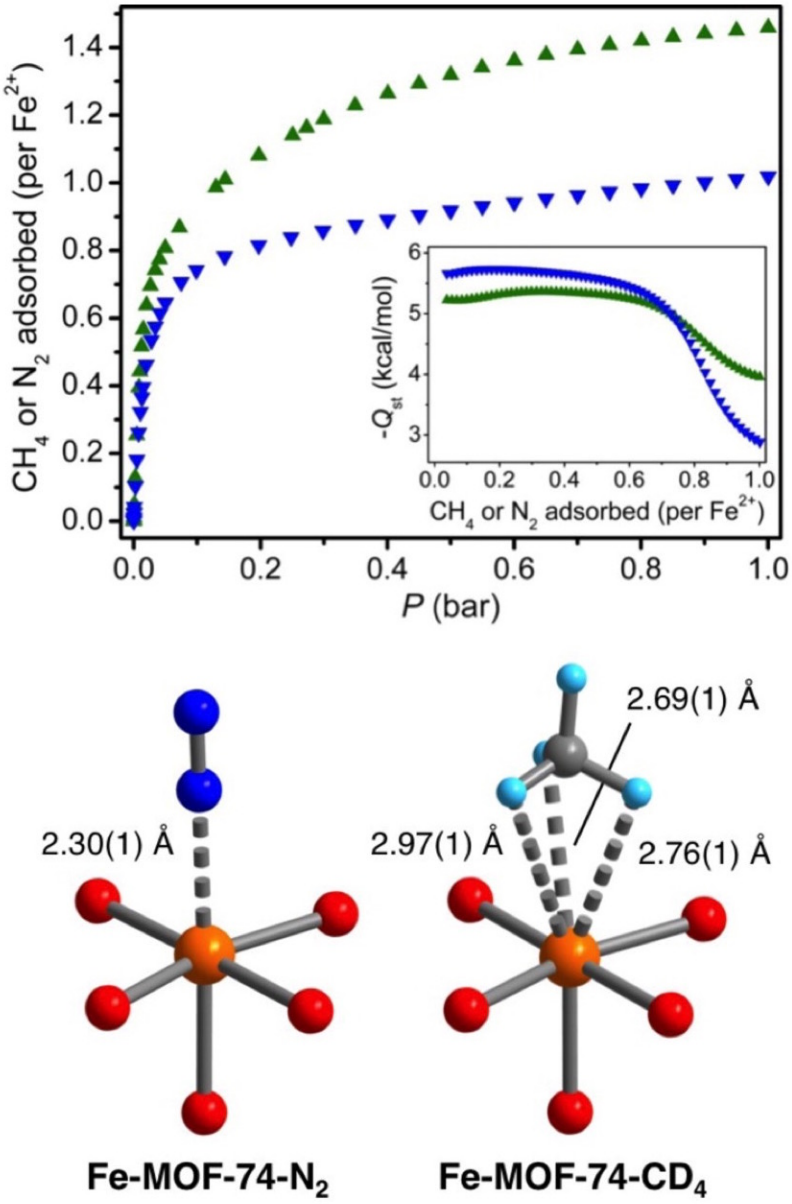

Figure 4.2: (Top) Adsorption of methane (green) and dinitrogen (blue) in Fe_2(dobdc) at 175 K. (Top inset) Isosteric heats of adsorption. (Bottom) First coordination spheres for the iron centers in the solid-state structures obtained upon dosing Fe-MOF-74 with dinitrogen or methane; orange, red, blue, gray, and light blue represent iron, oxygen, nitrogen, carbon, and deuterium, respectively.

In order to further verify the validity of these predictions, isosteric heats of CH_4 and N_2 adsorption in Fe_2(dobdc) were obtained experimentally from adsorption isotherms at 175 K. (Details of the experiment are in the Supporting Information.) As seen in Figure 4.2, the uptake of N_2 in Fe-MOF-74 is relatively steep and approaches one N_2 molecule per iron cation site at 1 bar and 175 K. Methane uptake, while similar at low pressure, reaches a higher value of approximately 1.5 CH_4 molecules per iron at 1 bar. These plots yield isosteric heats of adsorption for methane and dinitrogen that are both relatively low and quite similar; in particular, they are 5.3 ± 0.2 and 5.5 ± 0.2 kcal/mol, respectively, which yields an experimental difference of 0.2 ± 0.3 kcal/mol. These results differ from the previously reported values of 4.8 kcal/mol for CH_4[332] and 8.4 kcal/mol for N_2[300] both because of the lower temperature and because of the change in experimental procedure; the present results should be more accurate for the difference because they were done with isotherms at the same temperature on the exact same batch of sample. An attempt to obtain the same information for V-MOF-74 was not successful.

Experimental enthalpies of adsorption should not be compared directly to the energies of adsorption in Table 4.2. For the 88-atom cluster, however, we computed the enthalpies of adsorption at 175 K by a formula given previously.[301] The M06-L, M06, and M11-L levels of theory give predicted differences in adsorption enthalpy of 1.1, 0.5, and ?1.6 kcal/mol, respectively. The average difference in predicted adsorption enthalpy of 0.0 kcal/mol is in good agreement with the 0.2 kcal/mol difference observed experimentally.

Structural Parameters, Vibrational Frequencies, and Charges

Table 4.3 shows that the M–N distance is shorter in V-MOF-74 than in Fe-MOF-74, as anticipated above; there is also a smaller difference in the M–C distances for CH_4. Neutron powder diffraction experiments on Fe-MOF-74 at 10 K (see figure in the Supporting Information) indicate excellent agreement between the calculated and the experimentally observed structures of methane bound to Fe^{2+}. Specifically, the Fe–C distance of 2.98(1) Å is very close to the distance of 2.96 Å calculated for the 88-atom cluster. Differences in M–N distances are consistent with the energetic results presented above.

Table 4.3: M06-L Bond Distances, Adsorbate Frequencies, and Partial Atomic Charges

		small model		88-atom cluster	
	gas phase	V	Fe	V	Fe
structural descriptors					
binding N_2					
M–N (Å)		2.21	2.73	2.08	2.34
$\nu_{N–N}$ (cm^{-1})	2424	2357	2430	2252	2360
binding CH_4					
M–C (Å)		3.00	3.15	2.77	2.96
$\nu_{C–H}$ (cm^{-1})	3057	3037	3043	3017	3031
partial atomic charges					
bare MOF					
M		0.90	0.69	0.81	0.69
binding N_2					
M		0.89	0.66	0.88	0.70
N_2	0.00	0.01	0.07	−0.09	0.09
binding CH_4					
M		0.85	0.66	0.74	0.66
CH_4	0.00	0.06	0.03	0.05	0.08

The potential energy curves (given in Figure 4.3) provide further evidence for qualitatively different kinds of interaction; we give just one example, the interaction of N_2 with M in the small model, calculated by M06-L. Single-point energies were calculated by modifying the M–N_2 distance but keeping all other geometrical parameters unchanged from the geometric minima. Interestingly, the predicted interaction energy at 2.8 Å is nearly equivalent for N_2 with the Fe and V small models. At an M–N distance of 2.8 Å, the interaction energy is -4 kcal/mol for both V and Fe. As N_2 approaches more closely, the potential energy reaches a minimum of -4.3 kcal/mol at 2.73 Å for Fe but goes to a much deeper well at -9.1 kcal/mol at 2.21 Å for V. (This further reinforces the conclusion that the binding interaction to vanadium is quite different from that of other

metals studied.) For comparison, the Fe–N distance was determined to be 2.30±0.01 Å for N_2 adsorbed within Fe-MOF-74 by neutron diffraction experiments at 9 K. The predicted Fe–N distance for the 88-atom cluster compares favorably with the measured value of 2.30±0.01 Å.

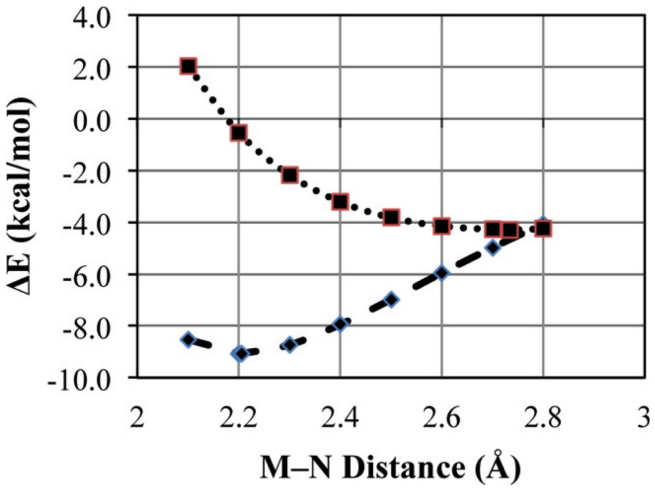

Figure 4.3: Potential energy curve as a function of M–N_2 distance for the small model as calculated with the M06-L exchange-correlation functional. The curve for M = V(II) is shown as a dashed line with diamond points indicating single-point energies. The curve for M = Fe(II) is shown as a dotted line with square points indicating single-point energies.

The N–N stretching frequency is a probe of back bonding, because these shifts result from weakening the bond by $d\pi \rightarrow \pi^*$ back-donation. Periodic vdW-DF2+U calculations show that, as compared to the isolated gas-phase diatomic vibrational frequency (2415 cm^{-1}), N_2 bound to V experiences a significant shift in the N–N stretch (-102 cm^{-1}), whereas N_2 bound to Fe shows a negligible change (-6 cm^{-1}). In contrast, vibrational frequency shifts for C–H modes in CH_4, where no back bonding is predicted, are negligible. For the 88-atom cluster, M06 calculations for N_2 bound to MOF show similar trends–a 103 cm^{-1} shift for V and a 4 cm^{-1} shift for Fe. M11-L also shows similar shifts: 101 and 5, respectively. Table 4.3 shows a more complete set of results for M06-L, and these too are consistent with our analysis.

Next we examine in more detail the amount of charge transfer between the metal and

the N_2 guest. Key charges in atomic units are given in Table 4.3. The total charge on the guest molecule is computed by summing the partial charges of the individual atoms of the guest molecule; this indicates the magnitude and direction of charge transfer between the MOF and the guest. For each of the three functionals, CM5 partial atomic charges for the 88-atom cluster indicate donation of negative charge from the central metal ion to the nitrogen molecule and an opposite direction of transfer for methane. This is also reflected in the charge on the metal ion being increased for N_2 adsorption and decreased for CH_4 adsorption when compared to the bare MOF. The increase or decrease in the positive charge of the central metal ion with N_2/CH_4 adsorption does not exactly equal the total charge on the guest molecule. This reflects charge change within the rest of the MOF framework.

We find that the direction of electron transfer from the metal center to the guest molecule for the Fe–N_2 system is opposite to what is observed for V–N_2. Specifically, the partial atomic charge on Fe is 0.66 in the presence of either N_2 or CH_4; these values are the same as the values of 0.66 for the bare Fe-MOF-74 framework. The partial atomic charge on the V ions in V-MOF-74 is significantly higher in all structures, and it is not very sensitive to the adsorbates in the small model, but in the 88-atom cluster the partial atomic charge on V increases by 0.07 upon adsorption of N_2 and decreases by 0.07 upon adsorption of CH_4. Overall, these changes are consistent with our interpretation of increased back bonding in the V–N_2 case.

Orbital Analysis

The nature of the M–N_2 bond of the small model was investigated using the extended transition state (ETS) method for energy decomposition analysis combined with the natural orbitals for chemical valence (NOCV) theory. ETS-NOCV analysis[333] separates bond formation energy into distortion of interacting subsystems, steric interaction (with electrostatic and exchange-correlation contributions), and an "orbital" term that represents a combination of the interactions between the occupied molecular orbitals on one bonding partner with the unoccupied molecular orbitals of the other and the intrafragment polarization. ETS-NOCV calculations carried out on the small model with M06-L show (see Figure 4.4) that both σ donation and π^* back-bonding interactions are weaker for Fe–N_2 than for V–N_2. Comparing the two largest alpha and beta spin-paired NOCV

contributions to the bond energy, the σ interactions are about eight times stronger for V than for Fe and the π^* back-bonding-type interactions are about twice as strong, with all other contributions being less than 1 kcal/mol for V and less than 0.5 kcal/mol for Fe. Such analyses of charge rearrangement are not unique, so we also performed natural bond order (NBO) analysis,[334] as described next, to test the robustness of this interpretation.

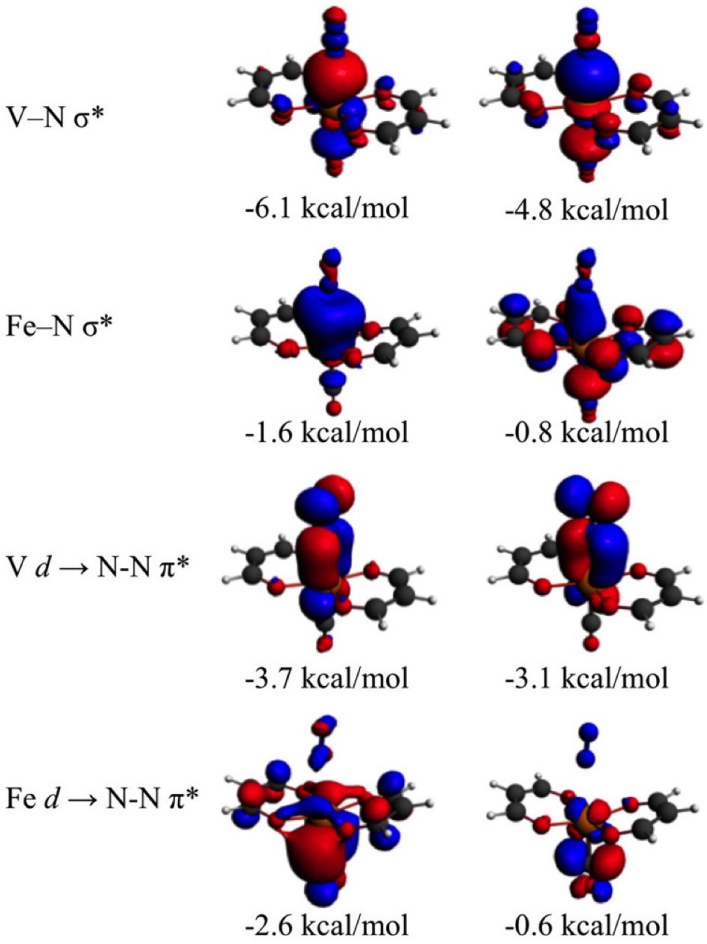

Figure 4.4: Contours of NOCVs for N_2 binding with V-MOF-74 and Fe-MOF-74. Four NOCV orbitals with the largest contributions to the binding energy are reported for each case, with the sum of the α and β spin contributions to the bond energy shown immediately below. Only the positive eigenvalue NOCVs are shown, as the negative eigenvalue NOCVs have similar character.

NBO analysis on the small model identifies a σ bond for V–N_2 but not for Fe–N_2. Second-order perturbation analysis of the Kohn-Sham matrix in the NBO basis shows that back bonding, defined as the interaction between occupied -type NBO orbitals and unoccupied π^*-type NBO orbitals of N_2, is stronger for V than for Fe. Summing the contribution from orbitals with occupations greater than 0.8 electrons, the total back-bonding interaction is 32 kcal/mol for V–N_2 and 13 kcal/mol for Fe–N_2.

Given its predicted N_2/CH_4 separation capabilities rationalized above, we initiated efforts to synthesize V-MOF-74. To date, isolation of crystalline material, rather than amorphous powders (as determined by powder X-ray diffraction), has proven elusive, highlighting another MOF challenge: the need for a greater understanding of the mechanisms by which metal-organic frameworks form. The present computational results strongly motivate continued efforts to realize both of these goals.

4.1.4 Conclusions

We predict that dinitrogen separation from methane can be accomplished by the as-yet-unsynthesized V-MOF-74, because the vanadium ions in this MOF have their interaction energies significantly increased by π back bonding with N_2 but not with CH_4. This provides a new M-MOF-74 target as a challenge to synthesis. Our qualitative analysis is placed on a quantitative footing by a variety of density functional and wave function calculations of relative binfding energies using models validated against experimental binding energies for the analogous Fe-MOF-74. Density functional calculations are also analyzed to provide detailed insights into bonding distances, charge transfer, vibrational frequency shifts, and orbital interactions.

4.1.5 Additional Information

Supplementary information is available in the online version of the paper. The Supporting Information includes: Additional details about the calculations, references for basis sets, powder diffraction experimental data, and gas adsorption measurements. This material is available free of charge at `http://pubs.acs.org`. Correspondence and requests for materials should be addressed to J.R.L., J.B.N., B. S., C.J.C., D.G.T., and L. G. The authors declare no competing financial interests.

Acknowledgements

We gratefully acknowledge Xuefei Xu, Joshua Borycz, Rémi Maurice, Robert Berger, Roberta Poloni, James Phillips, and Pere Miró for helpful discussions. This research was supported by the U.S. Department of Energy, Office of Basic Energy Sciences, Division of Chemical Sciences, Geosciences, and Biosciences under award DE-FG02-12ER16362. Portions of this work were performed at the Molecular Foundry, supported by the Office of Science, Office of Basic Energy Sciences, of the U.S. Department of Energy under Contract No. DEAC02-05CH11231. Portions of the computations were performed using NERSC. W.C.I. is grateful for a Kenneth E. and Marion S. Owens Endowed Fellowship. A.L.D. is grateful for support through the Louise T. Dosdall Fellowship. M.R.H. acknowledges the NIST NRC Postdoctoral Fellowship research program for support. E.D.B. was supported by a Gerald K. Branch fellowship in chemistry. P.V. acknowledges a Phillips 66 Departmental Excellence Fellowship.

4.2 Reversible CO Binding Enables Tunable CO/H_2 and CO/N_2 Separations in Metal-Organic Frameworks with Exposed Divalent Metal Cations

Six metal-organic frameworks of the M_2(dobdc) (M = Mg, Mn, Fe, Co, Ni, Zn; $dobdc^{4-}$ = 2,5-dioxido-1,4-benzenedicarboxylate) structure type are demonstrated to bind carbon monoxide reversibly and at high capacity. Infrared spectra indicate that, upon coordination of CO to the divalent metal cations lining the pores within these frameworks, the C–O stretching frequency is blue-shifted, consistent with nonclassical metal-CO interactions. Structure determinations reveal M–CO distances ranging from 2.09(2) Å for M = Ni to 2.49(1) Å for M = Zn and M–C–O angles ranging from 161.2(7)° for M = Mg to 176.9(6)° for M = Fe. Electronic structure calculations employing density functional theory (DFT) resulted in good agreement with the trends apparent in the infrared spectra and crystal structures. These results represent the first crystallographically

Adapted with permission from E. D. Bloch, M. R. Hudson, J. A. Mason, S. Chavan, V. Crocellà, J. D. Howe, K. Lee, A. L. Dzubak, W. L. Queen, J. M. Zadrozny, S. J. Geier, L. -C. Lin, L. Gagliardi, B. Smit, J. B. Neaton, S. Bordiga, C. M. Brown, J. R. Long. *J. Am. Chem. Soc.* 2014, *136*, 10752.[335] **Additional information may be found in section 4.2.5.**

characterized magnesium and zinc carbonyl compounds and the first high-spin manganese(II), iron(II), cobalt(II), and nickel(II) carbonyl species. Adsorption isotherms indicate reversible adsorption, with capacities for the Fe, Co, and Ni frameworks approaching one CO per metal cation site at 1 bar, corresponding to loadings as high as 6.0 mmol/g and 157 cm^3/cm^3. The six frameworks display (negative) isosteric heats of CO adsorption ranging from 52.7 to 27.2 kJ/mol along the series Ni > Co > Fe > Mg > Mn > Zn, following the Irving-Williams stability order. The reversible CO binding suggests that these frameworks may be of utility for the separation of CO from various industrial gas mixtures, including CO/H_2 and CO/N_2. Selectivities determined from gas adsorption isotherm data using ideal adsorbed solution theory (IAST) over a range of gas compositions at 1 bar and 298 K indicate that all six M_2(dobdc) frameworks could potentially be used as solid adsorbents to replace current cryogenic distillation technologies, with the choice of M dictating adsorbent regeneration energy and the level of purity of the resulting gases.

4.2.1 Introduction

The coordination of carbon monoxide to transition metals has been rigorously investigated for over a century and has played an essential role in the development of our understanding of chemical bonding.[336,337] Since the original synthesis of $Pt(CO)_2Cl_2$, carbonyl complexes have been isolated and characterized for nearly every transition metal, in varying oxidation states and overall coordination numbers.[338,339,340] The vast majority of these species feature CO irreversibly bound to low-valent, low-spin transition metal centers that are able to engage in the metal-to-CO π-backbonding required for strong binding. For systems in which π-backbonding is absent or diminished, such as complexes containing d^0 or high-spin metals in higher oxidation states, carbonyl complexes remain elusive.[341,342] Here, we show that CO can reversibly bind to the coordinatively unsaturated M^{2+} cations lining the surfaces within the metal-organic frameworks M_2(dobdc) (M = Mg, Mn, Fe, Co, Ni, Zn; $dobdc^{4-}$ = 2,5-dioxido-1,4-benzenedicarboxylate), providing the first crystallographically characterized magnesium and zinc carbonyl compounds and the first high-spin manganese(II), iron(II), cobalt(II), and nickel(II) carbonyl species. Although high-spin metals with open coordination sites typically either reject CO binding or undergo a reduction in spin upon CO coordination,

the weak-field ligand dobdc^{4-} enforces a high-spin electron configuration for the M^{2+} centers in M_2(dobdc)[343] even in the presence of the strong-field ligand CO. Furthermore, the metal-organic framework lattice likely helps to maintain a high-spin state, as these materials would have to undergo significant structural changes to accommodate the smaller low-spin M^{2+} ions. As a result, these materials can be anticipated to display weak to moderate CO binding and complete reversibility, a property that could potentially be exploited for removing CO from various gas mixtures, enabling, for example, the energy-efficient separation of CO from H_2 at high capacities and various levels of purity.

Indeed, in addition to its fundamental significance, carbon monoxide has become an increasingly important chemical for the synthesis of a variety of chemical commodities, including many monomers and polymers, ethanol and other alcohols, and acetic acid. There are currently a number of competing technologies for its synthesis, the main products of which are carbon monoxide and hydrogen (syngas), typically present in H_2:CO ratios between 1 and 3.[344] To use carbon monoxide as a feedstock, the ratio must be reduced. Although energy-intensive cryogenic distillation is currently employed to separate these mixtures, a number of alternative methods, including membrane[345] and adsorptive separations,[346] have recently been investigated for use in the production of pure carbon monoxide. Given their high density of coordinatively unsaturated metal cation sites, metal-organic frameworks of the M_2(dobdc) structure type[347,348,349,350,351,352,353] hold considerable promise for the adsorptive separation of gas streams, including mixtures of CO_2/N_2,[352,354,355,356] CO_2/H_2,[357] O_2/N_2,[353] CH_4/N_2,[358] paraffins/olefins,[359,360,361,362,363] and stand poised for the separation of gas mixtures containing carbon monoxide.

4.2.2 Experimental Section

Sample Preparation

All reagents were obtained from commercial vendors and used without further purification. The compounds Mg_2(dobdc),[352] Fe_2(dobdc),[353] Mn_2(dobdc),[361] Co_2(dobdc),[352] Ni_2(dobdc),[352] and Zn_2(dobdc)[352] were synthesized according to previously published methods.

Adsoroption Isotherm Fitting

Prior to fitting all CO, N_2, and H_2 adsorption isotherms, experimentally measured excess adsorption (n_{ex}) values were converted to total adsorption (n_{tot}) using eq 4.2, with the total pore volumes (V_p; Table S1, Supporting Information) calculated from 77 K N_2 isotherms ($P/P_0 = 0.9$) and the bulk gas density (ρ_{bulk}) at each temperature and pressure obtained from the NIST Refprop database.[364,365,366]

$$n_{tot} = n_{ex} + V_p \cdot \rho_{bulk}\,(P,T) \tag{4.2}$$

Total adsorption isotherms for each M_2(dobdc) compound were then fit with either a single-, dual-, or triple-site Langmuir equation (eq 4.3), where n is the total amount adsorbed in mmol/g, P is the pressure in bar, n_{sat},i is the saturation capacity in mmol/g, and b_i is the Langmuir parameter in bar^{-1} for up to three sites 1, 2 and 3.

$$n = \frac{n_{sat,1}\, b_1\, P}{1 + b_1 P} + \frac{n_{sat,2}\, b_2\, P}{1 + b_2 P} + \frac{n_{sat,3}\, b_3\, P}{1 + b_3 P} \tag{4.3}$$

$$b_i = \exp\left(-S_i/R\right) \exp\left(E_i \cdot 1000/RT\right) \tag{4.4}$$

The Langmuir parameter can be expressed using eq 4.4, where S_i is the site-specific molar entropy of adsorption in J/mol·K, E_i is the site-specific binding energy in kJ/mol, R is the gas constant in J/mol·K, and T is the temperature in K. The fitted parameters for CO and N_2 or H_2 adsorption can be found in Tables S2 and S3 (Supporting Information), respectively. Plots of the total adsorption isotherms with the corresponding single-, dual-, or triple-site Langmuir fits can be found in Figures S1-S6 (Supporting Information). Note that the CO adsorption isotherm data at 25, 35, and 45 °C were fit simultaneously for each material with a single set of parameters.

Isosteric Heat of Adsorption Calculations

Using the single-, dual-, and triple-site Langmuir fits, the isosteric heat of adsorption, -Q_{st}, was calculated for each compound as a function of the total amount of CO adsorbed using the Clausius-Clapeyron relation (eq 4.5).

$$-Q_{st} = RT^2 \left(\frac{\partial \ln P}{\partial T}\right)_n \tag{4.5}$$

where R is the ideal gas constant, P is the pressure, and T is the temperature.

Note that the isosteric heat of adsorption for a single-site Langmuir model is constant by definition. For dual- and triple-site Langmuir models, however, it is necessary to calculate the loading dependence of the isosteric heat of adsorption. As written, dual- and triple-site Langmuir equations specify the amount adsorbed as a function of pressure, while the pressure as a function of the amount adsorbed is needed to use the Clausius-Clapeyron relation. To calculate the isosteric heat of adsorption for evenly spaced loadings, each dual- and triple-site Langmuir equation was solved for the pressures that correspond to specific loadings at 25, 35, and 45 °C, and these calculated pressures were then used in eq 4.5 to determine the heat of adsorption as a function of the total amount of CO adsorbed. Note that the isosteric heat of adsorption is only reported over the CO loading range that was experimentally measured and mathematically fit for each compound.

Ideal Adsorbed Solution Theory Calculations

Since binary gas adsorption isotherms cannot be measured in a straightforward manner, it is often necessary to use an adsorption model, such as ideal adsorbed solution theory (IAST),[367] to predict mixed gas behavior from experimentally measured single-component isotherms. The accuracy of the IAST procedure has already been established for adsorption of a wide variety of different gases in zeolites and metal-organic frameworks.[360,368,369,370] Here, IAST is used to estimate the selectivity, S_{ads}, of all M_2(dobdc) analogues for mixtures of CO and H_2 at 25 °C and a total pressure of 1 bar. Note that the selectivity factor, S, is defined according to eq 4.6, where n_i is the amount adsorbed of each component as determined from IAST and xi is the mole fraction of each component in the gas phase at equilibrium.

$$S = \frac{n_{\text{CO}}/n_{\text{H}_2}}{X_{\text{CO}}/X_{\text{H}_2}} \tag{4.6}$$

It is important to note that calculated IAST selectivities are highly dependent on the adsorption model used to describe the single-component isotherm data. Specifically, isotherm fits at low pressures are most important for the strongest adsorbing component of a mixture (CO), while isotherms fits at high pressures are most important for the weakest adsorbing component (H_2). Here, the CO adsorption isotherms are very well

described by single-, dual-, and triple-site Langmuir models for all M_2(dobdc) frameworks, including in the steep low-pressure region of the isotherm (Figure S7, Supporting Information).

When fitting the H_2 isotherm data with Langmuir models, it is insufficient to consider just low-pressure adsorption, as was done for CO, even though the IAST calculations are performed at a total pressure of only 1 bar. This is because integrating the pure-component H_2 isotherms to calculate spreading pressure requires extrapolation to very high pressures. For instance, the IAST selectivity calculation for a 50:50 mixture of CO:H_2 in Fe_2(dobdc) at 1 bar and 25 °C involves integrating the pure-component CO and H_2 isotherms up to 0.501 and 254 bar, respectively. As a result, the IAST selectivity is particularly sensitive to the H_2 saturation capacity, n_{sat}, of the Langmuir model. Since estimating the saturation capacity of H_2 from low-pressure isotherm data is difficult, high-pressure H_2 isotherms for Ni_2(dobdc) and Mg_2(dobdc) at 25 °C were used to estimate the high-pressure H_2 loadings when performing all isotherm fits. Note that the high-pressure H_2 data for Mg_2(dobdc) was previously reported,[371] while the high-pressure H_2 isotherm for Ni_2(dobdc) was measured in this work. While the IAST selectivities are sensitive to the fitted H_2 saturation capacity, this sensitivity does not significantly affect the overall magnitude of the calculated selectivity factor or of the trends between different M_2(dobdc) frameworks. This was confirmed by fitting the H_2 isotherm data for Ni_2(dobdc), Fe_2(dobdc), and Mg_2(dobdc) with a range of plausible H_2 saturation capacities and performing IAST calculations (Figure S8, Supporting Information).

High-Pressure Gas Adsorption

The high-pressure H_2 adsorption isotherm for Ni_2(dobdc) was measured on a HPVA-II-100 from Particulate Systems, a Micromeritics company. A detailed discussion of the accuracy of high-pressure measurements on this instrument was previously reported.[372] Here, 0.43 g of activated sample was loaded into a tared 2 mL stainless steel sample holder inside a glovebox under an N_2 atmosphere. Prior to connecting the sample holder to the VCR fittings of the complete high-pressure assembly inside the glovebox, the sample holder was weighed to determine the sample mass. The fully assembled sample holder was transferred to an ASAP 2020 low-pressure adsorption instrument,

fitted with an isothermal jacket, and evacuated at the original activation temperature of the material for at least 1 h. Then, an N_2 adsorption isotherm was measured at 77 K. This data was used to verify that the high-pressure sample mass was correct and the sample was still of high quality by comparing the resulting Langmuir surface area to the expected. Note that a specially designed OCR adapter was used to connect the stainless steel high-pressure adsorption cell directly to the ASAP 2020 analysis port, allowing the measurement of accurate low-pressure isotherms on the exact same samples used for high-pressure measurements in the same sample holders. Prior to measuring Ni_2(dobdc), H_2 background measurements were performed at 25 °C on a sample holder containing nonporous glass beads that occupied a similar volume as a typical sample. A small positive background was observed, which may be due to errors in volume calibrations, temperature calibrations, and/or the equation of state used to perform the nonideality corrections. Regardless, the background H_2 adsorption was consistent across several measurements and was well described by a third order polynomial (Figure S9, Supporting Information). This polynomial was then used to perform a background subtraction on the raw high-pressure H_2 data for Ni_2(dobdc).

Infrared Spectroscopy

FTIR spectra were collected in transmission mode on a self-supported wafer of sample, in a controlled atmosphere using a custom-built infrared cell. The spectra were recorded at 2 cm^{-1} resolution on a Bruker IFS 66 FTIR spectrometer, equipped with a MCT detector. Adsorption and desorption of CO were followed at 77 K.

Mössbauer Spectroscopy

Mössbauer spectra of Fe_2(dobdc)·CO were measured at various temperatures between 20 and 275 K with a constant acceleration spectrometer, which utilized a rhodium matrix cobalt-57 source and was calibrated with α-iron foil. The absorber contained 55(1) mg/cm2 of powder mixed with boron nitride. The absorber was prepared in an N_2-filled glovebox and placed in a Schlenk flask. The flask was removed from the glovebox, evacuated, and filled with CO. The sample was then cooled to 77 K with liquid nitrogen and inserted into a precooled cryostat under dry helium.

Magnetic Susceptibility

Magnetic data were collected using a Quantum Design MPMS-XL SQUID magnetometer. Measurements on Fe_2(dobdc) were obtained with finely ground microcrystalline powders restrained with a plug of glass wool within a sealed quartz tube. No effects of crystallite torqueing were observed. Preparation of the CO-loaded sample was accomplished by attaching a sample of pure Fe_2(dobdc), loaded in a quartz tube, to a Micromeritics ASAP 2020 Surface Area and Porosity Analyzer. The pressure of the atmosphere of CO gas in the sample tube was then adjusted to 1 bar, the tube cooled in liquid N_2, and sealed with a hydrogen flame. Dc susceptibility measurements were collected in the temperature range of 2-300 K under a dc field of 1000 Oe. To avoid possible effects due to flash-freezing of the samples and sealed gas, the samples were cooled slowly from 300 to 2 K during the course of the measurement. Dc magnetic susceptibility data were corrected for diamagnetic contributions from the sample holder and glass wool, as well as for the core diamagnetism of each sample (estimated using Pascals constants).[373]

Neutron Powder Diffraction

Neutron powder diffraction (NPD) experiments were carried out on activated M_2(dobdc) samples (M = Co, Fe, Mg, Mn, Ni, Zn) using the high-resolution neutron powder diffractometer, BT1, at the National Institute of Standards and Technology Center for Neutron Research (NCNR). The samples were placed in a He purged glovebox and 0.9702, 0.7286, 1.0010, 0.8576, 1.078, and 1.0761 g Co_2(dobdc), Fe_2(dobdc), Mg_2(dobdc), Mn_2(dobdc), Ni_2(dobdc), and Zn_2(dobdc), respectively, loaded into vanadium sample cans equipped with a gas loading valve, and sealed using an indium O-ring. NPD data were collected using a Ge(311) monochromator with an in-pile 60' collimator corresponding to a wavelength of 2.078 Å. The samples were connected to a gas-manifold of known volume and exposed to a known dose of approximately 0.75 CO molecules per M^{2+} at 298 K (refined composition given in Tables S5-S12, Supporting Information). After equilibration times on the order of a hour, the sample cells were then placed in a dry ice bath to fully adsorb any residual CO, if any, as determined by a zero pressure reading on a pressure gauge and then allowed to equilibrate for another hour. The samples were sealed and

allowed to further equilibrate at room temperature for several hours before loading onto a bottom-loading closed cycle refrigerator and slow cooling, to ensure full equilibration and complete adsorption, to 10 K for the data collection. In the case of Fe_2(dobdc), two subsequent gas doses, 1.5 and 2.0 CO per Fe^{2+}, were considered for comparability with our previous adsorption studies on this system, heating the sample in-line to 298 and 250 K, respectively, before dosing additional CO to ensure that the dose occurred above the temperature of the previous full equilibration and then slowly cooling to 10 K for data collection.[360,361]

NPD data were analyzed using the Rietveld method as implemented in EXPGUI / GSAS.[374,375] Starting models for the activated M_2(dobdc) frameworks were taken from our previous data on the bare materials and the atomic positions and isotropic atomic displacement parameters (ADPs) were left free to refine during the analysis process.[351,360,361,376] Fourier difference methods were employed to locate the adsorbed CO molecules. A dose of 0.75 CO per M^{2+} was chosen to provide clarity in the structure model for the active site in eliminating potential CO intermolecular interactions based on previous knowledge of adsorption in M_2(dobdc). In each instance, the CO atomic coordinates and isotropic ADPs were left free to refine, as was the occupancy of both the carbon and oxygen atoms. The carbon and oxygen atoms refined to identical occupancies within one standard deviation; however, these values were eventually constrained to be identical in each case for consistency. For all samples, the refined CO bond distance was equivalent to the accepted value for carbon monoxide within error; however, in the cases of Mn_2(dobdc) and Zn_2(dobdc), the value trended too long and was restrained to the ideal case, while in Co_2(dobdc), the distance trended too short and was also restrained to the ideal value. As per the structural discussion in the text, the result was a metal-carbonyl interaction via the carbon (M^{2+}–CO). In particular for the Mg_2(dobdc), but in several instances, the model was refined with the reverse orientation of the carbon monoxide (i.e., Mg–OC) and attempts to freely refine the CO in this orientation resulted in a very low occupancy for the carbon (with a negative isotropic ADP) and a very high occupancy for the oxygen atom (and very large isotropic ADP), as the model attempted to fit the available excess scattering density almost entirely through the presence of the lone oxygen. This indicates the metal-carbonyl interaction is via the carbon with no possibility of a reverse conformation. The additional CO

molecules in the refinement of the 1.5 and 2.0 CO per Fe^{2+} NPD data were refined with constrained C and O occupancies and bond distances, and free isotropic ADPs. The 1.5 CO per Fe^{2+} shows an additional adsorption site in the channels of the framework in a similar location as determined for the secondary physisorption oxygen site, but at a perpendicular geometry to O_2.[344] The third CO adsorption site, observed in the 2.0 CO dose, refines to a location in the very central portion of the channel furthest from the framework. This was modeled with very large isotropic ADPs indicative of a large positional disorder and potential condensation of CO in the channels at very high CO loadings.

Density Functional Theory Calculations

To study CO adsorption in M_2(dobdc) systems from first-principles, we used density functional theory within the generalized gradient approximation of Perdew, Burke, and Ernzerhof (PBE)[377] and a van der Waals dispersion-corrected functional.[378] The VASP program package[379] with a planewave basis set and projector augmented wave[380] pseudopotentials was used for all calculations. A Hubbard-like U parameter[381,382] was employed to better treat the localized d-states of the transition metal centers. We used an energy cutoff of 1000 eV for the planewave basis set and Brillouin zone sampling at the Γ-point, leading to binding energies that converged to within 1 kJ/mol. To generate binding enthalpies, we first optimized periodic M_2(dobdc) crystals in a triclinic primitive unit cell of 54 atoms using a PBE+U approach, beginning from the experimental Zn_2(dobdc) structure and substituting in other divalent $3d$ transition metal cations (Mg, Mn, Fe, Co, and Ni) at all metal sites, until the residual forces were smaller than 0.01 eV/Å and the stress tensor components were smaller than 0.2 kbar. The computed lattice parameters are all within 2% of the experimental results. For open-shell cations, we employ Hubbard-like U corrections. Values of U used were 4.0, 4.0, 3.3, and 6.4 eV for Mn, Fe, Co, and Ni, respectively; these values were taken from Wang *et al.*,[383] where they were determined for each metal center to reproduce the experimental oxidation energy of the metal-monoxide to M_2O_3. For all M_2(dobdc) compounds, we found a high-spin ground state, and then assumed ferromagnetic ordering along the metal-oxide chain direction and antiferromagnetic ordering between the chains, as observed experimentally for the ground state magnetic ordering within Fe_2(dobdc).[384]

To predict adsorption geometries, molecules were relaxed inside M_2(dobdc) rigid periodic frameworks using vdW-DF2+U from Lee *et al.*[378] at a loading of one molecule per six metal sites. vdW-DF2 was shown in previous work to provide excellent binding energetics for CO_2 adsorption in M_2(dobdc) systems.[385] vdW-DF2+U was also used in single-point calculations to compute the energies of the bare M_2(dobdc) compounds for use in calculating binding enthalpies.

Binding enthalpies at 308 K were calculated by including quantum zero-point energies (ZPEs) and finite-temperature thermal energies (TEs) at the level of a harmonic approximation. The enthalpy of adsorption of a molecule in a MOF is calculated as

$$-\Delta H = H\,(\mathrm{CO} + \mathrm{MOF}) - H\,(\mathrm{CO}) - H\,(MOF) \tag{4.7}$$

where H(MOF), H(CO), and H(CO + MOF) are the enthalpies of the bare MOF without CO, the enthalpy of CO in the gas phase, and the enthalpy of the MOF with CO adsorbed, respectively.

ETS-NOCV Analysis

Cluster models were cropped from the experimental crystal structures, as shown in Figure S23 (Supporting Information). This model was designed[386] to retain the local structure of framework about the central metal ion while remaining small enough for the electronic structure calculations. For M = Mn, Fe, Co, Ni, the two exterior metal sites were substituted by closed shell Zn^{II} centers while the central metal that binds the CO remained in its high-spin (ground) state. Hydrogen atoms were used to cap the truncated cluster model.

Constrained geometry optimizations were performed where the experimental framework and CO were held fixed while the capping H atoms from the cluster truncation were relaxed. The PBE functional[387] was used in the TURBOMOLE V6.4 2012[388] software package. Resolution of the identity (RI)[389,390] and associated auxiliary basis functions[391,392,393] were employed. The def2[394] basis sets were used. For metal, oxygen, and the binding CO the def2-TZVP basis set was used, while for all C and H the def2-SVP basis set was used.

Bond Analysis

The extended transition state (ETS) method for energy decomposition, combined with the natural orbitals for chemical valence (NOCV) theory (ETS-NOCV)[395] was used to decompose the metal-CO bond into different components (e.g. σ, π) and evaluate the magnitudes of their contributions to the total bond energy. This analysis was performed with the Amsterdam Density Functional (ADF) version 2013 software package.[396,397,398] The M06-L functional[399] was used with the DZP basis set and an increased integration grid of 8. The zeroth order regular approximation (ZORA) was used to treat relativistic effects.

4.2.3 Results and Discussion

Infrared Spectroscopy

As an initial probe of the interaction of CO with the square pyramidal M^{2+} cations lining the 12-Å wide channels in M_2(dobdc), we turned to in situ infrared spectroscopy (Figure 4.5.[400] For all six frameworks, a single adsorption band is observed at low coverage between 2160 and 2178 cm^{-1},[401,402,403] which is blue-shifted with respect to the stretching mode of free CO (2143 cm^{-1})[401,402,403] (see the Supporting Information for further details on the infrared spectra). These values are consistent with those previously reported for M^{2+} ions in weak ligand field environments.[341,342] Most metal-CO interactions feature a synergistic interaction between σ charge donation and π back-donation.[404,405] For classical transition metal carbonyl complexes, the average ν(CO) is red-shifted, because the M $\rightarrow$ CO π back-donation is the dominant effect, significantly weakening the C–O bond compared to that of free CO. When back-donation is absent or diminished, ν(CO) is blue-shifted in a phenomenon that is termed nonclassical CO adsorption. Of the more than 20,000 reported M–CO stretching frequencies, only approximately 250-300 can be considered nonclassical.[342]

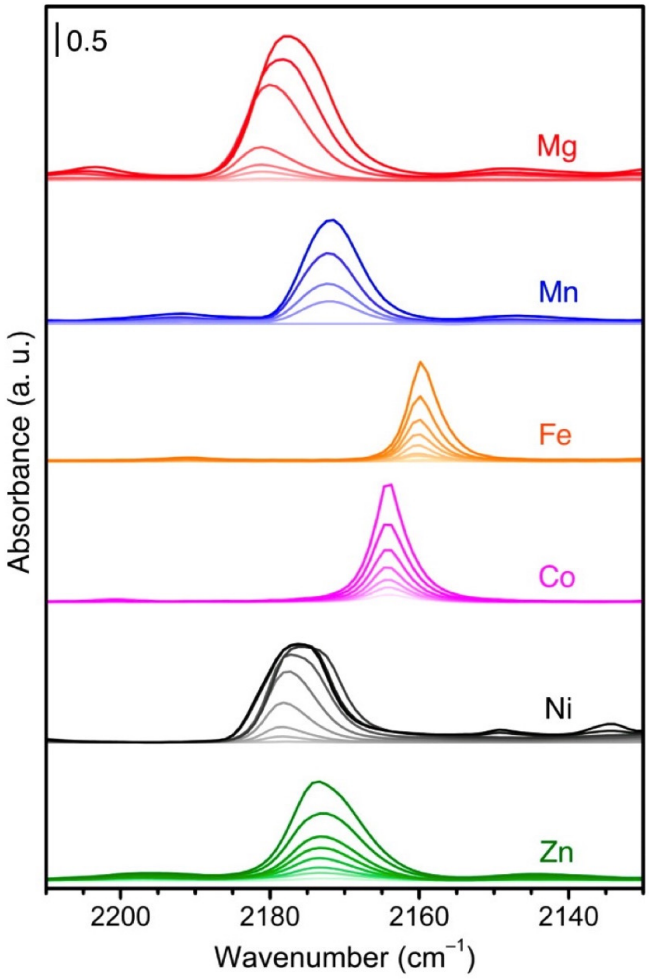

Figure 4.5: Background subtracted FTIR spectra of M_2(dobdc) collected at 77 K in the presence of CO. Light to dark lines represent increasing CO coverages on samples preactivated at 453 K. The C–O stretching frequencies for all six metals are blue-shifted with respect to free CO (2143 cm^{-1}).

Of the six materials investigated, carbonyl coordination is most simply described within Mg_2(dobdc) and Zn_2(dobdc). The Mg^{2+} ions in the former lack d electrons and are thus unable to back-donate into the empty CO π^* orbitals. Additionally, the empty Mg $3d$ levels are high in energy and do not provide a good match for σ donation from the lone pair electrons of CO. The Mg^{2+}–CO interaction is thus primarily electrostatic in

nature, an effected that is expected to increase the C–O stretching frequency as the CO bonding orbitals become less polarized toward the more electronegative oxygen and thus more covalent.[406] As a result, Mg_2(dobdc) displays the highest-energy infrared stretch of 2178 cm^{-1}, consistent with those reported for CO adsorption in Mg^{2+}-exchanged zeolites.[407] On the other hand, the Zn^{2+} ions in Zn_2(dobdc) have a fully occupied set of 3*d* orbitals that are therefore not available to accept σ donation from CO, resulting in a similarly high infrared stretch of 2173 cm^{-1}. In both cases, the metal-carbonyl interaction is primarily a result of ion-induced dipole interactions. Similar behavior is observed in the case of Mn_2(dobdc), in which the ν(CO) of 2172 cm^{-1} is red-shifted with respect to Mg_2(dobdc), as a result of diminished polarization by the larger-radius, softer Mn^{2+} ions and presumably only a very small, nearly negligible π backbonding contribution. The metal ions in both Fe_2(dobdc) and Co_2(dobdc) are smaller and more polarizing than Mn^{2+}; however, the C–O stretching frequencies displayed by these materials (2160 cm^{-1} for Fe2+ and 2164 cm^{-1} for Co2+) are the lowest reported here, suggesting slightly more pronounced π interactions. The compound Ni_2(dobdc) displays the highest CO stretching frequency among the transition metal cations (2178 cm^{-1}), since Ni^{2+} is the smallest and most polarizing ion. Given the small, charge-dense nature of Ni^{2+}, its lower energy π-type 3*d* orbitals are less well-suited for back-donation into CO than either Fe^{2+} or Co^{2+}.

Structural Characterization

Given our prior success in elucidating crystal structures of a number of adsorbent molecules in M_2(dobdc),[353,360,361] we turned to neutron powder diffraction experiments to further characterize the carbonyl adducts M_2(dobdc)·1.5CO (Figure 4.6). Consistent with the large range in CO infrared stretching frequencies, we see a range of M–C–O angles, from 161.2(7)° for Zn to 176.9(6)° for Fe, in excellent agreement with previous calculations on the Mg, Ni, and Zn analogues,[408] and with a good correlation observed between ν(CO) and the M–C–O angle (Figure 4.7). In the cases of the Fe and Co homologues, where a greater degree of π backbonding is observed via infrared spectroscopy, more linear carbonyl adducts are formed, while in the cases where electrostatic effects play a major role, bent structures are observed. Additionally, the structures display a large range in M–C bond distances, ranging from 2.09(2) Å for Ni to 2.49(1) Å for Zn,

with an excellent correlation between adsorption enthalpy and M–C distance (Figure 4.7). The Mn, Fe, Co, and Ni frameworks bind CO with M–CO distances of 2.44(2), 2.27(2), 2.18(2) and 2.09(2) Å, respectively, a trend that is consistent with the Irving-Williams stability order. The value for Ni is in good agreement with what was previously found from EXAFS data and *ab initio* molecular modeling.[409]

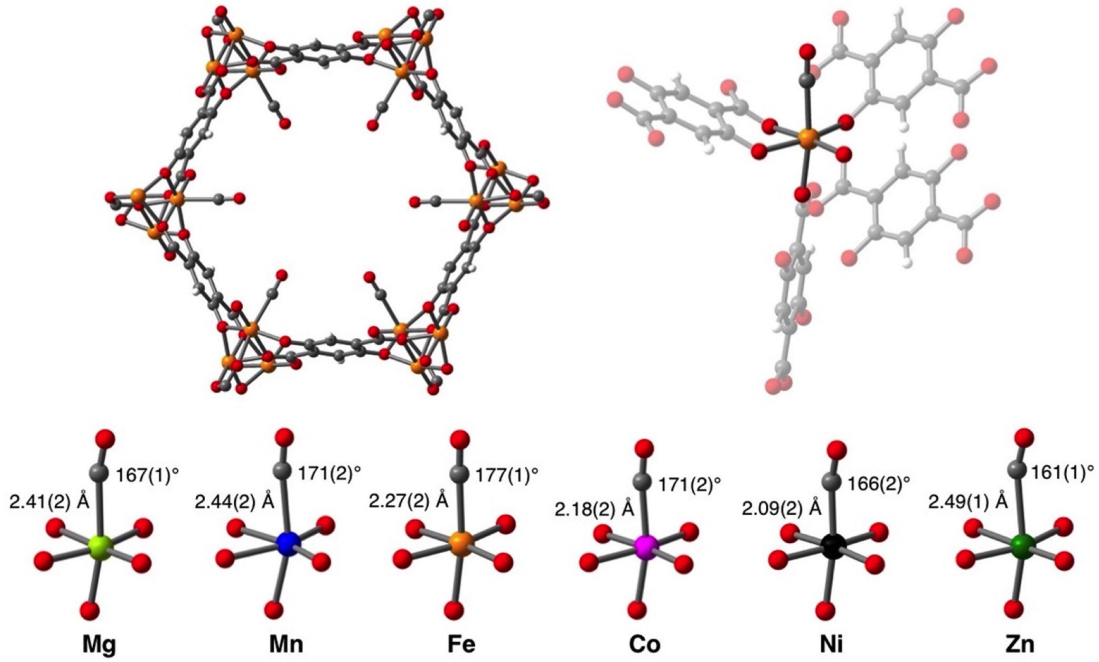

Figure 4.6: Structures from powder neutron diffraction. (Upper left) A view down a channel (along the c axis) in the structure of Fe_2(dobdc)·1.5CO, as determined by Rietveld analysis of powder neutron diffraction data. At this loading, the occupancy of the metal-bound CO molecules are all close to the expected value of 75%. (Upper right) Coordination environment for a single Fe^{2+} site in Fe_2(dobdc)·1.5CO. (Lower) First coordination sphere for the M^{2+} ions in M_2(dobdc)·1.5CO, with M–CO distances and M–C–O angles indicated.

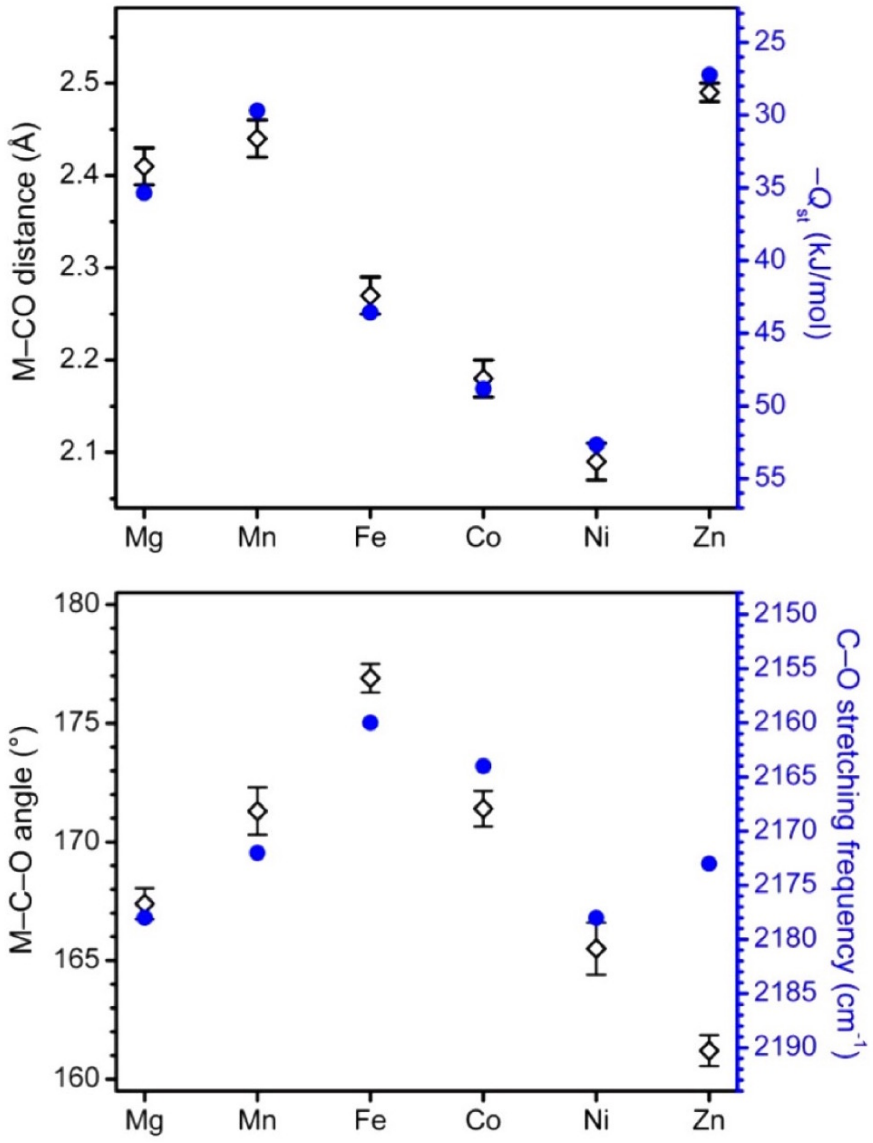

Figure 4.7: (Upper) Variations of M–C–O angle (open black diamonds) and C–O stretching frequency (blue circles) with metal center in M_2(dobdc), indicating the correlation between greater backbonding and a more linear metal-carbonyl adduct. (Lower) Variations of M–CO distance (open black diamonds) and isosteric heat of CO adsorption (Q_{st}, blue circles) with metal center in M_2(dobdc). Error bars indicate the estimated standard deviations from the crystal structure refinements.

Overall, these distances are much longer than those typically found for divalent first-row transition metal carbonyl complexes, which rarely exceed 2.0 Å.[341,342] Divalent manganese carbonyl complexes, often generated by the chemical[410,411] or electrochemical[412] one-electron oxidation of analogous manganese(I) complexes, are low-spin and feature Mn–C distances below 1.9 Å. A number of iron(II)-carbonyl species obtained by the binding of CO to coordinatively unsaturated iron cations of various overall coordination numbers have been isolated.[343] In all but three cases, the iron cations in these molecules are diamagnetic upon CO coordination and display Fe–C distances of 1.75 to 1.90 Å. Both nickel(II)- and cobalt(II)-carbonyl are similarly rare and feature low-spin metal cations and short M–C distances.[413,414,415,416,417,418,419] The unusually long M–C distances observed here are a result of the weak field oxo-donors of $dobdc^{4-}$ and the framework lattice enforcing an unprecedented high-spin configuration for each of these metals in the presence of CO. Furthermore, $Mg_2(dobdc)\cdot 1.5CO$ and $Zn_2(dobdc)\cdot 1.5CO$, with M–CO distances of 2.41(2) and 2.49(1) Å, respectively, represent the first crystallographically characterized magnesium and zinc carbonyl complexes, regardless of oxidation state.[407,420]

Spin-State Characterization

Magnetic susceptibility data were collected to confirm the high-spin character of the iron(II) centers in the CO-adsorbed phase $Fe_2(dobdc)\cdot 2CO$. At 300 K, the value of $\chi_M T$ for $Fe_2(dobdc)$ is 6.40 cm^3 K/mol, slightly higher than that expected (6.00 cm^3 K/mol) for two high-spin ($S = 2$) iron(II) centers with g = 2.00.[360] As the temperature is lowered, $\chi_M T$ gradually increases, reaching 7.88 cm^3 K/mol at 28 K, before dropping to 1.01 cm^3 K/mol at 2 K. In contrast, when dosed with carbon monoxide gas, $Fe_2(dobdc)\cdot 2CO$ displays a monotonic decrease in $\chi_M T$ with lowering temperature, falling from 6.49 cm^3 K/mol at 300 K (consistent with high-spin iron(II)) to 0.39 cm^3 K/mol at 2 K. The arrangement of metal ions in $Fe_2(dobdc)$ suggests two dominant magnetic interactions: magnetic coupling between ions along each chain and coupling between ions belonging to different chains. The Fisher model[421] was employed with a molecular field approximation[422] to fit the data and extract the relative strengths of these interactions for $Fe_2(dobdc)\cdot 2CO$, as has been done in previous work.[423] The

specific Hamiltonian used is represented as eq 4.8.

$$\hat{H} = -2J \sum_i \mathbf{S}_{\mathrm{Fe}(i)} \mathbf{S}_{\mathrm{Fe}(i+1)} - M\mathbf{B} \sum_i \mathbf{S}_{\mathrm{Fe}(i)} - zJ' \langle S_{\mathrm{Fe}} \rangle \mathbf{S}_{\mathrm{Fe}} \tag{4.8}$$

In eq 4.8, J is the intrachain Fe–Fe superexchange coupling constant, and $\mathbf{S}_{\mathrm{Fe}(i)}$ and $\mathbf{S}_{\mathrm{Fe}(i+1)}$ are the spin operators for the iron ions of the chain. $M\mathbf{S}_{\mathrm{Fe}(i)}$ corresponds to the magnetic moment of the Fe(i) spin, $\mathbf{B}$ is the applied field, z the number of interacting nearest-neighbors, J' the interchain coupling constant, and $\langle S_{\mathrm{Fe}} \rangle$ the mean value of the S_z component of the S_{Fe} operator. In this model, a positive sign for J and J' indicates a ferromagnetic interaction while a negative sign indicates an antiferromagnetic interaction. The best fits for Fe_2(dobdc)·2CO yielded J = -1.6(2) cm^{-1} and J' = -1.12(2) cm^{-1}, in contrast to J = -4.12(6) cm^{-1} and J' = -1.12(1) cm^{-1} for the bare framework (Figure S21, Supporting Information). Note that zero-field splitting was not accounted for with this analysis but could be substantial.[424] Previous work on the magnetic susceptibility of Fe_2(dobdc) in the presence of gases revealed a strong correlation between gas-binding strength and intrachain magnetic coupling.[360] Weakly binding gases weakened the magnitude of J but retained the sign. In contrast, strongly binding gases served to change the electron density around the iron(II) ions enough to invert the intrachain coupling from ferro- to antiferromagnetic in nature. As seen for Fe_2(dobdc)·2CO, $\chi_M T$ plots of the framework under strongly binding gases are thus devoid of any maximum at low temperatures.

Mössbauer spectra further confirm the assignments of high-spin iron(II) (Figure S22, Supporting Information). In the absence of CO, the spectra of Fe_2(dobdc) feature a simple quadrupole doublet, which at 40 K exhibits an isomer shift of 1.094(3) mm/s and a quadrupole splitting of 2.02(1) mm/s. In the presence of CO, these values shift slightly to 1.198(5) and 2.60(1) mm/s, respectively, consistent with high-spin iron(II) in an octahedral coordination environment. The result for Fe_2(dobdc)·2CO is without precedent. Of the nearly 9,000 iron-carbonyl structures reported in the Cambridge Crystal Structure Database, only three are paramagnetic, all featuring intermediate-spin ($S = 1$) iron(II) centers in a trigonal bipyramidal coordination environment, for which an $S = 0$ spin state is generally not possible.[425,426,427] Thus, Fe_2(dobdc)·2CO represents the first example of a paramagnetic octahedral iron carbonyl compound and, to our knowledge, the first reported $S = 2$ iron carbonyl.

Electronic Structure Calculations

Density functional theory calculations (vdW-DF2+U) were employed to explore CO binding from first principles. To account for distortions in the framework structure upon binding, CO-metal distances were fixed as predicted by the vdW-DF2+U calculation and a subsequent relaxation of the MOF+CO system was performed at the PBE+U level. A final relaxation of CO in the rigid but distorted MOF was then performed at the vdW-DF2+U level. This procedure leads to good agreement for both local adsorption geometries (which are well described with vdW-DF2+U) and lattice parameters (which are better described by PBE+U). As shown in Figure 4.8, we see excellent agreement between predicted and experimental values for a number of metrics. Specifically, DFT predicts blue-shifted CO stretching frequencies upon coordination to all six frameworks, with Fe_2(dobdc) displaying the least blue-shifted value. Accordingly, DFT also predicts a wide range of M–C–O angles. Although the calculated M–CO distances are slightly overestimated, from 0.12 Å for Mg to 0.27 Å for Ni, a known tendency of the vdW-DF2 functional, the trend in binding distance is captured quite accurately. Importantly, DFT predicts the Mn, Fe, Co, and Ni frameworks to have a high-spin ground state, which is maintained upon CO coordination. The accuracy of these DFT calculations is quite important as it can be extended to metal-organic frameworks for which synthetic conditions have yet to be realized.[358]

We also utilized electronic structure calculations to investigate the relative strength of the metalCO π^* back-donation by using the extended transition state (ETS) method, in combination with natural orbitals for chemical valence (NOCV) theory. The resulting contours are plotted in Figure S23 (Supporting Information). The largest eigenvalues that have π^* CO character are shown, along with the magnitude of their ΔE_{orb} contributions. The purpose of this decomposition is to gain a qualitative interpretation of the nature of this bond for M = Mn, Fe, Co, and Ni between two predefined fragments. In this case, fragment 1 (F1) was chosen to be the model cluster of the M_2(dobdc), and fragment 2 (F2) was chosen to be CO. From performing calculations on the two isolated fragments (in their complexed geometry) and then performing a calculation on the complex, a deformation density is calculated. This may then be partitioned into the NOCVs, which have just a few significant contributors to the bond. The sums of these

ΔE_{orb} terms involving CO π^* orbitals are reported in Table S13 (Supporting Information). In agreement with the interpretation of the infrared spectra, iron displays the strongest π back-bonding contribution, with Fe > Co > Ni $\gg$ Mn. A comparison of the relative energy contributions for σ- and π-type interactions reveals that back-bonding is the more important orbital interaction. As examples, the canonical molecular orbital with the largest contribution to CO binding in Fe_2(dobdc) is plotted in Figure 4.9. Bond analysis indicates that Fe $\rightarrow$ CO π back-donation accounts for approximately 70% of the orbital interaction energy. The same trend is found for Mn, Co, and Ni, and is expected as d_z^2 is singly occupied when these ions are in a high-spin octahedral coordination environment and thus poorly suited for CO $\rightarrow$ M σ donation.

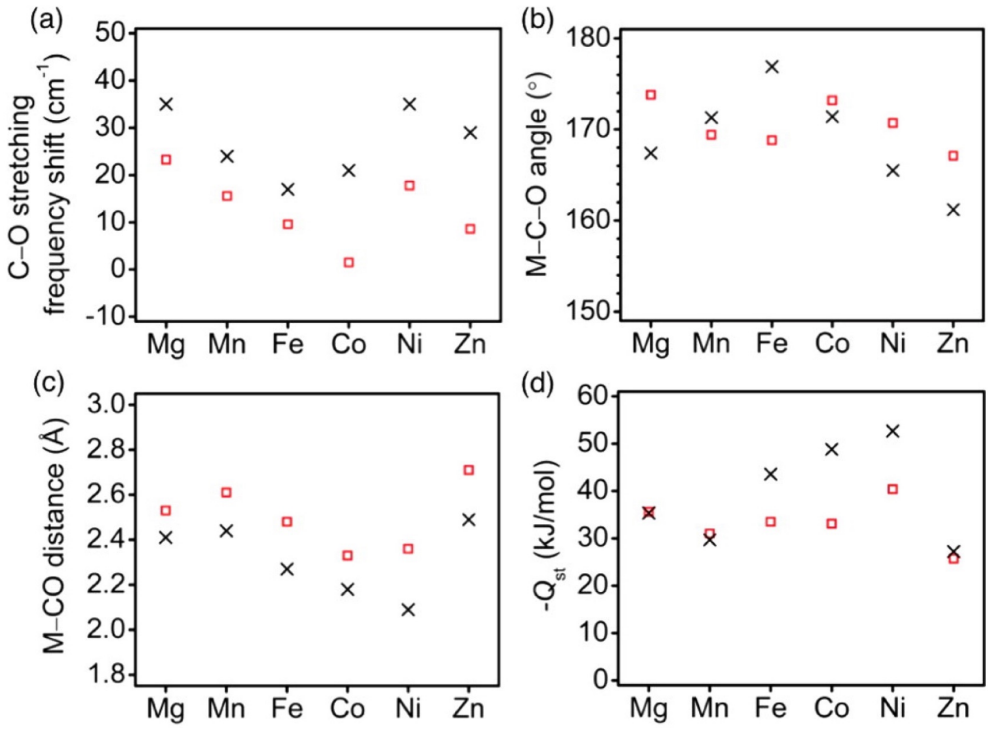

Figure 4.8: DFT calculated C–O stretching frequency shift relative to free isolated CO (upper left), M–C–O angle (upper right), M–CO distance (lower left), and binding enthalpy (lower right) in M_2(dobdc) in comparison to experimental values (black cross marks).

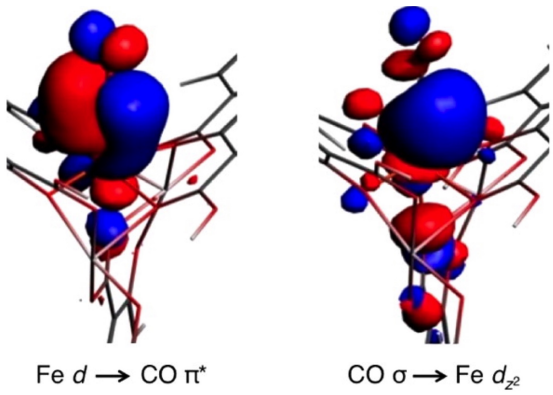

Figure 4.9: Contours of orbitals involved in CO binding in Fe_2(dobdc).

Gas Adsorption

To investigate the CO uptake within these frameworks under various conditions, pure component adsorption isotherms were measured at 298, 308, and 318 K, and isosteric heats of adsorption were calculated for each metal (Figure 4.10, Table 4.4). At 298 K, the CO adsorption isotherms for the Fe, Co and Ni frameworks approach the value expected for one CO molecule per open metal site. The loading capacities for these materials, which climb as high as 6.0 mmol/g and 156.8 cm^3/cm^3 for Fe_2(dobdc) at 298 K and 1.2 bar, are much greater than typically observed in metal-organic frameworks, a result of the high gravimetric density of open metal sites in the structures. Importantly, in all cases, the bound CO could be completely desorbed upon application of dynamic vacuum and/or heat, and subsequent CO adsorption isotherms showed no loss of uptake capacity. The isosteric heats of adsorption calculated from the data vary widely with metal, from -52.7 to -27.2 kJ/mol, with the CO binding strength following the order Ni > Co > Fe > Mg > Mn > Zn (Figure 4.10). The trend is in distinct contrast to that observed for CO_2 adsorption in these materials, an interaction that is predominately electrostatic in nature, where the Mg framework displays the highest binding enthalpy.[362,363] This suggests, as discussed above, that the coordination of carbon monoxide is not purely a result of electrostatics, but indeed involves some σ and π orbital interactions.

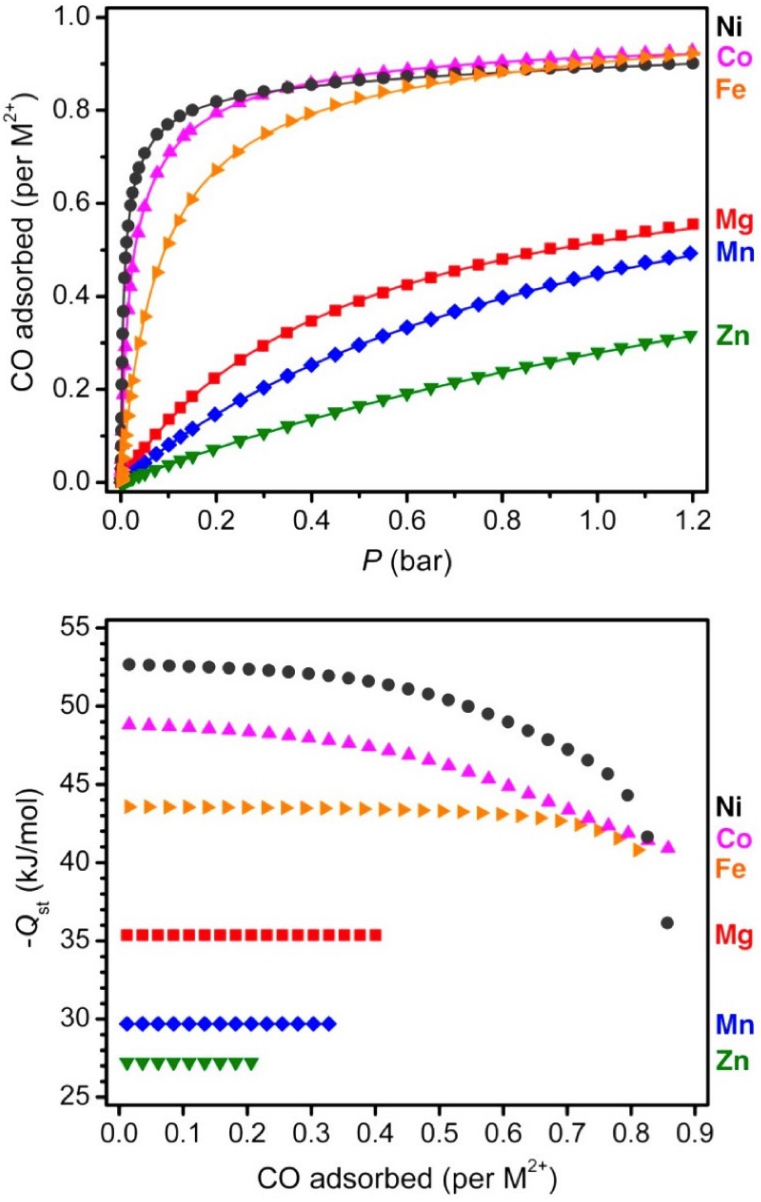

Figure 4.10: (Upper) Carbon monoxide isotherms measured at 298 K. For the Fe, Co, and Ni analogues, CO uptake approaches one molecule per metal cation site at 1.2 bar. (Lower) Isosteric heats of CO adsorption calculated from isotherms measured at 298, 308, and 318 K.

Table 4.4: Isosteric Heat of CO Adsorption, M–C Distance, M–C–O Angle, CO Capacity, CO/H_2 and CO/N_2 IAST Selectivities for M_2(dobdc)

					CO/H_2 IAST selectivity[b]		CO/N_2 IAST selectivity[b]	
	$-Q_{st}$ (kJ/mol)	M–C (Å)	M–C–O (deg)	capacity[a] (mmol/g)	CO:H_2 0.333	CO:H_2 1.0	CO:N_2 0.333	CO:N_2 1.0
Mg	35.4	2.41(2)	167(1)	4.58	188 (98.4)	170 (99.4)	11.3 (79.0)	10.3 (91.2)
Mn	29.7	2.44(2)	171(1)	3.24	91 (96.8)	86 (98.9)	10.7 (78.2)	10.3 (91.1)
Fe	43.6	2.27(2)	177(1)	6.04	634 (99.5)	507 (99.8)	80 (96.4)	68 (98.5)
Co	48.8	2.18(2)	171(2)	5.95	1420 (99.8)	1040 (99.9)	206 (98.6)	163 (99.4)
Ni	52.7	2.09(2)	166(2)	5.79	2448 (99.9)	1705 (99.9)	289 (99.0)	216 (99.5)
Zn	27.2	2.49(2)	161(1)	1.95	49 (94.2)	47 (97.9)	7.6 (71.7)	7.5 (88.2)

[a] 1.2 bar CO capacity, total adsorption at 298 K
[b] Values in parentheses represent the purity of CO gas achievable for the given selectivity

Isosteric heats of CO adsorption computed within a harmonic approximation agree with the experimental trend,[408] predicting isosteric heats of adsorption from -25.7 kJ/mol for Zn to -40.4 kJ/mol for Ni at 308 K. The comparison of calculated values to experimentally determined values of isosteric heats of adsorption is shown in Figure 4.8d. We note that the largest discrepancies arise for the metal centers that give rise to the strongest orbital interactions: Fe, Co, and Ni.

The extraordinary ability of these materials to bind CO reversibly and at high capacity suggests their application in removing CO from gas mixtures, such as CO/N_2[428,429] and CO/CH4,[430] and, in particular, for the purification of CO from syngas. In order to determine the CO/H_2 selectivities, we employed ideal adsorbed solution theory (IAST),[431] the accuracy of which has already been established for adsorption of a wide variety of different gases in zeolites and metal-organic frameworks (see the Supporting Information for details on the IAST calculations).[432] To reflect the varying H_2:CO ratios found in syngas, IAST selectivities were calculated over a range of compositions (Figure 4.11), and were found to vary widely, from a minimum of 45 in the case of Zn_2(dobdc) to over 5200 for Ni_2(dobdc) at low CO concentrations. Significantly, these selectivities are all much higher than those observed for metal-organic frameworks lacking coordinatively unsaturated metal cations, such as the value of 2.7 determined for MOF-5.[433]

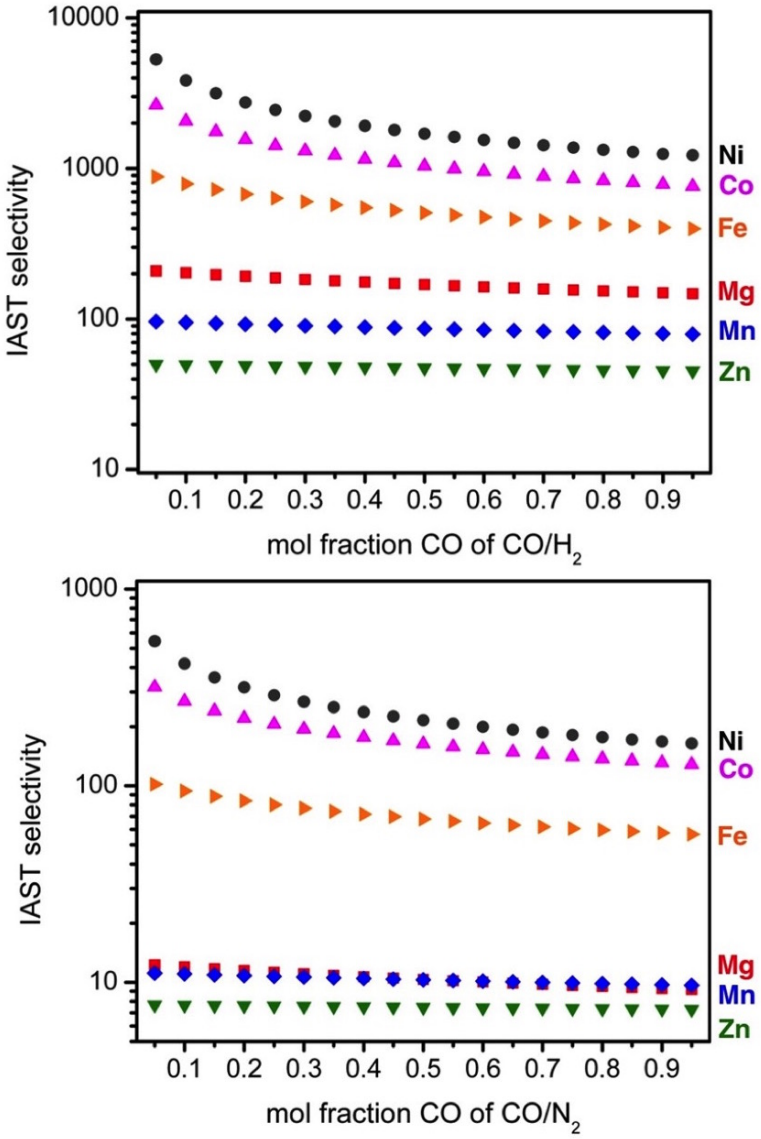

Figure 4.11: Ideal adsorbed solution theory (IAST) selectivities for mixtures of CO/H_2 (upper) and CO/N_2 (lower) of varying compositions at 298 K and 1 bar.

The IAST selectivities are indicative of the purity at which CO could be produced in a separation, with, for example, the values of 47 and 1705 for an equimolar CO/H_2 mixture at 1 bar and 298 K enabling Zn_2(dobdc) and Ni_2(dobdc) to produce CO with

purities of 97.9% and 99.9%, respectively. Thus, the importance of having materials exhibiting a range of different CO binding energies becomes clear: one can select the M_2(dobdc) compound that will provide just the minimum level of CO purity required, thereby minimizing the regeneration energy associated with CO desorption. Finally, we note that the high CO/N_2 selectivities of these materials (Figure 4.11) bodes particularly well for their use in the separation of CO from syngas contaminated with N_2.

4.2.4 Conclusions

Metal-organic frameworks of the M_2(dobdc) structure type provide an excellent platform for the investigation of new coordination chemistry via gaseous substrate binding at coordinatively unsaturated metal sites. Significantly, the weak ligand field presented by the oxo and carboxylate donor ligands enforces a high-spin electron configuration for the divalent metal cations, even in the presence of the prototypical strong field ligand CO. The rigidity of the evacuated materials, together with their highly crystalline nature, has thus enabled the generation and crystallographic characterization of the first high-spin manganese(II), iron(II), cobalt(II), and nickel(II) carbonyl species, as well as the first magnesium and zinc carbonyls. The fully reversible CO binding at high capacity and moderate adsorption enthalpies further make these materials outstanding candidates for applications in the efficient separation of CO from more weakly adsorbing gases, such as H_2 and N_2.

4.2.5 Additional Information

Supplementary information is available in the online version of the paper. The Supporting Information includes: Additional gas adsorption, structural, and spectroscopic data as well as further computational details. This material is available free of charge at `http://pubs.acs.org`. Correspondence and requests for materials should be addressed to J.R.L. The authors declare no competing financial interests.

Acknowledgements

The experimental portion of this research was supported through the Center for Gas Separations Relevant to Clean Energy Technologies, an Energy Frontier Research Center funded by the U.S. Department of Energy, Office of Science, Office of Basic Energy Sciences under Award DE-SC0001015. Computational studies were supported through the Nanoporous Materials Genome Center of the U.S. Department of Energy, Office of Basic Energy Sciences, Division of Chemical Sciences, Geosciences, and Biosciences, under Award Number DE-FG02-12ER16362. S.B., V.C., and S.C. acknowledge financial support from MIUR-PRIN (2010-2011). We thank Samuel Odoh for helpful discussions. We thank Gerald K. Branch and Arkema for fellowship support of E.D.B., the NIST/NRC Fellowship program for support of M.R.H., the National Science Foundation for fellowship support of J.A.M. Portions of this work were performed at the Molecular Foundry, supported by the U.S. Department of Energy, Office of Science, Office of Basic Energy Sciences.

Chapter 5

Multireference Treatment of Metal–Metal Bonds

5.1 A Combined Spectroscopic and Computational Study of a High-Spin S = 7/2 Diiron Complex with a Short Iron–Iron Bond

The nature of the iron–iron bond in the mixed-valent diiron tris(diphenylforamidinate) complex $Fe_2(DPhF)_3$, which was first reported by Cotton, Murillo *et al.* (*Inorg. Chim. Acta* **1994**, *219*, 7), has been examined using additional spectroscopic and theoretical methods. It is shown that the coupling between the two iron centers is strongly ferromagnetic, giving rise to an octet spin ground state. On the basis of Mössbauer spectroscopy, the two iron centers, formally mixed-valent Fe(II)Fe(I), are completely equivalent with an isomer shift $\delta = 0.65$ mm s^{-1} and quadrupole splitting $\Delta E_Q = +0.32$ mm s^{-1}. A large, positive zero-field splitting $D_{7/2} = 8.2$ cm^{-1} has been determined from magnetic susceptibility measurements. Multiconfigurational quantum studies of the complete molecule $Fe_2(DPhF)_3$ found one dominant configuration $(\sigma)^2(\pi)^4(\pi^*)^2(\sigma^*)1(\delta)^2(\delta^*)^2$,

Adapted with permission from C. M. Zall, D. Zherebetskyy, A. L. Dzubak, E. Bill, L. Gagliardi, C. C. Lu. *Inorg. Chem.* 2012, *51*, 728.[434] Copyright 2012, American Chemical Society. C. M. Z. and D. Z. contributed equally to this work. Additional information may be found in section 5.1.5.

which accounts for 73% of the ground-state wave function. By considering all the configurations, an estimated metal–metal bond order of 1.15 has been calculated. Finally, $Fe_2(DPhF)_3$ exhibits weak electronic absorptions in the visible and near-infrared regions, which are assigned as *d*–*d* transitions from the doubly occupied metal–metal π molecular orbital to half-occupied π^*, δ, and δ^* orbitals.

5.1.1 Introduction

Since the seminal discoveries of multiple bonding between transition metal centers in the $[Re_3Cl_{12}]^{3-}$ and $[(ReCl_4)_2]^{2-}$ ions during the 1960s,[435] the study of bimetallic coordination complexes has exposed a rich diversity in the range, nature, physical properties, and reactivity of metal–metal bonds. Continued interest in metal–metal bonds stems from their advantageous properties: the versatility in M–M bonding, the availability of multiple *d*-electrons, and additional coordination sites for substrate binding. These studies are also motivated from a theoretical standpoint: the varied possible orbital interactions between the two metals and the high degree of electron correlation have made for intriguing study and provided challenging tests for current computational methods.[436,437,438,439]

Bimetallic compounds with metal–metal bonds can be catalytically relevant. For example, Rh–Rh bonds play a central role in the dirhodium-catalyzed functionalization of inert C–H bonds.[440,441,442] The interesting photochemical properties of Rh–Rh bonds have been utilized in light-to-energy conversion schemes, as for example, in the reduction of protons to hydrogen.[443,444,445] Another highlight is the stoichiometric chop–chop reaction, wherein multiply bonded ditungsten W≡W compounds undergo metathesis with alkynes (or nitriles) to generate mononuclear tungsten alkylidynes W≡CR (and W≡N).[446,447,448] These examples have in common that they feature a second- or third-row transition metal and are diamagnetic. From a practical standpoint, first-row transition metals are ideal because they are inexpensive and earth abundant. Also, in the development of magnetic materials, first-row metal–metal bonds offer more diversity in spin states.[449]

On the theory side, density functional methods have been applied successfully to describe the metal–metal bonds featuring second- and third-row metals,[436,437] but the

extension to first-row metals has been problematic. One vexing issue is electron correlation,[438] and state-of-the-art quantum chemical methods are often necessary to produce satisfactory descriptions of the metal–metal interaction. A well-studied case is that of multiply bonded Cr_2. We have previously described the bond order in several Cr_2 complexes by using the concept of effective bond order (EBO),[450,451,452,453] which is determined from a multiconfigurational wave function.[454]

Going beyond Cr_2, we are interested in the spectroscopic properties and electronic structures of M–M complexes featuring other first-row transition metals. For iron, complexes with Fe–Fe bonds are well-known, particularly for iron carbonyl clusters and their derivatives. If we exclude compounds with carbonyl ligands, then the number of structurally characterized complexes with significant Fe–Fe interactions drastically decreases.[455] Some of these diiron compounds are shown in Figure 5.1. Collectively, they show great breadth in oxidation states, coordination numbers, geometries, and ligand types.[456,457,458,459,460] The diiron complex $[Fe_2(C_6H_3\text{-}2,6\text{-}(C_6H_3\text{-}2,6\text{-}^{i}Pr_2)_2)_2]$ has been postulated to be diamagnetic,[457] although this assignment does not match the $S = 3$ prediction from multiconfigurational quantum chemical calculations.[461] Indeed, the majority of the examples in Figure 5.1 are paramagnetic with $S \geq 1$, challenging the conventional wisdom that strong metal–metal interactions should be antiferromagnetic.[456] More remarkable, $Fe_2(DPhF)_3$ and $Fe_2(DPhF)_4$ (DPhF = diphenylforamidinate) both possess high-spin electronic configurations ($S = 7/2$ and 4, respectively), a feat that is unparalleled by other Fe–Fe complexes.[459,460] A hexairon complex was recently reported with a marvelously high magnetic moment, $S = 6$; but, for six ferrous centers, the analogous "high-spin" configuration would be $S = 12$.[462] To our knowledge, the only other high-spin Fe–Fe species are gas-phase $[Fe_2]^0$ and $[Fe_2]^-$ with $S = 4$ and $S = 7/2$ ground spin-states, respectively.[463,464] Of note, $Fe_2(DPhF)_3$ is also one of a few examples of a formally mixed-valent Fe(II)Fe(I), although these other complexes are low-spin in contrast to $Fe_2(DPhF)_3$.[465,466,467,468]

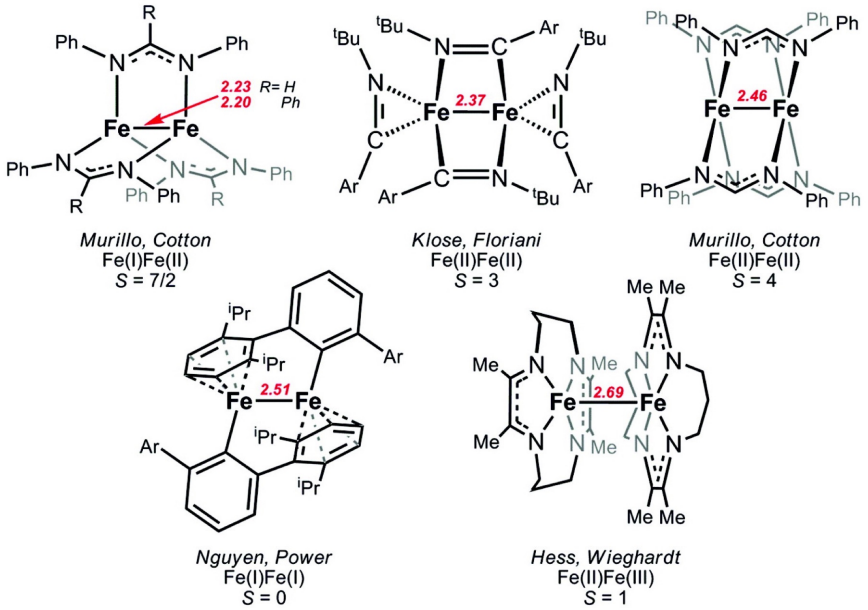

Figure 5.1: Diiron coordination complexes containing strong Fe–Fe bonds. Relevant characterization data such as Fe–Fe bond lengths (Å), formal oxidation states, and ground spin states are given.

In the present work, we examine the nature of the iron–iron bond in $Fe_2(DPhF)_3$, extending the previous studies by Cotton, Murillo *et al.*[459,469] Much of the spectroscopic characterization for $Fe_2(DPhF)_3$ is reported for the first time, including Mössbauer, magnetic susceptibility, and UV/visible/near-infrared (UV-vis-NIR) electronic absorption measurements. To complement the physical data, the electronic structure of $Fe_2(DPhF)_3$ has also been calculated by employing a combination of density functional theory (DFT) and multiconfigurational quantum chemical methods. When possible, spectroscopic parameters were calculated, and in general, good agreement was found with experimental values.

5.1.2 Experimental Section

Synthetic Considerations

All manipulations were performed under a dinitrogen atmosphere in a Vacuum Atmosphere glovebox or using standard Schlenk techniques. Standard solvents were deoxygenated by sparging with dinitrogen and dried by passing through activated alumina columns of a SG Water solvent purification system. Deuterated solvents were purchased from Cambridge Isotope Laboratories, Inc., dried over alumina, filtered, and stored over activated 4 Å molecular sieves.

The synthesis of $Fe_2(DPhF)_3$ is a modified preparation of the literature report,[459] although it is quite similar to the first reported synthesis.[469] $FeCl_2(HDPhF)_2$ (750 mg, 1.44 mmol) was dissolved in toluene (90 mL) and cooled to -78 °C. *n*-Butyllithium (in hexane, 2.15 mmol) was slowly added dropwise, and the reaction solution was allowed to slowly warm to room temperature over 12 h. The resulting brown mixture was filtered, giving a light yellow-brown solution. After removal of solvent under vacuum, the dried brown solid was redissolved in THF, layered with diethyl ether, and left to crystallize at -35 °C. Yellow crystals of $Fe_2(DPhF)_3$, which formed after 2 days, were filtered and dried under vacuum. Yield: 175 mg, 35%. ^{1}H NMR (500 MHz, THF-d_8, 23 °C): δ = 12.6 (12H, *meta*), -19.6 (6H, *para*), -40 (12H, *ortho*) (see Supporting Information, Figure 1); UV-vis-NIR (THF): λmax, nm (ϵ, M^{-1} cm^{-1}) = 280 (63000), 350 sh (13000), 650 (50), 700 sh (50), 825 (70), 1250 (80).

X-ray Crystallographic Data Collection and Refinement of the Structures

Single crystals of $Fe_2(DPhF)_3(C_6H_6)_{0.5}$ were grown from vapor diffusion of hexane into a saturated benzene solution of $Fe_2(DPhF)_3$ at room temperature. A thin yellow plate (0.3 mm × 0.3 mm × 0.1 mm) was placed on the tip of a glass capillary and mounted on a Siemens SMART Platform CCD diffractometer for data collection at 173 K. The data collection was carried out using Mo Kα radiation (graphite monochromator). The data intensity was corrected for absorption and decay (SADABS). Final cell constants were obtained from least-squares fits of all measured reflections. The structure was solved using SHELXS-97 and refined using SHELXL-97. A direct-methods solution was calculated which provided most non-hydrogen atoms from the E-map. Full-matrix least-squares/difference Fourier cycles were performed to locate the remaining

non-hydrogen atoms. All non-hydrogen atoms were refined with anisotropic displacement parameters. Hydrogen atoms were placed in ideal positions and refined as riding atoms with relative isotropic displacement parameters. Crystallographic data are summarized in Table 5.1.

Table 5.1: Crystallographic Details for $[Fe_2(DPhF)_3](C_6H_6)_{0.5}$

chemical formula	$C_{39}H_{33}N_6Fe_2(C_6H_6)_{0.5}$
formula wt	736.48
cryst syst	triclinic
space group	$P\bar{1}$
a (Å)	11.317(2)
b (Å)	11.954(2)
c (Å)	13.948(2)
α (deg)	108.303(2)
β (deg)	91.290(2)
γ (deg)	95.539(2)
V(Å^3)	1780.4(5)
Z	2
D_{calcd} (g cm^{-3})	1.374
λ (Å), μ (mm^{-1})	0.71073, 0.854
T (K)	173(2)
θ range (deg)	1.54–26.37
reflns collected	7222
unique reflns	4528
data/restraint/parameters	7222/0/451
R_1, wR_2 ($I > 2\sigma(I)$)	0.0599, 0.1056

Physical Measurements

NMR spectra were collected on a Varian Inova 500 MHz spectrophotometer. Room-temperature visible and near-infrared absorption data were collected on a Cary-14 spectrophotometer. UV wavelength absorption spectra were collected on a Cary 300

Bio UVvisible spectrophotometer. Samples of $Fe_2(DPhF)_3$ were recrystallized from THF/hexane prior to data collection, then redissolved in THF (UV, 7.07 μM; Vis-NIR, 6.70 mM).

Magnetic susceptibility data were measured from powder samples of solid material in the temperature range 2 to 300 K by using a SQUID susceptometer with a field of 1.0 T (MPMS-7, Quantum Design, calibrated with standard palladium reference sample, error <2%). Multiple-field variable-temperature magnetization measurements were done at 1 T, 4 T, and 7 T also in the range 2-300 K with the magnetization equidistantly sampled on a $1/T$ temperature scale. The experimental data were corrected for underlying diamagnetism by use of tabulated Pascals constants[470,471] as well as for temperature-independent paramagnetism. The susceptibility and magnetization data were simulated with the program julX for exchange-coupled systems.[472] The simulations are based on the usual spin-Hamiltonian operator for mononuclear complexes with spin $S = 7/2$ with consideration of only second-order terms for the zfs:

$$\hat{H} = g\beta\hat{\overrightarrow{S}} \cdot \overrightarrow{B} + D\left[\hat{S}_z^2 - 1/3S\left(S+1\right) + E/D\left(\hat{S}_x^2 - \hat{S}_y^2\right)\right] \tag{5.1}$$

where g is the average electronic g value, and D and E/D are the axial zero-field splitting and rhombicity parameters. Magnetic moments are calculated after diagonalization of the Hamiltonian from the eigenfunctions using the Hellman-Feyman theorem $\overrightarrow{\mu}_i(\overrightarrow{B}) = \langle\psi_i|(\mathrm{d}H)/(\mathrm{d}\overrightarrow{B})|\psi_i\rangle$. Powder summations were done by using a 16-point Lebedev grid.[473] Because the program is not equipped for individual spins larger than 5/2, we reproduced the octet ground state by adopting ferromagnetic coupling of $S_1 = 3/2$ and $S_2 = 2$ with a exceedingly large exchange coupling constant $J = +300$ cm^{-1}. This value is a conservative estimate of the true coupling of the mixed-valence diiron complex because the excited states are higher in energy so that thermal population cannot be detected.

Mössbauer data were recorded on an alternating constant-acceleration spectrometer. The minimum experimental line width was 0.24 mm s^{-1} (full width at half-height). The sample temperature was maintained constant in an Oxford Instruments Variox or an Oxford Instruments Mössbauer-Spectromag 2000 cryostat, which is a split-pair superconducting magnet system for applied fields (up to 8 T). The field at the sample is oriented perpendicular to the γ-beam. The ^{57}Co/Rh source (1.8 GBq) was positioned at room temperature inside the gap of the magnet system at a zero-field position. Isomer

shifts are quoted relative to iron metal at 300 K. Magnetic Mössbauer spectra were simulated using the spin-Hamiltonian given in (eq 5.1). The hyperfine interactions for ^{57}Fe were calculated with the usual nuclear Hamiltonian.[474]

Computational Methods

The $Fe_2(DPhF)_3$ complex was studied using density functional theory (DFT) and the complete active space self-consistent field (CASSCF) method,[454] followed by a multi-configurational second-order perturbation theory (CASPT2) method.[475] It has been demonstrated that this strategy is successful in predicting accurate results for ground and electronically excited states of bimetallic systems.[476,477,478,479,480]

DFT Calculations

Geometry optimizations of $Fe_2(DPhF)_3$ were performed for the various possible spin states at the DFT level employing the Perdew-Burke-Ernzerhof (PBE) exchange-correlation functional[481] using the TURBOMOLE 6.1 program package.[482] For all atoms, the double-ζ quality basis sets def-SV(P) were used. DFT calculations were performed with the broken symmetry option (unrestricted calculations) and the resolution-of-the-identity (RI) approximation.[483] Hyperfine parameters were calculated using the ORCA program package.[484] For Fe atoms, the CP(PPP) basis set designed by Neese and co-workers for accurate calculations of hyperfine coupling in transition metal compounds was used.[485,486] The all-electron Gaussian basis sets used were those reported by Ahlrichs and co-workers, including TZVP basis sets for N atoms and SV(P) for C and H atoms.[487,488] The DFT calculations of the hyperfine parameters were performed using four functionals B3LYP, BP86, TPSSh, and B2PLYP for comparison.

CASSCF/CASPT2 Calculations All CASSCF / CASPT2 calculations were performed with the MOLCAS-7.4 package[489] using the DFT-optimized structures with imposed 2-fold symmetry for all possible spin states. The relativistic all-electron ANO-RCC basis sets[490,491] were used for all elements. Because MOLCAS works in subgroups of D_{2h}, all calculations were performed in the C_2 point group to minimize computational cost. For the Fe and N atoms basis sets of double-ζ quality were used(ANO-RCC-VDZP) with the following contractions: [5s4p2d1f] for Fe and [3s2p1d] for N. The remaining C and H atoms have basis sets of minimal basis quality (ANO-RCC-MB) with a contraction of [2s1p] for C and [1s] for H. Scalar relativistic effects were included by using the

Douglas-Kroll-Hess Hamiltonian.[492] The two-electron integral evaluation was simplified by employing the Cholesky decomposition technique.[493,494,495]

The ground- and excited-state wave functions were computed at the CASSCF theory level, and corresponding energies were computed at the CASPT2 theory level. An imaginary level shift of 0.2 au was used to avoid intruder states.[496] The natural orbital occupation numbers were used for the evaluation of the effective bond order (EBO),[450,453] which is calculated as the difference between the total occupancies of the bonding and antibonding molecular orbitals of the Fe–Fe bond divided by two.

CAS Choice A complete active space was used consisting of all 13 valence electrons of both Fe ions distributed over 13 orbitals, denoted as AS (13, 13). This active space was optimized to include all the $3d$ Fe orbitals and three additional bonding orbitals, one σ- and two π-(Fe–Fe) MOs that primarily consist of atomic orbitals in the fourth shell of Fe atoms (for correlation effects between the third and fourth shell orbitals of the Fe atoms). Computations of the excited-state wave functions were performed using AS (13, 13) as well as AS (11, 15). The latter active space excludes the lowest doubly occupied σ-orbital formed by the $3d_z^2$-orbitals of Fe ions and includes three additional formally empty MOs of the fourth shell. Many electronic states were computed with the (13, 13) active space, namely the lowest eight octet states belonging to the A irreducible representation, the lowest six octet states belonging to the B irreducible representation, and the lowest six A and B sextet and quartet states. The intensities of the transitions among all the states including spin-orbit coupling were determined by using the complete active space state interaction method, CASSI,[497] which employs an effective one-electron spin-orbit (SO) Hamiltonian, based on the mean field approximation of the two electronic part.[498] To compute SO coupling, a SO Hamiltonian matrix was constructed using the basis of all 13/13 CASSCF wave functions corresponding to the octet, sextet, and quartet states within 2.2 eV of the ground state. A total of 14 octet, 12 sextet, and 12 quartet states were thus included, giving a total of 232 spin-orbit states. Dynamic correlation energy was introduced in the consideration by substituting the diagonal elements of the spin-orbit Hamiltonian matrix by the corresponding CASPT2 energies.

5.1.3 Results

Molecular Structure

The published solid-state structure of $Fe_2(DPhF)_3$ shows a distorted trigonal lantern geometry with one of the shortest Fe–Fe bonds, 2.2318(8) Å, known to date (Table 5.2).[469] A perpendicular C_2 axis bisects the metal–metal bond, symmetrizing the two iron atoms as well as each pair of N atoms. The distortion from idealized D_{3h} is observed in the N–Fe–N bond angles of 111.1°, 116.2°, and 132.6° ($\Delta = 22°$). Cotton and Murillo attributed the distortion to crystal packing forces as opposed to electronic effects. We have obtained another solid-state structure of $Fe_2(DPhF)_3$, in which the Fe–Fe bond is identical to the original report. The only remarkable difference is the tighter range of N–Fe–N bond angles: 113.7-125.8° ($\Delta = 12°$). In the DFT-optimized ground-state structure of $Fe_2(DPhF)_3$ (*vide infra*), the bond distances match those of the experimental structure within 0.04 Å, including a calculated Fe–Fe bond length of 2.188 Å. Additionally, the N–Fe–N bond angles are nearly equivalent with $\Delta = 3°$. These recent results support the original supposition that acute distortions from C_3 symmetry do not have an electronic basis.

Table 5.2: Selected Bond Lengths (Å) and Angles (deg) for Experimental and Calculated $Fe_2(DPhF)_3$ Structures

structure	$[(DPhF)_3Fe_2]$[459, 469]	$[(DPhF)_3Fe_2]\cdot(C_6H_6)_{0.5}$	$[(DPhF)_3Fe_2]$ *PBE/def-SV(P)*
Fe–Fe (Å)	2.2318(8)	2.2307(8)	2.188
Fe–N (Å)	2.033(2)	2.032(3)	2.034
	2.033(2)	2.022(3)	2.034
	2.025(2)	2.013(3)	2.034
	2.025(2)	2.005(3)	2.031
	2.017(2)	1.992(3)	2.031
	2.017(2)	1.988(3)	2.031
N–Fe–N (deg)	132.6(1)	125.8(1)	121.6
	132.6(1)	125.7(1)	121.6
	116.18(9)	120.5(1)	119.4
	116.18(9)	117.1(1)	119.4
	111.08(9)	116.9(1)	118.7
	111.08(9)	113.7(1)	118.7
N–Fe–Fe (deg)	92.29(6)	92.14(9)	92.2
	92.29(6)	91.67(9)	92.2
	90.98(6)	91.39(8)	92.0
	90.98(6)	91.21(8)	92.0
	89.77(7)	90.96(9)	91.8
	89.77(7)	90.15(8)	91.8
N–C–N (deg)	122.5(3)	122.5(3)	121.8
	122.5(3)	122.5(3)	121.7
	121.3(3)	122.3(4)	121.7

Magnetic Measurements

The ground spin state of $Fe_2(DPhF)_3$ of $S = 7/2$ was previously assigned based on an axial EPR spectrum with g-values of 7.94 and 1.99.[469] Magnetic susceptibility measurements of $Fe_2(DPhF)_3$ have been conducted with variable temperature (VT) and with variable temperature and field (VTVH). The data are shown in Figure 5.2. From 30 to 290 K, the effective magnetic moment is temperature independent at 7.4 μ_B. The plots in Figure 5.2 confirm the $S = 7/2$ ground spin state and indicate that the octet state is energetically well-isolated from the other spin states. To fit the data, we used a two-spin model consisting of the two iron centers, formally high-spin Fe(I) and Fe(II) with $S_{Fe} = 3/2$ and 2, respectively; otherwise, the iron centers were treated as equivalent. The spectrum can be simulated by adopting $g_{Fe} = 1.86$, which is near the real value of 2.0 (based on the EPR spectrum), and zero-field splitting parameter $D = 19.1$ cm^{-1} for both iron centers. The values correspond to a zero-field splitting of the ground state octet according to $D_{7/2} = 8.2$ cm^{-1}, as can be seen from spin projection coefficient ($D_{7/2} = 0.1429\ D_1 + 0.2857\ D_2$).[499] The coupling between the two iron centers is strongly ferromagnetic, with a simulated minimum value of the isotropic spin-spin coupling constant J of $+300$ cm^{-1} for the Hamiltonian EDIT WITH EQUATIONSThe inset in Figure 5.2 shows the VTVH dependence of the magnetization of $Fe_2(DPhF)_3$. The variable field data were globally fitted with the following parameters: $g_{Fe} = 1.87$, no rhombicity ($E/D = 0$), and $D = +19.1$ cm^{-1} for both iron centers. The large, positive zero-field splitting parameter is characteristic of high-spin iron centers and further pinpoints the $m_s = \pm 1/2$ as the ground energy level.

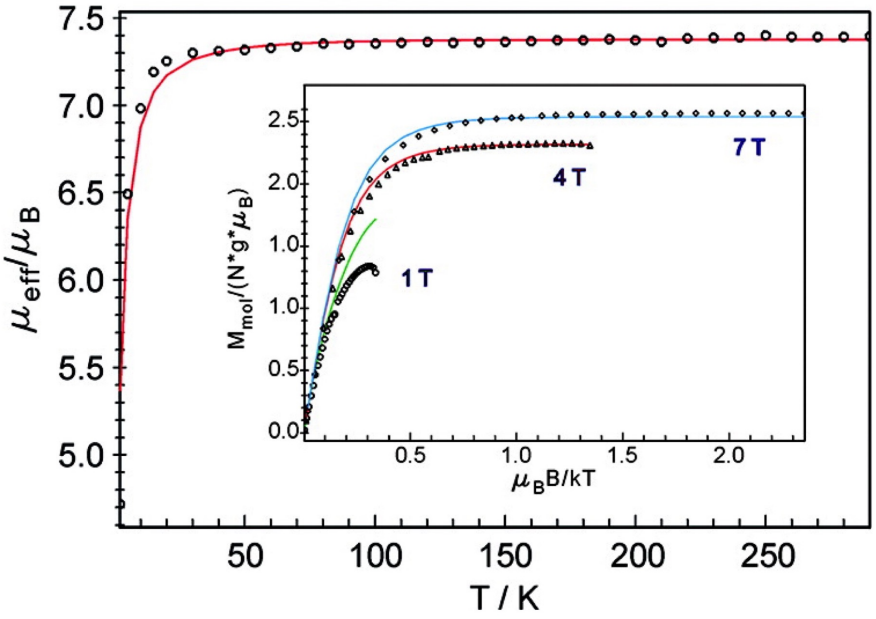

Figure 5.2: Temperature dependence of the effective magnetic moment, μ_{eff}, of $Fe_2(DPhF)_3$ (shown in open circles, 1 T, 2-290 K). The red solid line represents the best fit. Inset: isofield VTVH magnetization of $Fe_2(DPhF)_3$ as a function of μBB/kT (1, 4, and 7 T; 2290 K with corresponding simulation curves shown in green, red, and blue, respectively). The data were corrected for ?TIP of 0.375 $\times$ 103 emu. Intermolecular coupling was considered by introducing a Weiss constant, θ, of ?0.286 K to obtain a consistent fit of the low temperature data recorded at different fields. See text for simulation parameters.

We have performed geometry optimizations for the doublet, quartet, sextet, and octet spin-states using DFT (PBE/def-SV(P)). These optimized structures were then used for higher level CASSCF/CASPT2 calculations, wherein a 2-fold symmetry was imposed to reduce the computational cost. Although $Fe_2(DPhF)_3$ is better suited to 3-fold symmetry, point group constraints in MOLCAS are limited to D_{2h} and its subgroups. Therefore, we chose to impose C_2 symmetry, which enforces a 2-fold rotation axis perpendicular to the Fe–Fe vector. The relative energies for the various states calculated at these three levels of theory are reported in Table 5.3. All methods indicate that the ground state is the octet ^8A, as previously proposed.[500] Selected geometrical parameters of the structure of the ^8A state are reported in Table 5.2. Overall, the

agreement between theory and experiment is satisfactory.

Table 5.3: Calculated Relative Energies of $Fe_2(DPhF)_3$ for All Possible Spin States at DFT, CASSCF, and CASPT2 Levels of Theory

	symmetry	doublet	quartet	sextet	octet
ΔE_{DFT} (eV)	–	2.95	1.65	0.71	0.00
ΔE_{CASSCF} (eV)	A	1.63	1.10	1.30	0.00
	B	1.44	1.44	0.60	1.26
ΔE_{CASPT2} (eV)	A	1.50	1.22	1.17	0.00
	B	1.53	1.22	0.50	1.18

Mössbauer Spectroscopy

Applied-field Mössbauer spectra of $Fe_2(DPhF)_3$ recorded at 4.2 K are shown in Figure 5.3. Additional spectra collected at variable temperatures are provided in the Supporting Information (Figure 2). The spectra were globally fitted with an isotropic $g_{7/2} = 2.0$, $D_{7/2} = 8.2\ \mathrm{cm}^{-1}$, $E/D_{7/2} = 0$, and the Mössbauer parameters $\delta = 0.65\ \mathrm{mm\ s}^{-1}$ and $\Delta E_{\mathrm{Q}} = +0.32\ \mathrm{mm\ s}^{-1}$. On the basis of the fit, we can draw some conclusions. First, the g, D, and E/D values correspond well to those obtained in the magnetic susceptibility measurements. Second, the two iron sites are equivalent on the Mössbauer time scale ($10^7\ \mathrm{s}^{-1}$), and $Fe_2(DPhF)_3$ is a fully delocalized mixed-valent complex. The quantum-chemical treatment given below will show that the diiron core of the compound is best described by a coherent superposition of Fe(I) and Fe(II) wave functions.

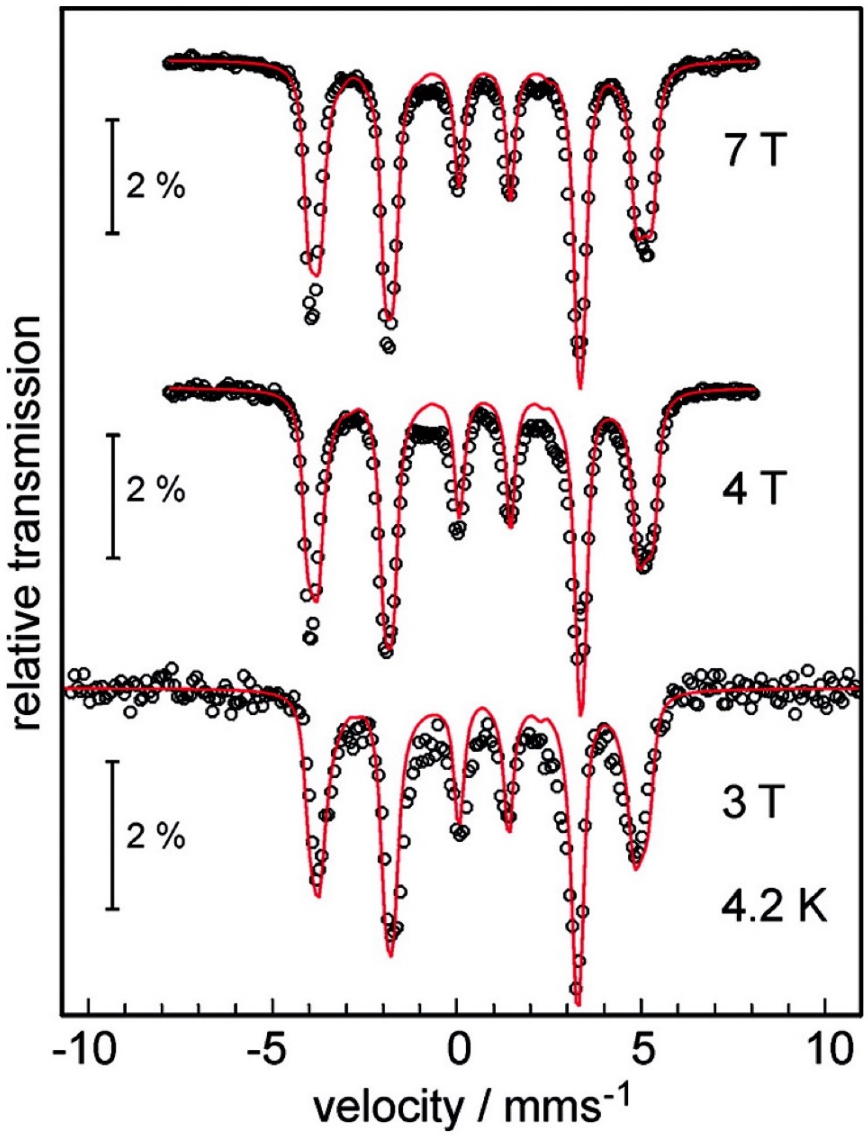

Figure 5.3: Applied field Mössbauer spectra of $Fe_2(DPhF)_3$ recorded at 4.2 K with fields of 3, 4, and 7 T. The solid lines represent spin Hamiltonian simulations for $S = 7/2$ with g7/2 = (2.0, 2.0, 2.0) fixed, $D_{7/2} = 8.2$ cm^{-1}, and E/$D_{7/2} = 0$, and with Mössbauer parameters δ = 0.65 mm s^{-1}, $\Delta E_Q = +0.32$ mm s^{-1}, asymmetry parameter ? = 0, line width = 0.26 mm s^{-1}, and magnetic hyperfine coupling constants Axx/gNβN = ?11.59 T; Ayy/gNβN = ?10.59; Azz/gNβN = ?30.81 T. The spin projection coefficients in the ionic limit of Fe(I), S1 = 3/2, and Fe(II), S2 = 2 would be AFe(I) = 2.333 A, and AFe(II) = 1.751 A, respectively, i.e., the local A values for the iron sites are about twice the total spin values given here.

There are limited examples of low-coordinate, high-spin Fe(II) and Fe(I) complexes for comparison. Holland *et al.* have reported Mössbauer parameters for a family of three-coordinate, high spin Fe(II) compounds with β-diketiminate ligands.[501] The isomer shifts range from 0.48 to 0.74 mm s^{-1} with —ΔE_Q— values between 1.11 and 1.74 mm s^{-1}. For a high-spin Fe(I) complex in the same system, a slightly lower isomer shift of 0.44 mm s^{-1} with ΔE_Q = 2.02 mm s^{-1} was reported.[502] Peters *et al.* have characterized a Fe(I)(μ-N_2)Fe(I) complex with δ = 0.53 mm s^{-1} and ΔE_Q = +0.89 mm s^{-1}.[503] The isomer shift reported here is comparable. Notably, the quadrupole splitting of Fe_2(DPhF)$_3$ is significantly smaller. The origin of the small quadrupole interaction is not known at this time, but it may be potentially related to the weak trigonal ligand field.

Table 5.4: Calculated Hyperfine Parameters of Fe_2(DPhF)$_3$ Relevant to Mössbauer Spectroscopy for Different DFT Functionals (B2PLYP, BP86, TPSSh, B3LYP)

	δ (mm/s)	ΔE_Q (mm/s)
B2PLYP	0.49	0.26
BP86	0.45	−0.45
TPSSh	0.48	−0.17
B3LYP	0.49	−0.27
B3LYP	0.51	−0.25
exp	0.65	0.32

[a]Input geometry from a PBE/SV(P) optimization
[b]Input geometry from a B3LYP/TZV(P) optimization

The Mössbauer parameters were calculated at the DFT level of theory using the ORCA program (Table 5.4).[484] Four different functionals were surveyed: B2PLYP, BP86, TPSSh, and B3LYP.[486,504] For the isomer shift, all the functionals gave similar predictions (within 0.20 mm s^{-1} of the experimental value). Although the range of quadrupole splittings is wider (from ?0.17 to 0.26 mm s^{-1}), essentially all these values are near zero, as is observed experimentally. The best agreement between theory and experiment was found for the B2PLYP functional with δ = 0.49 mm s^{-1} and ΔE_Q =

0.26 mm s^{-1}, where $\Delta = 0.16$ and 0.06 mm s^{-1}, respectively.

Details of Electronic Structure

The natural orbitals arising from the CASSCF calculations are displayed in Figure 5.4. Ten of the 13 orbitals are completely localized on the Fe–Fe bond. They are the σ, π, and δ bonding and antibonding orbitals, resulting from symmetry-adapted linear combinations of the Fe $3d$ atomic orbitals. The three remaining orbitals are primarily composed of the Fe $4s$, $4p$, and $4d$ atomic orbitals interacting to form σ and π bonding and antibonding orbitals with some minor contribution from the ligand N-atoms. The near degeneracy of each π- and δ-orbital pair is consistent with an approximate 3-fold symmetry about the Fe–Fe vector.

A multiconfigurational CASSCF/CASPT2 calculation revealed that the ^8A ground state has a single dominating configuration $(\sigma)^2(\pi)^4(\pi^*)^2(\sigma^*)^1(\delta)^2(\delta^*)^2$, which accounts for 73% of the wave function. Considering the total ground-state wave function, the natural orbital occupation numbers are: $(\sigma)^{1.85}(\pi)^{3.64}(\pi^*)^{2.30}(\sigma^*)^{1.06}(\delta)^{2.00}(\delta^*)^{2.00}(4\sigma)^{0.10}$ $(4\pi)^{0.06}$ with an estimated bond order (EBO) of 1.15. The non-negligible occupation of the iron orbitals in the fourth shell is also evident in the Mulliken population analysis: $4s^{0.12}3d^{6.32}4p^{0.28}4d^{0.11}$. Using an SCF-X$\alpha$-SW calculation on the truncated molecule Fe_2(HNCHNH)3, Cotton *et al.* previously computed a similar configuration $(\sigma)^2(\pi)^4(\pi^*)^2(\delta)^2(\sigma^*)^1(\delta^*)^2$ with a bond order of 1.5.[500] It is not surprising that our EBO value is lower than the value reported by Cotton because we account for the partial occupation of the high-lying antibonding orbitals not represented in the dominant configuration. Overall, the effect is to decrease the Fe–Fe bonding so that it is only slightly larger than a single bond. Finally, the charge and spin densities of the two iron atoms are identical with values of +1.17 and +3.49, respectively. These values reinforce the highly delocalized, high-spin $Fe^{1.5}Fe^{1.5}$ assignment for the diiron unit.

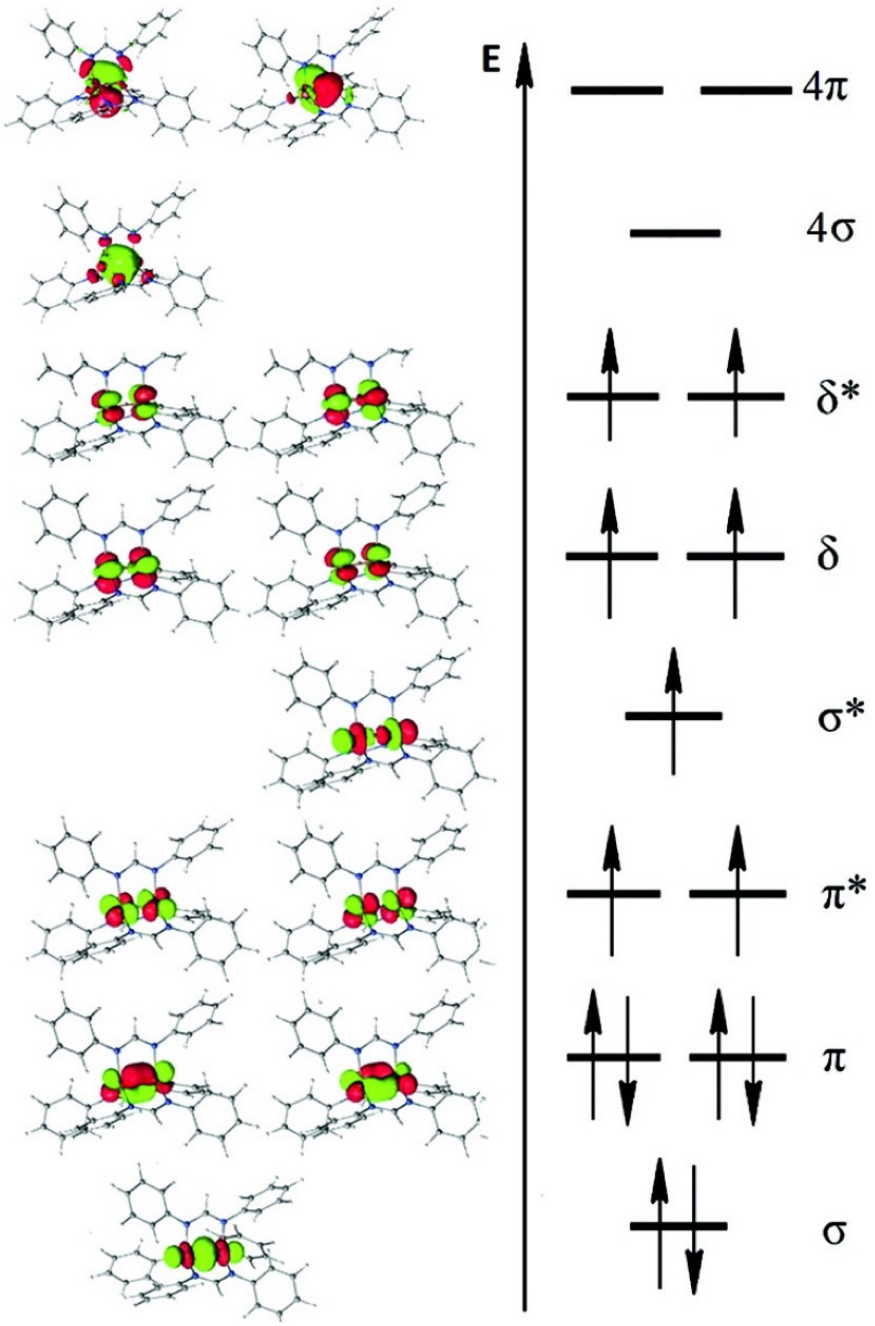

Figure 5.4: Qualitative MO diagram showing the natural orbitals for $Fe_2(DPhF)_3$ that arise from CASSCF calculations. The dominating electronic configuration (73%) is shown.

Electronic Absorption Spectroscopy

The electronic configuration in Figure 5.4 suggests that several d–d transitions are possible within the diiron core. Because the first coordination sphere of the diiron centers is approximately 3-fold symmetric, we first employed D_{3h} selection rules to qualitatively determine the allowed electric-dipole transitions (Figure 5.5). Electronic transitions from the $^8A_2$" ground-state are spin-allowed only if the excited electron is spin down, which constrains all transitions to originate from a doubly occupied molecular orbital such as $1a_1$"(σ) or 1e'(π). Within the d-orbital manifold, only five electric-dipole transitions are possible, from $1a_1$"(σ) to $1a_2$"(σ^*) or 2e'(δ), and from 1e'(π) to 1e"(π^*), 2e'(δ), or 2e"(δ^*). Of these five transitions, the energetically lowest transition is expected to be 1e'(π) $\rightarrow$ 1e"(π^*).

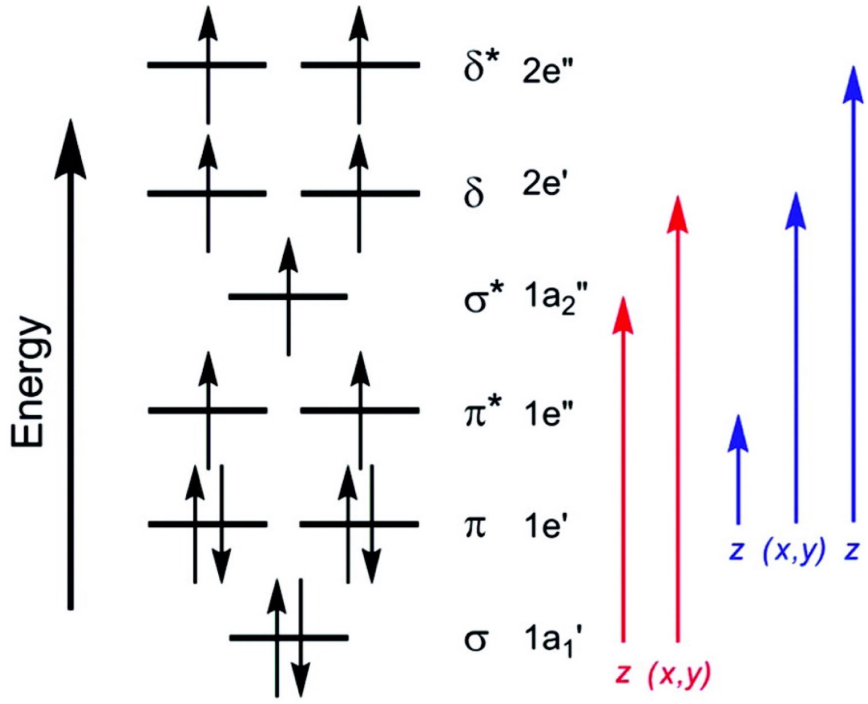

Figure 5.5: The allowed electric-dipole transitions of $Fe_2(DPhF)_3$ based on D_{3h} selection rules.

The Vis-NIR spectrum for $Fe_2(DPhF)_3$, which is shown in Figure 5.6, is characterized by several low energy bands between 650 and 1250 nm (15400 and 8000 cm^{-1}).

The Vis-NIR absorptions are independent of solvent as identical spectra are obtained in benzene and in THF (Supporting Information, Figure 3). These bands are surprisingly weak ($\epsilon < 100$ M^{-1} cm^{-1}) given the expectation that they should be both spin- and dipole-allowed. Indeed, metal–metal intervalence charge transfer bands exhibited by delocalized, mixed-valent bimetallics are typically intense (ϵ 103 M^{-1} cm^{-1}). One possible explanation for the observed weak absorptions is the significance of the Franck-Condon factor in modulating their intensity. Because the Fe–Fe bond distances in the $Fe_2(DPhF)_3$ excited states are expected to be perturbed from their ground-state values, it is plausible that the overlap of vibrational wave functions in the ground and excited electronic states is significantly decreased.

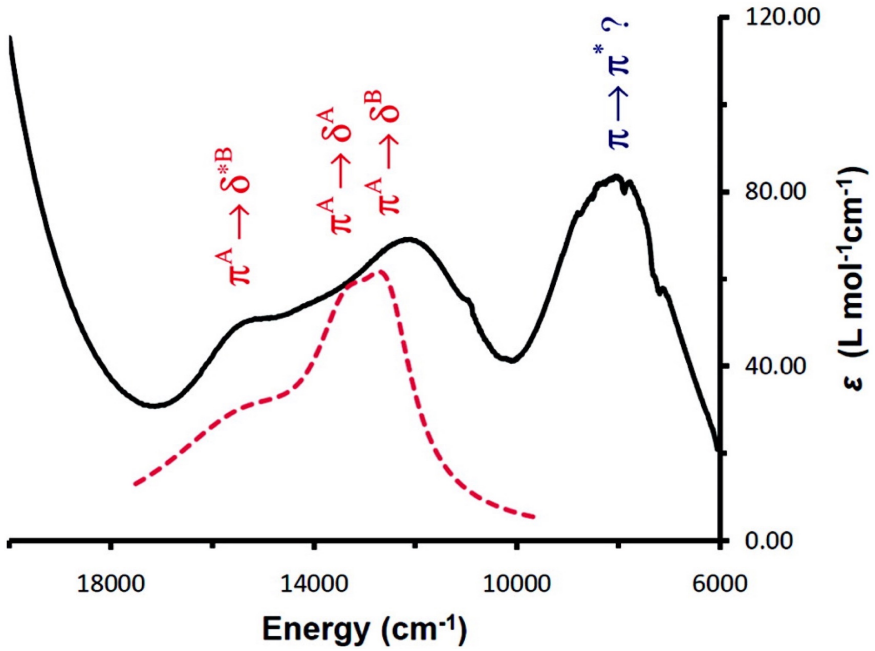

Figure 5.6: Electronic absorption spectrum of $Fe_2(DPhF)_3$ in THF (, black), with simulated spectrum from CASSCF/CASPT2 calculations (—, red) that include wave functions belonging to both A and B symmetry states (see Table 6). Experimental λmax, cm^{-1} (ϵ, L mol1 cm^{-1}) = 15380 (50), 14290 sh (50), 12120 (70), 8000 (80).

Computed Spin-Free Excited State Energies

As mentioned above, all CASSCF/CASPT2 calculations were performed with a C_2

symmetry constraint that corresponds to a 2-fold axis perpendicular to the internuclear axis. In the following discussion, all wave functions will belong either to the A or B symmetry states. Table 5.5 shows the vertical excitation energies and oscillator strengths for $Fe_2(DPhF)_3$ calculated at the spin-free CASSCF and CASPT2 levels using the (13, 13) active space, where the weight is the percent contribution of the major configuration in the excited wave function. All the octet excited states are reported up to 3.11 eV. Only one of the first eight predicted transitions (Table 5.5, in boldface) has an oscillator strength of any significance: the $\pi \rightarrow \delta$ transition is predicted to occur at 1.66 eV (13400 cm^{-1}) at the CASPT2 level with an oscillator strength of 2.56×10^{-4}. Of note, the large differences in ΔE (1 eV) between $\pi \rightarrow \delta$ and $\sigma \rightarrow \delta$ transitions suggest that the σ orbital lies significantly lower in energy. Consequently, transitions originating from the σ orbital do not contribute to the bands in the Vis-NIR region.

Table 5.5: Spin-Free Excitation Energies of $Fe_2(DPhF)_3$ for Octet Wave Functions Belonging to the A Symmetry States (All Transitions Correspond to $^8A \rightarrow {}^8A$)

	ΔE (eV)		oscillator	weight
transition	(CASSCF)	(CASPT2)	strength (a.u.)	(%)[a]
$\pi \rightarrow \pi^*$	1.23	1.42	0.235×10^{-7}	0.64
$\pi \rightarrow \pi^*$	1.28	1.45	$<0.1 \times 10^{-7}$	0.63
$\pi \rightarrow \delta$	1.77	1.60	0.788×10^{-5}	0.54
$\pi \rightarrow \delta$	1.82	1.66	0.256×10^{-3}	0.53
$\pi \rightarrow \sigma^*$	1.98	1.92	$<0.1 \times 10^{-7}$	0.51
$\pi \rightarrow \delta^*$	2.07	2.06	0.777×10^{-7}	0.27
$\pi \rightarrow \delta^*$	2.24	2.13	0.118×10^{-6}	0.34
$\sigma \rightarrow \delta$	2.79	2.51	0.827×10^{-4}	0.67

[a]Weight is the percent contribution of the major configuration to the wave function describing the excited state

Given the poor correspondence between theory and experimental excitation energies thus far, our next attempt to model the electronic spectrum included excited states belonging to both symmetry states A and B. Only the transitions with significant

oscillator strengths are shown in Table 5.6. The consideration of these additional wave functions resulted in two additional excitations.

Table 5.6: Selected Spin-Free Excitation Energies of $Fe_2(DPhF)_3$ for Octet Wave Functions Belonging to the A and B Symmetry States (All Transitions Correspond to $^8A \rightarrow {}^8A$ or $^8A \rightarrow$ 8B)

molecular orbital	state transition	ΔE (eV)	ΔE (cm^{-1})	oscillator strength (a.u.)	weight (%)[a]
$\pi^{\mathrm{A}} \rightarrow \delta^{\mathrm{A}}$	$^8A \rightarrow {}^8A$	1.66	13,400	0.14 × 10−3	54
$\pi^{\mathrm{A}} \rightarrow \delta^{\mathrm{B}}$	$^8A \rightarrow {}^8B$	1.56	12,560	0.13 × 10−3	45
$\pi^{\mathrm{A}} \rightarrow \delta^{*\mathrm{B}}$	$^8A \rightarrow {}^8B$	1.91	15,370	0.29 × 10−3	24

[a]Weight is the percent contribution of the major configuration to the wave function describing the excited state

Hence, three significant excited energies are predicted at 1.56, 1.66 and 1.91 eV, and they are interpreted as πA $\rightarrow$ δB, πA $\rightarrow$ δA, and πA $\rightarrow$ δ^*B transitions, respectively. Moreover, these computed energies agree well with the experimental spectrum from 18000 to 10000 cm^{-1}. The NIR band at 1250 nm (0.99 eV or 8000 cm^{-1}), however, remains unaccounted, prompting further investigation.

The Nature of the NIR Band at 8000 cm^{-1}

To better model the full Vis-NIR spectrum of $Fe_2(DPhF)_3$, spin-orbit coupling was taken into consideration. The most important excited energies correspond to transitions from pure (>99%) octet ground states (A) to octet-dominated excited states (84-97%) with limited mixing of the sextet configurations. Details of the prominent excited energies are available in the Supporting Information, Table 1. Because of the limited mixing, the calculated excited energies with spin-orbit coupling are essentially identical to those obtained from the spin-free calculations. Therefore, the NIR band at 8000 cm^{-1} is not reproduced by considering spin-orbit coupling.

Another strategy is to increase the active space. An attempt to increase the active space with three additional high-lying MOs, however, was unstable. A stable active

space was eventually formed by adding three high-lying MOs while removing the energetically low-lying, doubly occupied σ MO to generate an (11, 15) configuration. The vertical excited energies now include a low energy absorption at 0.80 eV (6500 cm^{-1}), which is interpreted as $\pi \rightarrow \pi^*$ transition. Although this excited energy corresponds well to the NIR band, the $\pi \rightarrow \delta/\delta^*$ transition energies shift to lower energies of 1.00 eV and, consequently, worsens the holistic fit. Ideally, employing an even larger active space should result in more accurate excitation energies, but such calculations are currently too expensive. We tentatively interpret the NIR band as a $\pi \rightarrow \pi^*$ transition.

5.1.4 Conclusions

The nature of the Fe–Fe bond in $Fe_2(DPhF)_3$ is strongly ferromagnetic, which essentially arises from the presence of a series of close lying nonbonding and antibonding metal–metal orbitals that are populated according to Hunds rule. Because this type of metal–metal bond is so rare, our study is only one of a few in-depth case studies of strong ferromagnetic interactions via metal–metal bonds.[462,505] Because of the high-spin electronic structure of the $[Fe_2]^{3+}$ unit, the estimated Fe–Fe bond order is low at 1.15, in spite of the relatively short Fe–Fe bond length. The MO analysis reveals that all d-electrons are involved in metal–metal σ/σ^*, π/π^*, and δ/δ^* bonds. Though the octet ground spin state is dominant above room temperature, *d–d* transitions occur from the π to the π^*, δ, and δ^* orbitals in the visible and near-infrared regions. Surprisingly, these *d–d* transitions are remarkably weak in intensity and hence appear to be forbidden, even though the analysis shows that they are indeed both spin- and dipole-allowed. The electronic structure of the mixed-valent diiron complex is highly delocalized, and the two iron centers are spectroscopically equivalent. Perhaps these will prove to be common features among bimetallics with strong ferromagnetic metal–metal bonds as more examples emerge. Future work will also focus on studying the reactivity of these strongly ferromagnetic metal–metal bonds.[506,507]

5.1.5 Additional Information

Supplementary information is available in the online version of the paper. The Supporting Information includes: Additional spectroscopic characterization and computational details for $Fe_2(DPhF)_3$ (PDF, CIF). This material is available free of charge at `http://pubs.acs.org`. Correspondence and requests for materials should be addressed to E.B., L.G., and C.C.L. The authors declare no competing financial interests.

Acknowledgements

ConocoPhillips is gratefully acknowledged for providing a graduate fellowship to C.M.Z. X-ray diffraction studies were performed at the X-ray Crystallographic Laboratory in the Department of Chemistry (UM) directed by Dr. Victor Young, Jr. Computing support and resources were provided by the Minnesota Supercomputing Institute, and funding for this work was provided by the University of Minnesota. C.C.L. thanks Prof. Karl Wieghardt, Prof. Ted Betley (Harvard University), and Prof. John Berry (University of Wisconsin–Madison) for sharing their thoughts on metal–metal interactions.

5.2 Assessing Metal–Metal Multiple Bonds in Cr–Cr, Mo–Mo, and W–W Compounds and a Hypothetical U–U Compound: A Quantum Chemical Study Comparing DFT and Multireference Methods

To gain insights into the trends in metal–metal multiple bonding among the Group 6 elements, density functional theory has been employed in combination with multiconfigurational methods (CASSCF and CASPT2) to investigate a selection of bimetallic, multiply bonded compounds. For the compound [Ar-MM-Ar] (Ar=2,6-$(C_6H_5)_2$-C_6H_3, M=Cr, Mo, W) the effect of the Ar ligand on the M_2 core has been compared with the analogous [Ph-MM-Ph] (Ph=phenyl, M=Cr, Mo, W) compounds. A set of $[M_2(dpa)_4]$ (dpa=2,2'-dipyridylamide, M=Cr, Mo, W, U) compounds has also been investigated.

Adapted with permission from G. Li Manni, A. L. Dzubak, A. Mulla, D. W. Brogden, J. F. Berry, L. Gagliardi. *Chem. Eur. J.* 2012, *18*, 1737.[508] Copyright 2012, John Wiley and Sons. Additional information may be found in section 5.2.6.

All of the compounds studied here show important multiconfigurational behavior. For the Mo_2 and W_2 compounds, the $\sigma^2\pi^4\delta^2$ configuration dominates the ground-state wavefunction, contributing at least 75 %. The Cr_2 compounds show a more nuanced electronic structure, with many configurations contributing to the ground state. For the Cr, Mo, and W compounds the electronic absorption spectra have been studied, combining density functional theory and multireference methods to make absorption feature assignments. In all cases, the main features observed in the visible spectra may be assigned as charge-transfer bands. For all compounds investigated the Mayer bond order (MBO) and the effective bond order (EBO) were calculated by density functional theory and CASSCF methods, respectively. The MBO and EBO values share a similar trend toward higher values at shorter normalized metal–metal bond lengths.

5.2.1 Introduction

Ever since the discovery of the multiple metal–metal bond in $[Re_2Cl_8]^{2-}$,[509,510] there has been a considerable amount of research dedicated to metal–metal multiple bonding. Electron-rich metal–metal units are of general interest because of their unique electronic and optical properties.[511] Several new examples of metal–metal multiply bonded compounds incorporating the Group 6 metals have recently been of interest. For example, various groups have shown interest in oligothiophene compounds incorporating metal–metal multiple bonds because of their potential applications in optoelectronic and magnetic devices. Burdzinski *et al.*[512] recently prepared oligomers of empirical formula $[Mo_2(TiPB)_2(O_2C(Th)\text{-}C_4(n\text{-hexyl})_2S\text{-}(Th)CO_2)]$ (TiPB=2,4,6-triisopropyl benzoate; Th=thiophene) and compounds of formulae *trans*-$[Mo_2(TiPB)_2L_2]$ in which L=Th, BTh (Bth=2,2'-bithiophene-5-carboxylate) and TTh (the corresponding thienylcarboxylate), which are considered as models for the oligomers. The X-ray analysis of *trans*-$[Mo_2(TiPB)_2BTh_2]$ (**1**; Figure 5.7) revealed the presence of Lπ^*–M$_2\delta$–Lπ^* conjugation, and density functional theory (DFT) calculations indicated that the HOMO is mainly a M_2 δ orbital and the LUMO is mainly based on the thienylcarboxylate π^* orbitals.

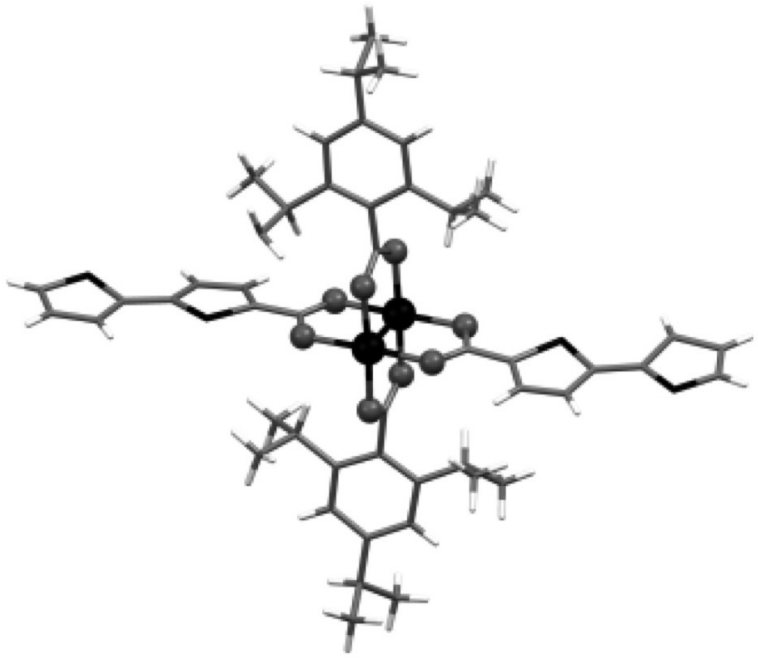

Figure 5.7: Experimentally determined structure of compound **1**. Color code: C=gray-capped stick, H=white-capped stick, S=black-capped stick, Mo=black ball, O=gray ball.

Burdzinski *et al.*[512] studied also the photophysical properties of these oligomers, which showed relatively slow metal-to-ligand charge-transfer (MLCT) triplet intersystem crossing compared to the majority of second- and third-row transition metal complexes. They noticed that the ^{1}MLCT–^{3}MLCT gap is relatively small in the Mo complexes, suggesting a large mixing of the metal δ and organic π systems. These Mo_2-based oligothiophenes have thus a unique metal-based triplet emission.

Alberding *et al.*[511] prepared the [MM'$(TiPB)_4$] compounds, in which M=Mo or W and M'=W and characterized them with various techniques. Electronic absorption, steady-state emission and transient absorption spectroscopy indicate that these compounds have strong absorptions in the visible region that are assigned to MM' δ to arylcarboxylate π^* transitions, ^{1}MLCT. Luminescence from two excited states also occurs, which are assigned as the ^{1}MLCT and ^{3}MM' δ–δ^* states.

Nippe *et al.*[513] reported the synthesis of [W_2(dpa)$_4$] (dpa=2,2'-dipyridylamide) (**2c**)

(Figure 5.8) and its characterization by X-ray crystallography and cyclic-voltammetry. They compared it with its earlier reported molybdenum analogue, $[Mo_2(dpa)_4]$ (**2b**).[514] They also synthesized one-electron oxidation products of $[W_2(dpa)_4]$ and $[Mo_2(dpa)_4]$, namely $[W_2(dpa)_4][BPh_4]$ and $[Mo_2(dpa)_4][BPh_4]$ (BPh_4=tetraphenylborate). The crystallographically determined metal–metal distances of 2.23 and 2.14 Å in $[W_2(dpa)_4][BPh_4]$ and $[Mo_2(dpa)_4][BPh_4]$, respectively, are in agreement with metal–metal bond orders of 3.5. The molecules $[W_2(dpa)_4]$ and $[Mo_2(dpa)_4]$ have been utilized along with the $[Cr_2(dpa)_4]$ analogue (**2a**) to prepare linear, trinuclear heterometallic molecules with an M–M$\cdots$M' chain, with M=Cr, Mo, or W, and M'=Cr, Mn, Fe, Co, Ni, and Zn.[515,516,517,518,519] The heterometallic molecules show rich optical and redox properties, and a better understanding of these properties can be greatly facilitated by a quantum chemical analysis of the Cr_2, Mo_2, and W_2 precursor molecules.

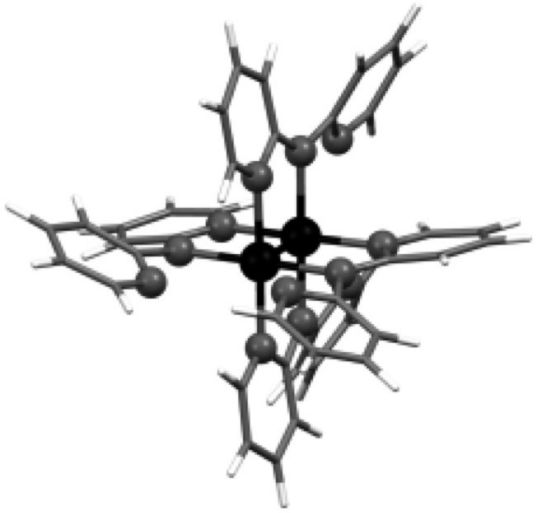

Figure 5.8: The experimental structure of compound 2c. Color code: C=gray-capped stick, H=white-capped stick, W=black ball, N=gray ball.

We have studied metal–metal multiple bonds in the Cr_2, Mo_2, and W_2 dimers by making use of the concept of effective bond order (EBO)[520,521,522,523] that arises from a multiconfigurational complete active space-SCF (CASSCF) wavefunction.[524] We have demonstrated that a sextuple bond exists in Mo_2 and W_2, but hardly in Cr_2.[520,521,525]

The weakness of the Cr–Cr bond is related to the difference in size between the $3d$ and $4s$ orbitals. The $4s$–$4s$ interaction occurs at a considerably longer distance than the $3d$–$3d$ interaction. This unbalance weakens the $3d$ bonds and makes the $4s$–$4s$ interaction repulsive at equilibrium geometry. Another important factor is the repulsive interaction between the closed $3p$ shells, which have about the same radial extension as the $3d$ orbitals. The unbalance between the s and d orbitals decreases for second-row transition metals and even more for the third row. Moreover, relativistic effects play an important role in making the two sets of orbitals more equal in size, which overall enhance the bond strength of the diatomics. Various low-valent Cr–Cr complexes recently synthesized present a multiple bond that, despite changes in the nature of the ligand or with the oxidation state of the Cr atom, yield EBO values in the relatively narrow range between 3.4 and 3.9 that correlate roughly with the Cr–Cr bond length.[526] In order to protect the dimetallic unit from possible oxidation or oligomerization, terphenyl ligands, the skeleton structure of which is 2,6-$(C_6H_5)_2$-C_6H_3 (Ar), have been employed to embed the metal dimer. Experimental and theoretical works have also shown that [Ar'-CrCr-Ar'] (**3a**, Figure 5.9) (Ar'=2,6-(2,6-iPr$_2$-C_6H_3)$_2$-C_6H_3) features a *trans*-bent geometry.[522,523,527,528,529] Since the Ar ligand successfully stabilizes dimers of main group elements and the Cr dimer, its capabilities in protecting dimers of Fe and Co were also investigated.[530,531,532] The flanking aryl/metal η^6 interaction makes the Fe–Fe and Co–Co bonds longer than in other compounds. In order to quantify the influence of the flanking aryl ring on the M–M bond, several simplified model systems containing a Co–Co and Fe–Fe core unit, but without ligands capable of giving η^6 interactions, were studied by DFT and CASSCF followed by perturbation theory to second order (CASPT2) and compared to the complexes featuring the η^6 interaction computed at the same level of theory.[529]

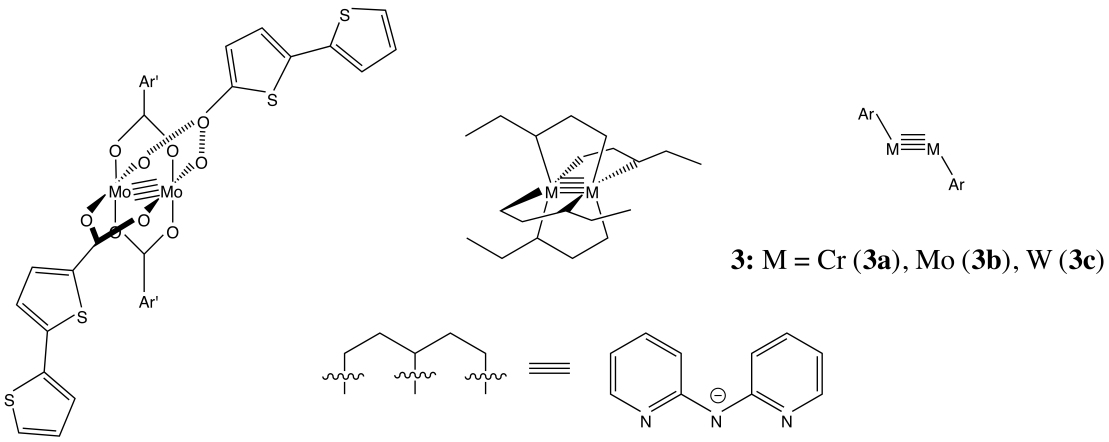

3: M = Cr (**3a**), Mo (**3b**), W (**3c**)

1: Ar' = 2,4,6-(*i*Pr)3C6H3 **2:** M = Cr (**2a**), Mo (**2b**), W (**2c**)

Figure 5.9: Compounds studied in this work.

In this paper we report the results of the study of several compounds containing Cr–Cr, Mo–Mo and W–W multiple bonds to reveal and interpret any generalized trends that may be present. First we will describe the trans-bent molecules [Ar-MM-Ar] (**3a**, M=Cr; **3b**, M=Mo; **3c**, M=W), for which the Mo and W analogs have not yet been synthesized up to date and have, to our knowledge, never been the subject of computational investigation. The effect of the Ar ligand on the different bimetallic units will be discussed and compared with the effect of phenyl (Ph) in the analogous [Ph-MM-Ph] compounds.

In the second part of the paper we will focus on the compounds synthesized by Burdzinski *et al.*[512] and Nippe *et al.*,[513] compounds **1** and **2**, respectively. We will report the results of our theoretical calculations on the Mo–Mo type **1** compound. For compounds **2** we will discuss the Cr–Cr, Mo–Mo and W–W species, **2a**, **2b**, and **2c**, respectively. In all cases our results will be compared with experimental data. Finally, we will discuss the hypothetical U–U equivalent of **2**, which, if synthesized, would represent a breakthrough in diuranium chemistry.[533,534,535] The aim of this study is to understand the nature of the metal–metal bonds in these compounds by a multiconfigurational quantum chemical characterization, inspect the most significant spectroscopic transitions and predict whether compound of type **2** containing a U–U

unit could also exist. Where possible, we include results from DFT calculations in addition to the CASPT2 results, so that comparisons between the two methods may be made. We also include a discussion of calculated metal–metal bond orders, which are particularly problematic since computations typically yield non-integer bond orders that differ significantly from what one expects from simple molecular orbital theory.

5.2.2 Computational Methods

The [Ph-MM-Ph] and [Ar-MM-Ar] species (M=Cr, Mo, W)

Initial geometry optimizations were performed at the DFT level of theory using the TURBOMOLE quantum chemistry software.[536] The PBE functional[537] was employed along with the triple-zeta valence plus polarization (def-TZVP) basis set on all the atoms. Vibrational frequency calculations were also performed in order to verify the nature of the stationary points. All structures reported in this study are local minima with all real frequencies, with the exception of the Ph-MM-Ph compounds, which exhibit two imaginary frequencies. Even if the planar [Ph-MM-Ph] structures are not local minima, we decided to characterize their electronic structure in order to compare them with the [Ar-MM-Ar] analogues. The DFT-optimized coordinates are reported in the Supporting Information for all the systems described in this study.

The multiconfigurational complete active space-SCF method[538] followed by second-order perturbation theory (CASSCF/CASPT2)[539] was employed to re-optimize selected bond lengths, namely the M–M (M=Cr, Mo and W) and M–C bonds. A numerical optimization procedure was employed, which consisted of varying the M–M and M–C distances, optimizing the structures at the DFT level while keeping the M–M and M–C distances fixed, and performing CASPT2 calculations at these geometries. Numerical gradients and hessians on the CASPT2 potential-energy surfaces were then computed to check the nature of the stationary points.

The CASSCF/CASPT2 calculations were performed using the MOLCAS-7.3 package.[540] Basis sets of the atomic natural orbital type[541,542] with triple-zeta plus polarization quality (ANO-RCC-VTZP) were used for the transition metal atoms, whereas basis sets of double-zeta basis set quality (ANO-RCC-VDZP) were used for the other

atoms. Scalar relativistic effects were included using the Douglas-Kroll-Hess Hamiltonian.[543] The two-electron integral evaluation was simplified by employing the Cholesky decomposition technique.[544,545,546] The decomposition threshold was chosen to be 10^{-4}, as this should correspond to an accuracy in total energies of the order of mHartree or higher. At the CASPT2 level of theory the frozen natural orbital approach with 70 % of the virtual orbitals taken into account was applied (FNO-CASPT2) to reduce the computational costs.[547] In order to prevent weak intruder states an imaginary shift of 0.2 units was added to the external part of the zero-order Hamiltonian. For all the investigated species, at the CASPT2 level, the $1s$ orbitals for all C atoms were kept frozen; moreover, for the [Ph-MoMo-Ph] compound orbitals up to and including the $3d$ for Mo atoms were kept frozen; for [Ph-WW-Ph] compound orbitals up to and including $4d$ for W atoms were kept frozen; for the [Ar-CrCr-Ar] only orbitals up to $2p$ for Cr were kept frozen, whereas for [Ar-MoMo-Ar] and [Ar-WW-Ar] orbitals up to $3d$ and $4d$, respectively, were kept frozen. At the CASSCF level, for all the species the active space contains 14 electrons distributed in 14 orbitals, CAS(14,14). This active space comprises all the nd (n=3, 4, or 5) orbitals forming the M–M multiple bond as well as two bonding and two antibonding orbitals describing the M–C interaction. Six active electrons come from each M atom, corresponding to the valence configuration nd^5 $(n+1)s^1$ (n=3, 4, and 5), and one electron comes from each C atom bonded to the transition metal, adding up to 14 electrons in total.

Calculations were performed on the ^1A_g ground state. In the [Ph-MM-Ph] calculations the geometries of the systems were constrained to C_{2h} symmetry, while in the [Ar-MM-Ar] calculations they were constrained to C_2 symmetry. For all species under investigation we have computed the effective bond order (EBO)[520,521,548] which quantifies the formation of a chemical bond from CASSCF wavefunctions. For a single bond the EBO is given by Equation 5.2, in which η_{b} and η_{ab} are the sums of the occupation numbers of the bonding and anti-bonding molecular orbital pair derived from the CASSCF wavefunction.

$$\mathrm{EBO} = \left(\eta_{\mathrm{b}} - \eta_{\mathrm{ab}}\right)/2 \tag{5.2}$$

In multiply bonded systems one has to add up the individual values generated from the various pairs of bonding and antibonding orbitals (e.g., σ, π, and δ) to obtain the total EBO. Note that η_{b} and η_{ab} can assume any value between zero and two and are

not necessarily integer numbers. Equation 5.2 thus implies that the EBO value will always be lower or at most equal to the bond order that one obtains from conventional molecular orbital theory, for which the orbitals have an occupation number always equal to either 2, 1, or 0.

There are various ways of quantifying bond orders.[549,550,551] The EBO concept relies on a multiconfigurational wavefunction and takes into account the effect of electron correlation involving the antibonding orbitals. Moreover, if used in combination with ANO basis sets optimized for multiconfigurational calculations (as done in this study), it provides stable values.

We have previously employed the CASSCF/CASPT2 approach to study several metal–metal multiply bonded species like the $[Re_2Cl_8]^{2-}$ system,[552] the octamethyldimetalate compounds of Cr^{II}, Mo^{II}, W^{II}, and Re^{III},[553] the octabromoditechnetate(III) compound[554] and the triply bonded $[Tc_2X_4(PMe_3)_4]$ (X=Cl, Br) complexes.[555] In all cases the approach has proven to be successful in describing the electronic structure of such compounds and the metal–metal multiple bond, because of its ability to describe the electronic structure of multiconfigurational species.

The Burdzinski Mo–Mo species

The original coordinates of **1** were obtained from the X-ray data.[512] In our calculations, the TiPB ligands were replaced with formate groups and the BTh groups with the simpler Th ones; this approximation was found to be adequate, because the external groups play mainly a steric role. As already discussed in Burdzinski *et al.*[512] the extension of the length of the thienyl groups may, on the other hand, affect the electronic structure of the Mo–Mo unit. In this context, however, we decided to focus on the simplest case. The reduced structure (Figure 5.10) was used for all subsequent calculations. The molecule has C_{2h} symmetry, which was maintained throughout all calculations.

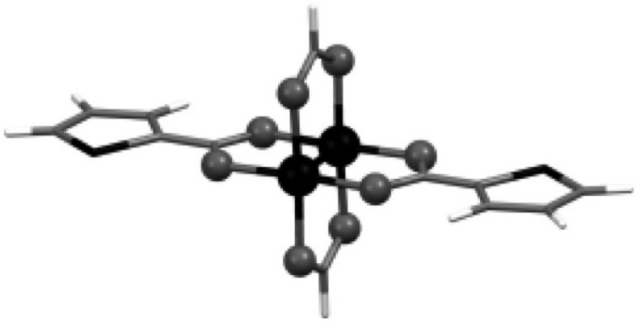

Figure 5.10: Simplified structure of 1 used for all calculations. Color code: C=gray capped stick, H=white capped stick, S=black capped stick, Mo=black ball, O=gray ball.

A DFT geometry optimization was performed for the singlet ground state using the PBE functional and the Stuttgart RSC 1997 ECP basis set, within Gaussian 09.[556] Subsequent CASSCF/CASPT2 single-point calculations (with ANO-RCC-VTZP type basis sets) were performed at the PBE-optimized geometry. The Mo–Mo bond was successively re-optimized at the CASPT2 level by using a numerical optimization procedure, analogous to the one described in the previous section. Several CASSCF calculations were initially performed in order to select the appropriate active space for this system and it was found that a reasonable active space for the ground state consists of eight active electrons in eight active orbitals. These orbitals are bonding and antibonding linear combinations of Mo 4*d* orbitals with σ, π and δ symmetry (the Results section for a detailed description) and they are localized on the Mo_2 unit. The two remaining MOs arising from the linear combination of the fifth 4*d* orbital on each Mo atom were not included in the active space because they are not in the HOMO-LUMO region and they are mainly metal-ligand orbitals. No metal-ligand (M-L) orbitals were included in the active space. In the [Ar-MM-Ar] case, it was not an issue of computational cost to include the M-L bonding and antibonding orbitals. In this case, on the other hand, including the M-L bonding and antibonding orbitals would add at least 16 orbitals to the active space, which would not be computationally tractable. The smaller active space of eight in eight is still satisfactory, as the multiconfigurational character is mainly localized in the Mo_2 unit and the ML interaction can be adequately treated

at the subsequent PT2 level. The lowest excited singlet and triplet states were also computed.

$[M_2(dpa)_4]$ (M=Cr, Mo, W) species

Initial coordinates for the geometry optimization of $[Cr_2(dpa)_4]$ (**2a**) were obtained from the crystallographic data for the compound in its crystal form that contains no solvent molecules.[550] Initial coordinates of $[Mo_2(dpa)_4]$ (**2b**) were obtained from Suen *et al.*[514] and initial coordinates for $[W_2(dpa)_4]$ (**2c**) were obtained from the Supporting Information of Nippe *et al.*[513] Geometry optimization and frequency calculations for **2a-c** were performed using the TURBOMOLE software package and the PBE functional. The def2-TZVP basis set was employed for N, Cr, Mo, and W atoms and the SV(P) basis set was used for all other atoms. In the CASSCF/CASPT2 calculations an ANO-RCC-TZVP basis set was used for N, Cr, Mo, and W, and the ANO-RCC-DZVP basis set was used for all other atoms. The molecules have C_2 symmetry, which was maintained throughout all calculations, except the $[Cr_2(dpa)_4]$ geometry optimization, for which D_2 symmetry was imposed. Molecular orbitals included in the active space are reported in the Supporting Information. TD-DFT calculations were performed using Gaussian 09, Revision B.0147 using the PBE functional. The StuttgartDresden electron core potential (SDD) was used for Cr, Mo, and W atoms. The TZVP basis set was employed for C and N atoms, and the SVP basis set for H atoms. Compositions of molecular orbitals and Mayer bond orders were calculated using the AOmix program.[557,558]

In the CASSCF calculations an active space of eight electrons in eight orbitals was chosen in analogy with the Burdzinski Mo–Mo calculation. These orbitals are linear combinations of $3d$, $4d$, and $5d$ orbitals with σ, π and δ symmetry for $[Cr_2(dpa)_4]$, $[Mo_2(dpa)_4]$ and $[W_2(dpa)_4]$, respectively (see the Results section for a detailed description). Also in this case two MOs arising from the $4d$ orbitals were not included in the active space, because they are not in the HOMO-LUMO region and they are delocalized between the metal and the ligand. Due to the larger than normal discrepancy of the DFT bond length with experiment, we optimized the W–W bond length at the CASPT2 level by following the same numerical procedure as for the other compounds. We computed several singlet and triplet excitations and their intensity, including spin-orbit coupling among the various states. The intensities and spin-orbit coupling were

determined by employing the complete active space state interaction method, CASSI[559] which employs an effective one-electron spin-orbit (SO) Hamiltonian, based on the mean field approximation of the two electronic parts.[560]

5.2.3 Results

[Ph-MM-Ph] (M=Cr, Mo, W)

The most relevant structural parameters of the DFT- and CASPT2-optimized [Ph-MM-Ph] systems in their ^1A_g ground state are reported in Table 5.7. Figure 5.11 depicts the DFT-optimized structure of [Ph-MoMo-Ph], the CrCr and WW analogues look similar. DFT predicts the Mo–Mo and W–W bond lengths to be 0.05 and 0.07 Å, respectively, longer compared to the corresponding CASPT2 values. The DFT and CASPT2 M–C predicted bond lengths differ by at most 0.01 Å.

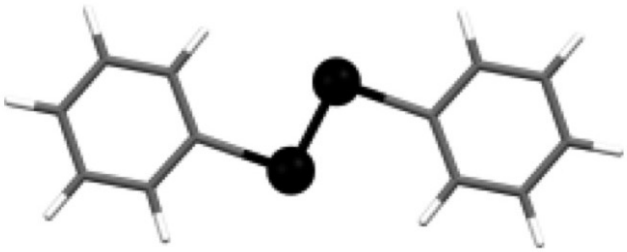

Figure 5.11: DFT structure of [Ph-MoMo-Ph]; Color code: C=gray capped stick, H=white capped stick, Mo=black ball.

Table 5.7: Most Significant Structural Parameters and Bond Order for the [Ph-MM-Ph] Systems

system/ theory	M–M (Å)	M–C (Å)	M-M-C (°)	BO[b]
[Ph-CrCr-Ph]				
DFT[a]	1.707	2.033	94.3	
CASPT2[a]	1.752	2.018	88.4	3.52
[Ph-MoMo-Ph]				
DFT	2.059	2.098	97.9	4.55
CASPT2	2.010	2.107	97.3	4.26
[Ph-WW-Ph]				
DFT	2.154	2.087	100.4	4.57
CASPT2	2.080	2.097	99.4	4.32

[a]From Brynda *et al.*[522,523] and La Macchia *et al.*[529]
[b]Mayer bond order from DFT and EBO from CASPT2

For [Ph-MoMo-Ph] the CASSCF calculation predicted natural orbital occupation numbers reported in the Supporting Information, which provide an EBO of 4.26. Inspection of the multideterminantal CASSCF wavefunction shows that the closed shell configuration, $\sigma_g^2\pi_u^4\delta_g^4$, dominates with a weight of 68 %, which corresponds to a formal quintuple bond. A few other configurations contribute with weights lower than 5 %; which correspond to double excitations from the bonding orbitals to their antibonding counterparts. For [Ph-WW-Ph], natural orbitals are reported in the Supporting Information with an EBO equal to 4.32. The closed shell $\sigma_g^2\pi_u^4\delta_g^4$ configuration, corresponding to a formal quintuple bond, is also dominant in this case with a weight of about 70 %. The EBO for [Ph-CrCr-Ph] reported in our prior studies[522,523,529] is equal to 3.52 and in this case the closed shell configuration has a weight of only 45 %. In the Mo–Mo and W–W compounds the calculated metal–metal bond order is about one unit larger than in the corresponding Cr–Cr compound. The same trend occurs in the diatomic molecules.[520,521]

[Ar-MM-Ar] (M=Cr, Mo, W) systems

While [Ar'-CrCr-Ar'] (**3a**) (Ar'=2,6-(2,6-iPr$_2$-C$_6$H$_3$)2-C$_6$H$_3$) has been synthesized,[527] the MoMo and WW analogues, **3b** and **3c**, have not been synthesized to date. In our study we employed Ar (2,6-(C$_6$H$_5$)$_2$-C$_6$H$_3$) as a simplified model for Ar'. Vibrational frequency analysis indicates that all three [Ar-MM-Ar] compounds are local minima on their potential-energy surface.

The most relevant structural parameters of the DFT- and CASPT2-optimized [Ar-MM-Ar] compounds in their ^1A_g ground state are reported in Table 5.8. Figure 5.12 depicts the DFT-optimized structure of **3a**; **3b** and **3c** analogues look similar.

Table 5.8: Most Significant Structural Parameters and Bond Order for the [Ar-MM-Ar] Systems

system/ theory	M–M (Å)	M–C (Å)	M–C$_{aryl}$ (Å)	M-M-C (°)	C-M-M-C (°)	BO[b]
[Ar-CrCr-Ar]						
DFT	1.729	2.086	2.260	101.6	164.9	3.82
CASPT2	1.836	2.132	2.258	99.2	180.0	3.07
exp[a]	1.8351(4)	2.131(1)	2.294(1)	102.78(1)	180[c]	
[Ar-MoMo-Ar]						
DFT	2.464	2.142	2.304	112.9	124.0	3.85
CASPT2	1.980	2.217	2.409	96.2	162.2	4.30
[Ar-WW-Ar]						
DFT	2.419	2.160	2.374	104.6	134.9	3.25
CASPT2	2.250	2.161	2.376	96.6	176.4	4.33

[a] From Nguyen *et al.*[527]
[b] Mayer bond order from DFT and EBO from CASPT2
[c] This angle is required to be 180° due to crystallographic symmetry

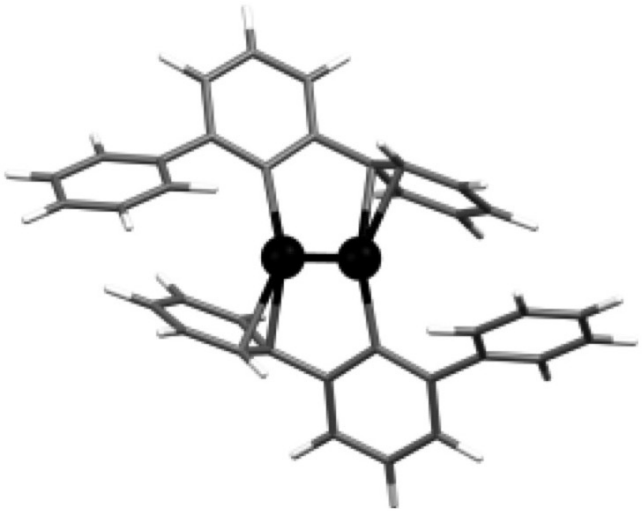

Figure 5.12: DFT structure of [Ar-CrCr-Ar]; Color code: C=gray capped stick, H=white capped stick, Cr=black ball.

The DFT value for the Cr–Cr distance in **3a** is about 0.1 Å shorter than the experimental value, while the CASPT2 Cr–Cr distance is in better agreement with experiment. The structure of **3a** was fully optimized at the DFT level by imposing only the constraints of C_2 symmetry instead of C_{2h}, and this is the reason why the DFT-optimized structure has a nonplanar C-Cr-Cr-C dihedral angle. On the other hand, CASPT2 predicts the structure with the planar C-Cr-Cr-C dihedral angle to lie 11.5 kJ mol^{-1} lower in energy than the structure with the dihedral angle of 166.7 (the DFT-relaxed structure with the M–M and M–C fixed). Overall the potential-energy surface for [Ar-CrCr-Ar] is quite flat both along the Cr–Cr coordinate and also the Cr C coordinate.

The occupation numbers for the natural orbitals (reported in Supporting Information) that make up the Cr–Cr bond provide an EBO of 3.07, similar to what is found for [Ph-CrCr-Ph]. The closed shell configuration, $\sigma_g^2\pi_u^4\delta_g^4$, corresponding to a formal quintuple bond, appears in the multiconfigurational wavefunction with a weight of only 33 %. The second most important configuration, $\sigma_g^2\pi_u^4\delta_g^2\delta_u^2$, has a weight of 8 %.

For **3b**, DFT predicts a Mo–Mo bond length almost 0.5 Å longer than CASPT2. This difference is mostly due to the fact that DFT predicts a strong Moaryl η^6 interaction, while CASSCF and CASPT2 predict a weaker one. The CASSCF molecular orbitals

are not delocalized between the Mo and aryl fragments. The occupation numbers for the natural orbitals (reported in Supporting Information) that make up the Mo–Mo bond provide an EBO of 4.3, similar to that found for [Ph-MoMo-Ph]. The closed shell configuration, $\sigma_g^2\pi_u^4\delta_g^4$, corresponding to a formal quintuple bond, dominates the multiconfigurational wavefunction with a weight of 70 %. Overall the potential-energy surface for [Ar-MoMo-Ar] is less flat both along the Mo–Mo reaction coordinate and the Mo–C reaction coordinate than the corresponding [Ar-CrCr-Ar] potential-energy surface.

For **3c**, the DFT W–W bond length is 0.17 Å longer than the CASPT2 bond length. The occupation numbers for the natural orbitals (reported in Supporting Information) that make up the W–W bond provide an EBO of 4.3. Analogously to the prior cases, the closed shell configuration, $\sigma_g^2\pi$u4δg4, which corresponds to a formal quintuple bond, dominates the multideterminantal wavefunction with a weight of 69 %.

A closer inspection of EBO values and weights of the dominating electronic configurations indicates that the magnitude of the M–M bond order goes as: Cr<Mo≈W, in agreement with the trend found for the simpler [Ph-MM-Ph] models and for the diatomic molecules.[520,521,548] The relative bond order is maintained along the series as Ph is replaced by Ar: the Mo–Mo and W–W bond orders are about one unit larger than the Cr–Cr bond order.

At the CASPT2 level the Cr–Cr bond is 0.08 Å longer in **3a** than in [Ph-CrCr-Ph], while the EBO remains the same. Steric encumbrance might be the reason for this bond lengthening. DFT predicts a larger effect on the Mo–Mo and W–W bonds due to the flanking aryl groups than does CASPT2.

The Burdzinski Mo–Mo system

The most significant structural parameters of our theoretical study on compound **1** (Figure 5.10), experimentally synthesized by Burdzinski *et al.*,[512] are reported in Table 5.9.

Table 5.9: Structural Parameters and Bond Order for Compound **1**

theory	Mo–Mo (Å)	M–O^b_{form} (Å)	M–$O_{S\text{-}side}$ (Å)	M–$O_{non\text{-}S\text{-}side}$ (Å)	Mo-Mo-O (°)	BO[c]
DFT	2.168	2.105	2.087	2.082	91.6–91.8	3.44
CASPT2	2.068	2.107	2.089	2.084	93.0–93.2	3.40
exp[a]	2.1032(6)	2.1093	2.1053	2.1033	90.9–92.8	

[a]From Burdzinski *et al.*[512]
[b]Oxygen atoms of the formate group
[c]Mayer bond order from DFT and EBO from CASPT2

The DFT/PBE Mo–Mo distance is on the larger side of the experimental value, while the CASPT2 value is slightly smaller. The ground state is a singlet ^1A_g state. The wavefunction is dominated, about 75 %, by the Hartree–Fock $\sigma_g^2\pi_u^4\delta_g^4$ configuration; the second most important configuration, about 7 %, corresponds to a double excitation. natural orbitals and their occupation number are reported in Figure 5.13.

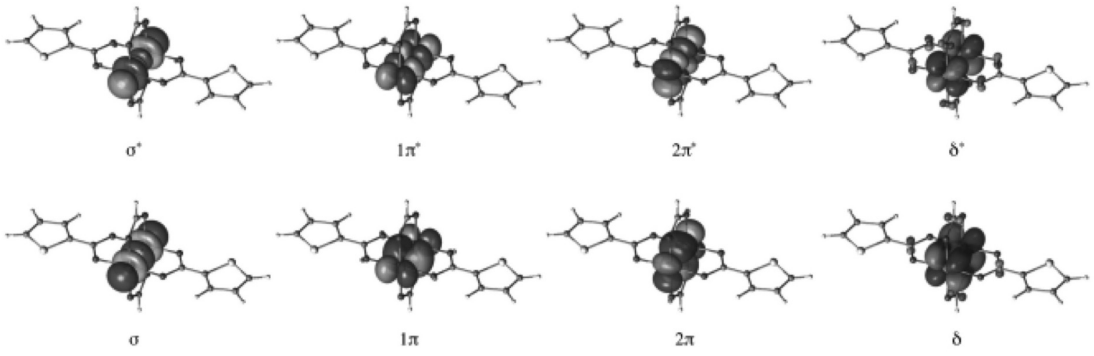

Figure 5.13: Natural orbitals for the ^1A_g ground state of compound **1**.

The EBO at the equilibrium bond length is equal to 3.4, which is very similar to the Mayer BO (3.44) calculated from DFT. In previous DFT calculations on this system,[512] the HOMO was found to be primarily of Mo_2 δ character, and the LUMO of Mo_2 δ^* character. This description is supported by inspection of the natural orbital occupation numbers for the ground state.

The excitation energies for the lowest singlet and triplet states and their electronic configurations are reported in Table 5.10. Burdzinski *et al.*[512] performed time-dependent DFT calculations which predicted the lowest-energy electronic transitions of high intensity to correspond to Mo_2 $\delta \rightarrow$ligand π^* and to move to lower energy with increasing number of rings. In the present study we determined only metal-based excitations because the orbitals included in the active space are exclusively metal based. The lowest Mo_2 $\delta \rightarrow Mo_2$ δ^* singletsinglet excitation is predicted to occur at 3.08 eV. The lowest singlet-triplet Mo_2 $\delta \rightarrow Mo_2$ δ^* excitation occurs at 1.61 eV. These values are consistent with experimental data for Mo_2 carboxylates, which show δ–δ^* transitions at about 2.85 eV.52

Table 5.10: Excitation Energies for the Lowest Singlet and Triplet States of Compound **1** and Their Electronic Configurations

state		$E(eV)$	configuration
S1	^1A_g	0.00	75% $\sigma^2\pi^4\delta^2$
T1	^3B_u	1.61	83% $\sigma^2\pi^4\delta^1\delta^{*1}$
S2	^1B_u	3.08	74% $\sigma^2\pi^4\delta^1\delta^{*1}$
T2	^3A_g	3.17	79% $\sigma^2\pi^4\delta^1\pi^{*1}$
T3	^3B_g	3.18	78% $\sigma^2\pi^4\delta^1\sigma^{*1}$
S4	^1B_g	3.62	83% $\sigma^2\pi^4\delta^1\sigma^{*1}$
S3	^1A_g	3.65	81% $\sigma^2\pi^4\delta^1\pi^{*1}$
T4	^3A_u	3.78	82% $\sigma^1\pi^4\delta^2\delta^{*1}$
S5	^1A_u	4.17	83% $\sigma^1\pi^4\delta^2\delta^{*1}$

$[M_2(dpa)_4]$ (M=Cr, Mo, W) species

Initially, a DFT geometry optimization of $[Cr_2(dpa)_4]$ (**2a**) was performed starting from the experimental geometry. The calculated geometric parameters are shown in Table 5.11, where they are compared to experimental values. The optimized Cr–Cr distance, 1.91 Å is very close to the experimental value of 1.94 Å and the calculated Mayer bond order is 3.26. The DFT geometry optimization reproduces well the Cr–N_a (2.05

Å), Cr–N_{py} (2.07 Å), and the nonbonding Cr$\cdots$N distances to the dangling pyridine groups (2.96 Å vs. experimental distances of 2.92 Å). Cotton and co-workers have defined a direction angle (ξ) as the angle between the pyridine plane and the Cr–N_a bond vector, as a means of evaluating the degree of electron donation from the dangling pyridine lone pair into the Cr_2 π^* orbital.[561] As ξ deviates from 0°, lone-pair/π^* overlap diminishes due to misdirection of the pyridine group. The sum of the direction angles, Σ ξ, for **2a** is experimentally found in the range of about 100-120°, signifying little N lone-pair overlap with the Cr_2 π^* orbitals.[562] The geometry optimization slightly underestimates the observed Σ ξ values at 81.2°. It is possible therefore that DFT may slightly overestimate electron delocalization between the free pyridine lone pairs and the Cr_2 unit. The long Cr N_{py} distance of 2.96 Å suggests, however, that such electron delocalization will be minimal. CASPT2 single-point calculations were performed at the DFT-optimized geometry. The ground-state wavefunction is highly multiconfigurational leading to an EBO of 3.25. The $\sigma^2\pi^4\delta^2$ configuration is found to account for 36 % of the ground state wavefunction. The second major contributing configuration $\pi^4\delta^2\delta^{*2}$ has a weight of 17 %.

Table 5.11: Calculated and Experimental Structural Data for $[Cr_2(dpa)_4]$,[561] $[Mo_2(dpa)_4]$,[514] and $[W_2(dpa)_4]$.[513] Average Values are Reported for All Structural Data Except for the M–M Distance for Which There is a Unique Value. Bond Lengths in (Å), Dihedral Angles in (°)

	M–M	M–N_a	M–N_{py}	M$\cdots$$N_{py}$	N_a-M--M-N_{py}	M-N_a--C-N_{py}	$\Sigma\xi$	Mayer BO	EBO
2a									
DFT	1.914	2.052	2.069	2.96	18.8	20.3	81.2	3.26	3.25
exp	1.943(2)	2.054(5)	2.068(5)	2.92(6)	5.1(2)	25.9(6)	104(3)		
$2CH_2Cl_2$	1.940(1)	2.045(3)	2.074(3)	2.92(3)	7.4	30.9	124(2)		
2b									
DFT	2.109	2.163	2.174	2.96	1.9	25.5	101.8	3.00	3.4
exp	2.097(1)	2.166(3)	2.178(3)	2.97	3.4	26.05	104		
2c									
DFT	2.241	2.173	2.175	2.92	1.0	24.7	98.8	2.98	
CASPT2	2.251	2.159							3.52
exp	2.1934(4)	2.132(5)	2.132(5)	2.932(5)	3.6(2)	26.7(5)	106.8		

The electronic absorption spectrum of **2a** (Figure 5.14) is characterized by a single peak at 522 nm. TD-DFT calculations were performed at the optimized geometry predicting a singlet δ–δ^* transition at 692 nm and two degenerate ligand-to-metal charge-transfer transitions at 554 nm (Figure 5.15). CASPT2 vertical excitation energies for the lowest singlet and triplet excited states with their intensities are reported in Table 5.12. In accordance with the multireference nature of **2a**, the lowest energy excitation to the triplet δ–δ^* state is calculated to be only 0.61 eV (ca. 4900 cm^{-1}; 2000 nm) above the ground-state energy level. This transition is forbidden and has zero calculated intensity. The singlet σ^2–δ^{*2} state (S2) at 348 nm is also calculated to have essentially zero intensity, since it is essentially a two-electron excitation. The higher energy excited states involve promotion of one of the σ electrons, though these bands are predicted in the UV and would not be observable due to concealment by charge transfer bands.

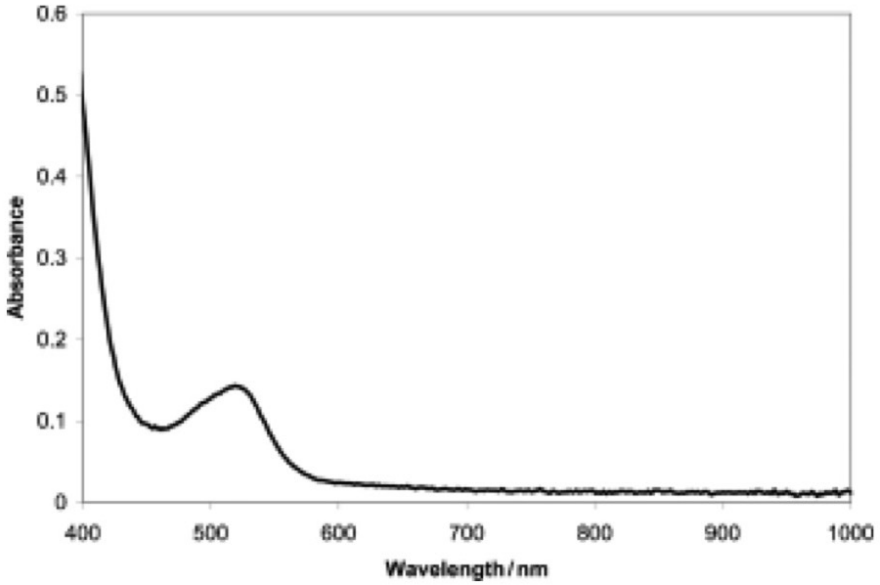

Figure 5.14: Electronic absorption spectrum of $[Cr_2(dpa)_4]$ (**2a**)

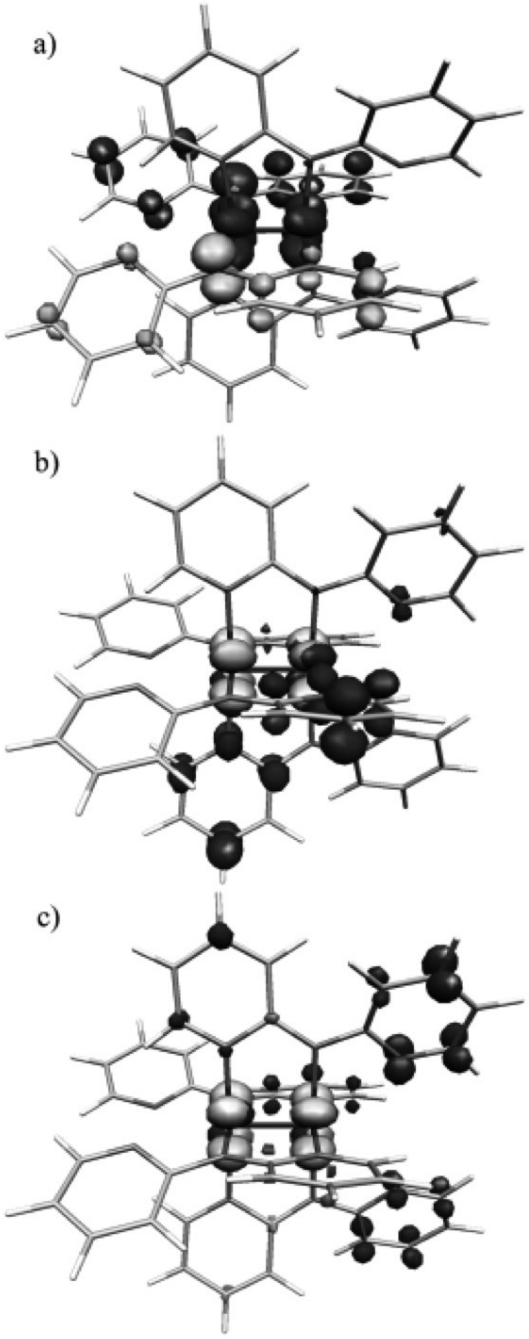

Figure 5.15: (a) Ligand-to-metal charge-transfer orbitals for $[Cr_2(dpa)_4]$ (b) Metal-to-ligand charge-transfer orbitals for $[Mo_2(dpa)_4]$ (c) Metal-to-ligand charge-transfer orbitals for $[W_2(dpa)_4]$. Black represents donating orbitals. Gray represents accepting orbitals.

Table 5.12: Excitation Energies from S1 in eV and nm for the Lowest Singlet and Triplet States (in D_2 Point Group), Intensities, and Their Electronic Configurations for $[Cr_2(dpa)_4]$ (**2a**)

state		E (eV)	intensity	E (nm)	configuration
S1	^1A	0.00		0	36% $\sigma^2\pi^4\delta^2$
					17% $\pi^4\delta^2\delta^{*2}$
T1	$^3B_3$	0.61	0.0	2000	90% $\sigma^2\pi^4\delta^1\delta^{*1}$
S2	^1A	3.56	0.2×10^6	348	28% $\pi^4\delta^2\delta^{*2}$
					13% $\sigma^2\pi^4\delta^2$
					12% $\sigma^1\pi^4\delta^2\delta^{*1}$
T2	^3A	3.69	0.7×10^5	336	92% $\sigma^2\pi^4\delta^1\delta^{*1}$
S3	$^1B_3$	3.71	0.2×10^3	335	55% $\sigma^1\pi^4\delta^2\pi^{*1}$
S4	$^1B_3$	3.75	0.2×10^3	331	45% $\sigma^1\pi^4\delta^2\delta^{*1}$
S5	$^1B_1$	3.83	0.2×10^4	324	55% $\sigma^1\pi^4\delta^2\delta^{*1}$

A DFT geometry optimization was performed on $[Mo_2(dpa)_4]$ **2b**, starting from the experimental geometry and then single-point energy calculations were performed at this optimized geometry at the CASPT2 level of theory. The optimized Mo–Mo bond length of 2.11 Å is in very good agreement with the experimentally determined distance of 2.10 Å. The calculated Mo–N bond lengths all agree with those determined crystallographically to within 0.01 Å. The calculated sum of the direction angles $\Sigma\ \xi$=101.8° also agrees very well with the experimental value of 104°. CASPT2 calculations reveal the ground-state wavefunction to be dominated by the closed-shell $\sigma^2\pi^4\delta^2$ electronic configuration, about 75 %, leading to an EBO equal to 3.4. DFT predicts a slightly lower Mayer bond order of 3.0.

The electronic absorption spectrum of **2b** (see Supporting Information) is characterized by intense transitions at 585 and 500 nm, and higher energy, <400 nm, absorptions. TD-DFT calculations predict the singlet δ–δ^* transition to be at 710 nm, which is unreasonably low in energy, and a doubly degenerate metal-to-ligand charge-transfer transition is predicted at 622 and 623 nm (Figure 8). The CASPT2 calculated absorption

energies, with their intensities are reported in Table 5.13. The singlet δ–δ^* transition is predicted to be at 431 nm.

Table 5.13: Excitation Energies from S1 in eV and nm for the Lowest Singlet and Triplet States, Intensities, and Their Electronic Configurations for $[Cr_2(dpa)_4]$ (**2b**)

state		E (eV)	intensity	E (nm)	configuration
S1	^1A	0.00		0	75% $\sigma^2\pi^4\delta^2$
T1	^3A	1.30	0.0	955	80% $\sigma^2\pi^4\delta^1\delta^{*1}$
S2	^1A	2.88	0.7×10^2	431	73% $\sigma^2\pi^4\delta^1\delta^{*1}$
T2	^3A	3.23	0.0	384	82% $\sigma^2\pi^4\delta^1\delta^{*1}$
S3	^1A	3.45	0.0	360	82% $\sigma^2\pi^4\delta^1\delta^{*1}$

The electronic structure of $[W_2(dpa)_4]$ (**2c**) was investigated in a similar fashion. A DFT geometry optimization of **2c** was performed followed by a re-optimization of the W–W distance at the CASPT2 level of theory. The most significant structural parameters are reported in Table 5.11, where they are compared to experimental results. CASPT2 calculations reveal that the ground-state wavefunction is dominated by the $\sigma^2\pi^4\delta^2$ electronic configuration, about 76 %, resulting in a EBO equal to 3.52. The Mayer BO calculated by DFT is lower at 2.98.

The vertical excitation energies for the lowest singlet and triplet excited states, with their intensities are reported in Table 5.14. Compound **2c** is characterized as having one broad absorption in the visible region at 610 nm and higher energy features, <400 nm (see Supporting Information for the spectrum). CASPT2 predicts the lowest δ–δ^* transition, a singlet to triplet excitation, at 615 nm to be weakly intense due to spin-orbit coupling. The lowest singlet δ–δ^* transition is predicted to be at 467 nm. Time-dependent DFT calculations performed on **2c** predict a singlet δ–δ^* transition at 804 nm, and two degenerate metal to ligand charge transfer transitions at 726 nm (Figure 5.15).

Table 5.14: Excitation Energies from S1 in eV and nm for the Lowest Singlet and Triplet States, Intensities, and Their Electronic Configurations for $[W_2(dpa)_4]$ (**2c**)

state		E (eV)	intensity	E (nm)	configuration
S1	^1A	0.00		0	76% $\sigma^2\pi^4\delta^2$
T1	^3A	2.02	0.1×10^6	615	81% $\sigma^2\pi^4\delta^1\delta^{*1}$
S2	^1A	2.66	0.1×10^1	467	74% $\sigma^2\pi^4\delta^1\delta^{*1}$
S3	^1A	3.63	0.7×10^5	342	59% $\sigma^2\pi^4\delta^{*2}$
S4	^1B	3.65	0.5×10^5	340	46% $\sigma^2\pi^4\delta^1\pi^{*1}$
					34% $\sigma^2\pi^4\delta^1\pi^{*1}$
S5	^1B	3.67	0.4×10^5	338	39% $\sigma^2\pi^4\delta^1\pi^{*1}$
					47% $\sigma^2\pi^4\delta^1\pi^{*1}$

The U–U hypothetical compound

The $[Cr_2(dpa)_4]$, $[Mo_2(dpa)_4]$, and $[W_2(dpa)_4]$ compounds (**2a-c**) were each made experimentally. We consider now, however, the U–U compound **2d** analogous to **2a-c**, which has not been synthesized. If good computational results on this hypothetical U_2 molecule can be obtained, then it may be reasonable to suggest this molecule as an interesting new target for synthetic chemists. Thus, we decided to perform a full electronic characterization of this species in order to see how different this species is from the analogous Cr–Cr, Mo–Mo, and W–W compounds and what are the chances that it may exist from an electronic structure point of view. We started from the X-ray coordinates of **2c** and replaced the two W atoms with two U atoms. Initially, DFT single-point energy calculations were performed for singlet, triplet, and quintet spin states to establish the nature of the ground state. The triplet was found to be the lowest energy spin state, with the quintet lying 0.2 eV higher and the singlet 0.6 eV higher in energy. A full geometry optimization of the triplet electronic state was performed at the DFT/PBE/SDD level of theory. At the triplet-optimized geometry single-point energy calculations for various spin states were performed at the CASSCF/CASPT2 level of theory using an active space of twelve electrons in twelve orbitals. These orbitals are linear combinations of U $6d$ and $5f$ orbitals and ligand-based orbitals of the appropriate

symmetry to bind with these U orbitals. The ^{3}A state is the ground state as determined by DFT and also at the CASPT2 level of theory. Calculations with 14 electrons in 14 active space orbitals confirmed these results. We then optimized the U–U distance at the CASPT2 level of theory for both the singlet and triplet state. The general features of the DFT- and CASPT2-optimized structures of **2d** are similar to each other, and differ slightly from those of **2a-c**. Whereas the Cr_2, Mo_2, and W_2 compounds each contain a dangling pyridine ring from each dpa ligand that does not coordinate to the metal centers, all of the dpa N atoms bind to one U atom or the other in **2d**. Thus, the dpa ligand assumes an unusual bridging/chelating coordinate mode in **2d** (Figure 5.16). Other reported examples of this coordination mode are found in the $[W_2(dpa)_3X_2]^+$,[513] $[W_2(dpa)_4]^{2+}$,[563] and the Ru_2[564] and V_2[565] analogues of these compounds. Some of the bond lengths in **2d** vary as a function of the spin state (Table 5.15). The U–Na bond and U–N_{py} bond to the non-chelating pyridine moiety are, however, almost invariant at about 2.40 and 2.52 Å, respectively. The two U atoms are clearly close enough to each other in this molecule to be considered bonded to one another. In the triplet ground state, an U–U distance of 2.38 Å is calculated, which increases to 2.44 Å in the singlet state. In the triplet state, the U–N distance to the chelating pyridine ligands is 2.58 Å, indicating a significant interaction. In support of this conclusion, the sum of the direction angles, $\Sigma\ \xi$, of 66.8° is far smaller than in **2a-c**. This U–N bond becomes even shorter in the singlet state, in which it is found to be 2.48 Å, which is approximately 0.05 Å shorter than the U–N bond to the bridging pyridyl moiety. There is a concomitant decrease in $\Sigma\ \xi$ to 30° in the singlet state.

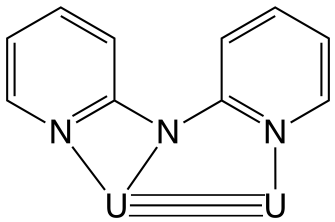

Figure 5.16: Compound **2d**.

Table 5.15: Calculated structural data for $[U_2(dpa)_4]$ (**2d**). Average values are reported for all structural data except for the U–U distance for which there is a unique value. Bond lengths in (Å), dihedral angles in (°)

	U–U	U–N_a	U–N_{py}	U$\cdots$$N_{py}$	N_a-U-U-N_{py}	ξ	$\Sigma\xi$
triplet, DFT	2.38	2.42	2.52	2.58	5.4	16.7	66.8
singlet, DFT	2.44	2.40	2.53	2.48	16.2	7.4	29.6

Unlike **3a-c**, which feature M_2^{4+} units having a formal quadruple bond between the metal atoms, the electronic structure of the U_2 compound is different in that there are only six U_2-based electrons. This situation indicates that this compound contains a U^{III}–U^{III} dimer and therefore that two electrons are added to the ligand orbitals formally reducing the two dpa^- ligands to radical dianions. From a chemical viewpoint, this electron disposition is sensible, as U^{2+} would be expected to be highly reducing and, to our knowledge, no U^{2+} complexes have been reported. This result suggests that the corresponding dication $[U_2(dpa)_4]^{2+}$ may be a more realistic synthetic target. The EBO calculated for the singlet state of **2d** is equal to 2.1 at a U–U bond length of 2.47 Å. This value corresponds to a formal U_2^{6+} triple bond arising from the dominating electronic configuration $\sigma^2\pi^4$ (see Supporting Information for the details of the occupation numbers) This result should be compared with the one for the analogous $[Cr_2(dpa)_4]$, $[Mo_2(dpa)_4]$, and $[W_2(dpa)_4]$ compounds. In compound **2c** the W–W bond length for the singlet ground state is equal to 2.225 Å and in compound **2b** the Mo–Mo distance is 2.109 Å, corresponding to an EBO of 3.5 and 3.4, respectively. The U–U compound has a U–U bond one unit lower than the corresponding $[Mo_2(dpa)_4]$ and $[W_2(dpa)_4]$ compounds, consistent with the U_2^{6+} oxidation state.

5.2.4 Discussion

Compounds with metal–metal multiple bonds have consistently posed a considerable challenge to electronic structure calculations. The earliest reported methods that provided useful results utilized the SCF-Xα-SW method, though this method has been superseded in recent years by DFT methods.[510] The main failing of Hartree-Fock based

computations on metal–metal multiply bonded compounds, especially on dichromium compounds, is the problem of electron correlation in systems in which many orbitals are energetically very closely spaced.[566,567] To some extent, this problem is ameliorated by DFT methods though it remains when hybrid functionals such as B3LYP or PBE0 are utilized,[568,569] but another problem inherent in DFT arises. Most density functionals within the Kohn-Sham approach have difficulties describing situations which are of multi-reference character in wavefunction based methods. For metal–metal multiply bonded compounds, the orbital energy separations are often small and several limiting electron configurations may contribute to the true ground-state wavefunction that must be described as a combination of multiple determinants.

The multireference method employed here, CASPT2, can describe, for the selected active space of electrons and orbitals, multiconfigurational electronic states. In this study on several different types of recently reported metal–metal multiply bonded molecules, we have employed both DFT and CASPT2 to compare calculated geometries and electronic excited states. Thus, it is now possible to provide a detailed assessment of the use of DFT versus multireference methods in treating metal–metal multiply bonded compounds. We will first discuss the computational results on molecular geometries obtained from DFT and CASSCF/CASPT2 and different assessments of metal–metal bond orders such as the Mayer bond order implemented in DFT and the EBO used with multireference wavefunctions. The electronic excited states will then be discussed.

DFT and CASPT2 geometry optimizations have been performed on the systems under examination. Since at the CASPT2 level, only selected bond lengths (metal–metal and metalnearest-neighbor) were re-optimized, it makes sense only to discuss the metal–metal bond lengths in detail. For most molecules there was less than 0.1 Å difference between the DFT and CASPT2-optimized metal–metal bond lengths. The [Ar-MM-Ar] systems, however, showed the biggest disparity. The greatest difference is 0.48 Å for the metal–metal distance in the [Ar-MoMo-Ar] molecule, due to the formation of an η^6 interaction between the Mo and Aryl fragments in the DFT optimization. Despite the reasonable geometries provided by DFT for Cr_2, Mo_2, and W_2 compounds, prediction of spectral properties are not nearly as accurate.

To better understand the electronic absorption spectra of the Group 6 compounds $[Cr_2(dpa)_4]$, $[Mo_2(dpa)_4]$, and $[W_2(dpa)_4]$, both TD-DFT and CASPT2 were used. The

reason for employing both methods is that, while CASPT2 is more accurate than TD-DFT, because of its multiconfigurational nature, it can describe only those transitions generated by the orbitals present in the active space. In our calculations we could only include metal-based orbitals in the active space, because otherwise the active space would have become prohibitively large and it was thus not possible to predict the metal-to-ligand (ML) or ligand-to-metal (LM) charge-transfer (CT) transitions at the CASPT2 level.

The absorption spectrum for $[Cr_2(dpa)_4]$ is characterized by an absorption at 520 nm with molar absorptivity 4500 M^{-1} cm^{-1} and higher energy transitions (<400 nm) that have yet to be unambiguously assigned. TD-DFT results predict the lowest singlet δ–δ^* transition to be at 692 nm and two degenerate LMCT bands at 554 nm, involving promotion of an electron from a doubly occupied, delocalized dpa π orbital to the Cr–Cr δ^* level. The lowest singlet transition predicted by CASPT2 calculations at 350 nm is notably not a δ–δ^* transition, but is instead a two-electron excitation. Notably, TD-DFT significantly underestimates all of the excited state energies, as evidenced by the fact that there are no experimental absorptions where TD-DFT predicts them to be. However, the fact that TD-DFT predicts charge transfer bands in the visible region of the spectrum is significant. Considering all these results we assign the major absorption at 520 nm to be a LMCT band. The δ–δ^* transition is likely present but cannot be directly observed as it is covered by the CT bands. TD-DFT is useful to assign the major feature of this spectrum as LMCT excitations, since these cannot be predicted by CASPT2.

The absorption spectrum of $[Mo_2(dpa)_4]$ is quite different from that of its Cr and W analogues. Two absorption bands are detected in the visible region at 500 and 585 nm. As per the discussion above, TD-DFT predicts both these peaks to be MLCT transitions, while CASPT2 predicts the singlet δ–δ^* transition to occur at 431 nm, which would be covered by the CT bands in the absorption spectrum. The CASPT2 prediction of the δ–δ^* transition at 431 nm is reasonable considering the energies of definitively assigned δ–δ^* transitions in the dimolybdenum tetracarboxylates, which appear at about 430 nm.[510] As in the Cr_2 case, TD-DFT poorly predicts the energy of this band at 702 nm, a region in which the experimental spectrum is empty.

The absorption spectrum of $[W_2(dpa)_4]$ is characterized by a broad peak at 610 nm,

which is assigned to be due to a combination of MLCT bands, based on TD-DFT results. CASPT2 calculations predict the singlet δ–δ^* transition to be at 467 nm, considerably higher in energy than TD-DFT (804 nm). The δ–δ^* transition is once again not observed due to the CT bands, and the CASPT2 δ–δ^* transition is more physically reasonable than the TD-DFT result.

For $[Cr_2(dpa)_4]$ the charge transfer bands are predicted to be LMCT as opposed to the MLCT bands predicted for $[Mo_2(dpa)_4]$ and $[W_2(dpa)_4]$. At this point we do not fully understand why the direction of the charge transfer changes in these molecules, but we note that chemical oxidation of $[Mo_2(dpa)_4]$ and $[W_2(dpa)_4]$ to their respective monocations has been established experimentally,[513,561] whereas oxidation of $[Cr_2(dpa)_4]$ leads to decomposition.

The results reported here emphasize the importance of analyzing electronic absorption spectra using both TD-DFT and CASPT2 methods. It should be noted that CASPT2 calculations including the ligand orbitals in the active space would provide the best assessment of the absorption spectrum, but this task is currently prohibitively expensive.

The final point of discussion involves bond orders for metal–metal bonds. Basic molecular orbital theory, in which metal–metal bonding and antibonding orbitals may be occupied by either 0, 1, or 2 electrons, yields simple, integer bond orders for compounds **3** (bond order of 5), and **1** and **2** (bond orders of 4). These are the bond orders that stem from a zero-th order assessment of metal oxidation states and orbital overlap. Calculated bond orders are different from these simple MO bond orders for three main reasons: 1) metal-ligand delocalization, 2) non-ideal metal–metal orbital overlap, and 3) multiconfigurational states. The MO bond orders are therefore an upper limit for the number of electron pairs that hold two metals together, and calculated bond orders are always lower than these idealized values.

In this work, we have presented two types of calculated bond orders. First, DFT results have been analyzed using the Mayer BO,[570] which is an extension of the Wiberg bond index used by semiempirical methods,[571] and results directly from Mulliken analysis of the wavefunction. For the multireference calculations presented here, the EBO method is used, which involves a summation of the bonding and antibonding orbital population for those orbitals in the active space. There are advantages and disadvantages

to both methods. The Mayer BO may accurately reflect metal-ligand delocalization and imperfect metal–metal orbital overlap, but, since DFT is an inherently monodeterminantal method, multiconfigurational character of the wavefunction is ignored. The EBO method, on the other hand, deals exclusively with the multiconfigurational nature of the wavefunction, and thereby deals correctly with the issue of poor orbital overlap. However, since ligand orbitals are not included in the active space, metal-ligand delocalization is not reflected in this value.

It may be naively expected that the metal–metal bond order of a molecule correlates with the bond length. In general this is the case, though there are a number of notable counter examples. For instance, the first quintuply-bonded molecule, synthesized by Power and co-workers,[530] has a longer Cr–Cr bond length (1.84 Å) than that of the shortest quadruple bond (1.83 Å).[572] Also, in electron-rich metal–metal multiply bonded systems, metal–metal bond lengths can be affected more by electron-electron repulsion and other charge considerations than by changes in metal–metal bond order.[573,574,575,576,577] Nevertheless, comparisons between bond lengths and bond orders for the compounds presented here are enlightening. The formal shortness ratio (FSR)[510] will be used here in comparing bond lengths between metals of different sizes. FSR values for all of the compounds studied here are given in Table 5.16, along with FSR values for optimized geometries and the Mayer bond order and EBO values.

Table 5.16: Comparison of FSRs and Calculated Bond Orders

	Exp FSR	DFT FSR	CASPT2 FSR	Mayer BO	EBO
1	0.811	0.836	0.798	3.44	3.40
2a	0.819	0.752		3.26	3.25
2b	0.809	0.814		3.10	3.40
2c	0.841	0.848	0.863	2.98	3.50
2d		0.856	0.866		2.10
3a	0.774	0.729	0.774	3.82	3.07
3b		0.951	0.734	3.85	4.30
3c		0.928	0.863	3.25	4.33

All of the compounds presented here that have been characterized expermentally have FSR values significantly less than one, consistent with metal–metal multiple bonding. The lowest FSR of 0.774 belongs to the quintuply bonded molecule **3a**. All of the quadruply bonded molecules have FSR values in the range of 0.809-0.841. The agreement between FSR values calculated from DFT or CASPT2 methods and the experimental FSRs mirrors the agreement between optimized and measured metal–metal bond lengths.

Our simplistic general expectation is that compounds having a smaller FSR should have larger bond orders, since these are the species whose metal–metal separations deviate most from the sum of the metallic radii. A correlation of bond order with FSR is shown in Figure 5.17, using only the data from Table 5.16 for real compounds that have been analyzed by both DFT and multireference methods (that is, **3a**, **1**, **2a**, **2b**, and **2c**). EBO data for "supershort" Cr_2 compounds reported in La Macchia *et al.*[526] are also included. Compounds **3b** and **3c** are not included in this analysis. Their calculated EBO values are anomalously high because the active space orbitals are not purely metal orbitals but contain significant ligand character due to arene–metal π interactions. Taking into account all of the available data, we see that, indeed the calculated bond orders (both Mayer BO and EBO) generally increase as the normalized metal–metal bonds become shorter. Some subtleties are worth pointing out, however. A somewhat counter intuitive result is the fact that the EBO values increase for the compounds studied here as the metal is changed from Cr to Mo or W, despite the fact that the Mo_2 and W_2 molecules have higher FSR values. This result can be rationalized by considering that the 4*d* (Mo) or 5d (W) orbitals are significantly larger than the Cr 3*d* orbitals. One may therefore expect Mo_2 and W_2 molecules to have greater orbital overlap, and hence larger computed bond orders, at longer normalized bond lengths than for the Cr_2 molecules.

It is unclear from the current set of data whether DFT bond orders also show this effect. This analysis of calculated bond orders as a function of metal–metal bond lengths should be considered with the following caveats in mind. Metalmetal bond lengths can be affected by steric factors such as the bite angle of the bridging ligands. Electronic factors can also be important. For example, increased covalency of metal–carbon bonds can affect the calculated bond orders. Local symmetry may also be important, as it can

lead to more polarized metal–metal interactions. Despite these complicating factors, both MBO and EBO bond order metrics show the anticipated trend with bond length. The agreement between the MBO and EBO metrics in this trend is remarkable, given the shortcomings of each method enumerated above.

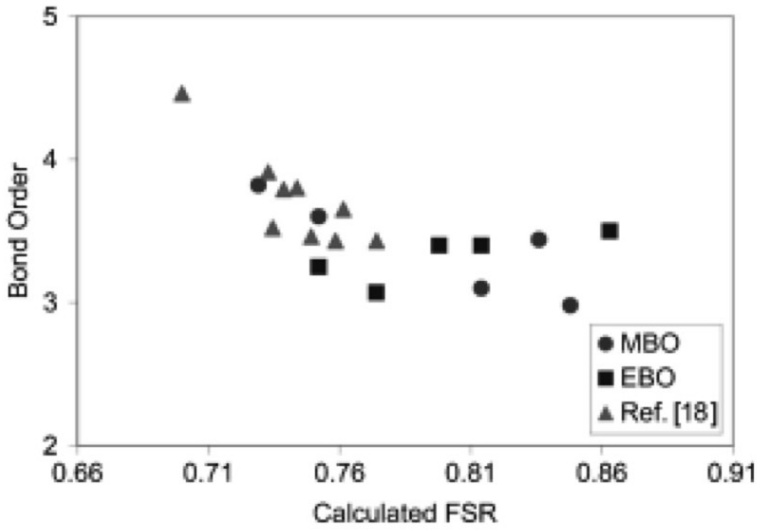

Figure 5.17: Correlation plot of bond order with formal shortness ratio

5.2.5 Conclusion

We have reported the results of a study of several Cr–Cr, Mo–Mo, and W–W compounds with different ligands and formal metal oxidation states. We have investigated the Mo and W analogue of the recently synthesized [Ar-CrCr-Ar] compound **3a**. The effect of Ar on the different bimetallic units has been compared with the effect of Ph in the analogous [Ph-MM-Ph] compounds. The metal–metal effective bond order obtained from the occupation numbers of the natural orbitals resulting from the CASSCF wavefunction is close to five in [Ph-MoMo-Ph] and [Ph-WW-Ph], while it is only close to four in [Ph-CrCr-Ph]. The EBO remains substantially invariant in the [Ar-MM-Ar] compounds, compared to the Ph analogues, indicating that the flanking aryl groups have mainly a steric effect, rather than an electronic one.

Compounds **1** and **2a-c**, which contain formal quadruple bonds between Cr_2, Mo_2,

and W_2 units, have also been investigated. Finally, the hypothetical U–U molecule $[U_2(dpa)_4]$ is described as an $U_2^{III,III}$ compound, with a formal U_2 triple bond, and two dpa ligands reduced to radical anions. We have also computed the lowest energy excited states of **1** and **2a-c** using both CASPT2 (for metal–metal excitations) and TD-DFT (for metalligand charge-transfer excitations). These combined methods allow us to assign the major features of the absorption spectra of **1** and **2a-c** as charge transfer bands, which cover up the δ–δ^* transitions that would otherwise be observed.

These results indicate that in general the Cr–Cr bond is more multiconfigurational than the Mo–Mo and W–W in analogous compounds leading to lower calculated EBO values. As already described in the case of the diatomics, the reason should be attributed to the more favorable interaction between the *d* orbitals for second- and third-row transition metals compared with first-row transition metals. It is interesting to note that, for the same metal, the bond order is similar in the [Ar-MM-Ar] (M=Cr, Mo, W), [MM'(TiPB)4] (M=Mo, W; M'=W) and $[M_2(dpa)_4]$ (M=Mo,W) compounds.

Comparing calculated bond orders to normalized bond lengths using the formal shortness ratio (FSR), we see that both Mayer bond orders, calculated from DFT methods, and effective bond orders, from CASSCF calculations, provide comparable reliability with respect to their correlation with FSR. Taking this result together with the results of excited state calculations reported here, there are clear advantages to the combined use of both DFT and multireference methods in describing compounds with the metal–metal multiple bonds.

We plan to study oligomeric species containing several of these units in order to explore the trend of the metal–metal multiple bonds for growing oligomers. We will also investigate the effect of the length of the thienyl groups on the CASSCF wavefunction and subsequent electronic properties of compounds of type **1**.

5.2.6 Additional Information

Supplementary information is available in the online version of the paper. The Supporting Information includes: Cartesian coordinates, total electronic energies, molecular orbitals, and electronic spectra. This material is available free of charge at `http://dx.doi.org/10.1002/chem.201103096`. Correspondence and requests for materials should be addressed to J.F.B. and L.G. The authors declare no competing financial

interests.

Acknowledgements

We thank the Office of Basic Energy Sciences, U. S. Department of Energy under Contract no. USDOE/DE-SC002183 for financial support and the University of Minnesota Supercomputing Institute. The National Science Foundation is gratefully acknowledged for support under CHE- 0745500.

References

[1] D. M. DAlessandro, B. Smit, J. R. Long. *Angew. Chem. Int. Ed.* **2010**, *49*, 6058.

[2] K. A. Lokhandwala, I. Pinnau, Z. He, K. D. Amo, A. R. DaCosta, J. G. Wijmans, R. W. Baker. *J. Membr. Sci.* **2010**, *346*, 270.

[3] C. R. Armstrong, M. Nyman, T. Shvareva, G. E. Sigmon, P. C. Burns, A. Navrotsky. *Proc. Natl. Acad. Sci. U.S.A.* **2012**, *109*, 1874.

[4] K. Sillar, A. Hofmann, J. Sauer. *J. Am. Chem. Soc.* **2009**, *131*, 4143.

[5] F. X. Coudert. *Chem. Mater.* **2015**, Article ASAP.

[6] M. J. Caplow. *J. Am. Chem. Soc.* **1968**, *90*, 6795.

[7] P. V. Danckwerts. *Chem. Eng. Sci.* **1979**, *34*, 443.

[8] P. D. Vaidya, E. Y. Kenig. *Chem. Eng. Technol.* **2007**, *30*, 1467.

[9] E. F. da Silva, H. F. Svendsen. *Ind. Eng. Chem. Res.* **2004**, *43*, 3413.

[10] J. E. Crooks, J. P. Donnellan. *J. Am. Chem. Soc. Perkin Trans.* **1989**, *2*, 331.

[11] P. D. Vaidya, E. Y. Kenig. *Chem. Eng. Technol.* **2010**, *33*, 1577.

[12] N. Ramachandran, A. Aboudheir, R. Idem, P. Tontiwachwuthikul. *Ind. Eng. Chem. Res.* **2006**, *45*, 2608.

[13] A. Hartono, E. F. da Silva, H. F. Svendsen. *Chem. Eng. Sci.* **2009**, *64*, 3205.

[14] A. Aboudheir, P. Tontiwachwuthikul, A. Chakma, R. Idem. *Chem. Eng. Sci.* **2003**, *58*, 5195.

[15] E. M. Hampe, D. M. Rudkevich. *Chem. Commun.* **2002**, 1450.

[16] E. M. Hampe, D. M. Rudkevich. *Tetrahedron* **2003**, *59*, 9619.

[17] A. L. Dzubak, L.-C. Lin, J. Kim, J. A. Swisher, R. Poloni, S. N. Maximoff, B. Smit, L. Gagliardi. *Nature Chem.* **2012**, *4*, 810.

[18] S. Pacala, R. Socolow. *Science* **2004**, *305*, 968.

[19] B. Metz, O. Davidson, H. deConinck, M. Loos, L. Meyer, *IPCC Special Report on Carbon Dioxide Capture and Storage*, Cambridge University Press, **2005**, Intergovernmental Panel on Climate Change.

[20] M. Ramezan, T. J. Skone, N. ya Nsakala, G. N. Liljedahl, *Carbon Dioxide Capture from Existing Coal-Fired Power Plants*, **2007**, Report No. DOE/NETL-401/110907. National Energy Technology Laboratory, US Department of Energy.

[21] D. M. D'Alessandro, B. Smit, J. R. Long. *Angew. Chem. Int. Ed.* **2010**, *49*, 6058.

[22] L.-C. Lin, A. H. Berger, R. L. Martin, J. Kim, J. A. Swisher, K. Jariwala, C. H. Rycroft, A. S. Bhown, M. W. Deem, M. Haranczyk, B. Smit. *Nat. Mater.* **2012**, *11*, 633.

[23] K. Sumida, D. L. Rogow, J. A. Mason, T. M. McDonald, E. D. Bloch, Z. R. Herm, T.-H. Bae, J. R. Long. *Chem. Rev.* **2012**, *112*, 724.

[24] L. Valenzano, B. Civalleri, K. Sillar, J. Sauer. *J. Phys. Chem. C* **2011**, *115*, 21777.

[25] S. S.-Y. Chui, S. M.-F. Lo, J. P. H. Charmant, A. G. Orpen, I. D. Williams. *Science* **1999**, *283*, 1148.

[26] A. R. Millward, O. M. Yaghi. *J. Am. Chem. Soc.* **2005**, *127*, 17998.

[27] P. D. C. Dietzel, V. Besikiotis, R. Blom. *J. Mater. Chem.* **2009**, *19*, 7362.

[28] J. A. Mason, K. Sumida, Z. R. Herm, R. Krishna, J. R. Long. *Energy Environ. Sci.* **2011**, *4*, 3030.

[29] L. S. Grajciar, O. Bludský, P. Nachtigall. *J. Phys. Chem. Lett.* **2010**, *1*, 3354.

[30] R. B. Getman, Y.-S. Bae, C. E. Wilmer, R. Q. Snurr. *Chem. Rev.* **2012**, *112*, 703.

[31] H. Wu, W. Zhou, T. Yildirim. *J. Am. Chem. Soc.* **2009**, *131*, 4995.

[32] T. M. McDonald, W. R. Lee, J. A. Mason, B. M. Wiers, C. S. Hong, J. R. Long. *J. Am. Chem. Soc.* **2012**, *134*, 7056.

[33] A. O. Yazaydin, R. Q. Snurr, T.-H. Park, K. Koh, J. Liu, M. D. LeVan, A. I. Benin, P. Jakubczak, M. Lanuza, D. B. Galloway, J. J. Low, R. R. Willis. *J. Am. Chem. Soc.* **2009**, *131*, 18198.

[34] B. Liu, B. Smit. *Langmuir* **2009**, *25*, 5918.

[35] R. Krishna, J. M. van Baten. *Phys. Chem. Chem. Phys.* **2011**, *13*, 10593.

[36] A. K. Rappe, C. J. Casewit, K. S. Colwell, W. A. Goddard, W. M. Skiff. *J. Am. Chem. Soc.* **1992**, *114*, 10024.

[37] D. Hagberg, G. Karlström, B. O. Roos, L. Gagliardi. *J. Am. Chem. Soc.* **2005**, *127*, 14250.

[38] O. Engkvist, P. O. Astrand, G. Karlström. *Chem. Rev.* **2000**, *100*, 4087.

[39] S. L. Mayo, B. D. Olafson, W. A. Goddard. *J. Phys. Chem.* **1990**, *94*, 8897.

[40] R. Krishna, J. M. van Baten. *J. Membr. Sci.* **2011**, *377*, 249.

[41] L. Gagliardi, R. Lindh, G. Karlström. *J. Chem. Phys.* **2004**, *121*, 4494.

[42] J. M. Simmons, H. Wu, W. Zhou, T. Yildirim. *Energy Environ. Sci.* **2011**, *4*, 2177.

[43] T. Vuong, P. A. Monson. *Langmuir* **1996**, *12*, 5425.

[44] J. Liu, A. I. Benin, A. M. B. Furtado, P. Jakubczak, R. R. Willis, M. D. LeVan. *Langmuir* **2011**, *27*, 11451.

[45] Z. B. Bao, L. A. Yu, Q. L. Ren, X. Y. Lu, S. G. Deng. *J. Colloid Interface Sci.* **2011**, *353*, 549.

[46] S. R. Caskey, A. G. Wong-Foy, A. J. Matzger. *J. Am. Chem. Soc.* **2008**, *130*, 10870.

[47] Z. R. Herm, J. A. Swisher, B. Smit, R. Krishna, J. R. Long. *J. Am. Chem. Soc.* **2011**, *133*, 5664.

[48] A. C. Kizzie, A. G. Wong-Foy, A. J. Matzger. *Langmuir* **2011**, *27*, 6368.

[49] K. Sillar, A. Hofmann, J. Sauer. *J. Am. Chem. Soc.* **2009**, *131*, 4143.

[50] K. S. Walton, A. R. Millward, D. Dubbeldam, H. Frost, J. J. Low, O. M. Yaghi, R. Q. Snurr. *J. Am. Chem. Soc.* **2008**, *130*, 406.

[51] S. F. Boys, F. Bernardi. *Mol. Phys.* **1970**, *19*, 553.

[52] G. Karlström, R. Lindh, P.-Å. Malmqvist, B. O. Roos, U. Ryde, V. Veryazov, P.-O. Widmark, M. Cossi, B. Schimmelpfennig, P. Neogrady, L. Seijo. *Comp. Mater. Sci.* **2003**, *28*, 222.

[53] F. Aquilante, T. B. Pedersen, R. Lindh. *J. Chem. Phys.* **2007**, *126*, 194106.

[54] F. Aquilante, P. Å. Malmqvist, T. B. Pedersen, A. Ghosh, B. O. Roos. *J. Chem. Theory Comput.* **2008**, *4*, 694.

[55] F. Aquilante, T. B. Pedersen, R. Lindh, B. O. Roos, A. Sánchez de Merás, H. Koch. *J. Chem. Phys.* **2008**, *129*, 024113.

[56] B. A. Hess. *Phys. Rev. A* **1986**, *33*, 3742.

[57] B. O. Roos, R. Lindh, P. Å. Malmqvist, V. Veryazov, P. O. Widmark. *J. Phys. Chem. A* **2004**, *108*, 2851.

[58] B. O. Roos, R. Lindh, P. Å. Malmqvist, V. Veryazov, P. O. Widmark. *J. Phys. Chem. A* **2005**, *109*, 6575.

[59] G. Kresse, J. Furthmuller. *Comp. Mater. Sci.* **1996**, *6*, 15.

[60] G. Kresse, J. Furthmuller. *Phys. Rev. B* **1996**, *54*, 11169.

[61] K. Lee, E. D. Murray, L. Z. Kong, B. I. Lundqvist, D. C. Langreth. *Phys. Rev. B* **2010**, *82*, 081101.

[62] R. Poloni, B. Smit, J. B. Neaton. *J. Phys. Chem. A* **2012**, *116*, 4957.

[63] J. M. Soler, E. Artacho, J. D. Gale, A. Garcia, J. Junquera, P. Ordejón, D. Sánchez-Portal. *J. Phys. Condens. Matter* **2002**, *14*, 2745.

[64] G. Román-Peréz, J. M. Soler. *Phys. Rev. Lett.* **2009**, *103*, 096102.

[65] A. Holt, J. Bostrom, G. Karlstrom, R. Lindh. *J. Comput. Chem.* **2010**, *31*, 1583.

[66] D. Frenkel, B. Smit, *Understanding Molecular Simulations: from Algorithms to Applications 2nd ed.*, Academic Press, **2002**.

[67] J. J. Potoff, J. I. Siepmann. *AIChE J.* **2001**, *47*, 1676.

[68] J. Borycz, L.-C. Lin, E. D. Bloch, J. Kim, A. L. Dzubak, R. Maurice, D. Semrouni, K. Lee, B. Smit, L. Gagliardi. *The Journal of Physical Chemistry C* **2014**, *118*, 12230.

[69] O. K. Farha, A. O. Yazaydin, L. Eryazici, C. D. Malliakas, B. Hauser, M. Kanatzidis, S. Nguyen, R. Snurr, J. Hupp. *Nat. Chem.* **2010**, *2*, 944.

[70] D. Lässig, J. Lincke, J. Moellmer, C. Reichenbach, A. Moeller, R. Gläser, G. Kalies, K. A. Cychosz, M. Thommes, R. Staudt, H. Krautscheid. *Angew. Chem., Int. Ed.* **2011**, *50*, 10344.

[71] K. Sumida, D. L. Rogow, J. A. Mason, T. M. McDonald, E. D. Bloch, Z. R. Herm, T.-H. Bae, J. R. Long. *Chem. Rev.* **2012**, *112*, 724.

[72] S. Chaemchuen, N. A. Kabir, K. Zhou, F. Verpoort. *Chem. Soc. Rev.* **2013**, 9304.

[73] E. D. Bloch, W. L. Queen, R. Krishna, J. M. Zadrozny, C. M. Brown, J. R. Long. *Science* **2012**, *335*, 1606.

[74] J. A. Mason, K. Sumida, Z. R. Herm, R. Krishna, J. R. Long. *Energy Environ. Sci.* **2011**, *4*, 3030.

[75] E. D. Bloch, L. J. Murray, W. L. Queen, S. Chavan, S. N. Maximoff, J. P. Bigi, R. Krishna, V. K. Peterson, F. Grandjean, G. J. Long, B. Smit, S. Bordiga, C. M. Brown, J. R. Long. *J. Am. Chem. Soc.* **2011**, *133*, 14814.

[76] P. D. C. Dietzel, V. Besikiotis, R. Blom. *J. Mater. Chem.* **2009**, *19*, 7362.

[77] S. L. Mayo, B. D. Olafson, W. A. Goddard. *J. Phys. Chem.* **1990**, *94*, 8897.

[78] A. K. Rappé, C. J. Casewit, K. S. Colwell, W. A. Goddard, W. M. Skiff. *J. Am. Chem. Soc.* **1992**, *114*, 10024.

[79] F. Salles, D. I. Kolokolov, H. Jobic, G. Maurin, P. L. Llewellyn, T. Devic, C. Serre, G. Ferey. *J. Phys. Chem. C* **2009**, *113*, 7802.

[80] S. Rives, H. Jobic, D. I. Kolokolov, A. A. Gabrienko, A. G. Stepanov, Y. Ke, B. Frick, T. Devic, G. Férey, G. Maurin. *J. Phys. Chem. C* **2013**, *117*, 6293.

[81] E. Atci, I. Erucar, S. Keskin. *J. Phys. Chem. C* **2011**, *115*, 6833.

[82] J. Yu, P. B. Balbuena. *J. Phys. Chem. C* **2013**, *117*, 3383.

[83] A. L. Dzubak, L.-C. Lin, J. Kim, J. A. Swisher, R. Poloni, S. N. Maximoff, B. Smit, L. Gagliardi. *Nat. Chem.* **2012**, *4*, 810.

[84] M. S. Gordon, Q. A. Smith, P. Xu, L. V. Slipchenko. *Annu. Rev. Phys. Chem.* **2013**, *64*, 553.

[85] N. Gresh, P. Claverie, A. Pullman. *Theor. Chem. Acc.* **1984**, *66*, 1.

[86] A. J. Misquitta, R. Podeszwa, B. Jeziorski, K. Szalewicz. *J. Chem. Phys.* **2005**, *123*, 214103.

[87] P. Verma, X. Xu, D. G. Truhlar. *J. Phys. Chem. C* **2013**, *117*, 12648.

[88] D. Ghosh, D. Kosenkov, V. Vanovschi, C. F. Williams, J. M. Herbert, M. S. Gordon, M. W. Schmidt, L. V. Slipchenko, A. I. Krylov. *J. Phys. Chem. A* **2010**, *114*, 12739.

[89] I. Adamovic, M. S. Gordon. *J. Phys. Chem. A* **2006**, *110*, 10267.

[90] H. Li, M. S. Gordon, J. H. Jensen. *J. Chem. Phys.* **2006**, *124*, 214108.

[91] D. N. Bowman, E. Jakubikova. *Inorg. Chem.* **2012**, *51*, 6011.

[92] K. P. Jensen, B. O. Roos, U. Ryde. *J. Inorg. Biochem.* **2005**, *99*, 45.

[93] M. Radoń, K. Pierloot. *J. Phys. Chem. A* **2008**, *112*, 11824.

[94] R. Maurice, P. Verma, J. M. Zadrozny, S. Luo, J. Borycz, J. R. Long, D. G. Truhlar, L. Gagliardi. *Inorg. Chem.* **2013**, *52*, 9379.

[95] J. P. Furtado, A. P. Rahalkar, S. Shanker, P. Bandyopadhyay, S. R. Gadre. *J. Chem. Phys. Lett.* **2012**, *3*, 2253.

[96] G. Kresse, J. Hafner. *Phys. Rev. B* **1993**, *47*, 558.

[97] G. Kresse, J. Hafner. *Phys. Rev. B* **1994**, *49*, 14251.

[98] G. Kresse, J. Furthmüller. *Comput. Mater. Sci.* **1996**, *6*, 15.

[99] G. Kresse, J. Furthmüller. *Phys. Rev. B* **1996**, *54*, 11169.

[100] P. E. Blöchl. *Phys. Rev. B* **1994**, *50*, 17953.

[101] G. Kresse, D. Joubert. *Phys. Rev. B* **1999**, *59*, 1758.

[102] J. P. Perdew, K. Burke, M. Ernzerhof. *Phys. Rev. Lett.* **1996**, *77*, 3865.

[103] S. L. Dudarev, G. A. Botton, S. Y. Savrasov, C. J. Humphreys, A. P. Sutton. *Phys. Rev. B* **1998**, *57*, 1505.

[104] Q. Zhang, B. Li, L. Chen. *Inorg. Chem.* **2013**, *52*, 9356.

[105] T. A. Manz, D. S. Sholl. *J. Chem. Theory Comput.* **2011**, *7*, 4146.

[106] F. Weigend, M. Häser, H. Patzelt, R. Ahlrichs. *Chem. Phys. Lett.* **1998**, *294*, 143.

[107] A. Schäfer, H. Horn, R. Ahlrichs. *J. Chem. Phys.* **1992**, *97*, 2571.

[108] F. Weigend, R. Ahlrichs. *Phys. Chem. Chem. Phys.* **2005**, *7*, 3297.

[109] TURBOMOLE V6.4 2012; University of Karlsruhe and Forschungszentrum Karlsruhe GmbH: Karlsruhe, 1989-2007; TURBOMOLE GmbH: Karlsruhe, 2007; available from `http://www.turbomole.com`.

[110] B. O. Roos, P. R. Taylor, P. E. Siegbahn. *J. Chem. Phys.* **1980**, *48*, 157.

[111] K. Andersson, P.-Å. Malmqvist, B. O. Roos. *J. Chem. Phys.* **1992**, *96*, 1218.

[112] G. Karlström, R. Lindh, P.-Å. Malmqvist, B. O. Roos, U. Ryde, V. Veryazov, P.-O. Widmark, M. Cossi, B. Schimmelpfennig, P. Neogrady. *Comput. Mater. Sci.* **2003**, *28*, 222.

[113] P. Canepa, Y. J. Chabal, T. Thonhauser. *Phys. Rev. B* **2013**, *87*, 094407.

[114] N. Forsberg, P.-Å. Malmqvist. *Chem. Phys. Lett.* **1997**, *274*, 196.

[115] F. Aquilante, P.-Å. Malmqvist, T. B. Pedersen, A. Ghosh, B. O. Roos. *J. Chem. Theory Comput.* **2008**, *4*, 694.

[116] F. Aquilante, T. B. Pedersen, R. Lindh, B. O. Roos, A. S. de Merás, H. Koch. *J. Chem. Phys.* **2008**, *129*, 024113.

[117] F. Aquilante, T. B. Pedersen, R. Lindh. *J. Chem. Phys.* **2007**, *126*, 194106.

[118] M. Douglas, N. M. Kroll. *Ann. Phys.* **1974**, *82*, 89.

[119] B. A. Hess. *Phys. Rev. A* **1986**, *33*, 3742.

[120] B. O. Roos, R. Lindh, P.-Å. Malmqvist, V. Veryazov, P.-O. Widmark. *J. Phys. Chem. A* **2004**, *108*, 2851.

[121] B. O. Roos, R. Lindh, P.-Å. Malmqvist, V. Veryazov, P.-O. Widmark. *J. Phys. Chem. A* **2005**, *109*, 6575.

[122] S. Boys, F. Bernardi. *Mol. Phys.* **1970**, *19*, 553.

[123] E. Haldoupis, S. Nair, D. S. Sholl. *J. Am. Chem. Soc.* **2012**, *134*, 4313.

[124] L. Gagliardi, R. Lindh, G. Karlström. *J. Chem. Phys.* **2004**, *121*, 4494.

[125] J. G. McDaniel, J. R. Schmidt. *J. Phys. Chem. A* **2013**, *117*, 2053.

[126] A. Holt, J. Boström, G. Karlström, R. Lindh. *J. Comput. Chem.* **2010**, *31*, 1583.

[127] A. Holt, *Modelling of Polarization by Molecular Force Fields: Further Development of the NEMO Potential*, Ph.D. thesis, Lund University, **2009**.

[128] A. J. Stone, *The Theory of Intermolecular Forces*, Clarendon: Oxford, **1997**.

[129] J. J. Potoff, J. I. Siepmann. *AIChE J.* **2001**, *47*, 1676.

[130] L.-C. Lin, J. Kim, X. Kong, E. Scott, T. M. McDonald, J. R. Long, J. A. Reimer, B. Smit. *Angew. Chem., Int. Ed.* **2013**, *52*, 4410.

[131] C. J. Casewit, K. S. Colwell, A. K. Rappé. *J. Am. Chem. Soc.* **1992**, *114*, 10035.

[132] D. Fairen-Jimenez, P. Lozano-Casal, T. Dueren, *Characterisation of Porous Solids VIII*, N. Seaton, F. R. Reinoso, P. Llewellyn, S. Kaskel (Eds.), The Royal Society of Chemistry: U.K., **2009**, chapter Assessing Generic Force Fields to Describe Adsorption on Metal-Organic Frameworks.

[133] H. A. Lorentz. *Ann. Phys.* **1881**, *248*, 127.

[134] D. Berthelot. *Compt. Rendus* **1898**, *126*, 1703.

[135] P. Miró, B. Vlaisavljevich, A. L. Dzubak, S. Hu, P. C. Burns, C. J. Cramer, R. Spezia, L. Gagliardi. *J. Phys. Chem. C* **2014**, *118*, 24730.

[136] C. R. Armstrong, M. Nyman, T. Shvareva, G. E. Sigmon, P. C. Burns, A. Navrotsky. *Proc. Natl. Acad. Sci. U.S.A.* **2012**, *109*, 1874.

[137] I. S. Dennis, A. P. Jeapes, *The Nuclear Fuel Cycle*, Oxford Science Publications: Oxford, U.K., **1996**.

[138] G. E. Sigmon, D. K. Unruh, J. Ling, B. Weaver, M. Ward, L. Pressprich, A. Simonetti, P. C. Burns. *Angew. Chem., Int. Ed.* **2009**, *48*, 2737.

[139] G. E. Sigmon, J. Ling, D. K. Unruh, L. Moore-Shay, M. Ward, B. Weaver, P. C. Burns. *J. Am. Chem. Soc.* **2009**, *131*, 16648.

[140] T. Z. Forbes, J. G. McAlpin, R. Murphy, P. C. Burns. *Angew. Chem., Int. Ed.* **2008**, *47*, 2824.

[141] P. C. Burns, K. A. Kubatko, G. Sigmon, B. J. Fryer, J. E. Gagnon, M. R. Antonio, L. Soderholm. *Angew. Chem., Int. Ed.* **2005**, *44*, 2135.

[142] J. Ling, J. Qiu, G. E. Sigmon, M. Ward, J. E. S. Szymanowski, P. C. Burns. *J. Am. Chem. Soc.* **2010**, *132*, 13395.

[143] P. C. Burns, J. Ling, J. Qiu, J. E. S. Szymanowski. *Chem. Eur. J.* **2011**, *17*, 2571.

[144] J. Ling, C. M. Wallace, J. E. S. Szymanowski, P. C. Burns. *Angew. Chem., Int. Ed.* **2010**, *49*, 7271.

[145] D. K. Unruh, J. Ling, J. Qiu, L. Pressprich, M. Baranay, M. Ward, P. C. Burns. *Inorg. Chem.* **2011**, *50*, 5509.

[146] J. Qiu, P. B. Burns. *Chem. Rev.* **2013**, *113*, 1097.

[147] M. Nyman, P. C. Burns. *Chem. Soc. Rev.* **2012**, *41*, 7354.

[148] P. W. Fowler, D. E. Manolopoulos, *An Atlas of Fullerenes*, Oxford University Press: Oxford, **1995**.

[149] P. Miró, S. Pierrefixe, M. Gicquel, A. Gil, C. Bo. *J. Am. Chem. Soc.* **2010**, *132*, 17787.

[150] B. Vlaisavljevich, L. Gagliardi, P. C. Burns. *J. Am. Chem. Soc.* **2010**, *132*, 14503.

[151] P. Miró, C. Bo. *Inorg. Chem.* **2012**, *51*, 3840.

[152] A. Gil, D. Karhanek, P. Miró, M. R. Antonio, M. Nyman, C. Bo. *Chem. Eur. J.* **2012**, *18*, 8340.

[153] T. Mitra, P. Miró, A. R. Tomsa, A. Merca, H. Bögge, J. B. Ávalos, J. M. Poblet, C. Bo, A. Müller. *Chem. Eur. J.* **2009**, *15*, 1844.

[154] E. M. Wylie, K. M. Peruski, J. L. Weidman, W. A. Phillip, P. C. Burns. *ACS Appl. Mater. Interfaces* **2014**, *6*, 473.

[155] W. Smith, T. R. Forester. *J. Mol. Graphics* **1996**, *14*, 136.

[156] W. L. Jorgensen, J. Chandrasekhar, J. D. Madura, R. W. Impey, M. L. Klein. *J. Chem. Phys.* **1983**, *79*, 926.

[157] S. H. Lee, J. C. Rasaiah. *J. Phys. Chem.* **1996**, *100*, 1420.

[158] D. Frenkel, B. Smit, *Understanding Molecular Simulation, From Algorithms to Applications 2nd ed.*, Academic: San Diego, CA, **1996**.

[159] M. P. Allen, D. J. Tildesley, *Computer Simulation of Liquids 1st ed.*, Clarendon: Oxford, **1989**.

[160] D. Fincham. *Mol. Simulat.* **1992**, *8*, 165.

[161] S. Nosé. *J. Chem. Phys.* **1984**, *81*, 511.

[162] W. G. Hoover. *Phys. Rev. A* **1985**, *31*, 1695.

[163] F. Aquilante, L. De Vico, N. Ferre, G. Ghigo, P.-Å. Malmqvist, P. Neogrady, T. B. Pedersen, M. Pitonak, M. Reiher, B. O. Roos, L. Serrano-Andres, M. Urban, V. Veryazov, R. Lindh. *J. Comput. Chem.* **2010**, *31*, 224.

[164] B. A. Hess. *Phys. Rev. A* **1986**, *33*, 3742.

[165] M. Douglas, N. M. Kroll. *Ann. Phys.* **1974**, *82*, 89.

[166] B. O. Roos, R. Lindh, P. Å. Malmqvist, V. Veryazov, P. O. Widmark. *Chem. Phys. Lett.* **2005**, *409*, 295.

[167] B. O. Roos, R. Lindh, P. Å. Malmqvist, V. Veryazov, P. O. Widmark. *J. Phys. Chem. A* **2004**, *108*, 2851.

[168] B. O. Roos, R. Lindh, P. Å. Malmqvist, V. Veryazov, P. O. Widmark, A. C. Borin. *J. Phys. Chem. A* **2008**, *112*, 11431.

[169] B. O. Roos, R. Lindh, P. Å. Malmqvist, V. Veryazov, P. O. Widmark. *J. Phys. Chem. A* **2005**, *109*, 6575.

[170] B. O. Roos, V. Veryazov, P. O. Widmark. *Theor. Chem. Acc.* **2004**, *111*, 345.

[171] F. Aquilante, L. Boman, J. Bostrom, H. Koch, R. Lindh, A. S. de Meras, T. B. Pedersen. *Linear-Scaling Tech. Comput. Chem. Phys.: Methods Appl.* **2011**, *13*, 301.

[172] F. Aquilante, L. Gagliardi, T. B. Pedersen, R. Lindh. *J. Chem. Phys.* **2009**, *130*.

[173] F. Aquilante, R. Lindh, T. B. Pedersen. *J. Chem. Phys.* **2008**, *129*.

[174] F. Aquilante, P. A. Malmqvist, T. B. Pedersen, A. Ghosh, B. O. Roos. *J. Chem. Theory Comput.* **2008**, *4*, 694.

[175] F. Aquilante, T. B. Pedersen, R. Lindh. *J. Chem. Phys.* **2007**, *126*.

[176] *ADF2010*, Theoretical Chemistry, Vrije Universiteit: Amsterdam, The Netherlands, available from `http://www.scm.com`.

[177] C. F. Guerra, J. G. Snijders, G. te Velde, E. J. Baerends. *Theor. Chem. Acc.* **1998**, *99*, 391.

[178] G. te Velde, F. M. Bickelhaupt, E. J. Baerends, C. F. Guerra, S. J. A. Van Gisbergen, J. G. Snijders, T. Ziegler. *J. Comput. Chem.* **2001**, *22*, 931.

[179] J. P. Perdew, K. Burke, M. Ernzerhof. *Phys. Rev. Lett.* **1996**, *77*, 3865.

[180] E. van Lenthe, A. Ehlers, E. J. Baerends. *J. Chem. Phys.* **1999**, *110*, 8943.

[181] E. van Lenthe, E. J. Baerends, J. G. Snijders. *J. Chem. Phys.* **1993**, *99*, 4597.

[182] E. van Lenthe, E. J. Baerends, J. G. Snijders. *J. Chem. Phys.* **1994**, *101*, 9783.

[183] E. van Lenthe, J. G. Snijders, E. J. Baerends. *J. Chem. Phys.* **1996**, *105*, 6505.

[184] E. van Lenthe, R. van Leeuwen, E. J. Baerends, J. G. Snijders. *Int. J. Quantum Chem.* **1996**, *57*, 281.

[185] A. Klamt, G. Schuurmann. *J. Chem. Soc.-Perkin Trans. 2* **1993**, 799.

[186] C. C. Pye, T. Ziegler. *Theor. Chem. Acc.* **1999**, *101*, 396.

[187] A. Klamt. *J. Phys. Chem.* **1995**, *99*, 2224.

[188] A. Klamt, V. Jonas. *J. Chem. Phys.* **1996**, *105*, 9972.

[189] D. Hagberg, G. Karlström, B. O. Roos, L. Gagliardi. *J. Am. Chem. Soc.* **2005**, *127*, 14250.

[190] P. Guildbaud, G. Wipff. *J. Mol. Struct.* **1996**, *366*, 55.

[191] N. Rai, S. P. Tiwari, E. J. Maginn. *J. Phys. Chem. B* **2012**, *116*, 10885.

[192] C. Møller, M. S. Plesset. *Phys. Rev.* **1934**, *46*, 618.

[193] W. Koch, M. C. Holthausen, *A Chemist's Guide to Density Functional Theory 2nd ed.*, Wiley-VCH Verlag: Weinheim, Germany, **2001**.

[194] B. O. Roos, P. O. Widmark, L. Gagliardi. *Faraday Discuss.* **2003**, *124*, 57.

[195] B. O. Roos, P. Å. Malmqvist, L. Gagliardi. *J. Am. Chem. Soc.* **2006**, *128*, 17000.

[196] X. F. Wang, L. Andrews, B. Vlaisavljevich, L. Gagliardi. *Inorg. Chem.* **2011**, *50*, 3826.

[197] B. Vlaisavljevich, L. Gagliardi, X. F. Wang, B. Y. Liang, L. Andrews, I. Infante. *Inorg. Chem.* **2010**, *49*, 9230.

[198] M. Swart, P. T. Van Duijnen, J. G. Snijders. *J. Comput. Chem.* **2001**, *22*, 79.

[199] M. Born, J. E. Mayer. *Z. Phys. A-Hadron Nucl.* **1932**, *77*, 1.

[200] M. L. Huggins, J. E. Mayer. *J. Chem. Phys.* **1933**, *1*, 643.

[201] J. E. Mayer. *J. Chem. Phys.* **1933**, *1*, 270.

[202] P. G. Allen, J. J. Bucher, D. K. Shuh, N. M. Edelstein, T. Reich. *Inorg. Chem.* **1997**, *36*, 4676.

[203] J. Neuefeind, L. Soderholm, S. Skanthakumar. *J. Phys. Chem. A* **2004**, *108*, 2733.

[204] R. Spezia, B. Siboulet, S. Abadie, R. Vuilleumier, P. Vitorge. *J. Phys. Chem. B* **2011**, *115*, 3560.

[205] M. Buhl, H. Kabrede. *Inorg. Chem.* **2006**, *45*, 3834.

[206] s. P. Nichol, E. J. Bylaska, G. K. Schenter, W. de Jong. *J. Chem. Phys.* **2008**, *128*, 124507.

[207] R. J. Frick, T. S. Hofer, A. B. Pribil, B. R. Randolf, B. M. Rode. *J. Phys. Chem. A* **2009**, *113*, 12496.

[208] P. C. Burns. *Can. Mineral.* **2005**, *43*, 1839.

[209] R. L. Johnson, C. A. Ohlin, K. Pellegrini, P. C. Burns, W. H. Casey. *Angew. Chem., Int. Ed.* **2013**, *52*, 7464.

[210] M. Garcia-Rates, P. Miró, J. M. Poblet, C. Bo, J. B. Avalos. *J. Phys. Chem. B* **2011**, *115*, 5980.

[211] T. Mitra, P. Miró, A. R. Tomsa, A. Merca, H. Bogge, J. B. Avalos, J. M. Poblet, C. Bo, A. Müller. *Chem. Eur. J.* **2009**, *15*, 1844.

[212] M. Nyman, T. M. Alam. *J. Am. Chem. Soc.* **2012**, *134*, 20131.

[213] B. de Courcy, J.-P. Piquemal, C. Garbay, N. Gresh. *J. Am. Chem. Soc.* **2010**, *132*, 3312.

[214] N. Planas, A. L. Dzubak, R. Poloni, L.-C. Lin, A. McManus, T. M. McDonald, J. B. Neaton, J. R. Long, B. Smit, L. Gagliardi. *J. Am. Chem. Soc.* **2013**, *135*, 7402.

[215] S. Solomon, D. Qin, M. Manning, M. Marquis, K. Averyt, M. M. B. Tignor, J. L. Miller Jr., Z. Chen (Eds.), *Climate Change 2007: The Physical Science Basis*, Cambridge University Press: Cambridge, U.K., **2007**, Contribution of Working Group I to the Fourth Assessment Report of the Intergovernmental Panel on Climate Change.

[216] S. Chu. *Science* **2009**, *325*, 1599.

[217] G. T. Rochelle. *Science* **2009**, *325*, 1652.

[218] T. M. McDonald, W. R. Lee, J. A. Mason, B. M. Wiers, C. S. Hong, J. R. Long. *J. Am. Chem. Soc.* **2012**, *134*, 7056.

[219] A. Demessence, D. M. D'Alessandro, M. L. Foo, J. R. Long. *J. Am. Chem. Soc.* **2009**, *131*, 8784.

[220] T. M. McDonald, D. M. D'Alessandro, R. Krishna, J. R. Long. *Chem. Sci.* **2011**, *2*, 2022.

[221] A. Danon, P. C. Stair, E. Weitz. *J. Phys. Chem. C.* **2011**, *115*, 11540.

[222] W. Lu, J. P. Sculley, D. Yuan, R. Krishna, Z. Wei, H.-C. Zhou. *Angew. Chem., Int. Ed.* **2012**, *51*, 7480.

[223] W. Lu, J. P. Sculley, D. Yuan, R. Krishna, H.-C. Zhou. *J. Phys. Chem. C.* **2013**, *117*, 4057.

[224] A. Das, M. Choucair, P. D. Southon, J. A. Mason, M. Zhao, C. J. Kepert, A. T. Harris, D. M. D'Alessandro. *Microporous Mesoporous Mater.* **2013**, *174*, 74.

[225] J. A. Mason, K. Sumida, Z. R. Herm, R. Krishna, J. R. Long. *Energy Environ. Sci.* **2011**, *4*, 3030.

[226] M. Caplow. *J. Am. Chem. Soc.* **1968**, *90*, 6795.

[227] P. V. Danckwerts. *Chem. Eng. Sci.* **1979**, *34*, 443.

[228] P. D. Vaidya, E. Y. Kenig. *Chem. Eng. Technol.* **2007**, *30*, 1467.

[229] E. F. da Silva, H. F. Svendsen. *Ind. Eng. Chem. Res.* **2004**, *43*, 3413.

[230] J. E. Crooks, J. P. Donnellan. *J. Chem. Soc., Perkin Trans. 2* **1989**, 331.

[231] P. D. Vaidya, E. Y. Kenig. *Chem. Eng. Technol.* **2010**, *33*, 1577.

[232] N. Ramachandran, A. Aboudheir, R. Idem, P. Tontiwachwuthikul. *Ind. Eng. Chem. Res.* **2006**, *45*, 2608.

[233] A. Hartono, E. F. da Silva, H. F. Svendsen. *Chem. Eng. Sci.* **2009**, *64*, 3205.

[234] A. Aboudheir, P. Tontiwachwuthikul, A. Chakma, R. Idem. *Chem. Eng. Sci.* **2003**, *58*, 5195.

[235] E. M. Hampe, D. M. Rudkevich. *Chem. Commun.* **2002**, 1450.

[236] E. M. Hampe, D. M. Rudkevich. *Tetrahedron* **2003**, *59*, 9619.

[237] D. J. Xiao, E. D. Bloch, J. A. Mason, W. L. Queen, M. R. Hudson, N. Planas, J. Borycz, A. L. Dzubak, P. Verma, K. Lee, F. Bonino, V. Crocella, J. Yano, S. Bordiga, D. G. Truhlar, L. Gagliardi, C. M. Brown, J. R. Long. *Nature Chem.* **2014**, *6*, 590.

[238] H. Arakawa, M. Aresta, J. N. Armor, M. A. Barteau, E. J. Beckman, A. T. Bell, J. E. Bercaw, C. Creutz, E. Dinjus, D. A. Dixon, K. Domen, D. L. DuBois, J. Eckert, E. Fujita, D. H. Gibson, W. A. Goddard, D. W. Goodman, J. Keller, G. J. Kubas, H. H. Kung, J. E. Lyons, L. E. Manzer, T. J. Marks, K. Morokuma, K. M. Nicholas, R. Periana, L. Que, J. Rostrup-Nielson, W. M. H. Sachtler, L. D. Schmidt, A. Sen, G. A. Somorjai, B. R. Stair, P. C. Stults, W. Tumas. *Chem. Rev.* **2001**, *101*, 953.

[239] R. G. Bergman. *Nature* **2007**, *446*, 391.

[240] International Energy Agency. *World Energy Outlook Special Report 2011* **2011**, available from `http://www.worldenergyoutlook.org/goldenageofgas`.

[241] R. A. Himes, K. D. Karlin. *Curr. Opin. Chem. Biol.* **2009**, *13*, 119.

[242] M. Costas, M. P. Mehn, M. P. Jensen, L. Que Jr. *Chem. Rev.* **2004**, *104*, 939.

[243] B. Meunier, S. P. de Visser, S. Shaik. *Chem. Rev.* **2004**, *104*, 3947.

[244] B. J. Wallar, J. D. Lipscomb. *Chem. Rev.* **1996**, *96*, 2625.

[245] J. Hohenberger, K. Ray, K. Meyer. *Nature Commun.* **2012**, *3*, 720.

[246] W. Nam. *Acc. Chem. Res.* **2007**, *40*, 522.

[247] L. Que. *Acc. Chem. Res.* **2007**, *40*, 493.

[248] S. P. Watton, C. M. Taylor, G. M. Kloster, S. C. Bowman. *Prog. Inorg. Chem.* **2002**, *51*, 333.

[249] N. E. Leadbeater, M. Marco. *Chem. Rev.* **2002**, *102*, 3217.

[250] G. I. Panov, V. I. Sobolev, K. A. Dubkov, V. N. Parmon, N. S. Ovanesyan, A. E. Shilov, A. A. Shteinman. *React. Kinet. Catal. Lett.* **1997**, *61*, 251.

[251] A. Zecchina, M. Rivallan, G. Berlier, C. Lamberti, G. Richhiardi. *Phys. Chem. Chem. Phys.* **2007**, *9*, 3483.

[252] J. W. Yoon, Y.-K. Seo, Y. K. Hwang, J.-S. Chang, H. Leclerc, S. Wuttke, P. Bazin, A. Vimont, M. Daturi, E. Bloch, P. L. Llewellyn, C. Serre, P. Horcajada, J.-M. Grenèche, A. E. Rodrigues, G. Férey. *Angew. Chem. Int. Ed.* **2010**, *49*, 5949.

[253] S. Ma, D. Yuan, J.-S. Chang, H.-C. Zhou. *Inorg. Chem.* **2009**, *48*, 5398.

[254] K. Sumida, S. Horike, S. S. Kaye, Z. R. Herm, W. L. Queen, C. M. Brown, F. Grandjean, G. J. Long, A. Dailly, J. R. Long. *Chem. Sci.* **2010**, *1*, 184.

[255] E. D. Bloch, L. J. Murray, W. L. Queen, S. Chavan, S. N. Maximoff, J. P. Bigi, R. Krishna, V. K. Peterson, F. Grandjean, G. J. Long, B. Smit, S. Bordiga, C. M. Brown, J. R. Long. *J. Am. Chem. Soc.* **2011**, *133*, 14814.

[256] E. D. Bloch, W. L. Queen, R. Krishna, J. M. Zadrozny, C. M. Brown, J. R. Long. *Science* **2012**, *335*, 1606.

[257] M. Märcz, R. E. Johnsen, P. D. C. Dietzel, H. Fjellvåg. *Micropor. Mesopor. Mater.* **2012**, *157*, 62.

[258] S. Bhattacharjee, J.-S. Choi, S.-T. Yang, S. B. Choi, J. Kim, W.-S. Ahn. *J. Nanosci. Nanotechnol.* **2010**, *10*, 135.

[259] W. B. Tolman. *Angew. Chem. Int. Ed.* **2010**, *49*, 1018.

[260] N. A. Piro, M. F. Lichterman, W. H. Harman, C. J. Chang. *J. Am. Chem. Soc.* **2011**, *133*, 2108.

[261] Y. Zhao, D. G. Truhlar. *Theor. Chem. Acc.* **2008**, *120*, 215.

[262] A. Delabie, C. Vinckier, M. Flock, K. Pierloot. *J. Phys. Chem. A* **2001**, *105*, 5479.

[263] A. Heyden, B. Peters, A. T. Bell. *J. Phys. Chem. B.* **2005**, *109*, 1857.

[264] F. Bottomley, W. V. F. Brooks. *Inorg. Chem.* **1977**, *16*, 501.

[265] C. B. Pamplin, E. S. F. Ma, N. Safari, S. J. Rettig, B. R. James. *J. Am. Chem. Soc.* **2001**, *123*, 8596.

[266] F. Paulat, T. Kuschel, Näther, V. K. K. Praneeth, O. Sander, N. Lehnert. *Inorg. Chem.* **2004**, *43*, 6979.

[267] A. E. Reed, L. A. Curtiss, F. Weinhold. *Chem. Rev.* **1998**, *88*, 899.

[268] C. E. Macbeth, A. P. Golombek, V. G. Young Jr., C. Yang, K. Kuczera, M. P. Hendrich, A. S. Borovik. *Science* **2000**, *289*, 938.

[269] D. H. Dolphin, J. R. Sams, T. B. Tsin, K. L. Wong. *J. Am. Chem. Soc.* **1978**, *100*, 1711.

[270] L. Que Jr, A. E. True. *Prog. Inorg. Chem.* **1990**, *38*, 97.

[271] H. S. Soo, A. C. Komor, A. T. Iavarone, C. J. Chang. *Inorg. Chem.* **2009**, *48*, 10024.

[272] L. J. J. Laarhoven, P. Mulder, D. D. M. Wayner. *Acc. Chem. Res.* **1999**, *32*, 342.

[273] C. R. Goldsmith, R. T. Jonas, T. D. P. Stack. *J. Am. Chem. Soc.* **2002**, *124*, 83.

[274] C. R. Goldsmith, T. D. P. Stack. *Inorg. Chem.* **2006**, *45*, 6048.

[275] E. V. Starokon, M. V. Parfenov, L. V. Pirutko, S. I. Abornev, G. I. Panov. *J. Phys. Chem. C* **2011**, *115*, 2155.

[276] J. P. Perdew, K. Burke, M. Ernzerhof. *Phys. Rev. Lett.* **1996**, *77*, 3865.

[277] C. Franchini, R. Kováčik, M. Marsman, S. S. Murthy, J. He, C. Ederer, G. Kreese. *J. Phys. Condens. Mater.* **2012**, *24*, 235602.

[278] P. Verma, X. Xu, D. G. Truhlar. *J. Phys. Chem. C* **2013**, *117*, 12648.

[279] R. Maurice, P. Verma, J. M. Zadrozny, S. Luo, J. Borycz, J. R. Long, D. G. Truhlar, L. Gagliardi. *Inorg. Chem.* **2013**, *52*, 9379.

[280] K. Andersson, P.-Å. Malmqvist, B. O. Roos. *J. Chem. Phys.* **1992**, *96*, 1218.

[281] K. Andersson, P. Å. Malmqvist, B. O. Roos, A. J. Sadlej, K. Wolinski. *J. Phys. Chem* **1990**, *94*, 5483.

[282] S. Shaik, H. Hirao, D. Kumar. *Acc. Chem. Res.* **2007**, *40*, 532.

[283] J. England, Y. Guo, E. R. Farquhar, V. G. Young Jr., E. Münck, L. Que Jr. *J. Am. Chem. Soc.* **2010**, *132*, 8635.

[284] D. C. Lacy, R. Gupta, K. L. Stone, J. Greaves, J. W. Ziller, M. P. Hendrich, A. S. Borovik. *J. Am. Chem. Soc.* **2010**, *132*, 12188.

[285] J. England, Y. Guo, K. M. Van Heuvelen, M. A. Cranswick, G. T. Rohde, E. L. Bominaar, E. Münck, L. Que Jr. *J. Am. Chem. Soc.* **2011**, *133*, 11880.

[286] J. P. Bigi, W. H. Harman, B. Lassalle-Kaiser, D. M. Robles, T. A. Stich, R. D. Britt, C. J. Chang. *J. Am. Chem. Soc.* **2012**, *134*, 1536.

[287] O. Pestovsky, S. Stoian, E. L. Bominaar, X. Shan, E. Münck, L. Que Jr., A. Bakac. *Angew. Chem. Int. Ed.* **2005**, *44*, 6871.

[288] K. Lee, W. C. Isley, A. L. Dzubak, P. Verma, S. J. Stoneburner, L.-C. Lin, J. D. Howe, E. D. Bloch, D. A. Reed, M. R. Hudson, C. M. Brown, J. R. Long, J. B. Neaton, B. Smit, C. J. Cramer, D. G. Truhlar, L. Gagliardi. *J. Am. Chem. Soc.* **2014**, *136*, 698.

[289] A. D. Allen, C. V. Senoff. *J. Chem. Soc., Chem. Commun.* **1965**, *24*, 621.

[290] M. D. Fryzuk, S. A. Johnson. *Coord. Chem. Rev.* **2000**, *200-202*, 379.

[291] A. D. Allen, R. O. Harris, B. R. Loescher, J. R. Stevens, R. N. Whiteley. *Chem. Rev.* **1973**, *73*, 11.

[292] K. A. Lokhandwala, I. Pinnau, Z. He, K. D. Amo, A. R. DaCosta, J. G. Wijmans, R. W. Baker. *J. Membr. Sci.* **2010**, *346*, 270.

[293] T. Duren, Y. S. Bae, R. Q. Snurr. *Chem. Soc. Rev.* **2009**, *38*, 1237.

[294] J. R. Li, R. J. Kuppler, H. C. Zhou. *Chem. Soc. Rev.* **2009**, *38*, 1477.

[295] T. M. McDonald, W. R. Lee, J. A. Mason, B. M. Wiers, C. S. Hong, J. R. Long. *J. Am. Chem. Soc.* **2012**, *134*, 7056.

[296] N. L. Rosi, J. Kim, M. Eddaoudi, B. Chen, M. O'Keeffe, O. M. Yaghi. *J. Am. Chem. Soc.* **2005**, *127*, 1504.

[297] P. D. C. Dietzel, Y. Morita, R. Blom, H. Fjellvag. *Angew. Chem., Int. Ed.* **2005**, *44*, 6354.

[298] P. D. C. Dietzel, B. Panella, M. Hirscher, R. Blom, H. Fjellvag. *Chem. Commun.* **2006**, 959.

[299] N. Nijem, J. F. Veyan, L. Kong, K. Li, S. Pramanik, Y. Zhao, J. Li, D. Langreth, Y. J. Chabal. *J. Am. Chem. Soc.* **2010**, *132*, 1654.

[300] E. D. Bloch, L. J. Murray, W. L. Queen, S. Chavan, S. N. Maximoff, J. P. Bigi, R. Krishna, V. K. Peterson, F. Grandjean, G. J. Long, B. Smit, S. Bordiga, C. M. Brown, J. R. Long. *J. Am. Chem. Soc.* **2011**, *133*, 14814.

[301] P. Verma, X. Xu, D. G. Truhlar. *J. Phys. Chem. C* **2013**, *117*, 12648.

[302] H. Wu, W. Zhou, T. Yildirim. *J. Am. Chem. Soc.* **2009**, *131*, 4995.

[303] L. Valenzano, B. Civalleri, S. Chavan, G. T. Palomino, C. O. Arean, S. Bordiga. *J. Phys. Chem. C* **2010**, *114*, 11185.

[304] A. Yamamoto, *Organotransition Metal Chemistry*, Wiley: New York, **1986**.

[305] R. H. Crabtree, *The Organometallic Chemistry of the Transition Metals 2nd ed.*, Wiley: New York, **1994**.

[306] W. Kohn, A. D. Becke, R. G. Parr. *J. Phys. Chem.* **1996**, *100*, 12974.

[307] M. Dion, H. Rydberg, E. Schroder, D. C. Langreth, B. I. Lundqvist. *Phys. Rev. Lett.* **2004**, *92*, 246401.

[308] K. Lee, E. D. Murray, L. Kong, B. I. Lundqvist, D. C. Langreth. *Phys. Rev. B.* **2010**, *82*, 081101.

[309] A. I. Liechtenstein, V. I. Anisimov, J. Zaanen. *Phys. Rev. B* **1995**, *52*, R5467.

[310] Y. Zhao, D. G. Truhlar. *Acc. Chem. Res.* **2008**, *41*, 157.

[311] Y. Zhao, D. G. Truhlar. *Chem. Phys. Lett.* **2011**, *502*, 1.

[312] Y. Zhao, D. G. Truhlar. *J. Chem. Phys.* **2006**, *125*, 194101.

[313] Y. Zhao, D. G. Truhlar. *Theor. Chem. Acc.* **2008**, *120*, 215.

[314] R. Peverati, D. G. Truhlar. *J. Phys. Chem. Lett.* **2012**, *3*, 117.

[315] A. D. Becke. *J. Chem. Phys.* **1993**, *98*, 1372.

[316] F. Neese, A. Hansen, D. G. Liakos. *J. Chem. Phys.* **2009**, *131*, 064103.

[317] K. Andersson, P. A. Malmqvist, B. O. Roos. *J. Chem. Phys.* **1992**, *96*, 1218.

[318] L. Fohlmeister, S. Liu, C. Schulten, B. Moubaraki, A. Stasch, J. D. Cashion, K. S. Murray, L. Gagliardi, C. Jones. *Angew. Chem., Int. Ed.* **2012**, *51*, 8294.

[319] G. Li Manni, A. L. Dzubak, A. Mulla, D. W. Brogden, J. F. Berry, L. Gagliardi. *Chem. Eur. J.* **2012**, *18*, 1737.

[320] R. Sanz, F. Martinez, G. Orcajo, L. Wojtas, D. Briones. *Dalton Trans.* **2013**, *42*, 2392.

[321] A. V. Marenich, S. V. Jerome, C. J. Cramer, D. G. Truhlar. *J. Chem. Theor. Comput.* **2012**, *8*, 527.

[322] A. V. Marenich, C. J. Cramer, D. G. Truhlar, *CM5PAC*, **2011**, University of Minnesota: Minneapolis.

[323] M. J. Frisch, et al., *Gaussian 09, Revision C.01*, **2010**, Gaussian, Inc.: Wallingford, CT.

[324] Y. Zhao, R. Peverati, K. R. Yang, D. G. Truhlar, *MN-GFM 6.4*, **2012**, University of Minnesota: Minneapolis.

[325] G. Kresse, J. Furthmuller. *Phys. Rev. B* **1996**, *54*, 11169.

[326] F. Neese. *WIREs Comput. Mol. Sci.* **2012**, *2*, 73.

[327] F. Aquilante, et al. *J. Comput. Chem.* **2010**, *31*, 224.

[328] E. J. Baerends, et al., *ADF2013, SCM*, **2013**, Theoretical Chemistry, Vrije Universiteit: Amsterdam, The Netherlands, available from `http://www.scm.com`.

[329] G. te Velde, F. M. Bickelgaupt, S. J. A. van Gisbergen, C. Fonseca Guerra, E. J. Baerends, J. G. Snijders, T. Ziegler. *J. Comput. Chem.* **2001**, *22*, 931.

[330] C. Fonseca Guerra, J. G. Snijders, G. te Velde, E. J. Baerends. *Theor. Chem. Acc.* **1998**, *99*, 391.

[331] G. Kresse, A. Gil, P. Sautet. *Phys. Rev. B* **2003**, *68*, 073401.

[332] E. D. Bloch, W. L. Queen, R. Krishna, J. M. Zadrozny, C. M. Brown, J. R. Long. *Science* **2012**, *335*, 1606.

[333] M. Mitoraj, A. Michalak, T. Ziegler. *J. Chem. Theor. Comput.* **2009**, *5*, 962.

[334] A. E. Reed, L. A. Curtiss, F. Weinhold. *Chem. Rev.* **1998**, *88*, 899.

[335] E. D. Bloch, M. R. Hudson, J. A. Mason, S. Chavan, V. Crocell, J. D. Howe, K. Lee, A. L. Dzubak, W. L. Queen, J. M. Zadrozny, S. J. Geier, L.-C. Lin, L. Gagliardi, B. Smit, J. B. Neaton, S. Bordiga, C. M. Brown, J. R. Long. *J. Am. Chem. Soc.* **2014**, *136*, 10752.

[336] A. J. E. Welch. *Rep. Prog. Chem.* **1941**, *38*, 71.

[337] J. S. Anderson. *Q. Rev. Chem.* **1947**, *1*, 331.

[338] C. R. Schützenberger. *Bull. Soc. Chim. Paris* **1868**, *10*, 188.

[339] J. E. Ellis, W. Beck. *Angew. Chem., Int. Ed. Engl.* **1995**, *34*, 2489.

[340] J. A. Timney. *Organomet. Chem.* **1999**, *27*, 132.

[341] F. Aubke, C. Wang. *Coord. Chem. Rev.* **1994**, *137*, 483.

[342] A. J. Lupinetti, S. H. Strauss, G. Frenking. *Prog. Inorg. Chem.* **2001**, *49*, 1.

[343] D. Benito-Caragorri, I. Lagoja, L. F. Veiros, K. A. Kirchner. *Dalton Trans.* **2011**, *40*, 4778.

[344] F. G. Kerry, *Industrial Gas Handbook: Gas Separation and Purification*, CRC: Boca Raton, FL, **2007**.

[345] F. P. McCandless. *Ind. Eng. Chem. Process Des. Dev.* **1972**, *11*, 470.

[346] H. Miyajima, A. Kodama, M. Goto, T. Hirose. *Adsorption* **2005**, *11*, 625.

[347] N. L. Rosi, J. Kim, M. Eddaoudi, B. Chen, M. O'Keeffe, O. M. Yaghi. *J. Am. Chem. Soc.* **2005**, *127*, 1504.

[348] P. D. C. Dietzel, Y. Morita, R. Blom, H. Fjellvåg. *Angew. Chem., Int. Ed.* **2005**, *44*, 6354.

[349] P. D. C. Dietzel, B. Panella, M. Hirscher, R. Blom, H. Fjellvåg. *Chem. Commun.* **2006**, 959.

[350] P. D. C. Dietzel, R. Blom, H. Fjellvåg. *Eur. J. Inorg. Chem.* **2008**, 3624.

[351] W. Zhou, H. Wu, T. Yildirim. *J. Am. Chem. Soc.* **2008**, *130*, 15268.

[352] S. R. Caskey, A. G. Wong-Foy, A. J. Matzger. *J. Am. Chem. Soc.* **2008**, *130*, 10870.

[353] E. D. Bloch, L. J. Murray, W. L. Queen, S. Chavan, S. N. Maximoff, J. P. Bigi, R. Krishna, V. K. Peterson, F. Grandjean, G. J. Long, B. Smit, S. Bordiga, C. M. Brown, J. R. Long. *J. Am. Chem. Soc.* **2011**, *133*, 14814.

[354] J. A. Mason, K. Sumida, Z. R. Herm, R. Krishna, J. R. Long. *Energy Environ. Sci.* **2011**, *4*, 3030.

[355] G. Férey, C. Serre, T. Devic, G. Maurin, H. Jobic, P. L. Llewellyn, G. De Weireld, A. Vimont, M. Daturi, J.-S. Chang. *Chem. Soc. Rev.* **2011**, *40*, 550.

[356] J.-R. Li, J. Sculley, H.-C. Zhou. *Chem. Rev.* **2012**, *112*, 869.

[357] Z. R. Herm, J. A. Swisher, B. Smit, R. Krishna, J. R. Long. *J. Am. Chem. Soc.* **2011**, *133*, 5664.

[358] K. Lee, W. C. Isley, A. L. Dzubak, P. Verma, S. J. Stoneburner, L.-C. Lin, J. D. Howe, E. D. Bloch, D. A. Reed, M. R. Hudson, C. M. Brown, J. R. Long, J. B. Neaton, B. Smit, C. J. Cramer, D. G. Truhlar, L. Gagliardi. *J. Am. Chem. Soc.* **2013**, *136*, 698.

[359] Z. Zhang, S. Xiang, B. Chen. *CrystEngComm* **2011**, *13*, 5983.

[360] E. D. Bloch, W. L. Queen, R. Krishna, J. M. Zadrozny, C. M. Brown, J. R. Long. *Science* **2012**, *335*, 1606.

[361] Y.-S. Bae, C. Y. Lee, K. C. Kim, O. K. Farha, P. Nickias, J. T. Hupp, S. T. Nguyen, R. Q. Snurr. *Angew. Chem., Int. Ed.* **2012**, *51*, 1857.

[362] D. Yu, A. O. Yazaydin, J. R. Lane, P. D. C. Dietzel, R. Q. Snurr. *Chem. Sci.* **2013**, *4*, 3544.

[363] R. Poloni, K. Lee, R. F. Berger, B. Smit, J. B. Neaton. *J. Phys. Chem. Lett.* **2014**, *5*, 861.

[364] E. W. Lemmon, R. Span. *J. Chem. Eng. Data* **2006**, *51*, 785.

[365] E. W. Lemmon, M. L. Huber, M. O. McLinden, *NIST Standard Reference Database 23: Reference Fluid Thermodynamic and Transport Properties-REFPROP, Version 8.0*, National Institute of Standards and Technology, Standard Reference Data Program: Gaithersburg, MD, **2007**.

[366] J. W. Leachman, R. T. Jacobsen, E. W. Lemmon. *J. Phys. Chem. Ref. Data* **2009**, *38*, 721.

[367] A. L. Myers, J. M. Prausnitz. *AIChE J.* **1965**, *11*, 121.

[368] R. Krishna, S. Calero, B. Smit. *Chem. Eng. J.* **2002**, *88*, 81.

[369] R. Krishna, J. M. van Baten. *Chem. Eng. J.* **2007**, *133*, 121.

[370] R. Krishna, J. M. van Baten. *Phys. Chem. Chem. Phys.* **2011**, *13*, 10593.

[371] K. Sumida, C. M. Brown, Z. R. Herm, S. Chavan, S. Bordiga, J. R. Long. *Chem. Commun.* **2011**, *47*, 1157.

[372] J. Mason, M. Veenstra, J. R. Long. *Chem. Sci.* **2014**, *5*, 32.

[373] G. A. Bain, J. F. Berry. *J. Chem. Educ.* **2008**, *85*, 532.

[374] B. H. Toby. *J. Appl. Crystallogr.* **2001**, *34*, 210.

[375] A. C. Larson, R. B. Von Dreel. *Los Alamos Natl. Lab., [Rep.] LA (U. S.)* **1994**, 86.

[376] W. L. Queen, E. D. Bloch, C. M. Brown, M. R. Hudson, J. A. Mason, L. J. Murray, A. J. R.-Cuesta, V. K. Peterson, J. R. Long. *Dalton Trans.* **2012**, *41*, 4180.

[377] J. Perdew, K. Burke, M. Ernzerhof. *Phys. Rev. Lett.* **1996**, *77*, 3865.

[378] K. Lee, É. D. Murray, L. Kong, B. I. Lundqvist, D. C. Langreth. *Phys. Rev. B: Condens. Matter Mater. Phys.* **2010**, *82*, 081101.

[379] G. Kresse, D. Joubert. *Phys. Rev. B: Condens. Matter Mater. Phys.* **1999**, *59*, 1758.

[380] P. E. Blöchl. *Phys. Rev. B: Condens. Matter Mater. Phys.* **1994**, *50*, 17953.

[381] V. I. Anisimov, J. Zaanen, O. K. Andersen. *Phys. Rev. B: Condens. Matter Mater. Phys.* **1991**, *44*, 943.

[382] S. L. Dudarev, G. A. Botton, S. Y. Savrasov, C. J. Humphreys, A. P. Sutton. *Phys. Rev. B: Condens. Matter Mater. Phys.* **1998**, *57*, 1505.

[383] L. Wang, T. Maxisch, G. Ceder. *Phys. Rev. B: Condens. Matter Mater. Phys.* **2006**, *73*, 195107.

[384] P. Canepa, Y. J. Chabal, T. Thonhauser. *Phys. Rev. B: Condens. Matter Mater. Phys.* **2013**, *87*, 094407.

[385] R. Poloni, B. Smit, J. B. Neaton. *J. Phys. Chem. A* **2012**, *116*, 4957.

[386] P. Verma, X. Xu, D. G. Truhlar. *J. Phys. Chem. C* **2013**, *117*, 12648.

[387] J. P. Perdew, K. Burke, M. Enzerhof. *Phys. Rev. Lett.* **1996**, *77*, 3865, Erratum **1997**, ibid., *78*, 1396.

[388] TURBOMOLE V6.4 2012; University of Karlsruhe and Forschungszentrum Karlsruhe GmbH: Karlsruhe, 1989-2007; TURBOMOLE GmbH: Karlsruhe, 2007; available from `http://www.turbomole.com`.

[389] M. Von Arnim, R. Ahlrichs. *J. Comput. Chem.* **1998**, *19*, 1746.

[390] R. Ahlrichs. *Phys. Chem. Chem. Phys.* **2004**, *6*, 5119.

[391] K. Eichkorn, O. Treutler, H. Öhm, M. Häser, R. Ahlrichs. *Chem. Phys. Lett.* **1995**, *242*, 652.

[392] K. Eichkorn, F. Weigend, O. Treutler, R. Ahlrichs. *Theor. Chem. Acc.* **1997**, *97*, 119.

[393] F. Weigend. *Phys. Chem. Chem. Phys.* **2006**, *8*, 1057.

[394] F. Weigend, R. Ahlrichs. *Phys. Chem. Chem. Phys.* **2005**, *7*, 3297.

[395] M. Mitoraj, A. Michalak, T. Ziegler. *J. Chem. Theory Comput.* **2009**, *5*, 962.

[396] G. te Velde, F. M. Bickelhaupt, S. J. A. van Gisbergen, C. Fonseca Guerra, E. J. Baerends, J. G. Snijders, T. Ziegler. *J. Comput. Chem.* **2001**, *22*, 931.

[397] C. Fonseca Guerra, J. G. Snijders, G. te Velde, E. J. Baerends. *Theor. Chem. Acc.* **1998**, *99*, 391.

[398] E. J. Baerends, et al., *ADF2013, SCM*, **2013**, Theoretical Chemistry, Vrije Universiteit: Amsterdam, The Netherlands, available from `http://www.scm.com`.

[399] Y. Zhao, D. G. Truhlar. *J. Chem. Phys.* **2006**, *125*, 194101.

[400] C. Lamberti, A. Zecchina, E. Groppo, S. Bordiga. *Chem. Soc. Rev.* **2010**, *39*, 4951.

[401] S. Chavan, J. G. Vitillo, E. Groppo, F. Bonino, C. Lamberti, P. D. C. Dietzel, S. Bordiga. *J. Phys. Chem. C* **2009**, *113*, 3292.

[402] L. Valenano, B. Civalleri, S. Chavan, G. T. Palomino, C. O. Areán, S. Bordiga. *J. Phys. Chem. C* **2010**, *114*, 11185.

[403] S. Bordiga, F. Bonino, K. P. Lillerud, C. Lamberti. *Chem. Soc. Rev.* **2010**, *39*, 4885.

[404] M. J. S. Dewar. *Bull. Soc. Chim. Fr.* **1951**, *18*, C79.

[405] J. Chatt, L. A. Duncanson. *J. Chem. Soc.* **1953**, 2939.

[406] A. J. Lupinetti, S. Fau, G. Frenking, S. H. Strauss. *J. Phys. Chem. A* **1997**, *101*, 9551.

[407] P. Li, Y. Xiang, V. H. Grassian, S. C. Larsen. *J. Phys. Chem. B* **1999**, *103*, 5058.

[408] L. Valenzano, B. Civalleri, K. Sillar, J. Sauer. *J. Phys. Chem. C* **2011**, *115*, 21777.

[409] L. Valenzano, J. G. Vitillo, S. Chavan, B. Civalleri, F. Bonino, S. Bordiga, C. Lamberti. *Catal. Today* **2012**, *182*, 67.

[410] R. H. Reimann, E. Singleton. *J. Chem. Soc., Dalton Trans.* **1973**, 2658.

[411] F. Bombin, G. A. Carriedo, J. A. Miguel, V. Riera. *J. Chem. Soc., Dalton Trans.* **1981**, 2049.

[412] A. M. Bond, R. Colton, M. E. McDonald. *Inorg. Chem.* **1978**, *17*, 2842.

[413] J. J. Bishop, A. Davison. *Inorg. Chem.* **1971**, *10*, 832.

[414] C. G. Pierpont, R. Eisenberg. *Inorg. Chem.* **1972**, *11*, 828.

[415] C. Saint-Joly, A. Mari, A. Gleizes, M. Dartiguenave, Y. Dartiguenave, J. Galy. *Inorg. Chem.* **1980**, *19*, 2403.

[416] C. A. Ghilardi, S. Midollini, L. Sacconi. *J. Organomet. Chem.* **1980**, *186*, 279.

[417] S. K. Janikowski, L. J. Radonovich, T. J. Groshens, K. J. Klabunde. *Organometallics* **1985**, *4*, 396.

[418] A. Miedaner, C. J. Curtis, S. A. Wander, P. A. Goodson, D. L. DuBois. *Organometallics* **1996**, *15*, 5185.

[419] A. D. Wilson, K. Fraze, B. Twamley, S. M. Miller, D. L. DuBois, M. R. DuBois. *J. Am. Chem. Soc.* **2008**, *130*, 1061.

[420] T. R. Krawietz, D. H. Barich, L. W. Beck, T. Howard, T. Xu, J. F. Haw. *J. Am. Chem. Soc.* **1995**, *117*, 10407.

[421] R. Georges, J. J. Borras-Almenar, E. Coronado, J. Curely, M. Drillon, *Magnetism: Molecules to Materials I: Models and Experiments*, J. S. Miller, M. Drillon (Eds.), Wiley-VCH: Weinheim, Germany, **2002**.

[422] O. Kahn, *Molecular Magnetism*, Wiley-VCH: New York, **1993**.

[423] S. J. Geier, J. A. Mason, E. D. Bloch, W. L. Queen, M. R. Hudson, C. M. Brown, J. R. Long. *Chem. Sci.* **2013**, *4*, 2054.

[424] R. Maurice, P. Verma, J. M. Zadrozny, S. Luo, J. Borycz, J. R. Long, D. G. Truhlar, L. Gagliardi. *Inorg. Chem.* **2013**, *52*, 9379.

[425] M. Ray, A. P. Golombek, M. P. Hendrich, V. G. Young, A. S. Borovik. *J. Am. Chem. Soc.* **1996**, *118*, 6084.

[426] D. H. Nguyen, H.-F. Hsu, M. Millar, S. A. Koch. *J. Am. Chem. Soc.* **1996**, *118*, 8963.

[427] S. C. Davies, D. L. Hughes, R. L. Richards, J. R. Sanders. *Chem. Commun.* **1998**, 2699.

[428] J. C. M. Farla, C. A. Hendriks, K. Blok. *Clim. Change* **1995**, *29*, 439.

[429] H. Sato, W. Kosaka, R. Matsuda, A. Hori, Y. Hijikata, R. V. Belosludov, S. Sakaki, M. Takata, S. Kitagawa. *Science* **2014**, *343*, 167.

[430] J. Billy, F. Fuentes, N. Sosson, **2001**, US Patent 6,173,585.

[431] A. L. Myers, J. M. Prausnitz. *AIChE J.* **1965**, *11*, 121.

[432] R. Krishna, J. M. van Baten. *Phys. Chem. Chem. Phys.* **2011**, *13*, 10593.

[433] D. Saha, S. Deng. *J. Chem. Eng. Data* **2009**, *54*, 2245.

[434] C. M. Zall, D. Zherebetskyy, A. L. Dzubak, E. Bill, L. Gagliardi, C. C. Lu. *Inorg. Chem.* **2012**, *51*, 728.

[435] F. A. Cotton, *Reactivity of Metal-Metal Bonds*, *Vol. 155*, M. H. Chisholm (Ed.), American Chemical Society: Washington, D. C., **1981**, chapter Metal-Metal Multiple Bonds and Metal Clusters, pp. 1–16.

[436] F. A. Cotton, X. Feng. *J. Am. Chem. Soc.* **1998**, *120*, 3387.

[437] F. A. Cotton, X. Feng. *J. Am. Chem. Soc.* **1997**, *119*, 7514.

[438] M. B. Hall. *Polyhedron* **1987**, *6*, 679.

[439] S. Petrie, R. Stranger. *Inorg. Chem.* **2004**, *43*, 2597.

[440] D. J. Timmons, M. P. Doyle, *Multiple Bonds Between Metal Atoms 3rd ed.*, F. A. Cotton, C. A. Murillo, R. A. Walton (Eds.), Springer Science: New York, **2005**, chapter Chiral Dirhodium(II) Catalysts and Their Applications, pp. 591–632.

[441] H. M. L. Davies, R. E. J. Beckwith. *Chem. Rev.* **2003**, *103*, 2861.

[442] M. P. Doyle, T. Ren. *Prog. Inorg. Chem.* **2001**, *49*, 113.

[443] J. L. Dempsey, A. J. Esswein, D. R. Manke, J. Rosenthal, J. D. Soper, D. G. Nocera. *Inorg. Chem.* **2005**, *44*, 6879.

[444] A. F. Heyduk, A. M. Macintosh, D. G. Nocera. *J. Am. Chem. Soc.* **1999**, *121*, 5023.

[445] A. F. Heyduk, D. G. Nocera. *Science* **2001**, *293*, 1639.

[446] R. R. Schrock, M. L. Listemann, L. G. Sturgeoff. *J. Am. Chem. Soc.* **1982**, *104*, 4291.

[447] H. Strutz, R. R. Schrock. *Organometallics* **1984**, *3*, 1600.

[448] M. H. Chisholm, E. R. Davidson, M. Pink, K. B. Quinlan. *Chem. Commun.* **2002**, 2770.

[449] P. Angaridis, *Multiple Bonds Between Metal Atoms 3rd ed.*, F. A. Cotton, C. A. Murillo, R. A. Walton (Eds.), Springer Science: New York, **2005**, chapter Ruthenium Compounds, pp. 377–430.

[450] B. O. Roos, A. C. Borin, L. Gagliardi. *Angew. Chem., Int. Ed.* **2007**, *46*, 1469.

[451] G. La Macchia, G. Li Manni, T. K. Todorova, M. Brynda, F. Aquilante, B. O. Roos, L. Gagliardi. *Inorg. Chem.* **2010**, *49*, 5216.

[452] G. La Macchia, V. Veryazov, B. O. Roos, L. Gagliardi. *Inorg. Chem.* **2008**, *47*, 11455.

[453] M. Brynda, L. Gagliardi, B. O. Roos. *Chem. Phys. Lett.* **2009**, *471*, 1.

[454] B. O. Roos, P. R. Taylor, P. E. M. Siegbahn. *Chem. Phys.* **1980**, *48*, 157.

[455] F. Allen. *Acta Crystallogr., Sect. B: Struct. Sci.* **2002**, *58*, 380.

[456] C. R. Hess, T. Weyhermüller, E. Bill, K. Wieghardt. *Angew. Chem., Int. Ed.* **2009**, *48*, 3703.

[457] T. Nguyen, W. A. Merrill, C. Ni, H. Lei, J. C. Fettinger, B. D. Ellis, G. J. Long, M. Brynda, P. P. Power. *Angew. Chem., Int. Ed.* **2008**, *47*, 9115.

[458] A. Klose, E. Solari, C. Floriani, A. Chiesi-Villa, C. Rizzoli, N. Re. *J. Am. Chem. Soc.* **1994**, *116*, 9123.

[459] F. A. Cotton, L. M. Daniels, L. R. Falvello, J. H. Matonic, C. A. Murillo. *Inorg. Chim. Acta* **1997**, *256*, 269.

[460] F. A. Cotton, L. M. Daniels, J. H. Matonic, C. A. Murillo. *Inorg. Chim. Acta* **1997**, *256*, 277.

[461] G. La Macchia, L. Gagliardi, P. P. Power, M. Brynda. *J. Am. Chem. Soc.* **2008**, *130*, 5104.

[462] Q. Zhao, T. D. Harris, T. A. Betley. *J. Am. Chem. Soc.* **2011**, *133*, 8293.

[463] D. G. Leopold, J. Almlöf, W. C. Lineberger, P. R. Taylor. *J. Chem. Phys.* **1988**, *88*, 3780.

[464] O. Hübner, J. Sauer. *Chem. Phys. Lett.* **2002**, *358*, 442.

[465] T. Liu, M. Y. Darensbourg. *J. Am. Chem. Soc.* **2007**, *129*, 7008.

[466] A. K. Justice, M. J. Nilges, T. B. Rauchfuss, S. R. Wilson, L. De Gioia, G. Zampella. *J. Am. Chem. Soc.* **2008**, *130*, 5293.

[467] A. K. Justice, T. B. Rauchfuss, S. R. Wilson. *Angew. Chem., Int. Ed.* **2007**, *46*, 6152.

[468] C. M. Thomas, M. Y. Darensbourg, M. B. Hall. *J. Inorg. Biochem.* **2007**, *101*, 1752.

[469] F. A. Cotton, L. M. Daniels, L. R. Falvello, C. A. Murillo. *Inorg. Chim. Acta* **1994**, *219*, 7.

[470] C. J. O'Connor, *Prog. Inorg. Chem.*, *Vol. 29*, S. J. Lippard (Ed.), John Wiley & Sons, Inc.: New Jersey, **1982**, chapter Magnetochemistry-Advances in Theory and Experimentation, pp. 203–283.

[471] R. C. Weast, M. J. Astle, *CRC Handbook of Chemistry and Physics*, CRC Press Inc.: Boca Raton, FL, **1979**.

[472] E. Bill, *julX version 141*, available from `http://ewww.mpi-muelheim.mpg.de/bac/logins/bill/julX_en.php`.

[473] V. I. Lebedev, D. N. Laikov. *Dokl. Math.* **1999**, *59*, 477.

[474] A. X. Trautwein, E. Bill, E. L. Bominaar, H. Winkler. *Struct. Bonding (Berlin)* **1991**, *78*, 1.

[475] K. Andersson, P.-Å. Malmqvist, B. O. Roos. *J. Chem. Phys.* **1992**, *96*, 1218.

[476] L. Gagliardi, B. O. Roos. *Inorg. Chem.* **2003**, *42*, 1599.

[477] F. Ferrante, L. Gagliardi, B. E. Bursten, A. P. Sattelberger. *Inorg. Chem.* **2005**, *44*, 8476.

[478] F. Poineau, P. M. Forster, T. K. Todorova, L. Gagliardi, A. P. Sattelberger, K. R. Czerwinski. *Inorg. Chem.* **2010**, *49*, 6646.

[479] F. Poineau, L. Gagliardi, P. M. Forster, A. P. Sattelberger, K. R. Czerwinski. *Dalton Trans.* **2009**, 5954.

[480] B. N. Briggs, D. R. McMillin, T. K. Todorova, L. Gagliardi, F. Poineau, K. R. Czerwinski, A. P. Sattelberger. *Dalton Trans.* **2010**, *39*, 11322.

[481] J. P. Perdew, A. Zunger. *Phys. Rev. B* **1981**, *23*, 5048.

[482] TURBOMOLE V6.1 2010; University of Karlsruhe and Forschungszentrum Karlsruhe GmbH: Karlsruhe, 1989-2007; TURBOMOLE GmbH: Karlsruhe, 2007; available from `http://www.turbomole.com`.

[483] R. Ahlrichs, M. Bar, M. Haser, H. Horn, C. Kolmel. *Chem. Phys. Lett.* **1989**, *162*, 165.

[484] F. Nesse, *ORCA version 2.8-20*, available from `http://www.thch.uni-bonn.de/tc/orca`.

[485] F. Neese. *Inorg. Chim. Acta* **2002**, *337*, 181.

[486] S. Sinnecker, L. D. Slep, E. Bill, F. Neese. *Inorg. Chem.* **2005**, *44*, 2245.

[487] A. Schäfer, H. Horn, R. Ahlrichs. *J. Chem. Phys.* **1992**, *97*, 2571.

[488] A. Schäfer, C. Huber, R. Ahlrichs. *J. Chem. Phys.* **1994**, *100*, 5829.

[489] F. Aquilante, L. De Vico, N. Ferré, G. Ghigo, P.-Å. Malmqvist, T. Pedersen, M. Pitonak, M. Reiher, B. O. Roos, L. Serrano-Andrés, M. Urban, V. Veryazov, R. Lindh. *J. Comput. Chem.* **2010**, *31*, 224.

[490] B. O. Roos, R. Lindh, P.-Å. Malmqvist, V. Veryazov, P. O. Widmark. *J. Phys. Chem. A* **2004**, *108*, 2851.

[491] B. O. Roos, R. Lindh, P.-Å. Malmqvist, V. Veryazov, P. O. Widmark. *J. Phys. Chem. A* **2005**, *109*, 6575.

[492] B. A. Hess. *Phys. Rev. A* **1986**, *33*, 3742.

[493] F. Aquilante, T. B. Pedersen, R. Lindh. *J. Chem. Phys.* **2007**, *126*, 194106.

[494] F. Aquilante, T. B. Pedersen, R. Lindh, B. O. Roos, A. S. De Meras, H. Koch. *J. Chem. Phys.* **2008**, *129*, 24113.

[495] F. Aquilante, P.-Å. Malmqvist, T. B. Pedersen, A. Ghosh, B. O. Roos. *J. Chem. Theory Comp.* **2008**, *4*, 694.

[496] N. Forsberg, P.-Å. Malmqvist. *Chem. Phys. Lett.* **1997**, *274*, 196.

[497] P.-Å. Malmqvist. *Int. J. Quantum Chem.* **1986**, *30*, 479.

[498] B. O. Roos, P.-Å. Malmqvist. *Phys. Chem. Chem. Phys.* **2004**, *6*, 2919.

[499] A. Bencini, D. Gatteschi, *Electron Paramagnetic Resonance of Exchange Coupled Systems*, Springer Verlag: Berlin, **1990**.

[500] F. A. Cotton, X. Feng, C. A. Murillo. *Inorg. Chim. Acta* **1997**, *256*, 303.

[501] H. Andres, E. L. Bominaar, J. M. Smith, N. A. Eckert, P. L. Holland, E. Münck. *J. Am. Chem. Soc.* **2002**, *124*, 3012.

[502] S. A. Stoian, Y. Yu, J. M. Smith, P. L. Holland, E. L. Bominaar, E. Münck. *Inorg. Chem.* **2005**, *44*, 4915.

[503] M. P. Hendrich, W. Gunderson, R. K. Behan, M. T. Green, M. P. Mehn, T. A. Betley, C. C. Lu, J. C. Peters. *Proc. Natl. Acad. Sci. U.S.A.* **2006**, *103*, 17107.

[504] M. Römelt, S. Ye, F. Neese. *Inorg. Chem.* **2009**, *48*, 784.

[505] G. H. Timmer, J. F. Berry. *C. R. Chim.* **2011**.

[506] T. M. Powers, A. R. Fout, S.-L. Zheng, T. A. Betley. *J. Am. Chem. Soc.* **2011**, *133*, 3336.

[507] T. D. Harris, T. A. Betley. *J. Am. Chem. Soc.* **2011**, *133*, 13852.

[508] G. L. Manni, A. L. Dzubak, A. Mulla, D. W. Brogden, J. F. Berry, L. Gagliardi. *Chem. Eur. J.* **2012**, *18*, 1737.

[509] F. A. Cotton, C. B. Harris. *Inorg. Chem.* **1965**, *4*, 330.

[510] F. A. Cotton, C. A. Murillo, R. A. Walton, *Multiple Bonds Between Metal Atoms 3rd ed.*, Springer: Berlin, **2005**.

[511] B. G. Alberding, M. H. Chisholm, Y. H. Chou, J. C. Gallucci, Y. Ghosh, T. L. Gustafson, N. J. Patmore, C. R. Reed, C. Turro. *Inorg. Chem.* **2009**, *48*, 4394.

[512] G. T. Burdzinski, M. H. Chisholm, P. T. Chou, Y. H. Chou, F. Feil, J. C. Gallucci, Y. Ghosh, T. L. Gustafson, M. L. Ho, Y. Liu, R. Ramnauth, C. Turro. *Proc. Natl. Acad. Sci. USA* **2008**, *105*, 15247.

[513] M. Nippe, E. Victor, J. F. Berry. *Inorg. Chem.* **2009**, *48*, 11889.

[514] M. C. Suen, Y. Y. Wu, J. D. Chen, T. C. Keng, J. C. Wang. *Inorg. Chim. Acta* **1999**, *288*, 82.

[515] M. Nippe, J. F. Berry. *J. Am. Chem. Soc.* **2007**, *129*, 12684.

[516] M. Nippe, E. Victor, J. F. Berry. *Eur. J. Inorg. Chem.* **2008**, 5569.

[517] M. Nippe, G. H. Timmer, J. F. Berry. *Chem. Commun.* **2009**, 4357.

[518] M. Nippe, J. F. Wang, E. Bill, H. Hope, N. S. Dalal, J. F. Berry. *J. Am. Chem. Soc.* **2010**, *132*, 14261.

[519] D. Aydin-Cantürk, H. Nuss. *Z. Anorg. Allg. Chem.* **2011**, *637*, 543.

[520] B. O. Roos, A. C. Borin, L. Gagliardi. *Angew. Chem.* **2007**, *119*, 1491.

[521] B. O. Roos, A. C. Borin, L. Gagliardi. *Angew. Chem. Int. Ed.* **2007**, *46*, 1469.

[522] M. Brynda, L. Gagliardi, P. O. Widmark, P. P. Power, B. O. Roos. *Angew. Chem.* **2006**, *118*, 3888.

[523] M. Brynda, L. Gagliardi, P. O. Widmark, P. P. Power, B. O. Roos. *Angew. Chem. Int. Ed.* **2006**, *45*, 3804.

[524] B. O. Roos, P. Linse, P. E. M. Siegbahn, M. R. A. Blomberg. *Chem. Phys.* **1982**, *66*, 197.

[525] B. O. Roos. *Collect. Czech. Chem. Commun.* **2003**, *68*, 265.

[526] G. La Macchia, G. L. Manni, T. K. Todorova, M. Brynda, F. Aquilante, B. O. Roos, L. Gagliardi. *Inorg. Chem.* **2010**, *49*, 5216.

[527] T. Nguyen, A. D. Sutton, M. Brynda, J. C. Fettinger, G. J. Long, P. P. Power. *Science* **2005**, *310*, 844.

[528] C. R. Landis, F. Weinhold. *J. Am. Chem. Soc.* **2006**, *128*, 7335.

[529] G. La Macchia, L. Gagliardi, P. P. Power, M. Brynda. *J. Am. Chem. Soc.* **2008**, *130*, 5104.

[530] T. Nguyen, A. Panda, M. M. Olmstead, A. F. Richards, M. Stender, M. Brynda, P. P. Power. *J. Am. Chem. Soc.* **2005**, *127*, 8545.

[531] T. Nguyen, W. A. Merrill, C. Ni, H. Lei, J. C. Fettinger, B. D. Ellis, G. L. Long, M. Brynda, P. P. Power. *Angew. Chem.* **2008**, *120*, 9255.

[532] T. Nguyen, W. A. Merrill, C. Ni, H. Lei, J. C. Fettinger, B. D. Ellis, G. L. Long, M. Brynda, P. P. Power. *Angew. Chem. Int. Ed.* **2008**, *47*, 9115.

[533] L. Gagliardi, B. O. Roos. *Chem. Soc. Rev.* **2007**, *36*, 893.

[534] B. O. Roos, L. Gagliardi. *Inorg. Chem.* **2006**, *45*, 803.

[535] L. Gagliardi, P. Pyykko, B. O. Roos. *Phys. Chem. Chem. Phys.* **2005**, *7*, 2415.

[536] R. Ahlrichs, M. Bar, M. Haser, H. Horn, C. Kolmel. *Chem. Phys. Lett.* **1989**, *162*, 165.

[537] J. P. Perdew, A. Zunger. *Phys. Rev. B* **1981**, *23*, 5048.

[538] B. O. Roos, P. R. Taylor, P. E. M. Siegbahn. *Chem. Phys.* **1980**, *48*, 157.

[539] K. Andersson, P.-Å. Malmqvist, B. O. Roos. *J. Chem. Phys.* **1992**, *96*, 1218.

[540] F. Aquilante, L. De Vico, N. Ferré, G. Ghigo, P.-Å. Malmqvist, T. Pedersen, M. Pitonak, M. Reiher, B. O. Roos, L. Serrano-Andrés, M. Urban, V. Veryazov, R. Lindh. *J. Comput. Chem.* **2010**, *31*, 224.

[541] B. O. Roos, R. Lindh, P.-Å. Malmqvist, V. Veryazov, P. O. Widmark. *J. Phys. Chem. A* **2005**, *109*, 6575.

[542] B. O. Roos, R. Lindh, P.-Å. Malmqvist, V. Veryazov, P. O. Widmark. *J. Phys. Chem. A* **2004**, *108*, 2851.

[543] B. A. Hess. *Phys. Rev. A* **1986**, *33*, 3742.

[544] F. Aquilante, T. B. Pedersen, R. Lindh. *J. Chem. Phys.* **2007**, *126*, 194106.

[545] F. Aquilante, P.-Å. Malmqvist, T. B. Pedersen, A. Ghosh, B. O. Roos. *J. Chem. Theory Comput.* **2008**, *4*, 694.

[546] F. Aquilante, T. B. Pedersen, R. Lindh, B. O. Roos, A. S. De Meras, H. Koch. *J. Chem. Phys.* **2008**, *129*, 024113.

[547] F. Aquilante, T. K. Todorova, L. Gagliardi, T. B. Pedersen, B. Roos. *J. Chem. Phys.* **2009**, *131*, 034113.

[548] M. Brynda, L. Gagliardi, B. O. Roos. *Chem. Phys. Lett.* **2009**, *471*, 1.

[549] F. Weinhold, C. R. Landis. *Science* **2007**, *316*, 61.

[550] A. E. Reed, L. A. Curtiss, F. Weinhold. *Chem. Rev.* **1988**, *88*, 899.

[551] F. R. Wagner, A. Noor, R. Kempe. *Nat. Chem.* **2009**, *1*, 529.

[552] L. Gagliardi, B. O. Roos. *Inorg. Chem.* **2003**, *42*, 1599.

[553] F. Ferrante, L. Gagliardi, B. E. Bursten, A. P. Sattelberger. *Inorg. Chem.* **2005**, *44*, 8476.

[554] F. Poineau, L. Gagliardi, P. M. Forster, A. P. Sattelberger, K. R. Czerwinski. *Dalton Trans.* **2009**, 5954.

[555] F. Poineau, P. M. Forster, T. K. Todorova, L. Gagliardi, A. P. Sattelberger, K. R. Czerwinski. *Inorg. Chem.* **2010**, *49*, 6646.

[556] M. Frisch, G. Trucks, H. Schlegel, G. Scuseria, M. Robb, J. Cheeseman, G. Scalmani, V. Barone, B. Mennucci, G. Petersson, H. Nakatsuji, M. Caricato, X. Li, H. Hratchian, A. Izmaylov, J. Bloino, G. Zheng, J. Sonnenberg, M. Hada, M. Ehara, K. Toyota, R. Fukuda, J. Hasegawa, M. Ishida, T. Nakajima, Y. Honda, O. Kitao, H. Nakai, T. Vreven, J. M. andJr., J. Peralta, F. Ogliaro, M. Bearpark, J. Heyd, E. Brothers, K. Kudin, V. Staroverov, R. Kobayashi, J. Normand, K. Raghavachari, A. Rendell, J. Burant, S. Iyengar, J. Tomasi, M. Cossi, N. Rega, J. Millam, M. Klene, J. Knox, J. Cross, V. Bakken, C. Adamo, J. Jaramillo, R. Gomperts, R. Stratmann, O. Yazyev, A. Austin, R. Cammi, C. Pomelli, J. Ochterski, R. Martin, K. Morokuma, V. Zakrzewski, G. Voth, P. Salvador, J. Dannenberg, S. Dapprich, A. Daniels, Ö. Farkas, J. Foresman, J. Ortiz, J. Cioslowski, D. Fox, *Gaussian 09, RevisionB.01*, Gaussian, Inc., Wallingford CT, **2009**.

[557] S. I. Gorelsky, A. B. P. Lever. *J. Organomet. Chem.* **2001**, *635*, 187.

[558] S. I. Gorelsky, University of Ottawa, **2011**.

[559] P.-Å. Malmqvist. *Int. J. Quantum Chem.* **1986**, *30*, 479.

[560] B. O. Roos, P.-Å. Malmqvist. *Phys. Chem. Chem. Phys.* **2004**, *6*, 2919.

[561] F. A. Cotton, G. Wilkinson, C. A. Murillo, M. Bochmann, *Advanced Inorganic Chemsitry 6th ed.*, Wiley: New York, **1999**.

[562] F. A. Cotton, L. M. Daniels, C. A. Murillo, I. Pascual, H.-C. Zhou. *J. Am. Chem. Soc.* **1999**, *121*, 6856.

[563] M. Nippe, S. M. Goodman, C. G. Fry, J. F. Berry. *J. Am. Chem. Soc.* **2011**, *133*, 2856.

[564] J. F. Berry, F. A. Cotton, C. A. Murillo. *Inorg. Chim. Acta* **2004**, *357*, 3847.

[565] F. A. Cotton, L. M. Daniels, C. A. Murillo, H. C. Zhou. *Inorg. Chim. Acta* **2000**, *305*, 69.

[566] M. B. Hall. *Polyhedron* **1987**, *6*, 679.

[567] P. M. Atha, I. H. Hillier, A. A. Macdowell, M. F. Guest. *J. Chem. Phys.* **1982**, *77*, 195.

[568] C. J. Cramer, D. G. Truhlar. *Phys. Chem. Chem. Phys.* **2009**, *11*, 10757.

[569] G. Timmer, J. Berry. *Chem. Sci.* **2012**, *3*, 3038.

[570] I. Mayer. *Chem. Phys. Lett.* **1983**, *97*, 270.

[571] K. B. Wiberg. *Tetrahedron* **1968**, *24*, 1083.

[572] F. A. Cotton, S. A. Koch, M. Millar. *Inorg. Chem.* **1978**, *17*, 2084.

[573] J. F. Berry, E. Bill, E. Bothe, F. A. Cotton, N. S. Dalal, S. A. Ibragimov, N. Kaur, C. Y. Liu, C. A. Murillo, S. Nellutla, J. M. North, D. Villagran. *J. Am. Chem. Soc.* **2007**, *129*, 1393.

[574] F. A. Cotton, K. R. Dunbar, L. R. Falvello, M. Tomas, R. A. Walton. *J. Am. Chem. Soc.* **1983**, *105*, 4950.

[575] B. E. Bursten, F. A. Cotton, P. E. Fanwick, G. G. Stanley, R. A. Walton. *J. Am. Chem. Soc.* **1983**, *105*, 2606.

[576] P. A. Kozmin, T. B. Larina, M. D. Surazhskaya. *Russ. J. Coord. Chem.* **1982**, *8*, 451.

[577] F. A. Cotton, L. D. Gage. *Nouv. J. Chim.* **1977**, *1*, 441.